



THE UNIVERSITY OF QUEENSLAND  
AUSTRALIA

**Microstructure Formation in Reinforced Sn-Cu Lead-free Solder Alloys**

Mohd Arif Anuar Mohd Salleh

B. Eng., M.B.A., M. Eng.

*A thesis submitted for the degree of Doctor of Philosophy at  
The University of Queensland in 2016  
School of Mechanical and Mining Engineering*

## Abstract

Electronics manufacturers are pushing the limits in reducing the physical size of circuitry while simultaneously increasing the number of transistors to satisfy Moore's Law [1]. This includes investing in new materials, and configuring new ways to manufacture complex 3D (three dimensional) electronic packaging [1]. One key requirement of new materials and techniques is ensuring the high reliability of the resultant products in various challenging operating environments including thermal and mechanical extremes [2-4]. A viable method to enhance the properties and performance of a solder joint is by incorporation of reinforcement particles to the solder matrix, either by intrinsic or extrinsic methods. In this thesis a series of Sn-Cu Pb-free solder alloys with extrinsic or intrinsic phase reinforcement were manufactured and the microstructure and soldering behavior were investigated in detail.

Additions of extrinsic reinforcement in the form of nano-sized ceramic material were made using a microwave sintering powder metallurgy (PM) method, which is a viable method to improve the mechanical and thermal properties of Pb-free solder materials. In addition, the advanced processing routes ensures a homogenous distributions of reinforcement particles is present. To investigate the performance of the reinforced bulk solders including thermal and mechanical properties and relate this to the microstructure, samples were investigated using techniques such as synchrotron micro-XRF, HRTEM, SEM, XPS, dilatometry, DSC and shear and microhardness testing. A hypothesis of how reinforcement improves solder properties is developed and discussed. Synchrotron X-ray radiography imaging (SXRI) was used to analyse the development of microstructure and the complex interactions occurring in the solders. Based on the properties of the fabricated solder, the microwave sintering PM route was discussed as a promising method for the reinforcement of Pb-free solders.

The initial formation of interfacial IMC products was studied in Sn-Cu based solder alloys by in situ experiment techniques such as SXRI and UHV-TEM. The results provide direct experimental evidence of real-time initial  $\text{Cu}_6\text{Sn}_5$  layer development during soldering and also the stress creation and release events that arise due to the polymorphic transformations of the  $\text{Cu}_6\text{Sn}_5$  phase and the associated volumetric change.

In addition, the nucleation and growth behavior of primary intermetallics which can be considered an intrinsic reinforcing material in solder joints was studied. Here, the nucleation and growth behavior of primary  $\text{Cu}_6\text{Sn}_5$  and  $\beta\text{-Sn}$  crystals in some of the most commonly used solder alloys including Sn-0.7Cu and Sn-3.0Ag-0.5Cu is explained. This also includes the effects of Ni additions for refining primary  $\text{Cu}_6\text{Sn}_5$  in Sn-Cu solder joints. Using SXRI, observations were made during solder joint solidification, which is difficult using conventional methods. The initial nucleation and solidification kinetics of primary  $\text{Cu}_6\text{Sn}_5$  crystals were discussed.

The growth of primary and interfacial  $\text{Cu}_6\text{Sn}_5$  intermetallics after multiple reflow and annealing and the effect of this growth on the solder joint shear strength was studied to understand the effect of electronic component assembly processes on microstructure development. It was found that additions of  $\text{TiO}_2$  reinforcement were able to reduce the number and total length of primary  $\text{Cu}_6\text{Sn}_5$  particles and suppress the interfacial layer during multiple reflows. It is possible that  $\text{TiO}_2$  particles in intimate contact with the interfacial  $\text{Cu}_6\text{Sn}_5$  hinder the Cu dissolution paths. By reducing the undercooling, additions of  $\text{TiO}_2$  result in a lower average thickness in the interfacial IMC and a more stable growth morphology.

The collective results of this thesis demonstrate a detailed understanding of the manufacture of reinforced Sn-Cu Pb-free solder alloys and the mechanism of microstructure formation. The results are of significance scientifically and have industrial relevance and implications in controlling the microstructure and improving the performance and reliability of Pb-free solder joints.

## **Declaration by author**

This thesis is composed of my original work, and contains no material previously published or written by another person except where due reference has been made in the text. I have clearly stated the contribution by others to jointly-authored works that I have included in my thesis.

I have clearly stated the contribution of others to my thesis as a whole, including statistical assistance, survey design, data analysis, significant technical procedures, professional editorial advice, and any other original research work used or reported in my thesis. The content of my thesis is the result of work I have carried out since the commencement of my research higher degree candidature and does not include a substantial part of work that has been submitted to qualify for the award of any other degree or diploma in any university or other tertiary institution. I have clearly stated which parts of my thesis, if any, have been submitted to qualify for another award.

I acknowledge that an electronic copy of my thesis must be lodged with the University Library and, subject to the policy and procedures of The University of Queensland, the thesis be made available for research and study in accordance with the Copyright Act 1968 unless a period of embargo has been approved by the Dean of the Graduate School.

I acknowledge that copyright of all material contained in my thesis resides with the copyright holder(s) of that material. Where appropriate I have obtained copyright permission from the copyright holder to reproduce material in this thesis.



## **Publications during candidature**

### **Peer-reviewed journal papers**

1. K. Nogita, **M. A. A. Mohd Salleh**, E. Tanaka, G. Zeng, S. D. McDonald, S. Matsumura, In-situ TEM observations of Cu<sub>6</sub>Sn<sub>5</sub> polymorphic transformations in reaction layers between Sn-0.7Cu solder and Cu substrate. **JOM** (2016). Accepted on the 25<sup>th</sup> May 2016.
2. **M. A. A. Mohd Salleh**, S. D. McDonald, C.M. Gourlay, S.A. Belyakov, H. Yasuda, K. Nogita, Effect of Ni on the formation and growth of primary Cu<sub>6</sub>Sn<sub>5</sub> intermetallics in Sn-0.7wt%Cu solder pastes on Cu substrates during soldering process, **Journal of Electronic Materials**, 45 Issue 1 (2016) 154-163.
3. **M. A. A. Mohd Salleh**, S. D. McDonald, Y. Terada, H. Yasuda, K. Nogita, Development of a microwave sintered TiO<sub>2</sub> reinforced Sn-0.7wt%Cu-0.05wt%Ni alloy, **Materials & Design**, 82 (2015) 136-147.
4. **M. A. A. Mohd Salleh**, S. D. McDonald, H. Yasuda, A. Sugiyama, K. Nogita, Rapid Cu<sub>6</sub>Sn<sub>5</sub> growth at liquid Sn/solid Cu interfaces, **Scripta Materialia**, 100 (2015) 17-20.
5. **M. A. A. Mohd Salleh**, S. D. McDonald, H. Yasuda, A. Sugiyama, K. Nogita, In-situ soldering process technique by synchrotron X-ray imaging, **Applied Mechanics and Materials**, 754-755 (2015) 508-512.
6. **M. A. A. Mohd Salleh**, S. D. McDonald, K. Nogita, Non-metal reinforced lead-free composite solder fabrication methods and its reinforcing effects to the suppression of intermetallic formation: Short review, **Applied Mechanics and Materials**, 421 (2013) 260-266.
7. **M. A. A. Mohd Salleh**, Al Bakri, A.M.M., Somidin, F., Sandu, A.V., Saud, N., Kamaruddin, H., McDonald, S.D., Nogita, K. A comparative study of solder properties of Sn-0.7Cu lead-free solder fabricated via the powder metallurgy and casting methods, **Revista de Chimie**, 64 (7) (2013), 725-728.

### **Conference presentations**

1. **M. A. A. Mohd Salleh**, C.M. Gourlay, J.W. Xian, S.A. Belyakov, H. Yasuda, S. D. McDonald, K. Nogita, Nucleation events and growth behavior of primary Cu<sub>6</sub>Sn<sub>5</sub> intermetallic and  $\beta$ -Sn crystals in Pb-free solder joints, 2016 TMS Annual Meeting & Exhibition, Nashville, Tennessee, USA, 14-18 February (2016).

2. **M. A. A. Mohd Salleh**, H. Yasuda, S. D. McDonald, K. Nogita, Development of a microwave sintered TiO<sub>2</sub> reinforced Sn-0.7wt%Cu-0.05wt%Ni solder alloy, 2016 TMS Annual Meeting & Exhibition, Nashville, Tennessee, USA, 14-18 February (2016).
3. **M. A. A. Mohd Salleh**, J. Read, X. Tran, S. D. McDonald, K. Nogita, Effects of trace additions of phosphorus in Sn-Cu-Ni-Ge solders, 2016 TMS Annual Meeting & Exhibition, Nashville, Tennessee, USA, 14-18 February (2016).
4. **M. A. A. Mohd Salleh**, C.M. Gourlay, J.W. Xian, S.A. Belyakov, H. Yasuda, S. D. McDonald, K. Nogita, In-situ synchrotron real-time imaging of soldering: Experimental methods and post experiment analysis, 24<sup>th</sup> Australian Conference on Microscopy & Microanalysis, Melbourne, Australia, 31 January – 4 February (2016).
5. **M. A. A. Mohd Salleh**, R. M. Said, N. Saud, H. Yasuda, S. D. McDonald, K. Nogita, In-situ soldering process imaging of Sn-Cu lead-free solder systems on Cu substrate: Initial intermetallic compound formation and its subsequent growth, 1<sup>st</sup> Electronic Packaging Interconnect Technology Symposium (EPITS), Penang, Malaysia, 21 November (2015).
6. **M. A. A. Mohd Salleh**, S. D. McDonald, H. Yasuda, A. Sugiyama, K. Nogita, In-situ soldering process imaging of Sn-Cu lead-free solder systems on Cu substrate: Initial intermetallic compound formation and its subsequent growth. 2015 TMS Annual Meeting & Exhibition, Orlando, Florida, USA, 15-19 March (2015).
7. **M. A. A. Mohd Salleh**, S. D. McDonald, K. Nogita, In-situ imaging of Sn-Cu lead-free soldering on Cu substrates: Intermetallic compound formation and growth, EAIT Postgraduate Conference, University of Queensland, Australia, 10 June (2015).
8. **M. A. A. Mohd Salleh**, S. D. McDonald, H. Yasuda, A. Sugiyama, K. Nogita, In-situ soldering process technique by synchrotron X-ray imaging, 3rd International Conference on Advanced Materials Engineering and Technology (ICAMET), Vietnam, 4-5 December (2014).
9. **M. A. A. Mohd Salleh**, S. D. McDonald, K. Nogita, The development of Sn-Cu based reinforced composite lead-free solder, EAIT Postgraduate Conference, University of Queensland, Australia, 11 June (2014).
10. **M. A. A. Mohd Salleh**, S. D. McDonald, K. Nogita, Non-metal reinforced lead-free composite solder fabrication methods and its reinforcing effects to the suppression of intermetallic formation: Short review, 4th International Conference on Information Technology for Manufacturing Systems (ITMS), Auckland, New Zealand, 28-29th August (2013).

### **Publications included in this thesis**

1. **M. A. A. Mohd Salleh**, S. D. McDonald, Y. Terada, H. Yasuda, K. Nogita, Development of a microwave sintered TiO<sub>2</sub> reinforced Sn-0.7wt%Cu-0.05wt%Ni alloy, **Materials & Design**, 82 (2015) 136-147. – incorporated as Chapter 3.

Contributor	Statement of contribution
Author Mohd Arif Anuar Mohd Salleh (Candidate)	Designed experiments (90%) Wrote the paper (80%)
Author Stuart D. McDonald	Wrote and edited paper (10%)
Author Yasuko Terada	Assisted with synchrotron micro-X-ray fluorescence (5%)
Author Hideyuki Yasuda	Assisted with synchrotron micro-X-ray fluorescence (5%)
Author Kazuhiro Nogita	Designed experiments (10%) Wrote and edited paper (10%)

2. **M. A. A. Mohd Salleh**, S. D. McDonald, H. Yasuda, A. Sugiyama, K. Nogita, In-situ soldering process technique by synchrotron X-ray imaging, **Applied Mechanics and Materials**, 754-755 (2015) 508-512. – incorporated as Chapter 3.

Contributor	Statement of contribution
Author Mohd Arif Anuar Mohd Salleh (Candidate)	Designed experiments (90%) Wrote the paper (80%)
Author Stuart D. McDonald	Wrote and edited paper (10%)
Author Hideyuki Yasuda	Assisted with synchrotron X-ray radiography (5%)
Author Akira Sugiyama	Assisted with synchrotron X-ray radiography (5%)
Author Kazuhiro Nogita	Designed experiments (10%) Wrote and edited paper (10%)

3. **M. A. A. Mohd Salleh**, S. D. McDonald, H. Yasuda, A. Sugiyama, K. Nogita, Rapid  $\text{Cu}_6\text{Sn}_5$  growth at liquid Sn/solid Cu interfaces, **Scripta Materialia**, 100 (2015) 17-20. – incorporated as Chapter 4.

Contributor	Statement of contribution
Author Mohd Arif Anuar Mohd Salleh (Candidate)	Designed experiments (90%) Wrote the paper (80%)
Author Stuart D. McDonald	Wrote and edited paper (10%)
Author Hideyuki Yasuda	Assisted with synchrotron X-ray radiography (5%)
Author Akira Sugiyama	Assisted with synchrotron X-ray radiography (5%)
Author Kazuhiro Nogita	Designed experiments (10%) Wrote and edited paper (10%)

4. K. Nogita, **M. A. A. Mohd Salleh**, E. Tanaka, G. Zeng, S. D. McDonald, S. Matsumura, In-situ TEM observations of  $\text{Cu}_6\text{Sn}_5$  polymorphic transformations in reaction layers between Sn-0.7Cu solder and Cu substrate. **JOM** (2016). Accepted on the 25<sup>th</sup> May 2016. – incorporated as Chapter 4.

Contributor	Statement of contribution
Author Kazuhiro Nogita	Designed experiments (50%) Wrote and edited paper (50%)
Author Mohd Arif Anuar Mohd Salleh (Candidate)	Designed experiments (50%) Wrote and edited paper (40%)
Author Eishi Tanaka	Assisted with high voltage TEM (5%)
Author Guang Zeng	Wrote and edited paper (5%)
Author Stuart D. McDonald	Wrote and edited paper (5%)
Author Syo Matsumura	Assisted with high voltage TEM (5%)

5. **M. A. A. Mohd Salleh**, S. D. McDonald, C.M. Gourlay, S.A. Belyakov, H. Yasuda, K. Nogita, Effect of Ni on the formation and growth of primary Cu<sub>6</sub>Sn<sub>5</sub> intermetallics in Sn-0.7wt%Cu solder pastes on Cu substrates during soldering process, **Journal of Electronic Materials**, 45 Issue 1 (2016) 154-163. – incorporated as Chapter 5.

Contributor	Statement of contribution
Author Mohd Arif Anuar Mohd Salleh (Candidate)	Designed experiments (85%) Wrote the paper (85%)
Author Stuart D. McDonald	Wrote and edited paper (5%)
Author Christopher M. Gourlay	Designed experiments (5%) Wrote and edited paper (5%)
Author Sergey A. Belyakov	Assisted with annealing and microscopy observation (5%)
Author Hideyuki Yasuda	Assisted with synchrotron X-ray radiography (5%)
Author Kazuhiro Nogita	Designed experiments (10%) Wrote and edited paper (5%)

6. **M. A. A. Mohd Salleh**, S. D. McDonald, C.M. Gourlay, H. Yasuda, K. Nogita, **Suppression of Cu<sub>6</sub>Sn<sub>5</sub> in TiO<sub>2</sub> reinforced solder joints after multiple reflow cycles**, **Materials & Design**, 108 (2016) 418-428. – incorporated as Chapter 6.

Contributor	Statement of contribution
Author Mohd Arif Anuar Mohd Salleh (Candidate)	Designed experiments (85%) Wrote the paper (85%)
Author Stuart D. McDonald	Wrote and edited paper (5%)
Author Christopher M. Gourlay	Designed experiments (5%) Wrote and edited paper (5%)
Author Hideyuki Yasuda	Assisted with synchrotron X-ray radiography (5%)
Author Kazuhiro Nogita	Designed experiments (10%) Wrote and edited paper (5%)

**Contributions by others to the thesis**

No contributions by others

**Statement of parts of the thesis submitted to qualify for the award of another degree**

None.

## **Acknowledgements**

My greatest appreciation goes to my supervisor, Associate Professor Kazuhiro Nogita for his invaluable advices and knowledge, providing encouragement throughout the research and study. I would also like to express my gratitude to my co-supervisor, Dr Stuart McDonald and Professor Han Huang, for his guidance and advices throughout the whole time. Without them, this whole research study could never run smoothly.

I would like to also thank Dr Christopher Gourlay, Dr Sergey Belyakov and Mr. Jing Wei for their support and discussions during my 3 month attachment period at Imperial College, London, England.

Many thanks to the Nihon Superior Centre for the Manufacture of Electronic Materials staff and group members; Mr. Jonathan Read, Dr Jerome Wu, Mr. Guang Zeng and Mr. Xuan Quy Tran. I sincerely thank Professor H. Yasuda from Kyoto University for his valuable technical support and advice for synchrotron experiments and other researchers in the team. Without them, most of the analysis and testing results obtained in this study could never be satisfactory.

I would like to acknowledge the Ministry of Higher Education Malaysia and Universiti Malaysia Perlis (UniMAP) for providing me a scholarship to pursue my study. Support of financial and raw materials from Nihon Superior (Japan) Ltd. and Nihon Superior (Malaysia) throughout this research study are indeed appreciated. Many thanks to Dr Yasuko Terada and Dr Kentaro Uesugi from SPring-8 Synchrotron Japan for providing me great opportunities to run my experiments.

Most importantly, not to forget, thanks to my parents Mohd Salleh Hj Din and Maziah Onn, my wife Noor Farhani and son Muhammad Danish for their continuous support, encouragement and understanding during the period of my study.

**Keywords**

Leadfree soldering, nanocomposite, reinforcement, sintering, synchrotron, kinetics, nucleation, interfacial reaction, intermetallic, solidification

**Australian and New Zealand Standard Research Classifications (ANZSRC)**

ANXSRC code: 091207, Metals and Alloy materials, 100%

**Fields of Research (FoR) Classification**

FoR code: 0912, Materials Engineering, 100%



# Table of Contents

Abstract .....	i
Acknowledgements .....	x
List of Figures .....	xiv
List of Tables .....	xvi
List of Abbreviations .....	xvii
<b>Chapter 1 Introduction .....</b>	<b>1</b>
1.1 Motivation .....	1
1.2 Problem Statement .....	3
1.3 Research Study Objectives .....	3
1.4 Thesis Structure.....	4
<b>Chapter 2 Literature Review .....</b>	<b>6</b>
2.1 The development of lead-free solders .....	6
2.2 The development of reinforced solders.....	8
2.3 Fabrication methods of reinforced solders .....	10
2.4 Interfacial intermetallic compound (IMC) layer of reinforced solder .....	16
2.5 Microstructure of reinforced solder .....	22
2.6 Mechanical properties of reinforced solder .....	29
2.7 Summary and remarks .....	33
<b>Chapter 3 Fabrication method of extrinsic ceramic reinforced solders and methods of in-situ soldering observations using synchrotron X-ray radiography imaging (SXRI) techniques. ....</b>	<b>35</b>
Paper 1: Development of a microwave sintered TiO <sub>2</sub> reinforced Sn-0.7wt%Cu-0.05wt%Ni alloy .....	36
Paper 2: In-situ soldering process technique by synchrotron X-ray imaging .....	66
<b>Chapter 4 Interfacial intermetallic compound (IMC) layer formation in Sn-Cu solders in early stages of soldering and phase transformation.....</b>	<b>75</b>
Paper 3: Rapid Cu <sub>6</sub> Sn <sub>5</sub> growth at liquid Sn/solid Cu interfaces .....	76
Paper 4: In-situ TEM observations of Cu <sub>6</sub> Sn <sub>5</sub> polymorphic transformations in reaction layers between Sn-0.7Cu solder and Cu substrate .....	87
<b>Chapter 5 Nucleation and growth behavior of primary intermetallics as an intrinsic reinforcing material in solder joints.....</b>	<b>103</b>
Paper 5: In situ imaging of microstructure formation in electronic interconnects .....	104
Paper 6: Effect of Ni on the formation and growth of primary Cu <sub>6</sub> Sn <sub>5</sub> intermetallics in Sn-0.7wt%Cu solder paste on Cu substrates during the soldering process.....	134

**Chapter 6 Assembly processing and operating conditions: the effects of intrinsic and extrinsic reinforcement of solder joints.** ..... 154

    Paper 7: Suppression of Cu<sub>6</sub>Sn<sub>5</sub> in TiO<sub>2</sub> reinforced solder joints after multiple reflow cycles ..... 155

    Paper 8: Effects of Ni and TiO<sub>2</sub> additions in as-reflowed and annealed Sn0.7Cu solders on Cu substrates ..... 184

**Chapter 7 Summary and future work** ..... 207

**Bibliography** ..... 210

## List of Figures

Figure 1: The global initiatives and regulations implementation timeline for the restriction of the use of toxic materials in electronic products [37]. .....	7
Figure 2 : Reinforced Pb-free solder classification.....	10
Figure 3: Methods of reinforced solder fabrication process [50]. .....	11
Figure 4: Common powder metallurgy process method [80].....	13
Figure 5: Temperature distribution samples for: (a) conventional heating (b) microwave heating (c) hybrid microwave heating [18]. .....	14
Figure 6: Bonding of particles during sintering [86].....	15
Figure 7: Pore structure reduction during sintering [86]. .....	16
Figure 8: Prism like intermetallic compound formation of Sn-3.5Ag-0.5Cu-1Al <sub>2</sub> O <sub>3</sub> [57]. ....	18
Figure 9: The relationship of intermetallic compound thickness to ageing time and temperature for (a) Sn-3.5Ag-0.5Cu and (b) Sn-3.5Ag-0.5Cu + nano-size TiO <sub>2</sub> reinforced solder [105]. .....	19
Figure 10: Backscattered images of (a) Sn-Ag-Cu solder after 10 days annealing, (b) Sn-Ag-Cu-0.5SrTiO <sub>3</sub> solder after 10 days annealing, (c) Sn-Ag-Cu solder after 40 days annealing and (d) Sn-Ag-Cu-0.5SrTiO <sub>3</sub> solder after 40 days annealing [106].....	21
Figure 11: Backscattered images of interfacial Cu <sub>6</sub> Sn <sub>5</sub> layer on (a) Sn-3.5Ag-0.7Cu after one time reflow (b) Sn-3.5Ag-0.7Cu-Mo after one time reflow (c) Sn-3.5Ag-0.7Cu after six time reflow and (d) Sn-3.5Ag-0.7Cu-Mo after six time reflow [108]. .....	22
Figure 12: Microstructure of as-solidified (a) Sn–6.5Cu and (b) Sn–6.5Cu–0.2Al [111]. ....	23
Figure 13: Backscattered electron SEM images of etched sample of: (a) Sn–0.7Cu, (b) Sn–0.7Cu–2Ag and (c) Sn–0.7Cu–2In and (d) image of selected EDS area conducted in the study [112]. .....	24
Figure 14: (a) Microstructure of Sn–Ag–Zn (b) with 0.05% SiC additions and (c) with 0.1% SiC additions [113]. .....	25
Figure 15: Backscattered electron SEM images (a) Sn-3.0-0.5Ag solder matrix, (b) Sn-3.0-0.5Ag-0.7SiC solder matrix (c) EDS result analysis of (a), and (d) EDS result of (b) [46]. .	26
Figure 16: Backscattered electron SEM images of Sn-1.0Ag-0.5Cu-0.75SiC with sub-grains of primary $\beta$ -Sn [58]. .....	26
Figure 17: Backscattered electron SEM images of (a) Sn-Ag-Cu, (b) Sn-Ag-Cu-0.25Al <sub>2</sub> O <sub>3</sub> , (c) Sn-Ag-Cu-0.5Al <sub>2</sub> O <sub>3</sub> and (d) Sn-Ag-Cu-1Al <sub>2</sub> O <sub>3</sub> [44]. .....	27
Figure 18: Backscattered electron SEM images of (a) Sn-Ag-Cu, (b) Sn-Ag-Cu–0.5Al <sub>2</sub> O <sub>3</sub> , and (c) Sn-Ag–Cu–1Al <sub>2</sub> O <sub>3</sub> [57]. .....	27

Figure 19: Backscattered electron SEM images of (a, b) Sn–Ag–Cu and (c, d) Sn–Ag–Cu–1ZrO <sub>2</sub> soldered on Cu-OSP substrate for 5 minutes (a and c) and 30 minutes (b and d) at 250 °C [115].	28
Figure 20: Creep test results comparing Sn–0.7Cu, Sn–0.7Cu–In and Sn–0.7Cu–Ag [112].	29
Figure 21: Hardness result of SiC reinforcement additions to Sn–Ag–Zn solders [113].	30
Figure 22: Shear strength of reinforced Al <sub>2</sub> O <sub>3</sub> Sn-3.0Ag-0.5Cu solder joint [120].	31
Figure 23: Secondary electron SEM images of fractured surface Ag modified graphene reinforced Sn-Ag-Cu solder [123].	31
Figure 24: Secondary electron image of MWCNT reinforced Sn-3.5Ag-0.7Cu tensile fracture surface [124].	32
Figure 25: Tensile strength results of TiO <sub>2</sub> reinforced solder comparing with non-reinforced Sn-0.7Cu solder [128].	32

## **List of Tables**

Table 1: Pb-free solder categories and available alloys in current market [38]. .....	8
---	---

## List of Abbreviations

Alumina ( $\text{Al}_2\text{O}_3$ )	Powder metallurgy (PM)
Aluminum (Al)	Printed circuit board (PCB)
Cadmium (Cd)	Restriction of hazardous Substances Directive (RoHS)
Carbon nanotubes (CNTs)	Scanning electron microscopy (SEM)
Cobalt (Co)	Silicon carbide (SiC)
Copper (Cu)	Silicon nitride ( $\text{Si}_3\text{N}_4$ )
Differential scanning calorimetry (DSC)	Silver (Ag)
Energy dispersive X-ray spectroscopy (EDS)	Single-wall carbon nanotubes (SWCNT)
Electronic waste recycling act (EWRA)	Synchrotron X-ray radiography imaging (SXRI)
European Union (EU)	Tin (Sn)
Fraction solid (fs)	Tin oxide ( $\text{SnO}_2$ )
Gold (Au)	Titanium oxide ( $\text{TiO}_2$ )
Hexavalent chromium ( $\text{Cr}^{6+}$ )	Titanium diboride ( $\text{TiB}_2$ )
High resolution transmission electron microscopy (HRTEM)	Transmission electron microscopy (TEM)
Intermetallic compounds (IMC)	Ultra-high voltage transmission electron microscopy (UHV-TEM)
Iron (Fe)	Waste from Electronic Equipment (WEEE)
Lead (Pb)	X-ray fluorescence (XRF)
Mercury (Hg)	X-ray photoelectron spectroscopy (XPS)
Metal matrix composite (MMC)	Zinc (Zn)
Molybdenum (Mo)	Zirconia ( $\text{ZrO}_2$ )
Multi-wall carbon nanotubes (MWCNT)	
National Electronics Manufacturing Initiative (NEMI)	
Nickel (Ni)	
Polybrominated diphenyl ether (PBDE)	
Polybrominated biphenyls (PBB)	
Polyhedral oligomeric silsesquioxane (POSS)	

# Chapter 1 Introduction

## 1.1 Motivation

The electronic industry is constantly adapting to the requirements of the latest generation electronic devices. The advances in electronics today are accompanied by advances in soldering technology since interconnect materials such as solders are used in electronic packaging to electrically and mechanically join components to form functional circuits. In electronic assemblies, the solder alloy plays a critical role in performance and reliability [5, 6].

Development of solder alloys has also been driven by a need to reduce the consumption of lead (Pb) in the Sn-Pb solders used in previous generation electronic packaging industries. Initiatives such as Waste from Electronic Equipment (WEEE) and Restriction of hazardous Substances Directive (RoHS) which took effect on 1 July 2006 [7] have seen the EU minimize the use of hazardous substances such as Pb, halogen (Hg), cadmium (Cd), hexavalent chromium ( $\text{Cr}^{6+}$ ), polybrominated biphenyls (PBB) and polybrominated diphenyl ether (PBDE). In addition, there is a consumer preference for using environmental safe products as the concern on health awareness due to the toxicity of certain materials used in conventional electronic products have increased. Due to legislation implementation throughout the world and high demand in the consumer product market, the electronic industries have been focusing on the development of Pb-free solders. This change has been driven with the help of other government and public agencies throughout the world. Recently, Sn-Ag-Cu or known as SAC solder are the most widely used commercial Pb-free solder in high technology of electronic products while Sn-Cu and Sn-Cu-Ni are used as a low cost solder alternative in wave soldering for large electronic interconnections. Although currently there is a wide range of commercial Pb-free solders provided by the solder manufacturers, there is still a need to develop new Pb-free solders to meet the rapidly advancing technology in electronic products that requires high reliability solder joints in extreme environments. This includes the requirement of miniaturization of interconnections in an electronic product with higher functional densities [8, 9].

Amongst the numerous research activities aimed at improving the Pb-free solder properties and performance is the use of reinforcing additions. This viable method of enhancing the Pb-free solder properties and solder joint performance involves the use of a reinforcing phase either intrinsic or extrinsic, embedded in the solder matrix [10]. In the early stages of solder composite technology development, Guo [11] stressed that the development of composite Pb-free solder is likely to improve the service temperature capabilities and thermal stability of the solder joints. In addition, these reinforced solder could have improved joint strength [10]. Shen and Chan [12] discussed the benefits in terms of enhanced creep strength and thermo-mechanical fatigue resistance of solder materials while outlining the latest nano-composite solder development studies.

Generally, a composite solder involves a eutectic solder alloy reinforced with other materials to improve the mechanical properties. Reinforcing materials in solder alloys may be present in the matrix intrinsically or introduced by additions (extrinsic). Examples of intrinsic reinforcement in Pb-free solder solders include the commonly occurring  $\text{Cu}_6\text{Sn}_5$  or  $\text{Ag}_3\text{Sn}$  intermetallic phases [13-15].

Ceramic reinforcement is an example of an extrinsic reinforcing. Ceramic reinforcing is an approach to enhance the alloy based solder matrix mechanical properties without the concern of new excessive phase formation during either fabrication or normal product use. In the fabrication of reinforced Pb-free solders, one of the best methods of ensuring the particle is homogeneously distributed in the matrix is by utilizing the powder metallurgy method [16]. However, using conventional sintering, requires a high amount of energy, cost and time. To overcome the drawbacks of the conventional sintering process, Gupta et al. [17] have introduced a microwave sintering method for producing solder composite materials. With the unique characteristic heating mechanism present in the microwave sintering technique, significant advantages can be imparted to mechanical properties of the sintered material [18-20]. The homogenous distribution of reinforcement and the improvement of physical and mechanical properties makes this sintering technique an attractive method to investigate in the manufacture of solder alloys.



## 1.2 Problem Statement

Among commercial Pb-free solders in the current market, the Sn-0.7Cu solder alloy is the most economical solder widely used in the wave soldering processes [21]. However, Sn-0.7Cu alloys are known to result in poor mechanical properties as a result of high interfacial intermetallic compound (IMC) layer growth rate and normally couples with a thick  $\text{Cu}_3\text{Sn}$  interfacial layer that leads to serious reliability issues [22].

Recent research on intrinsic  $\text{Cu}_6\text{Sn}_5$  or  $\text{Ag}_3\text{Sn}$  intermetallics reinforcement have resulted in the improvement of creep and thermomechanical properties of Pb-free solders [13-15]. In addition, extrinsic reinforcement particles such as silicon carbide ( $\text{SiC}$ ), alumina ( $\text{Al}_2\text{O}_3$ ), zirconia ( $\text{ZrO}_2$ ), tin oxide ( $\text{SnO}_2$ ), titanium oxide ( $\text{TiO}_2$ ) and silicon nitride ( $\text{Si}_3\text{N}_4$ ) additions, have also shown solder property improvements [23-36]. These ceramic reinforced solders are also reported to prevent or minimise the growth of interfacial IMCs. An in depth understanding of reinforcing effects and their interactions during soldering are needed to further develop Sn-Cu Pb-free solder composite technology.

## 1.3 Research Study Objectives

With current legislative demands and emerging technologies, solder joints of higher reliability and dimensional stability are in demand. Thus it is important for manufacturers and researchers to enhance current available solder performance or to synthesize future solder materials while limiting manufacturing costs. In achieving these goals, it is important to fully understand the properties and performance of the synthesized Pb-free solder and the subsequent solder joints. This study relates to enhancing the performance of several eutectic solder systems by using reinforcements and has the following objectives:

1. To investigate the effects of ceramic reinforcement additions and microwave sintering on the physical, thermal and mechanical properties of reinforced solders. This includes an understanding of the effects of reinforcement on the thermal and mechanical properties of the solder.
2. To investigate the interfacial  $\text{Cu}_6\text{Sn}_5$  growth kinetics during early stages of soldering and the phase transformation mechanisms in Sn-Cu solder joint by developing characterisation methods for in situ observations including ultra-high voltage

transmission electron microscopy (UHV-TEM) and in situ synchrotron X-ray radiography imaging (SXRI).

3. To investigate the nucleation and growth behavior of intrinsic reinforcing materials during soldering focusing on primary  $\text{Cu}_6\text{Sn}_5$  intermetallics in soldered joints.
4. To investigate the effect of assembly processing and operating condition on intrinsic and extrinsic reinforced solder joints.

## **1.4 Thesis Structure**

This thesis is largely presented as a collection of peer-reviewed published papers, supplemented with accompanying text to address the thesis objectives and is presented in the following chapters:

Chapter 1 – Introduction.

Chapter 2 – Literature review.

This chapter is a comprehensive review on the development of reinforced Pb-free solder alloys.

Chapter 3 - Fabrication method of extrinsic ceramic reinforced solders and methods of in-situ soldering observations using synchrotron X-ray radiography imaging (SXRI) techniques.

This chapter covers the methodology used in the development of microwave sintered  $\text{TiO}_2$  reinforced solder including investigating the mechanical and thermal properties of the solder material. It also covers the developed method of an SXRI technique for in situ soldering observation used throughout the study.

Chapter 4 - Interfacial intermetallic compound (IMC) layer formation in Sn-Cu solders in early stages of soldering and phase transformation.

This chapter covers a detailed study on the initial growth kinetics of interfacial  $\text{Cu}_6\text{Sn}_5$  of common base reinforced solder materials during the soldering and its phase transformation using in situ techniques.

Chapter 5 - Nucleation and growth behavior of primary intermetallics as an intrinsic reinforcing material in solder joints.

This chapter is an in-depth study on the nucleation and growth of primary  $\text{Cu}_6\text{Sn}_5$  during solidification and the effect of trace element additions such as Ni on primary  $\text{Cu}_6\text{Sn}_5$  formation.

Chapter 6 - Assembly processing and operating conditions: the effects of intrinsic and extrinsic reinforcement of solder joints.

This chapter covers the effect of assembly processing and operating conditions on the mechanical shear strength of intrinsic and extrinsic reinforced solder joints. This includes a focus on the effects of multiple-reflow and annealing conditions on the solder ball joint strength.

Chapter 7 Summary and future work.

# Chapter 2 Literature Review

A comprehensive review of advances in the development of reinforced Sn-Cu Pb-free solders is given in this chapter. The chapter reviews recent studies relating to reinforced Pb-free solders regarding solder material development, reactions during solidification, interfacial reactions and improvements to solder properties.

## 2.1 The development of lead-free solders

Solder materials are widely used as electronic interconnections in electronic circuits connecting one device to another. In the old days, Pb-containing solders were mostly used in the electronic industry. One of the most typical Pb solders used in the electronic industry is the eutectic Sn-37Pb solder alloy since it provides a wide range of benefits. For example, this solder alloy has a relatively low melting point, is easy for manufacturing and rework for assemblies, and has excellent ductility and solder joint reliability. Pb-containing solders were widely used until the rise of environmental and health awareness, and in the last decade have become banned due to the toxicity content. The concern over the toxicity of electronic products originates from the toxic waste produced by manufacturers and electronic products disposed of by consumers. Toxic elements normally used in electronic assemblies are banned by the European Union (EU). These elements include Pb, Hg, Cd, Cr<sup>6+</sup>, PBB and PBDE [7].

In the last decade, various programs and legislations took place to ban the use of toxic materials in electronic products, particularly lead. In the early stages of implementation, the United States, through National Electronics Manufacturing Initiative (NEMI), took the initiative in searching for solutions to the implementation of the toxic materials restriction in the manufacturing of electronic products. This initiative had been expanded to other countries such as in Europe and Japan. In Europe, the RoHS and WEEE regulations ban the use of Pb-containing solders. While in 2001, in Japan, the Enforcement Order of the Law for Promotion of Effective Utilization of Resources restricted the usage of Pb in electronic products. Since then, the RoHS, which was originally initiated in Europe in 2002, took effect in 2005 and until now has been widely used in most countries around the world. The initiatives and regulations implementation timeline for the restriction of the use of toxic materials in electronic products, including the usage of Pb is summarized in Figure 1 [37].

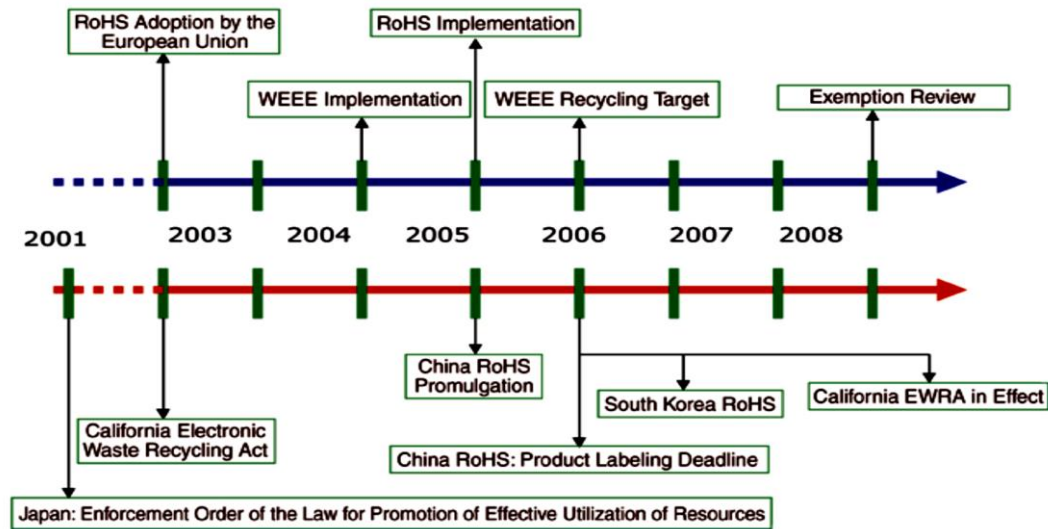


Figure 1: The global initiatives and regulations implementation timeline for the restriction of the use of toxic materials in electronic products [37].

Since the implementation of RoHS, manufacturers and researchers have worked closely in producing solder materials that could meet current processing demands and contribute to product reliability. Various properties need to be considered in the development of new Pb-free solders which covers the properties related to the manufacturing of and the performance and reliability of the solder joints. Properties related to the manufacturing covers its liquidus temperature, wettability performance with the substrate, manufacturability into various solder forms such as solder bars, wire and paste, recyclability, availability of materials and cost [5]. On the other hand, properties related to the performance and reliability of the solder joints covers the electrical and thermal conductivity, coefficient of thermal expansion (CTE), thermo-mechanical properties, mechanical properties such as shear and tensile, creep resistance, fatigue and corrosion resistance [5].

Currently, there are various commercial Pb-free solders on the market. However, there is still a need to develop new solder material that meets current challenging technology requirements. As electronic technology emerges and becomes more sophisticated, there is a need to produce a highly reliable solder joint. In addition to that, the suitability of manufacturing using current soldering processes needs to be evaluated. Current typical commercial Pb-free solder alloys can also be categorised based on its liquidus temperature application range including low melting temperature ( $<180\text{ }^{\circ}\text{C}$ ), low-mid range melting temperature ( $180\text{-}200\text{ }^{\circ}\text{C}$ ), middle range melting temperature ( $200\text{-}230\text{ }^{\circ}\text{C}$ ) and high melting

temperature range ( $>230\text{ }^{\circ}\text{C}$ ). Table 1 shows the typical Pb-free solder categories and available alloys on the current market [38].

Table 1: Pb-free solder categories and available alloys on the current market [38].

Category	Pb-free Solder Alloy	Liquidus Temperature, $^{\circ}\text{C}$
Low melting temperature ( $<180\text{ }^{\circ}\text{C}$ )	In-48Sn	118
	Sn-58Bi	138
	Sn-57Bi-1Ag	138
	In-3Ag	143
Low-mid range melting temperature ( $180\text{-}200\text{ }^{\circ}\text{C}$ )	In-9Zn	199
Middle range melting temperature ( $200\text{-}230\text{ }^{\circ}\text{C}$ )	Sn-2.5Ag-0.8Cu-0.5Sb	217-218
	Sn-3.0Ag-0.5Cu	217-218
	Sn-4.0Ag-0.5Cu	217-218
	Sn-3.5Ag	221
	Sn-5Ag	221-240
	Sn-0.7Cu-0.05Ni	227
	Low silver Sn-Ag-Cu	227
	Sn-0.7Cu	227
High melting temperature ( $>230\text{ }^{\circ}\text{C}$ )	Sn-3Sb	232-238
	Sn-5Sb	232-240
	Au-20Sn	281
	Sn-3Cu	227-300
	Sn-25Ag-10Sb	260-300
	Au-12Ge	356

## 2.2 The development of reinforced solders

Recently, there have been various research studies done on developing new solder alloys or in improving current available solder materials. One suggestion to improve the current available solder material is by incorporating reinforcements to the solder. Reinforcement to solder materials can also be categorised by intrinsic reinforcements and extrinsic reinforcements. Intrinsic reinforcement is categorised as reinforcement to the bulk solder

produced by forming intermetallic phase particles particularly during the soldering solidification or subsequent annealing. Extrinsic reinforcement is categorised as reinforcement particles incorporated into the solder externally. Examples of compounds used as intrinsic reinforcement to solder joints are primary intermetallic compounds such as  $\text{Ag}_3\text{Sn}$ ,  $\text{Cu}_6\text{Sn}_5$ ,  $(\text{Cu,Ni})_6\text{Sn}_5$  and  $\text{AuSn}_4$ . On the other hand, extrinsic reinforcements can be classified into metallic reinforcements and non-metallic reinforcements. Metallic reinforcements can be in the form of any single-element particles such as Al, Fe, Zn, Ni and Co or they can be in the form of any intermetallic compound particles such as  $\text{Ag}_3\text{Sn}$ ,  $\text{Cu}_6\text{Sn}_5$ ,  $(\text{Cu,Ni})_6\text{Sn}_5$  and  $\text{AuSn}_4$  [39-42]. Non-metallic reinforcements can be in the form of ceramic particles such as particle oxides and non-oxides or carbon base materials (e.g., carbon nanotubes, activated carbons, graphite or diamonds). Examples of oxide particles includes  $\text{TiO}_2$ ,  $\text{Al}_2\text{O}_3$ ,  $\text{ZrO}_2$ , and  $\text{SnO}_2$  [33, 43-45]. Moreover, examples of non-oxides are carbide, nitride, boride or silicide particles. This includes  $\text{SiC}$ ,  $\text{Si}_3\text{N}_4$  and  $\text{TiB}_2$  [31, 46, 47]. These reinforcement particles are in various shapes and sizes where they could be in the form of micro-size or nano-size particles. These shapes are flaky or spherical, and fibres or rods/tubes [48]. Overall, the reinforced Pb-free solders can be classified on the basis of Figure 2.

The development of these reinforced solders are similar to the concept of metal matrix composite (MMC) materials in which the matrix used are alloys from a metal group and reinforcements are either metallic or non-metallic particles. In the development of reinforced solders, it is essential to meet certain criteria in order for the solder to be effectively used in current soldering technology applications. Several criteria are to be considered such as wettability of reinforcement to the solder matrix, wettability of solder to substrate, solubility of the reinforcement, optimal particle size and meet current solder processing and operating conditions [49, 50].

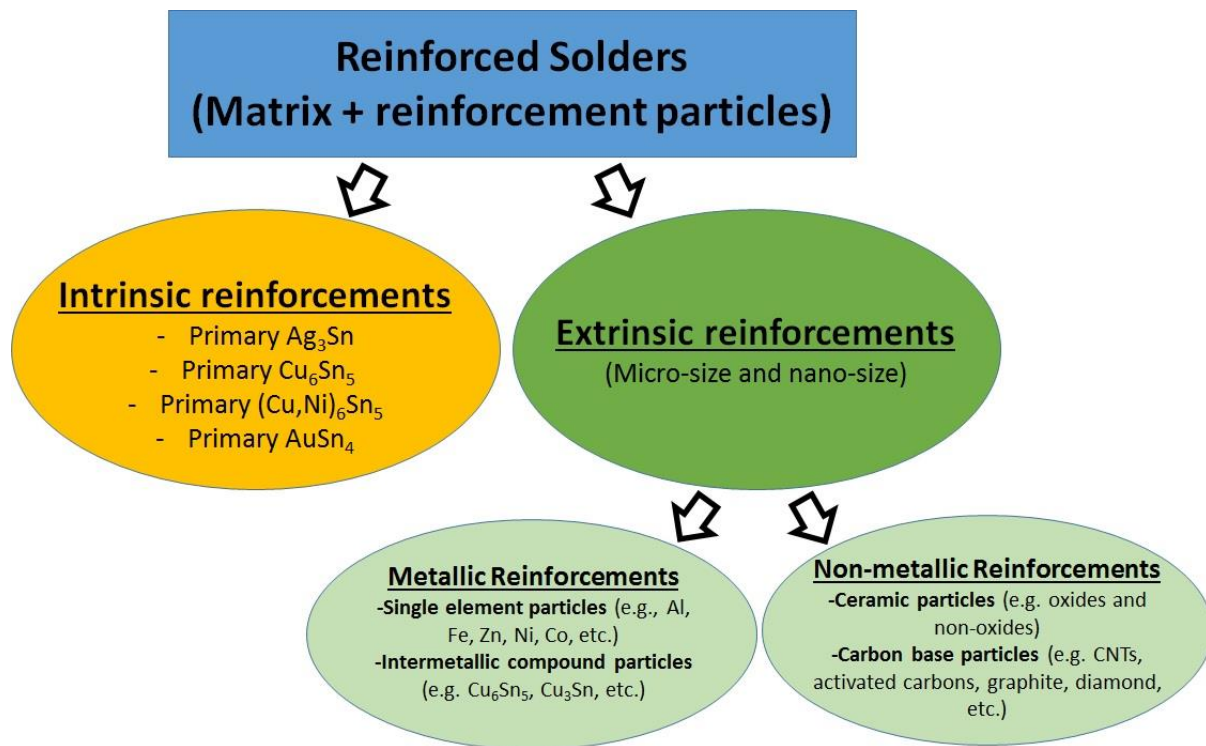


Figure 2 : Reinforced Pb-free solder classification.

### 2.3 Fabrication methods of reinforced solders

There are various methods in the fabrication of reinforced solders reported on in the current literature. However, the fabrication process of reinforced solders may be generalized into two main methods: mechanical mixing and in-situ method, as in Figure 3 [50]. In the fabrication of in-situ method, it may also be referred to as the intrinsic reinforcing method in forming primary intermetallic particles during soldering solidification [51]. Examples of primary particles in common Sn Pb-free solder alloys includes  $\text{Cu}_6\text{Sn}_5$ ,  $\text{Ag}_3\text{Sn}$ ,  $(\text{Cu,Ni})_6\text{Sn}_5$  and  $\text{AuSn}_4$ . These primary intermetallics, which form during soldering, may act as intrinsic reinforcements to strengthen the solder joint. However, it is known that these intermetallics are brittle. Excessive and large primary intermetallics may deteriorate the solder joint strength depending on the location [52]. Large primary intermetallics located near the solder joint surface may create a weak point and a crack may be initiated. In the study of failure mechanisms of solder joints, Wang et al. [53] and Monlevade et al. [52] indicate that large intermetallics, which includes the primary and interfacial intermetallic compound layer, could promote crack initiation in solder joints. Xian et al. [54] report that primary  $\text{Cu}_6\text{Sn}_5$  formation in the bulk solder is shown to be affected by the increasing Cu content of the liquid due to the Cu dissolution, the change in phase equilibria and the degree of undercooling for  $\beta$ -Sn.



Hung et al. [55] also report that Cu% in Sn-Cu solders influences the Cu-Sn intermetallic formation where increasing the Cu content increases the Cu-Sn intermetallic and refines the Sn-rich phase. Lewis et al. [56] and Park et al. [57] report that in eutectic Sn-Ag-Cu solder alloy,  $\text{Cu}_6\text{Sn}_5$  intermetallic are the dominant intermetallic to form. Large plate-like primary  $\text{Ag}_3\text{Sn}$  were able to be observed on a high silver content solder alloy [58, 59]. In addition, several studies indicate that in Sn-Cu and Sn-Ag-Cu solder alloys, the non-planar  $\text{Cu}_6\text{Sn}_5$  primary intermetallic typically forms in branches where it is hypothesized that it grows from a central point before separating into distinct branches [60, 61]. In addition to decreasing the cooling rate, the increase in Cu alloying could decrease the inter-branch spacing [60, 62]. On the other hand, Tian et al. [63] report that grooves are formed and become deeper and longer after the complete formation of the prime-type  $\text{Cu}_6\text{Sn}_5$  crystals which forms into branches. Tian et al. [63] also report that the hollowed  $\text{Cu}_6\text{Sn}_5$  crystals structure in Sn-3.0Ag-0.5Cu/Cu was attributed to the growth rates of different crystal planes.

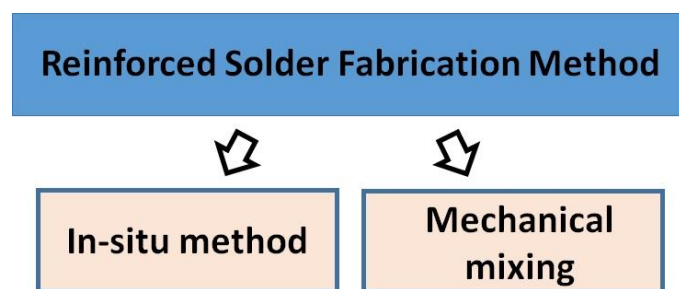


Figure 3: Methods of reinforced solder fabrication process [50].

Another method in the fabrication of reinforced solders is categorised as the mechanical mixing method. This method is utilized by extrinsically adding reinforcement particles (micro-size or nano-size) into the solder alloy matrix and it involves a mixing step to ensure a homogenous distribution of reinforced particles. Various mechanical methods have been reported on in the literature which include: (i) mixing solder pastes with reinforcement particles, (ii) mixing molten solder alloy with reinforcement particles, (iii) mixing solder component powders with reinforcement particles, and (iv) mixing solder alloy powders with reinforcement particles [50].

One of the simple processes in fabricating the reinforced solder is mixing solder paste with reinforcement particles. It is a simple direct fabrication method and does not require any further process after mixing. In this process, solder paste, which consists of a mixture of flux and solder alloy spheres, is directly mixed with the reinforcement particles [29, 64].

Mixing molten solder alloy with reinforcement particles involves the melting of solder matrix and adding reinforcement particles in the molten solder alloy. Shen et al. [65] report on fabricated ZrO<sub>2</sub> reinforced Sn-Ag solder. ZrO<sub>2</sub> nano-size particles to the amount of 2% were added to the molten Sn-3.5Ag solder alloy in an arc melting furnace with argon gas atmosphere to reduce the effect of oxidation. The mixture was then mechanically mixed for 30 minutes using an electromagnetic stirrer and subsequently cooled until it solidified.

Mixing solder component powders with reinforcement is generally a method of weighing the amount of each component materials, e.g. Sn and Cu powders, and mixing the metal powders with reinforcement materials. This method is normally known as the mechanical alloying method in the fabrication of reinforced solders [66-69]. Mixing solder alloy powders with reinforcement particles is a method by mixing pre-casted solder alloy powders and then mechanical mixing with reinforcement particles. Lin et al. [70] [71, 72] and Liu et al. [73] fabricated reinforced solders by mixing nano-sized particles with Sn-Pb solder powders. Nano-sized Ag and TiO<sub>2</sub> powders were mechanically mixed for 15-30 minutes in Sn-Pb solder powders with water soluble flux by Lin and Liu respectively. Then the solder mixture was melted on a heating plate to obtain the reinforced solder. In addition, the powder metallurgy method could be used by mixing the solder alloy powder with reinforcement particles which were reported on in several studies [10, 26, 30, 31, 36, 74-79].

The powder metallurgy method consists of several steps which include mixing, forming and sintering as in Figure 4. The first step in the powder metallurgy process is weighing the desired mixture composition and subsequently blending the mixture homogenously. This step is important in ensuring the creation of a well homogenised mixture before further steps are taken. Secondly, homogenously mixed powders are then formed by a compaction method which may consist of hot compaction, warm compaction or cold compaction. Cold compaction is the most commonly used compaction method while hot compaction is the least used in forming the mixed reinforced solder [26].

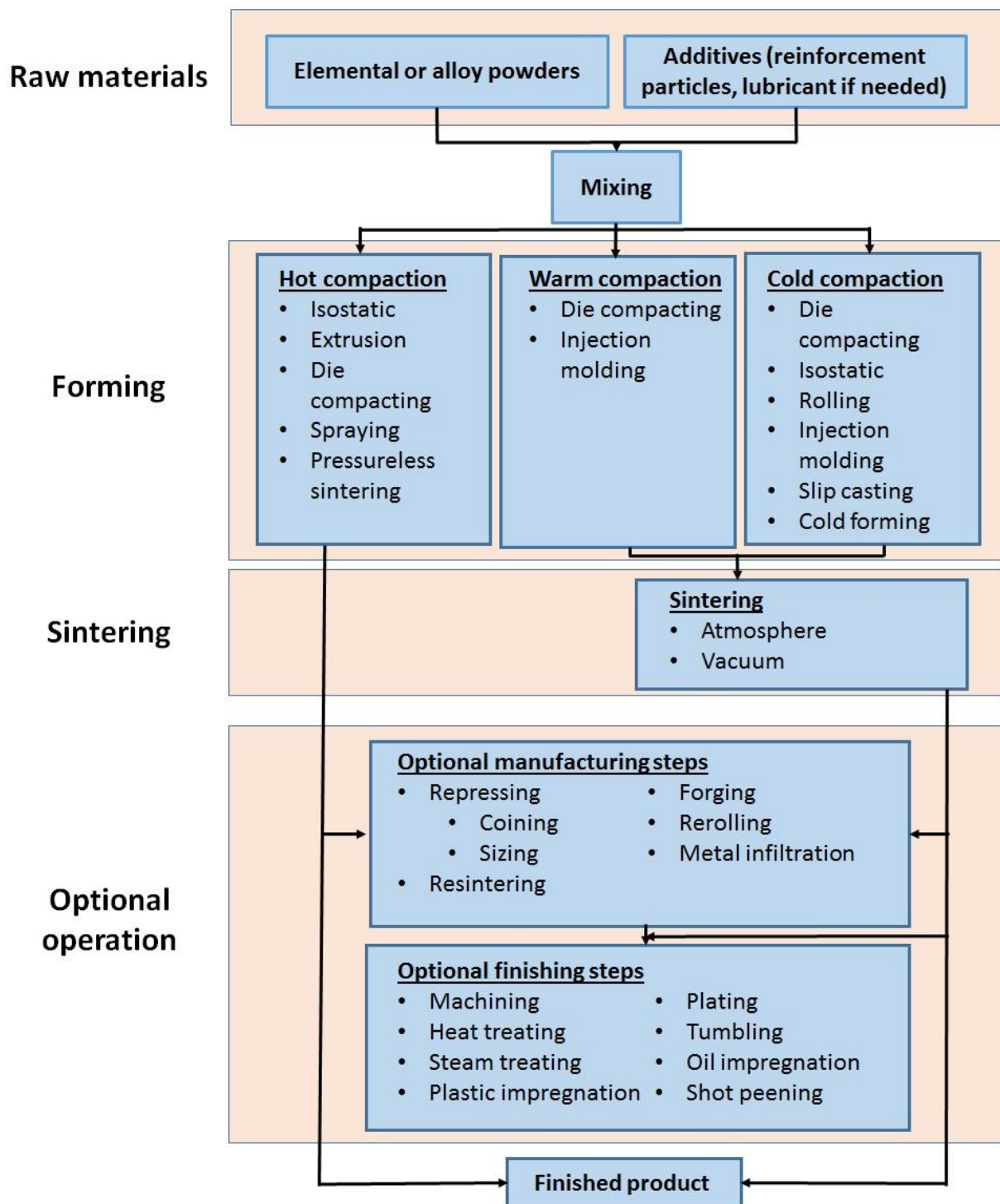


Figure 4: Common powder metallurgy process method [80].

The final important procedure in the PM process of the fabrication of reinforced solder is sintering. Sintering is essentially the most important procedure in ensuring the toughness of the compacted powders for further subsequent processing. The sintering method is whereby the formed mixture is heated below the melting point of the matrix and normally heated to 70-80% of its liquidus temperature [81-83]. The sintering process can be either conventional sintering or microwave sintering. Conventional sintering is the process of heating the

compacted powders in normal ovens. Where conventional sintering would normally consume time and energy, microwave sintering is more efficient and only requires a short sintering time [84]. The use of microwave sintering in the fabrication of reinforced solders offers more than just densification of the metal compact. Microwave sintering also provides a unique heating characteristic of the metal compact with distinctive results. Conventional resistance heating from the outside to the inside of the compacted powder preform often results in poor microstructural characteristics at the core of the preform. Moreover, green compacts of solder sintered using conventional sintering are easily exposed to oxidation since long durations are required for homogenization of temperature while in microwave heating, the holding time is not required. Oxidation is highly detrimental in soldering because it prevents the solder reacting with the metal substrate. Oxidized sintered solder bulk can be considered useless for soldering.

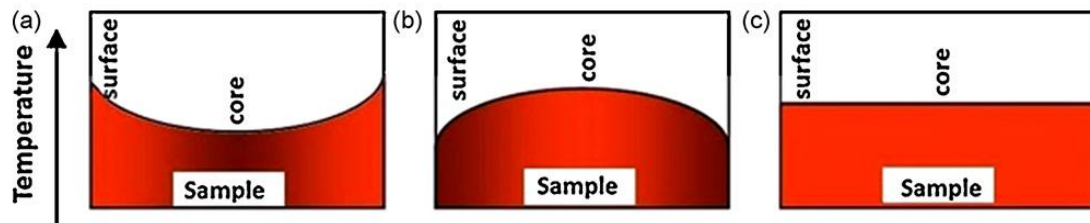


Figure 5: Temperature distribution samples for: (a) conventional heating (b) microwave heating (c) hybrid microwave heating [18].

Microwave heating is unique and different from conventional heating because of the special heating characteristics including penetrating radiation, rapid heating, controllable field distributions, and selective heating of materials and self-limiting [85]. There are two methods of microwave heating which can be used. They are direct heating by pure microwaves and the microwave hybrid technique. Pure microwave heating is where the samples are placed directly inside the microwave cavity and exposed to microwave energy while the hybrid technique, using a susceptor material, absorbs microwave energy to improve heating. Therefore, this is a more rapid sintering process compared to conventional and direct microwave heating. Morteza et al. [18] illustrate the heat distribution comparison during sintering using conventional microwave and hybrid microwave heating as shown in the temperature profiles schematics of Figure 5. The red colour in this Figure indicates the distributed heat and contrasts conventional heating, which results in heat being transferred from the outer to inner areas, with the situation in microwave heating, where heat is transferred from the inner to outer areas. The well distributed heat achieved by using hybrid

microwave heating results in a homogenous fine microstructure and reduces the porosity which may translate into increased solder reliability.

Both conventional and microwave sintering are normally conducted with the aid of inert gas, such as argon or nitrogen, to eliminate oxidation [82]. The sintering procedure is used to fuse particles by solid-state bonding where the melted particle will cover the unmelted particles. Figure 6 indicates the particle bonding mechanism in sintering [86]. During the early stage of heating in the sintering process, particles will make contact, a neck growth will form, and the neck will subsequently grow larger. If the sintering time is prolonged, the particles will fully coalesce forming larger particle grains that are approximately 1.26 times larger than the diameter of the original single particle. In addition, pores that are initially entrapped between the particles will be reduced during sintering. Figure 7 shows the porosity reduction during sintering where the pores between the grain boundary are reduced producing a denser sintered material. These initial large pores become more spherical and smaller after sintering [86].

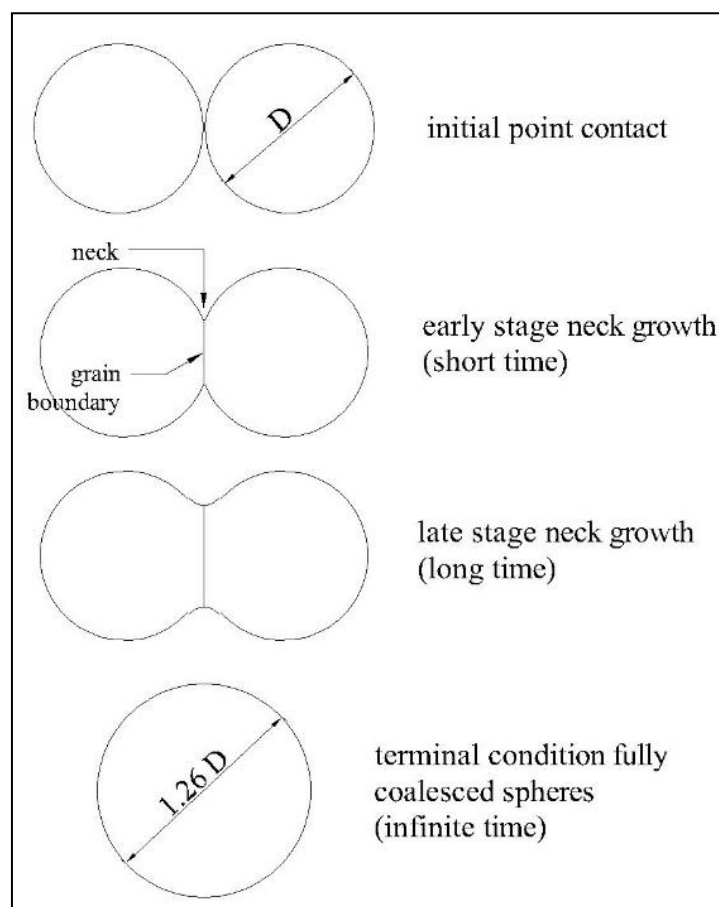


Figure 6: Bonding of particles during sintering [86].

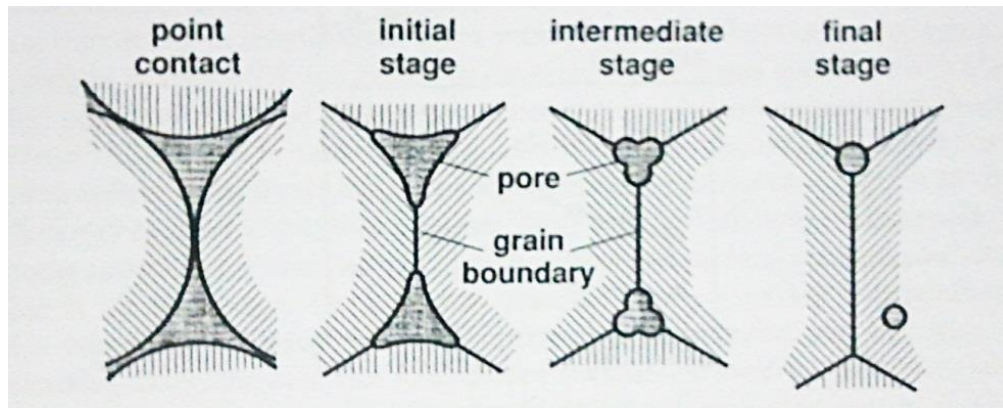


Figure 7: Pore structure reduction during sintering [86].

After the sintering process, the sintered samples may be further processed to form the desired end product. In the fabrication of reinforced solder, sintered samples may be rolled or extruded. The extrusion method is reported as the secondary process after sintering of reinforced solders which creates higher solder strength, and could reduce the microstructural defects of the sintered solder [23, 36, 87].

## 2.4 Interfacial intermetallic compound (IMC) layer of reinforced solder

The majority of the Pb-free solder alloy systems used in the production of electronic products, utilise Sn-rich solders. Since Sn-rich solders have excellent solderability on Cu, Cu substrate has been widely used in electronic assembly. Typically, during the soldering of Sn-Cu solder systems on Cu substrate,  $\eta$ -Cu<sub>6</sub>Sn<sub>5</sub> and  $\epsilon$ -Cu<sub>3</sub>Sn phases are common interfacial layers that form between the solder/Cu substrate [5, 59, 88, 89]. During the liquid-solid interaction of molten solder and Cu substrate, it is believed that a rapid dissolution of Cu into molten solder with a lower Cu concentration occurs immediately after the Cu oxide film has been removed by the actions of the flux. This rapid direct dissolution of Cu occurs until the conditions become favorable for the nucleation and growth of IMCs such as  $\eta$ -Cu<sub>6</sub>Sn<sub>5</sub> and  $\epsilon$ -Cu<sub>3</sub>Sn [90-92]. The formation of interfacial IMC layers are based on two main reactions: (i) dissolving of the metal substrate into the molten metal and (ii) bonding of the active constituent elements in solder material with the substrate material [93].

The presence of interfacial IMCs is favourable because it shows the existence of metallurgical bonding between the two metallic surfaces, however, excessive formation of interfacial IMCs will degrade the reliability of the formed joint [94-96]. Therefore,

understanding the bonding reaction between the solder-substrate interfaces is fundamentally essential to understanding the reliability of solder interconnections. In improving the solder joint reliability, many researchers have investigated the growth behaviour of interfacial IMCs and several models have been developed to describe interfacial IMC growth during solder wetting reactions and solid-state ageing [90, 91, 97-103]. In understanding the IMC growth mechanisms, recent kinetic studies of interfacial IMC growth have focussed on solid state ageing effects rather than the wetting reaction during the liquid-solid interaction. This solid state ageing is more favourable for laboratory examinations as the kinetic processes are much slower compared to the wetting reaction [104].

Solid state diffusion mechanism directly controls the progression of the intermetallic phase. The thickness of the intermetallic layer which is a result of time and the connection against the thickness of the intermetallic layer ( $Y$ ), and the deterioration time ( $t$ ) can be described by Equation 1,

$$Y = Y_0 + \sqrt{Dt} \quad (\text{Equation 1, [89]})$$

Where  $Y_0$  is the thickness of the intermediate layer at  $t = 0$  and  $D$  is the diffusion coefficient. By plotting the thickness of the intermetallic layer ( $Y$ ) versus the square root of deterioration time ( $t^{1/2}$ ), the gradient of the graph is equivalent to the square of the diffusion coefficient of the intermetallic phase at a different deteriorating temperature. The diffusion coefficient is a function of temperature by Arrhenius equation as described in Equation 2,

$$D = D_0 e^{-Q/RT} \quad (\text{Equation 2, [89]})$$

Where the temperature independent constant is identified as the frequency factor  $D_0$ , for diffusion to occur the activation energy is  $Q$ , while the universal gas constant is  $R$  and the absolute temperature which is in Kelvin is  $T$ . By using the natural logarithm in Equation 2 the activation energy of the intermetallic phase can be determined, which can then be expressed as Equation 3 as the diffusion coefficient.

$$\ln D = \ln D_0 - \frac{Q}{R} \left( \frac{1}{T} \right) \quad (\text{Equation 3, [89]})$$



This equation will the form of  $y = mx + C$ , in which  $\ln D$  is the dependent variable and  $1/T$  is the independent variable. When the diffusion coefficient ( $D$ ) is plotted versus the reverse deteriorating temperature ( $1/T$ ), the activation energy ( $Q$ ) can be determined from the gradient of the graph, and the frequency factor ( $D_0$ ) can be computed from the intercept of the graph.

Microstructures and intermetallic formation in a solder joint are often closely associated with solder joint reliability [61]. Most research on non-metal reinforced solders reports that additions of non-metal reinforcement either in micro-size or nano-size such as  $\text{TiO}_2$ ,  $\text{Al}_2\text{O}_3$ ,  $\text{SiC}$ ,  $\text{Si}_3\text{N}_4$ , single-wall carbon nanotubes (SWCNT) and multi-wall carbon nanotubes (MWCNT) reinforcements have suppressed intermetallic formation. In the study of Sn-3.5Ag-0.5Cu with additions of  $\text{Al}_2\text{O}_3$  nano-sized reinforcement, Tsao et al. [35] report that the  $\text{Cu}_6\text{Sn}_5$  IMCs formed in prism like shapes rather than scallop like shapes in Sn-3.5Ag-0.5Cu solders based on cross sectioned samples (Figure 8).

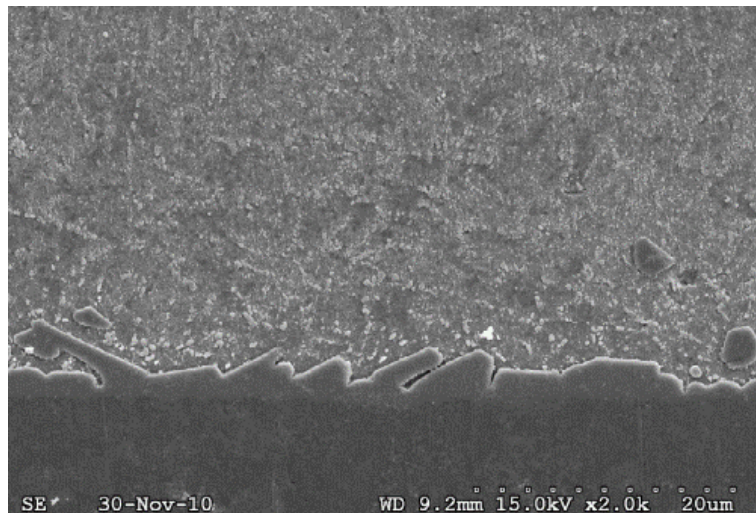


Figure 8: Prism like intermetallic compound formation of Sn-3.5Ag-0.5Cu-1Al<sub>2</sub>O<sub>3</sub> [35].

Tsao et. al. [35] hypothesized that the  $\text{Al}_2\text{O}_3$  nanoparticles are absorbed in a liquid nanocomposite solder/Cu substrate interface which then suppresses the Cu dissolution in the liquid solder and in return reduces the  $\text{Cu}_6\text{Sn}_5$  formation, retarding the IMC layer. This hypothesis is supported by the Gibbs-Thomson effect which may explain the growth rate of  $\text{Cu}_6\text{Sn}_5$  between scalloped or prism like grain morphology with respect to the ripening flux ( $J_r$ ) and interfacial reaction flux ( $J_i$ ) [35, 61]. In addition, El-Daly et al. [24] report that by adding SiC nanoparticles to a Sn-1.0Ag-0.5Cu (SAC105) solder, the plasticity of SAC105 is altered due to the structural refinement of sub-grain sizes of primary  $\beta$ -Sn. El-Daly



hypothesize that SiC nanoparticles could act as additional nucleation sites where the rate of solidification of  $\beta$ -Sn will be faster and limit the time for the  $\text{Ag}_3\text{Sn}$  and  $\text{Cu}_6\text{Sn}_5$  to grow. This somehow limits the diffusion reaction in the solder alloy where in other words, the reinforcement acts as a barrier to  $\text{Ag}_3\text{Sn}$  and  $\text{Cu}_6\text{Sn}_5$  IMC formation. This mechanism was also reported by Liu et al. in the reinforcing with graphene nanosheets to Sn-Ag-Cu solder alloys where the graphene nanosheet enhanced the thermodynamic resistance of the IMC growth and the surface diffusion of the IMC was suppressed by the reinforcement [105]. Based on differential scanning calorimetry, the undercooling of Sn-1.0Ag-0.5Cu-0.75SiC was reported to be lower compared to SAC105 and the larger undercooling is associated with more extensive IMC growth [61]. Another study by Tsao [106], as in Figure 9, reveals the intermetallic suppression of Sn-3.0Ag-0.5Cu with nano-size  $\text{TiO}_2$  after thermal ageing. The report by Nai et. al [64] indicates that carbon nanotubes (CNT) reinforced Sn-Ag-Cu solder has minimal effect on the suppression of interfacial IMC during soldering but suppresses the interfacial IMC layer during the later isothermal annealing. It is reported that CNT reinforced Sn-Ag-Cu solder results in a lower diffusion coefficient compared to non-reinforced solder where the reinforcement retards the diffusion of Cu and Sn atoms by acting as a diffusion barrier.

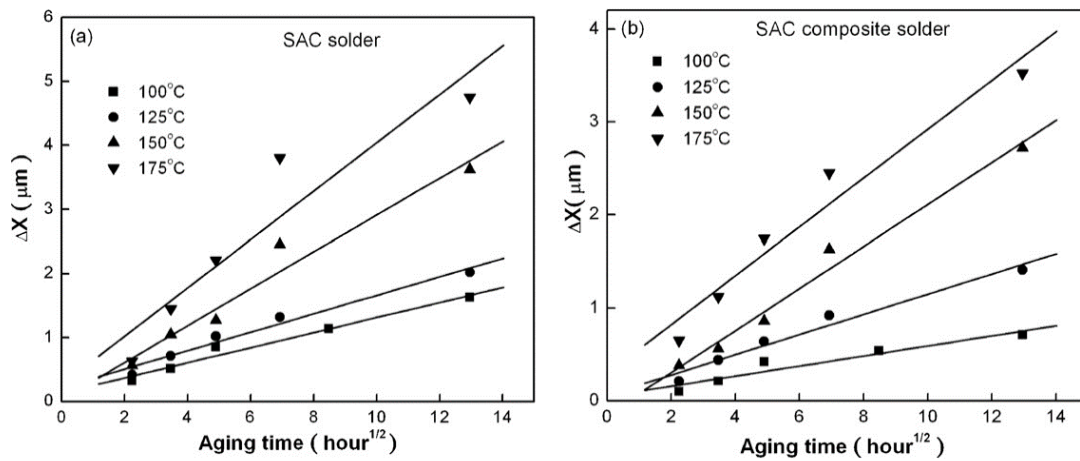


Figure 9: The relationship of intermetallic compound thickness to ageing time and temperature for (a) Sn-3.5Ag-0.5Cu and (b) Sn-3.5Ag-0.5Cu + nano-size  $\text{TiO}_2$  reinforced solder [106].

Study on the  $\text{SrTiO}_3$  nano-size particle reinforcement additions on Sn-3.0Ag-0.5Cu was conducted by Fouzder et al. [107]. In their report, it is shown that  $\text{SrTiO}_3$  suppresses the interfacial IMC layer which also results in a finer dispersion of IMC. The fine dispersion of IMC results in the  $\text{SrTiO}_3$  reinforced solder after multiple-reflow and annealing due to the

high surface free energy and nucleation density on the solder/Cu interface. In addition, Gain and Chan [108] investigated the effect of  $\text{ZrO}_2$  reinforcement particles to Sn-Ag-Cu solder after annealing and found that the additions of the nano-size particles also resulted in a decrease to the interfacial layer with a more planar interfacial  $\text{Cu}_6\text{Sn}_5$  and  $\text{Cu}_3\text{Sn}$  layer.

Besides the additions of non-metallic reinforcements, several single element reinforcement particles have been reported to effect the suppression of the interfacial IMC. Haseeb et al. [109] report that additions of Mo nano-size particles could suppress the formation of interfacial IMC in Sn-3.5Ag-0.7Cu/Cu solder joint after reflow and subsequent numbers of reflow. As Figure 10 shows, with the additions of Mo, a significant thickness reduction and width of the interfacial  $\text{Cu}_6\text{Sn}_5$  layer occurs. Haseeb hypothesized that the Mo nano-particles had suppressed the interfacial IMC through a discrete particle effect being absorbed by the interfacial IMC grain boundaries. Haseeb also conducted a study [110] on the Co nano-size particle additions to the Sn-Ag solder where the interfacial  $\text{Cu}_6\text{Sn}_5$  in the solder joint changed from a scallop shape to a more planar interfacial layer. Additions of Co reinforcement particles reduced the thickness of the  $\text{Cu}_3\text{Sn}$  interfacial layer and increased the  $\text{Cu}_6\text{Sn}_5$  layer. Co nano-sized particle additions reduced the effective interdiffusion coefficient in  $\text{Cu}_3\text{Sn}$  and thus reduced its growth. In addition, during multiple reflow, it is reported that nano-sized Zn particles were able to suppress the interfacial  $\text{Cu}_6\text{Sn}_5$  layer on Sn-3.8Ag-0.7Cu [111]. It was reported that the thickness of interfacial  $\text{Cu}_6\text{Sn}_5$  decreases as the Zn particles increases.

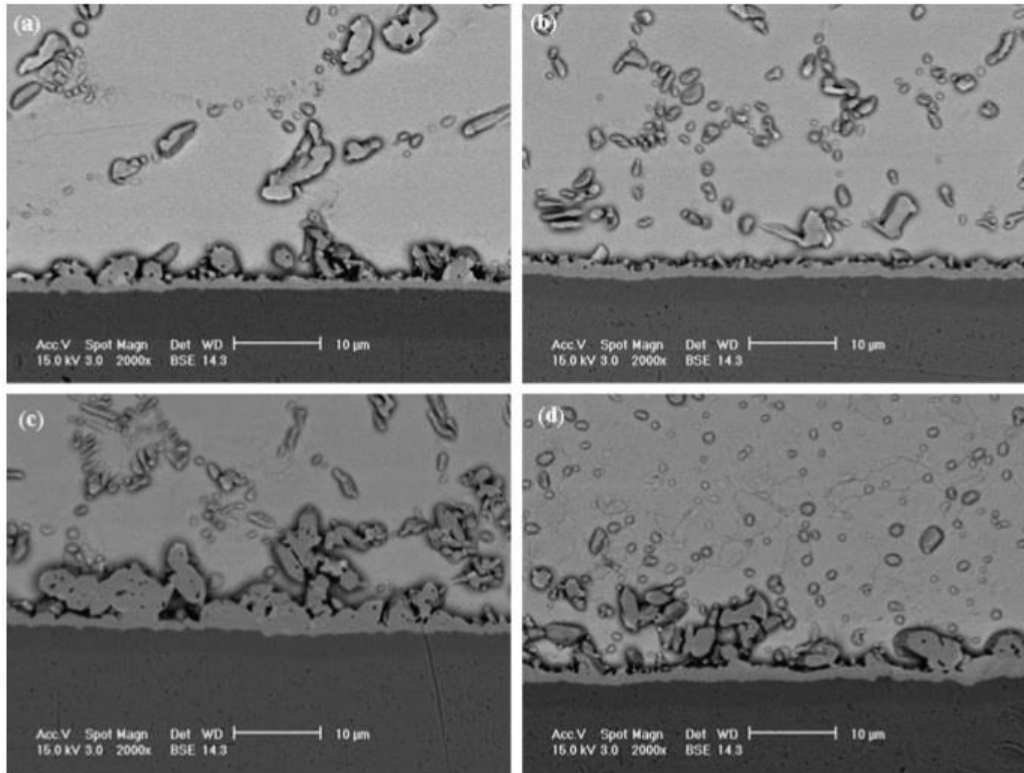


Figure 10: Backscattered images of (a) Sn-Ag-Cu solder after 10 days annealing, (b) Sn-Ag-Cu-0.5SrTiO<sub>3</sub> solder after 10 days annealing, (c) Sn-Ag-Cu solder after 40 days annealing and (d) Sn-Ag-Cu-0.5SrTiO<sub>3</sub> solder after 40 days annealing [107].

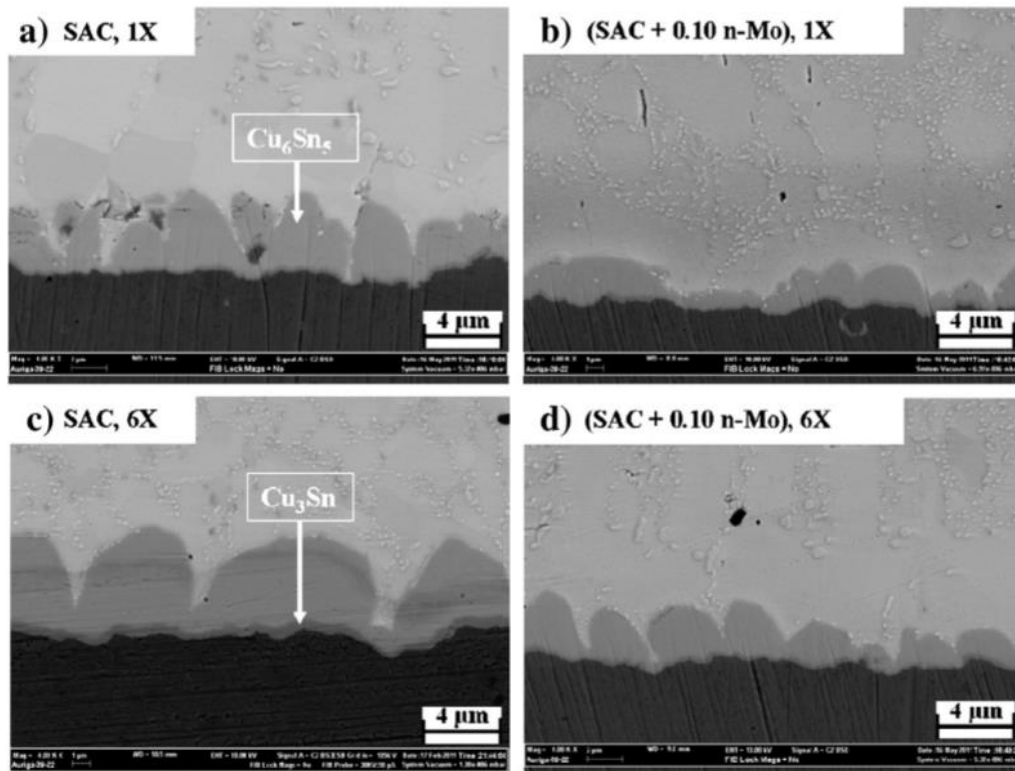


Figure 11: Backscattered images of interfacial  $\text{Cu}_6\text{Sn}_5$  layer on (a) Sn-3.5Ag-0.7Cu after one time reflow (b) Sn-3.5Ag-0.7Cu-Mo after one time reflow (c) Sn-3.5Ag-0.7Cu after six time reflow and (d) Sn-3.5Ag-0.7Cu-Mo after six time reflow [109].

## 2.5 Microstructure of reinforced solder

As explained in section 2.2, intrinsic reinforcement is considered as reinforcing particles in the bulk solder produced by forming primary IMC particles during the soldering solidification or subsequent annealing while extrinsic reinforcement is incorporated in the solders externally. Microstructure observation and analysis of the solder matrix could determine the phases that form and also assist in understanding its distribution across the solder joint. This subsection is a review on microstructures of intrinsic and extrinsic reinforced solder.

Wang et al. [112] investigated the growth of primary  $\text{Cu}_6\text{Sn}_5$  in Sn-6.5Cu solder with the additions of 0.2 wt% Al trace element. Using a high resolution SXRI technique, it was reported that Al addition refined the size of the primary  $\text{Cu}_6\text{Sn}_5$  (Figure 12). From the findings, it is suggested that based on the EDS analysis made on the primary intermetallic particles, Cu-Al intermetallic was also observed near to the primary  $\text{Cu}_6\text{Sn}_5$ . It is suggested that the Cu-Al intermetallic formation suppressed the primary  $\text{Cu}_6\text{Sn}_5$  from growing. In the study, Wang also reported different shapes of primary  $\text{Cu}_6\text{Sn}_5$  were observed in both Sn-

6.5Cu solder and Al addition solder samples including I-shape, Y-shape and X-shape which resulted in a different growth rate during solidification.

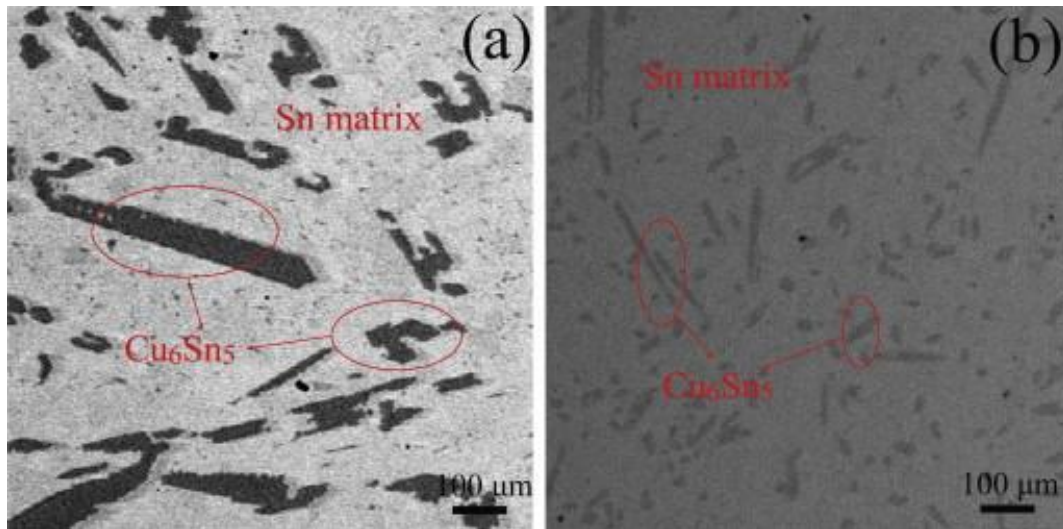


Figure 12: Microstructure of as-solidified (a) Sn–6.5Cu and (b) Sn–6.5Cu–0.2Al [112].

Effects of Ag and In additions is reported to result in formations of fine primary Ag<sub>3</sub>Sn fibers and Cu<sub>6</sub>Sn<sub>5</sub> eutectic microstructure [113]. As shown in Figure 13, the additions of Ag and In result in a refining of β-Sn grains and may improve the creep resistance properties of the solder. With the increase of Ag to 2% into the solder alloy, more Ag<sub>3</sub>Sn fibres were observed which may act as a pinning effect between the Sn grain boundaries. On the other hand, with In additions, γ-SnIn<sub>4</sub> precipitation was observed in the eutectic microstructure and Cu<sub>6</sub>Sn<sub>5</sub> eutectic were able to be reduced.

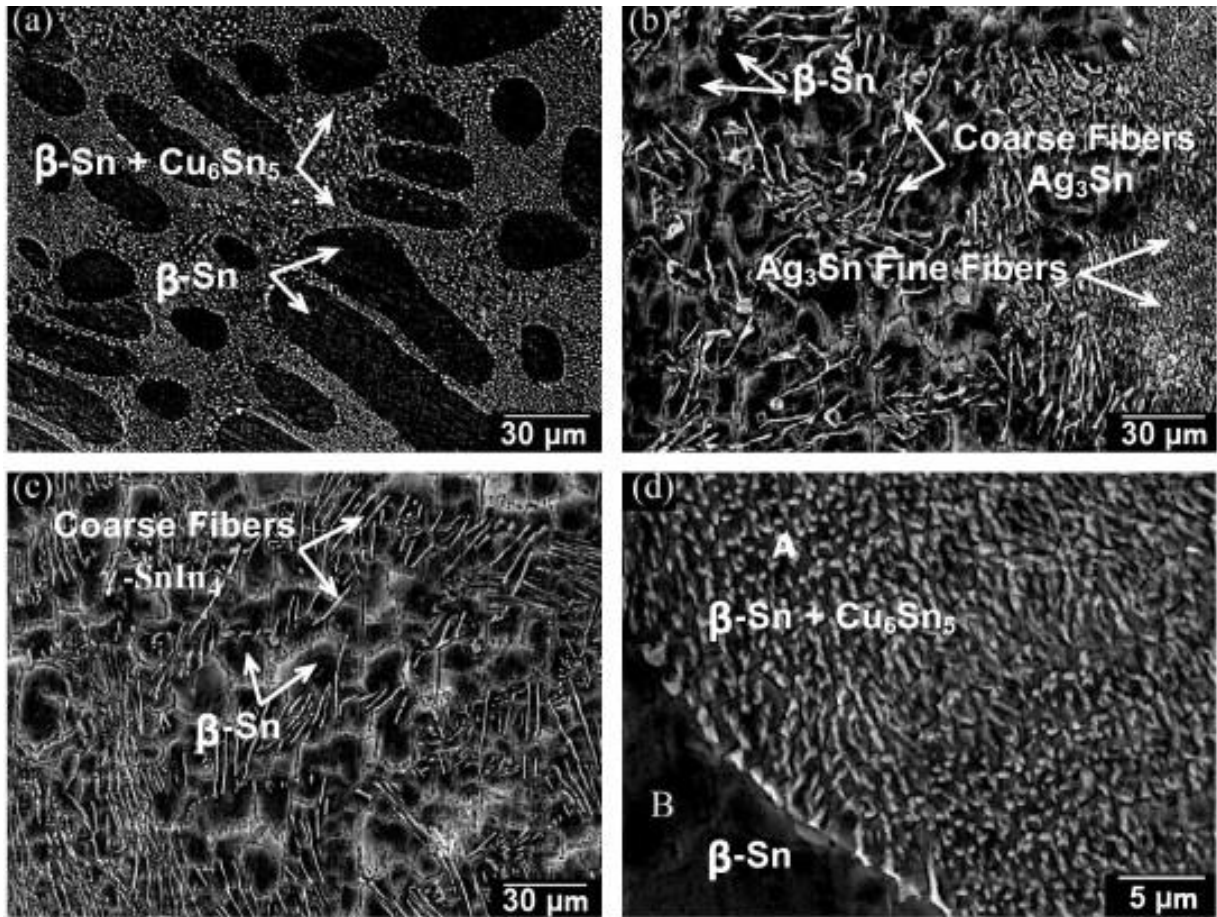


Figure 13: Backscattered electron SEM images of etched sample of: (a) Sn–0.7Cu, (b) Sn–0.7Cu–2Ag and (c) Sn–0.7Cu–2In and (d) image of selected EDS area conducted in the study [113].

In a study for investigating the SiC micro-sized particles (1  $\mu\text{m}$ ) effect to the bulk solder, Wang et al. [114] report that primary IMC size and Sn dendrites were able to be reduced with additions of the reinforcement particles in Sn–3.7Ag–0.9Zn as shown in Figure 14. It is reported that due to the heterogeneous nucleation of Sn dendrites from the reinforcement particles and acting as nucleation sites, more and finer Sn dendrites could be produced.

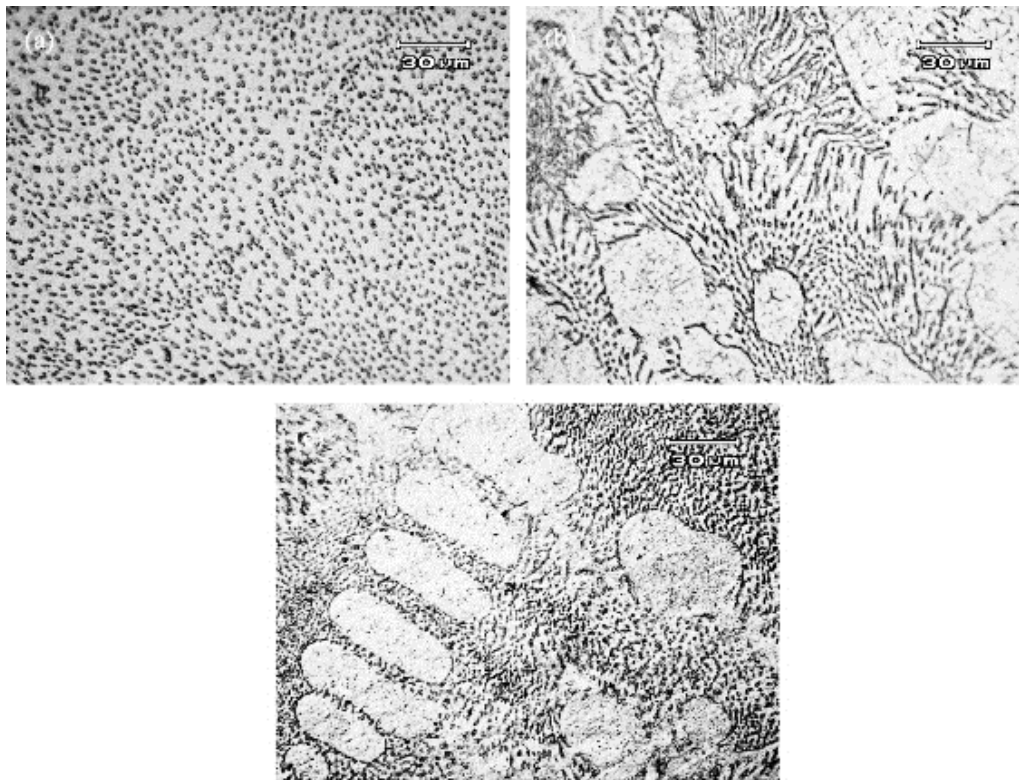


Figure 14: (a) Microstructure of Sn–Ag–Zn (b) with 0.05% SiC additions and (c) with 0.1% SiC additions [114].

Investigations of SiC reinforcing effects were also conducted by El-Daly et al. [115] with maximum 0.75% additions of nano-sized SiC particles into Sn–1.0Ag–0.5Cu solder. It was found that there are limitations of reinforcement particles which efficiently benefit the primary  $\text{Cu}_6\text{Sn}_5$  suppression and Sn grain refinements due to the effect of heterogeneous nucleation in the solder matrix. They also suggest that the reinforcing particles could reduce the velocity growth of intermetallic in the solder. Similar effects of Sn grains and primary IMC suppression observed in Sn–3.0Ag–0.5Cu solder (Figure 15) was reported due to the additions of nucleation sites [46]. Additionally, El-Daly et al. [24] report SiC nano-sized particles added to a Sn–1.0Ag–0.5Cu altered the plasticity of the solder due to the structural refinement of sub-grain sizes of primary  $\beta$ -Sn (Figure 16).

Tsao et. al. [35] report that  $\text{Al}_2\text{O}_3$  nanoparticles are absorbed in a liquid nanocomposite solder/Cu substrate interface which then suppresses the Cu dissolution in the liquid solder [35, 61]. As shown in Figure 17 and 18 shows additions of  $\text{Al}_2\text{O}_3$  nano-sized particles also reported to refine  $\text{Ag}_3\text{Sn}$  and  $\text{Cu}_6\text{Sn}_5$  intermetallic during the solidification of Sn–3.5Ag–0.5Cu and Sn–0.7Cu respectively [35, 44]. Tsao et al. report the refinement of primary  $\text{Ag}_3\text{Sn}$  and  $\text{Cu}_6\text{Sn}_5$  is due to the adsorption effect of  $\text{Al}_2\text{O}_3$  reinforcements.



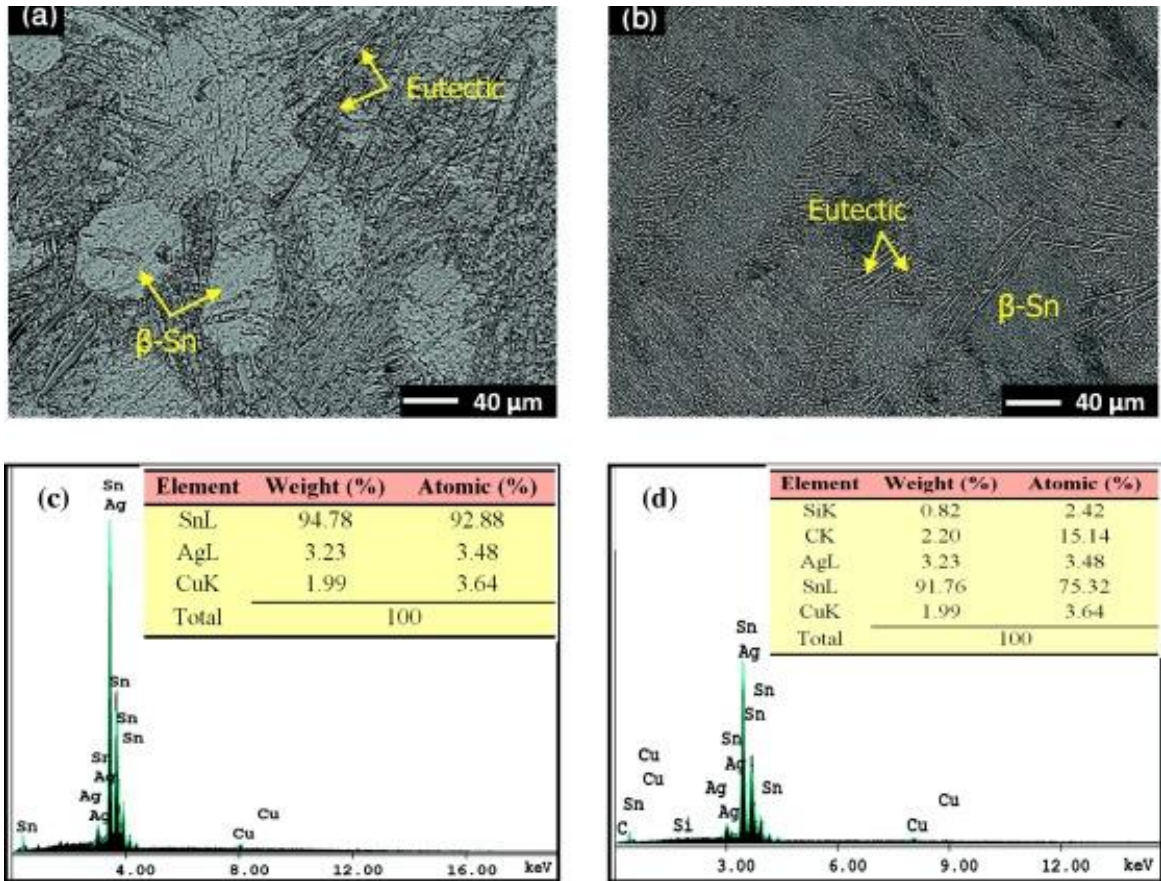


Figure 15: Backscattered electron SEM images (a) Sn-3.0Ag-0.5Cu solder matrix, (b) Sn-3.0Cu-0.5Ag-0.7SiC solder matrix (c) EDS analysis results for (a), and (d) EDS analysis results for (b) [46].

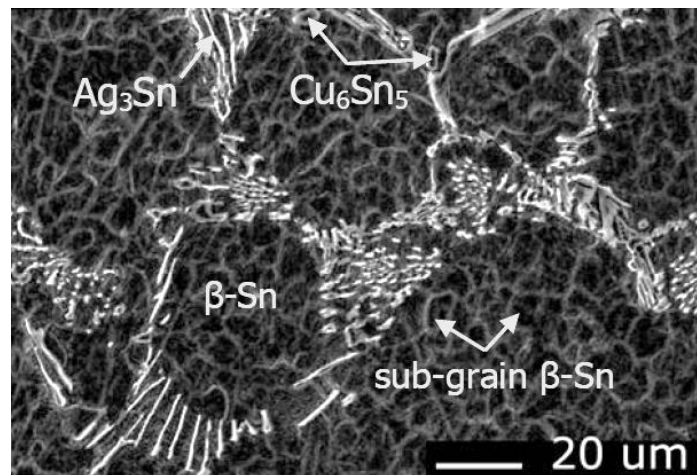


Figure 16: Backscattered electron SEM images of Sn-1.0Ag-0.5Cu-0.75SiC with sub-grains of primary  $\beta\text{-Sn}$  [24].



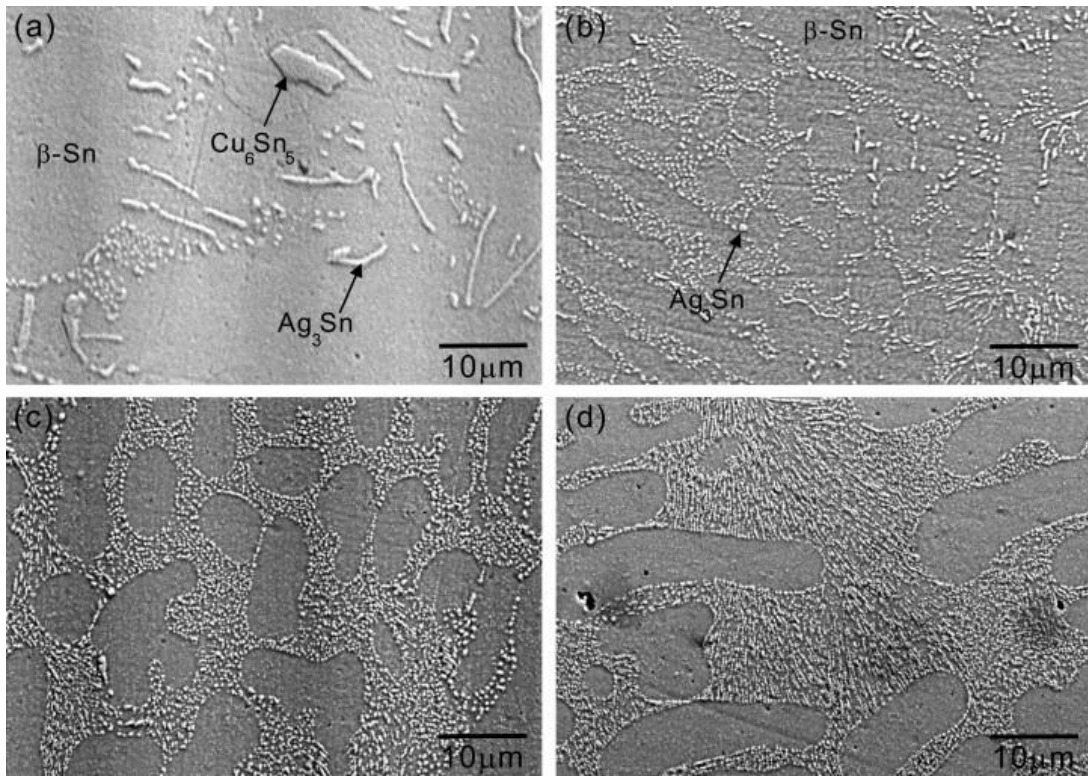


Figure 17: Backscattered electron SEM images of (a) Sn-Ag-Cu, (b) Sn-Ag-Cu-0.25Al<sub>2</sub>O<sub>3</sub>, (c) Sn-Ag-Cu-0.5Al<sub>2</sub>O<sub>3</sub> and (d) Sn-Ag-Cu-1Al<sub>2</sub>O<sub>3</sub> [44].

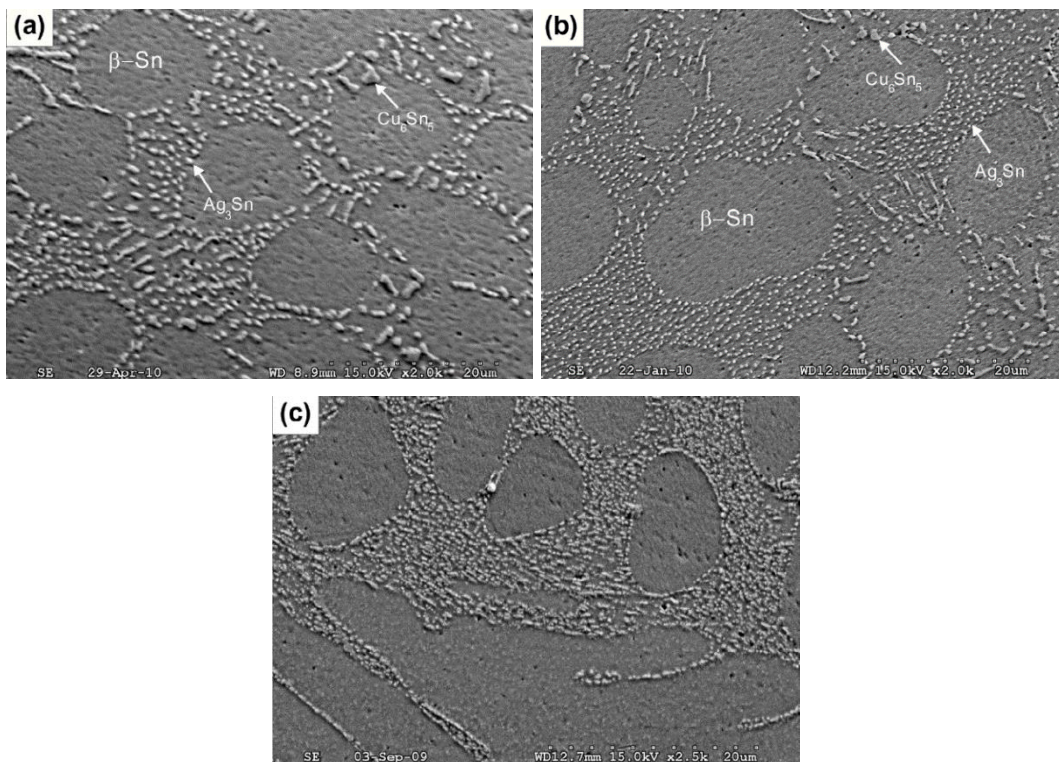


Figure 18: Backscattered electron SEM images of (a) Sn-Ag-Cu, (b) Sn-Ag-Cu-0.5Al<sub>2</sub>O<sub>3</sub>, and (c) Sn-Ag-Cu-1Al<sub>2</sub>O<sub>3</sub> [35].

With the effect of nano-sized particles of  $\text{ZrO}_2$ , Gain et al. [108, 116] report that the reinforcement reduces the  $\text{Cu}_6\text{Sn}_5$  eutectics in the solder matrix (Figure 19). Similar to other non-metallic reinforcement effects, they also agree that the  $\text{ZrO}_2$  particles were being adsorbed at the surface of Sn and intermetallic phases and hence refined the microstructure.

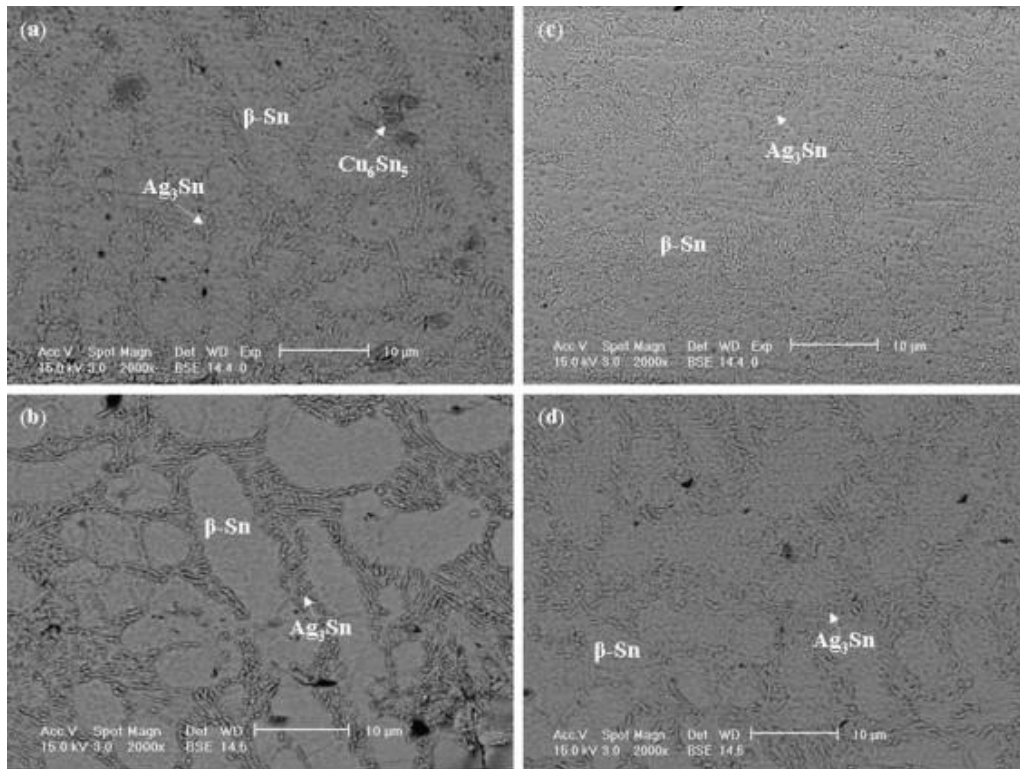


Figure 19: Backscattered electron SEM images of (a, b) Sn–Ag–Cu and (c, d) Sn–Ag–Cu–1ZrO<sub>2</sub> soldered on Cu-OSP substrate for 5 minutes (a and c) and 30 minutes (b and d) at 250 °C [116].

In other studies, Tsao et al. report that the effect of  $\text{TiO}_2$  nano-sized reinforcement additions to Sn-0.7Cu [34] and Sn-3.5Ag-0.5Cu [117] also suppress the primary intermetallic. The effect of nano-sized  $\text{TiO}_2$  particles added to Sn-3.0Ag-0.5Cu was also investigated by Tang et al. with maximum of 0.6% of reinforcement [118]. A similar phenomenon was also found in their study with El-Daly et al. [115] where they report that with the increase of  $\text{TiO}_2$  nano-sized particles added to the solder, the amount of needle-like  $\text{Ag}_3\text{Sn}$  decreases and becomes more significant after longer reflow time. Hence, the majority of the literature suggests that additions of the non-metallic reinforcements were able to reduce the Sn grain size and other intermetallic in the bulk solder. However, there is yet solid proof to show that the hypothesis explanation of the reinforcement effect results in a finer microstructure.

## 2.6 Mechanical properties of reinforced solder

This section is a report on the current literature on reinforcing effects to the mechanical properties of the solder joint. It is reported that the weak point in a solder joint is on the interface of the joint, where interfacial IMC layers form where cracks may be initiated [39]. During operating conditions of an electronic interconnection, severe environmental stress and loading is applied and hence weakens the solder joint. Hence, by using reinforced solder joints, precipitation hardening is possible and could potentially strengthen the solder joint [39].

Tai et al [119] report that additions of nano-structured POSS to Sn-3.5Ag increased the hardness value of the reinforced solder with a relatively smaller  $\text{Ag}_3\text{Sn}$  intermetallic and spacing. In the studies of El-Daly and Hammad [113, 120] the effects of Ag and In to the creep properties of Sn-0.7Cu are investigated and reported on. By suppressing the primary  $\text{Cu}_6\text{Sn}_5$  intermetallic in the bulk solder and introducing small flake-like  $\text{Ag}_3\text{Sn}$  in the bulk, creep resistance of the solder joint may increase (Figure 20).

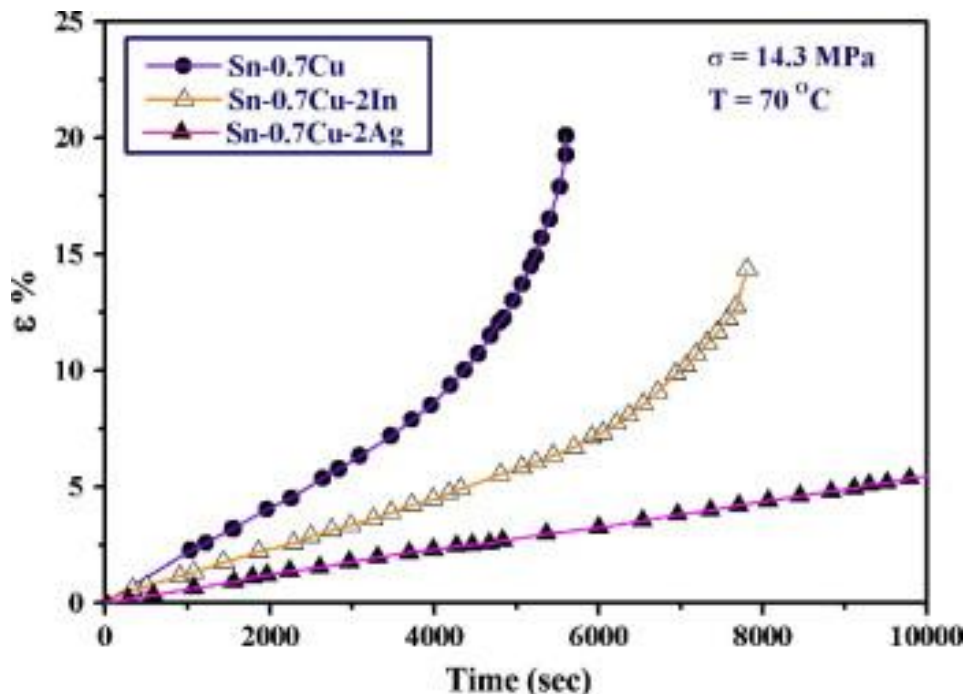


Figure 20: Creep test results comparing Sn-0.7Cu, Sn-0.7Cu-In and Sn-0.7Cu-Ag [113].

Increasing amount of SiC reinforcement also resulted in an increase of the microhardness value of the reinforced solder. The findings of Wang et al. [114], on studying the influence of SiC reinforcements to Sn–3.7Ag–0.9Zn where  $\beta$ -Sn dendrites, Ag<sub>3</sub>Sn and AgZn intermetallics were able to be refined, can be observed in Figure 21. Similarly, Tsao et al. [44] added 0.25-1wt% of Al<sub>2</sub>O<sub>3</sub> nano-sized reinforcement particles in Sn-3.5Ag-0.5Cu where an increase of microhardness of the reinforced solders were achieved. The increase of microhardness was reported to be related to the dispersion strengthening of the Al<sub>2</sub>O<sub>3</sub> reinforcement particles and the intermetallic in the solder matrix.

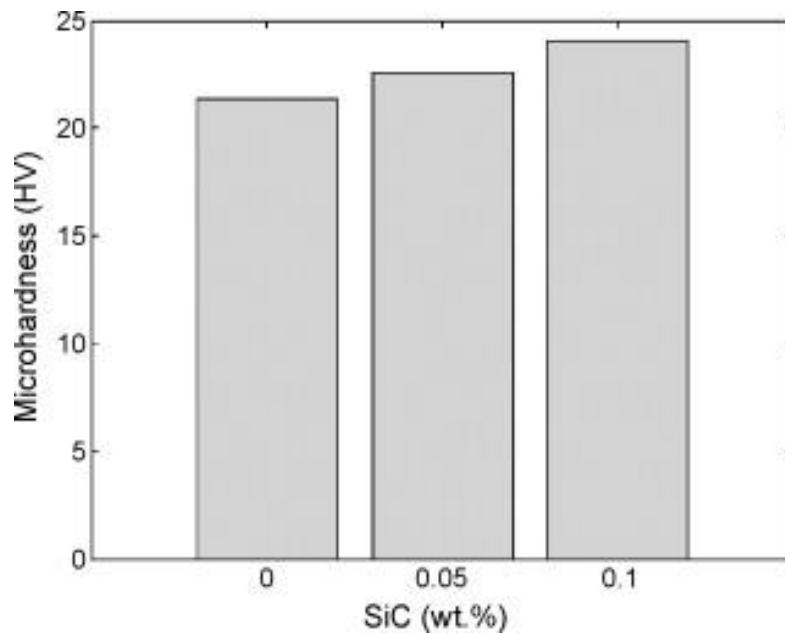


Figure 21: Hardness result of SiC reinforcement additions to Sn–Ag–Zn solders [114].

El-Daly et al. [46] report that SiC (0.7wt%) reinforced Sn–3.0Ag–0.5Cu refined the microstructure and significantly increased the solder joint strength and elastic modulus. Additions of SiC also resulted in a slight increase of liquidus temperature. Additions of Al<sub>2</sub>O<sub>3</sub> to Sn-3.0Ag-0.5Cu increased the reliability of the solder joint by increasing the solder joint strength by conducting a shear test after thermal shock which also resulted in the size reduction of Sn dendrites and increased the area of eutectic microstructure [121]. As in Figure 22, additions of Al<sub>2</sub>O<sub>3</sub> up to 1% increased the shear strength to approximately 4000 gf from approximately 3750 gf on the non-reinforced Sn-3.0Ag-0.5Cu solder joint [121]. Effects of Fe<sub>2</sub>O<sub>3</sub> [122] relatively increased the solder joint of low silver Sn-Ag-Cu solder joints where smaller particle size (20 nm) resulted in the highest shear strength. This is majorly due to the suppression of the interfacial IMC which was reported by Gu et al [123]. Adding the reinforced silver modified graphene nanosheets to Sn-Ag-Cu solder alloy resulted in a



high ultimate tensile strength after additions of 0.05 wt% where from fracture surface analysis of the tensile test sample had indicated an accumulation of the reinforcement on the fracture surface of the solder, as can be observed in Figure 23 [124]. However the elongation of the solder had reduced with the increase of reinforcing additions [124], which is similar to MWCNT reinforcement additions to Sn-3.5Ag-0.7Cu where results of ultimate tensile strength increased by 0.07% of the reinforcement addition [125]. These CNTs were able to be observed on the fractured tensile samples as in Figure 24. Han et al. [126] report that additions of 0.5 wt% CNTs to Sn-3.5Ag-0.7Cu increased the ultimate tensile strength and yield strength but the ductility of the reinforced solder had reduced with the increase amount of reinforcement.

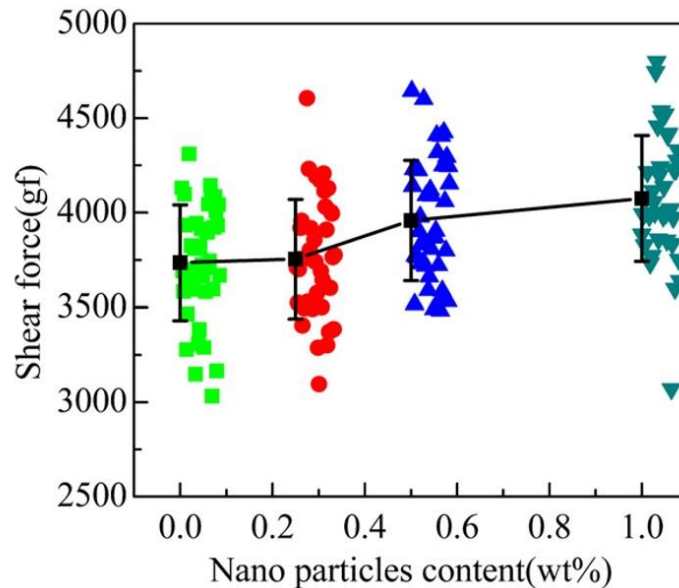


Figure 22: Shear strength of reinforced  $\text{Al}_2\text{O}_3$  Sn-3.0Ag-0.5Cu solder joint [121].

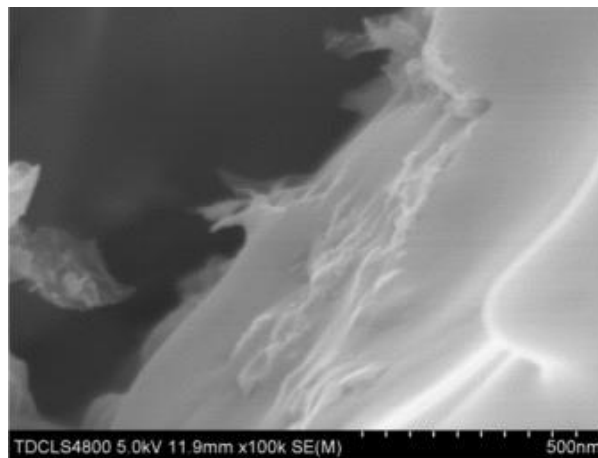


Figure 23: Secondary electron SEM images of fractured surface Ag modified graphene reinforced Sn-Ag-Cu solder [124].

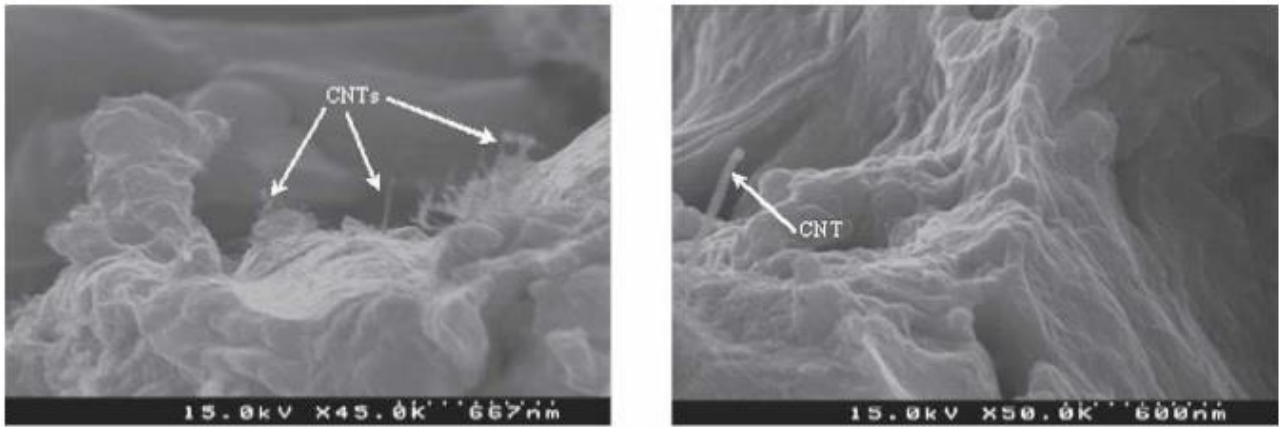


Figure 24: Secondary electron image of MWCNT reinforced Sn-3.5Ag-0.7Cu tensile fracture surface [125].

In addition, aluminium borate ( $\text{Al}_{18}\text{B}_4\text{O}_{33}$ ) whisker reinforcement added to Sn-Bi solder reduced the interfacial intermetallic layer compared to non-reinforced solder joint after multiple melting cycles and thermal annealed samples. It was reported that the whiskers reinforcement could hinder Sn dislocation slip and strengthen the solder joints [127]. Micro-sized  $\text{Si}_3\text{N}_4$  particles could be also used as reinforcing particles in Sn-0.7Cu solder which in the lap-shear test resulted in an increase of hardness and ultimate shear strength of the solder joint [128].

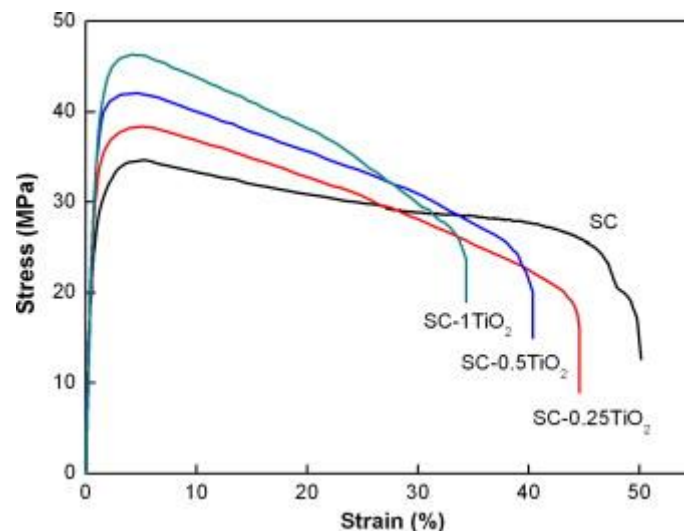


Figure 25: Tensile strength results of  $\text{TiO}_2$  reinforced solder comparing with non-reinforced Sn-0.7Cu solder [129].

In most of the studies of Tsao et al., the  $\text{TiO}_2$  reinforced solder had improved the mechanical properties of a solder joint [129-133].  $\text{TiO}_2$  additions to Sn-1.5Sb-1Ag resulted in refinements to  $\text{Ag}_3\text{Sn}$  intermetallic in the bulk solder and resulted in a higher microhardness

and tensile strength on fast and slow cooled samples [133].  $\text{TiO}_2$  particle additions on Sn-0.7Cu solder were reported to increase the tensile strength to a more uniform eutectic microstructure with finer  $\text{Cu}_6\text{Sn}_5$  intermetallic in the bulk solder [129]. As can be observed in Figure 25, a higher amount of  $\text{TiO}_2$  (1wt%) in Sn-0.7Cu increased the tensile strength of the reinforced solder [129].

In general, most of the reinforcement additions were reported to increase the mechanical properties of the solder by increasing the tensile strength and hardness and increasing the solder joint shear strength. This was majorly due to the reinforcement additions that were able to pin to the dislocation slides in the bulk solder, suppressing the interfacial intermetallic layer and also refining the microstructure in the bulk solder.

## **2.7 Summary and remarks**

In summary, reinforcement to solder materials can be categorised by intrinsic reinforcements and extrinsic reinforcements. Intrinsic reinforcement is categorised as reinforcement to the bulk solder produced by forming intermetallic phase particles particularly during the soldering solidification or subsequent annealing while extrinsic reinforcement is categorised as reinforcement particles incorporated to the solders externally. Based on the current literature, reinforcing solder materials with either intrinsic or extrinsic reinforcement particles is a viable method in improving solder joint properties such as the hardness and shear strength. Various reinforcement particles, of either nano or micro size, have been widely selected and used in solder alloys. Most of the findings widely report that nano-sized non-metallic particles were able to suppress the interfacial intermetallic layer of a solder joint and refine the microstructure in the solder matrix. Due to this effect, the mechanical properties of a solder joint were widely reported to have improved. The mechanism of the reinforcement additions to the refinements of the intermetallic (either in the interfacial layer or the matrix) of a solder joint is still not strongly proven or understood. In addition, the majority of reinforcement effect studies of solder joints were conducted on Sn-Ag-Cu solder alloy and less study reports were conducted on Sn-Cu solder alloys. Since complex reactions happen during soldering, especially in the reinforced solder joints, further in-depth investigation of the microstructure formation in reinforced solder joints is needed to fully understand the reactions. The purpose of this research study is to investigate the microstructure formations in reinforced Sn-Cu based solder in both intrinsic and extrinsic

reinforced solders. This includes investigating the effects of reinforced solder during single reflow, multiple reflow and annealing experiments. Solder joint strength of the reinforced solder will then be also evaluated.

It is known that the microstructure of a material is an important factor in both materials processing and performance, and microstructure control plays is critical in determining properties in many applications [134]. In solder joints specifically, the microstructure can affect the performance including the fatigue life during thermal cycling [135], the tolerance to drop impacts [136] and the resistance to electromigration [137]. Since the mechanism by which reinforcement particle additions cause a refinement in the the intermetallics present in are unclear, this study focuses on the microstructure formation in reinforced solder joints. This is an important area of research in the electronic packaging field [2, 138] particularly considering the need to develop more advanced electronic joining technologies while meeting the global environmental demands required of Pb-free solder joints [1, 4]. The mechanisms relating to microstructure formation in the reinforced solder will have potential to be used as a basis in controlling the microstructure in the development of high-performance solder joints for both general and specific applications.



## **Chapter 3 Fabrication method of extrinsic ceramic reinforced solders and methods of in-situ soldering observations using synchrotron X-ray radiography imaging (SXRI) techniques.**

This chapter focuses on the methodology which was used throughout the study to fabricate extrinsic ceramic reinforced solders and a method of in situ soldering observation using an SXRI technique. Fabrication of TiO<sub>2</sub> reinforced solder using a PM method involving microwave sintering technique and characterization of the bulk solder materials is presented in Paper 1 of this thesis titled “Development of a microwave sintered TiO<sub>2</sub> reinforced Sn-0.7wt%Cu-0.05wt%Ni alloy”. In this paper, characterization of the fabricated reinforced solder materials was performed including microstructure, thermal properties the coefficient of thermal expansion and mechanical properties using microhardness indentation. Using XPS and advance characterization analytical tools such as synchrotron micro-XRF and HRTEM, the distribution of TiO<sub>2</sub> throughout the solder matrix after microwave sintering was investigated. These results were used as a basis in understanding the bulk properties of the fabricated reinforced solder before soldering. Based on the superior properties of the fabricated solder, the microwave sintering PM route was discussed as a promising method for fabrication of reinforced Pb-free solders.

In analysing complex and rapid reactions during soldering, an in situ soldering observation technique was successfully developed which enabled reactions during soldering to be observed in real-time. The technique development is outlined in Paper 2 of this thesis and is titled “In-situ soldering process technique by synchrotron X-ray imaging”. This paper is a major achievement and represents the first in situ observation of the soldering process. This allowed complex reactions during soldering to be observed including the reactive wetting of molten solder on a Cu substrate, flux void formation and the initial formation of interfacial Cu<sub>6</sub>Sn<sub>5</sub>. This paper explains the experimental setup of the in situ soldering experiment using SXRI including methods for determining the optimum beam energy used for observation. This technique is used as a basis for other experiments in this thesis and was critical in understanding the microstructure formation of the reinforced solders. It is a technique which can be further developed and is likely to find application in the analysis of complex reactions that cannot be observed using other techniques.

# **Paper 1: Development of a microwave sintered TiO<sub>2</sub> reinforced Sn-0.7wt%Cu-0.05wt%Ni alloy**

Mohd Arif Anuar Mohd Salleh, Stuart D. McDonald, Yasuko Terada, Hideyuki  
Yasuda, Kazuhiro Nogita

**Materials & Design**, 82 (2015), 136-147

# **Development of a microwave sintered TiO<sub>2</sub> reinforced Sn-0.7wt%Cu-0.05wt%Ni alloy**

M. A. A. Mohd Salleh<sup>a,b,\*</sup>, S. D. McDonald<sup>a</sup>, Y. Terada<sup>c</sup>, H. Yasuda<sup>d</sup>, K. Nogita<sup>a</sup>

<sup>a</sup>Nihon Superior Centre for the Manufacture of Electronic Materials (NS CMEM), School of Mechanical and Mining Engineering, The University of Queensland, 4072 St Lucia, Queensland, Australia.

<sup>b</sup>Centre of Excellence Geopolymer and Green Technology, School of Materials Engineering, Universiti Malaysia Perlis (UniMAP), Taman Muhibbah 02600, Jejawi, Arau, Perlis, Malaysia.

<sup>c</sup>The Japan Synchrotron Radiation Research Institute, Mikazuki-cho, Hyogo 679-5198, Japan.

<sup>d</sup>Department of Materials Science and Engineering, Kyoto University, Sakyo-ku, Kyoto 606-8501, Japan.

\*Corresponding author: Room 634, 49 Jocks Rd., St Lucia, Brisbane, QLD 4072, Australia

Email: m.mohdsalleh@uq.edu.au / arifanuar@unimap.edu.my

Tel: +61 435 946 670

## **Abstract**

The use of reinforcing nano-size ceramic particulates is a promising method to improve the mechanical and thermal properties of lead-free solder materials. In addition, advanced fabrication processes routes such as microwave sintering powder metallurgy (PM) enhance properties in the fabrication of composite solders. To elucidate the mechanisms underlying the improvements in mechanical and thermal properties, Sn-Cu-Ni with TiO<sub>2</sub> nano-composite additions, fabricated via a microwave sintering PM method, were investigated using state-of-the-art characterization techniques. Synchrotron micro-X-ray fluorescence (XRF) results detected trace Ti in the solder matrix. This was consistent with X-ray photoelectron spectroscopy (XPS) and high resolution transmission electron microscopy (HRTEM) results which indicated that nano crystals were within the Sn matrix. It is possible these nano crystal form due to the migration of Ti during the rapid high energy microwave heating. A hypothesis of improved thermal and mechanical properties of nano-composite

solders is discussed based on the results and the microwave sintering PM route was discussed as a promising method for next generation lead-free solder processing.

## **1. Introduction**

Over the past few years the electronic packaging industry has grown rapidly becoming more advanced and sophisticated and is constantly adapting to the requirements of the latest generation electronic devices. Advances in electronics today are accompanied by advances in soldering technology since interconnect materials such as solders are used in electronic packaging to electrically and mechanically join components to form functional circuits. In electronic assemblies, the solder alloy plays a critical role in performance and reliability [1, 2].

Development of solder alloys has also been driven by a need to reduce the consumption of lead in the tin-lead (Sn-Pb) solders used in previous generation electronic packaging industries. Initiatives such as WEEE (Waste from Electronic Equipment) and RoHS (Restriction of hazardous Substances Directive) which took effect on 1 July 2006 [3] have seen the European Union (EU) minimize the use of hazardous substances such as lead (Pb), mercury (Hg), cadmium (Cd), hexavalent chromium (Cr<sup>6+</sup>), polybrominated biphenyls (PBB) and polybrominated diphenyl ether (PBDE). In addition, there is a consumer preference for 'green' products in appliances as environmental and a health concern over the toxicity of electronic waste is increasing. This has driven the development of lead-free solders in the electronic packaging industries. Many organizations such as the Institute of Printed Circuits (IPC), the National Institute of Standard and Technology (NIST), the National Center for Manufacturing Science (NCMS), and The National Electronics Manufacturing Initiative (NEMI) have assisted the electronic industries in implementing lead-free solders into their products [4]. Among the wide choices of eutectic-based alloys for lead-free solder tin-silver-copper (Sn-Ag-Cu) is the most selected alloy in the industry while tin-copper (Sn-Cu) and tin-copper-nickel (Sn-Cu-Ni) are frequently chosen as a lower cost alternative for wave soldering techniques [5]. Although there is a broad variety of lead-free solder provided by the solder manufacturing industries, there is still no consensus on a definitive replacement for traditional Sn-Pb solders [6-10].

The current trend in the electronic packaging industry towards miniaturization of electronic devices has been constantly pressuring the microelectronic industries to develop finer pitch interconnects. Until now, higher functional densities in printed circuit boards (PCB) are made

possible by surface mount technology (SMT). However, SMT processes demand higher reliability and dimensional stability of solder joints as less and less solder is allowed for each joint. Therefore, the reliability of solder joints becomes extremely important in ultra-fine pitch technology [11, 12].

Significant research has been directed at matching the existing lead-free solder properties with the processing and property constraints of current PCB materials. Due to the unique characteristics of Sn-Pb solders such as low cost and ease of manufacturing, finding suitable alternatives free of lead is a challenging issue. Not only must the lead-free alternatives meet health, environment and safety requirements, as well as solder joint reliability and performance expectations, they must also be compatible with the existing soldering processes. This includes the thermal properties of the solder such as liquidus temperature, melting range, undercooling and coefficient of thermal expansion (CTE).

One of the emerging technologies in upgrading existing solder alloys involves using a composite technology approach to form metal matrix composites (MMCs). A viable way to enhance the performance and properties of solder is to introduce a second phase to the matrix, forming a composite solder where precipitation and dispersion hardening can be utilised [13]. In the early stages of solder composite technology development, Guo [14] stressed that the development of composite lead-free is likely to improve the service temperature capabilities and thermal stability of the solder joints. Shen and Chan [15] discussed the benefits in terms of enhanced creep strength and thermo-mechanical fatigue resistance of solder materials while outlining the latest nano-composite solder development studies.

Generally, a composite solder involves a eutectic alloy solder reinforced or mixed with additional metals or non-metals that have low solubility and diffusivity. Ceramic reinforcement is a convenient approach in enhancing the alloy based solder matrix mechanical properties without the concern of excessive phase formation either during fabrication or later because of the high melting temperature difference between the alloy and the ceramic. However, the fabrication of such a composite solder with a homogenous distribution of reinforcement particles in an alloy is a challenge, especially when using conventional solidification processing methods. Solid state processing, commonly referred as powder metallurgy (PM) methods are a leading options to produce these lead-free ceramic composite solders with homogenous distribution of particles [16]. However, in PM

methods, a conventional sintering step is quite a challenge in adopting this fabrication method since it consumes a significant amount of energy, time and cost and could increase the tendency for surface oxidation. Hence, a novel heat treatment process such as microwave sintering can be a viable way to development lead-free composite solders in order to overcome the inherent disadvantages of conventional sintering [17]. In fabricating such composite solder, an end product of a homogenously distributed reinforced composite pre-form solder is expected to be achieved for further use in a reflow soldering process with the objective of producing a solder joint of high integrity and strength.

Recent research on the incorporation of small additions of ceramic reinforcement in a variety of solder matrices including silicon carbide (SiC) [18-20], alumina ( $\text{Al}_2\text{O}_3$ ) [10, 21, 22], zirconia ( $\text{ZrO}_2$ ) [23-26], titanium oxide ( $\text{TiO}_2$ ) [27-32] and silicon nitride ( $\text{Si}_3\text{N}_4$ ) [8, 33] have shown improved mechanical and thermal properties of the resulting solder. Tsao [21] hypothesized that with the addition of ceramic reinforcement, these nano-sized ceramic particles are absorbed in the liquid during soldering and suppress the dissolution of the Cu substrate and in return retard the growth of the intermetallic compound (IMC). El-Daly [34] has hypothesized that ceramic nanoparticles could act as additional nucleation sites where the rate of solidification of  $\beta$ -Sn will be faster and thereby limit the growth of IMC's such as  $\text{Ag}_3\text{Sn}$  and  $\text{Cu}_6\text{Sn}$  and in return reduce the brittleness of the solder joint [34]. However, these hypotheses are not strongly supported by experimental evidence. Research in the file of reinforced solder alloy has focused on developing the composite solder by using a powder metallurgy route which comprises of mixing, compaction and sintering of a solder pre-form [8, 17, 22, 35, 36]. In recent studies, microwave assisted sintering has been shown to result in superior solder performance, especially with respect to mechanical properties [8, 9, 37, 38], [17, 39]. However, it is currently unclear how the combination of ceramic reinforcement and sintering technique act to improve properties. This paper aims to compare the processes of microwave sintering and conventional sintering on the microstructure, microhardness and thermal properties of a novel Sn-Cu-Ni solder reinforced with nano-scale  $\text{TiO}_2$ . Several advanced characterization techniques such as differential scanning calorimetry (DSC), dilatometry, high resolution transmission electron microscopy (HRTEM) and scanning electron microscopy (SEM) coupled with energy dispersive X-ray spectroscopy (EDX), synchrotron micro-X-ray Fluorescence (XRF) mapping and X-ray photoelectron spectroscopy (XPS) were used throughout this study.

## 2. Experiment Details

### 2.1 Sample Fabrication

In this study, Sn-0.7wt%Cu-0.05wt%Ni solder powders in spherical shape with an average particle size of 45  $\mu\text{m}$  supplied by Nihon Superior Co. Ltd. (Figure 1a and 1b) were used for the base matrix materials, along with 99.7% purity  $\text{TiO}_2$  anatase powder supplied by Sigma Aldrich, which had an average particle size of <50 nm (Figure 1c). The chemical composition of the Sn-0.7wt%Cu-0.05wt%Ni solder powder is shown in Table 1. To fabricate the Sn-Cu-Ni with  $\text{TiO}_2$  nano-composite solder, 1wt% of  $\text{TiO}_2$  particles were incorporated into the Sn-0.7wt%Cu-0.05wt%Ni solder matrix using a powder metallurgy route. The composite solder materials were homogeneously mixed with the base matrix powder in an airtight container using a tubular mixer for 1 hour. The solder mixtures were uniaxially compacted in a 12-mm diameter mold at 120 bar, and the compacted billets were conventionally and microwave sintered in an inert argon atmosphere. Conventional sintering was carried out using a horizontal tube furnace (VT furnace) of 6kW power in an argon controlled environment at 10  $^{\circ}\text{C}/\text{min}$  heating rate. Sintering temperatures are normally between  $0.75T_m$  to  $0.98T_m$  and from previous studies, the sintering temperatures of Sn base materials for either conventional sintering or microwave sintering are in the range of  $0.8T_m$  [8, 9, 17, 33, 36, 37, 39-41]. Hence, in this study, a sintering temperature at 185  $^{\circ}\text{C}$  ( $\sim 0.8T_m$ ) was used for both conventional and microwave sintering. To ensure homogenous heating 2 hours of sintering time was used for conventional sintering [39, 42].

A schematic diagram of the microwave sintering setup used in this study is shown in Figure 1d. In this study, a microwave oven with an output power of 1,000W at full power was used with further details as in Table 2. Approximately 3 minutes of microwave sintering time was taken to achieve the sintering temperature.

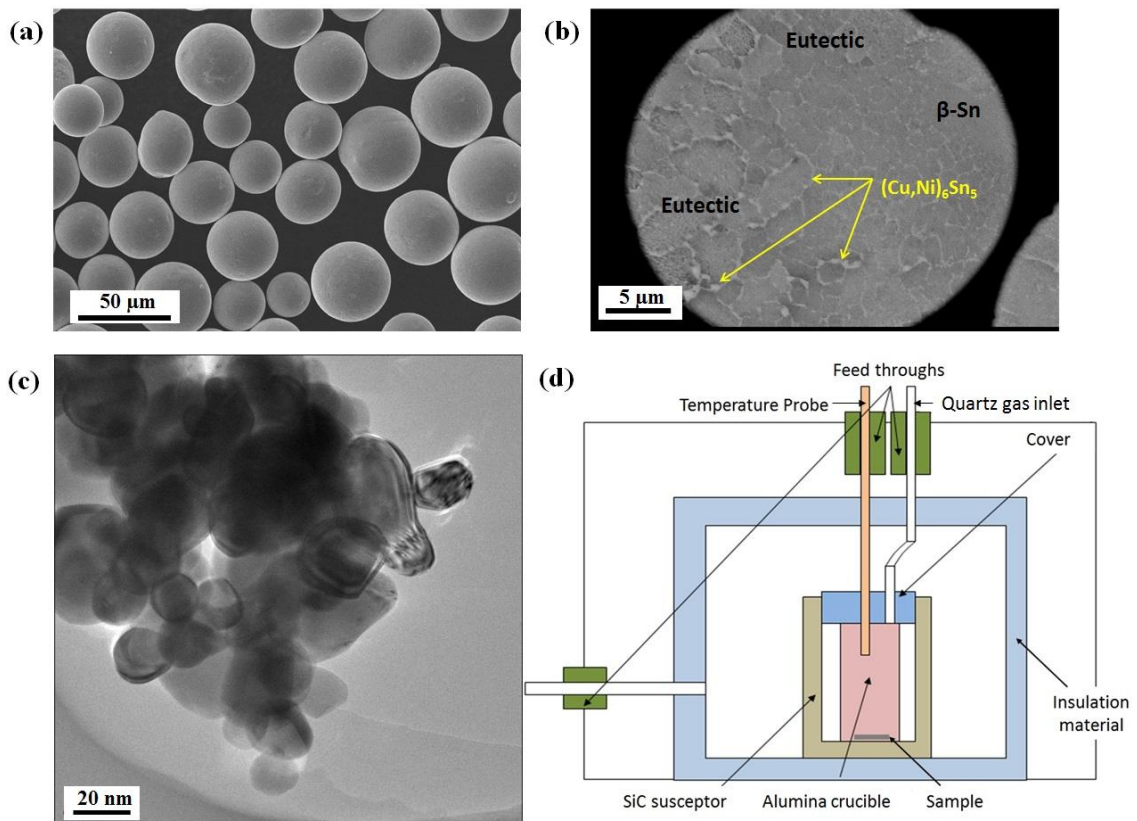


Figure 1: (a) SEM image of Sn-0.7wt%Cu-0.05wt%Ni solder, (b) cross-section of as supplied Sn-0.7wt%Cu-0.05wt%Ni powder, (c) bright field TEM image of nano-size TiO<sub>2</sub> particulates and (d) schematic diagram of the microwave sintering setup.

Table 1: Chemical composition of the Sn-0.7wt%Cu-0.05wt%Ni solder powder.

	Sn	Cu	Ni	Sb	Bi	Zn	Al	As	Cd	Pb
Wt %	Balance	0.62	0.05	0.00	0.01	0.00	<0.00	0.00	<0.00	0.03
	e	0	6	8	0	4	1	3	1	1



Table 2: Microwave sintering set up specification.

<b>Microwave Oven Specification</b>	
<b>Power source</b>	120 V, 60 Hz
<b>Frequency</b>	2450 MHz
<b>Output power</b>	1000 Watts
<b>Cavity dimensions</b>	330 mm x 330 mm x 205 mm
<b>Sintering Cell Specification</b>	
<b>Susceptor material</b>	Silicon Carbide
<b>Susceptor dimension</b>	Inner diameter: 40 mm Outer diameter: 52 mm Height: 76 mm
<b>Insulation material</b>	Alumina + Silica
<b>Insulation material internal dimension</b>	150 mm x 150 mm x 155mm
<b>Insulation material thickness</b>	25 mm

## 2.2 Analysis and characterization

The microstructures of the sintered samples were observed using a JEOL 6610 SEM in backscattered electron imaging mode at an accelerating voltage of 25 kV. A solution of 2% HCl, 3% HNO<sub>3</sub> and 95% C<sub>2</sub>H<sub>6</sub>O was used to micro-etch the samples. Microhardness values of the samples were obtained using a Vickers microhardness test machine operated according to the ASTM B933-09 standard test method. The test was conducted on the flat polished surface of each of the 12-mm diameter samples using an indentation load of 1 kg.f for a 10-s dwell time. A Mettler Toledo DSC was used to characterise the thermal reactions of the reinforced solders during melting and solidification. The total weight of each sample slice was kept below 10 mg following the requirement of the DSC equipment and was placed into a Cu pan, which was heated to a temperature of 250 °C and cooled down to room temperature using a heating and cooling rate of 10 °C/mm under a protective nitrogen atmosphere. The coefficient of thermal expansion (CTE) was measured using a Linseis L75HX1600 horizontal dilatometer from room temperature to 160 °C. The CTE of the samples were determined by measuring the displacement of the samples at a certain values of temperature. The test was conducted according to the ASTM E831-03 standard test method. Density measurement of three samples of each type were conducted by using Archimedes principle with Galden liquid.

The microstructures of the samples were examined using micro- XRF mapping and TEM analysis. Micro-XRF using a highly focused beam of extremely intense synchrotron radiation X-rays can detect very small trace metal element additions down to the pico level which can't be achieved using conventional methods such as EDX or electron probe microanalysis (EPMA) [43]. In this study micro-XRF was used to detect Ti, Cu and Ni throughout a specific area of the sample. TEM analysis was conducted to further visualize and analyze the morphologic and crystallographic features at the nanometer scale. Synchrotron XRF mapping experiments were carried out at the beamline BL37XU of the SPring-8 Japan synchrotron with conditions identical to that used elsewhere [44-46]. A high flux 300 nm focused X-ray beam with  $1.4 \times 10^{12}$  photons  $s^{-1}$  was used at an X-ray energy of 12 keV. The data was then analyzed and processed using Igor 6.32A software from Wavemetrics, USA. Electron microscopy was conducted on a F20 Tecnai and a Jeol 2100 TEM equipped with a scanning transmission electron microscope (STEM)/ EDX. In preparing TEM cross-section samples, a focussed ion beam (FIB) was used to mill samples <100  $\mu m$  in thickness. For further elemental composition analysis and potential chemical state bonding change due to the microwave and conventional sintering, XPS analysis was performed. XPS data was acquired using a Kratos Axis ULTRA X-ray Photoelectron Spectrometer incorporating a 165mm hemispherical electron energy analyser. The incident radiation was Monochromatic Al K $\alpha$  X-rays (1486.6eV) at 225W (15kV, 15ma). Survey (wide) scans were taken at analyser pass energy of 160eV and multiplex (narrow) high resolution scans at 20eV. Survey scans were carried out over 1200-0eV binding energy range with 1.0eV steps and a dwell time of 100ms. Narrow high-resolution scans were run with 0.05eV steps and 250ms dwell time. Base pressure in the analysis chamber was  $1.0 \times 10^{-9}$  torr and during sample analysis  $1.0 \times 10^{-8}$  torr. Atomic concentrations were calculated using the CasaXPS version 2.3.14 software and a Shirley baseline with Kratos library Relative Sensitivity Factors (RSFs). Peak fitting of the high-resolution data was also carried out using the CasaXPS software. Since XPS is a surface quantitative spectroscopy technique, in order to detect possibilities of a change in chemical state bonding with TiO<sub>2</sub> additions and sintering, the samples was argon-ion etched to remove the oxidation layer and any contamination of the surface prior to XPS analysis.

### **3. Results and Discussion**

#### **3.1 Thermal Properties**

The thermal expansion of a solder material is important as heat during operation or processing can result in expansion and contraction during heating or cooling. With higher

values of the coefficient of thermal expansion, a solder material will expand and contract more and create higher amounts of stress particularly at the solder joint. It is also important that the difference of CTE between a solder material and a particular substrate is minimized.

CTE measurements were conducted on microwave sintered and conventionally sintered Sn-Cu-Ni samples with and without  $\text{TiO}_2$ . CTE results of these materials were measured from room temperature to 200 °C as shown in Figure 2. Results indicated that the CTE of Sn-Cu-Ni with  $\text{TiO}_2$  samples sintered either by microwave or conventional sintering processes have a similar behavior with respect to the CTE temperature relationship. The microwave sintered Sn-Cu-Ni with  $\text{TiO}_2$  samples have slightly higher (approximately  $1.00 \times 10^{-6}/\text{K}$ ) values of CTE compared to conventional sintered samples. With the addition of nano-sized  $\text{TiO}_2$  particles, it is observed that the CTE values of both microwave sintered and conventionally sintered samples increases compared to samples free of  $\text{TiO}_2$  particles. Microwave sintering and the addition of reinforcement particles may increase the density of the sample and increase the amount of fine intermetallics as observed in the microstructure, which in return increases the CTE. In addition, By comparing the CTE values at 150 °C, the CTE value of microwave sintered Sn-Cu-Ni with  $\text{TiO}_2$  was the highest ( $21.33 \times 10^{-6}/\text{K}$ ) while the microwave sintered Sn-Cu-Ni sample had the lowest CTE value ( $9.33 \times 10^{-6}/\text{K}$ ). In comparison with common metal substrates used in electronic joining, at 150 °C, pure Cu has a CTE value of approximately  $25.00 \times 10^{-6}/\text{K}$  [47]. Thus, although the CTE of microwave sintered Sn-Cu-Ni with  $\text{TiO}_2$  samples have slightly higher values compared to conventionally sintered samples, the CTE mismatch compared to pure Cu is relatively small compared to the other samples tested.

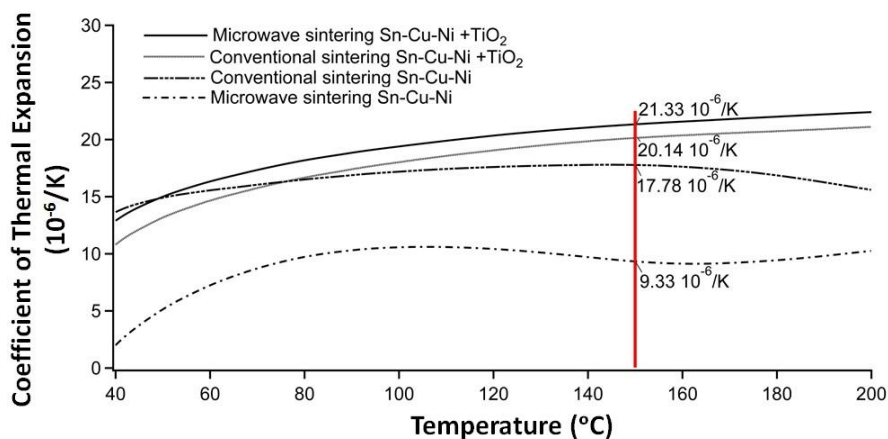


Figure 2: Coefficient of thermal expansion of microwave and conventionally sintered Sn-Cu-Ni samples with and without  $\text{TiO}_2$ .

In order to determine the liquidus temperature, freezing range and undercooling, DSC measurements were carried out during heating from room temperature to 250 °C and cooling to room temperature at a rate of 10 °C.mm<sup>-1</sup> in both cases. Figure 3 (a) shows the results for conventionally sintered Sn-Cu-Ni, (b) microwave sintered Sn-Cu-Ni, (c) conventionally sintered Sn-Cu-Ni with TiO<sub>2</sub> and (d) microwave sintered Sn-Cu-Ni with TiO<sub>2</sub>. The results of the thermal properties are shown in Table 3. The liquidus temperature of the solder is defined as where the alloy is completely molten. During heating in DSC measurement, the liquidus temperature of microwave and conventional sintered Sn-Cu-Ni with TiO<sub>2</sub> were about 233.50 °C and 235.96 °C respectively which are slightly higher than the Sn-Cu-Ni samples sintered by either the microwave or conventional methods. The addition of TiO<sub>2</sub> had a bigger effect on raising the liquidus temperature in the conventionally sintered samples (approximately 4.3 °C) compared to the microwave sintered samples (approximately 1.8 °C). In addition, based on the DSC curve, the freezing range can be measured as  $T_{\text{endset heating}} - T_{\text{onset heating}}$ . As in Table 3, samples with TiO<sub>2</sub> additions resulted in a higher freezing range compared to samples with TiO<sub>2</sub> additions where microwave sintered Sn-Cu-Ni with TiO<sub>2</sub> samples have a smaller solidification range compared to conventionally sintered Sn-Cu-Ni with TiO<sub>2</sub> samples with 5.94 °C and 8.73 °C respectively. The effect of TiO<sub>2</sub> was to increase the freezing range and this effect was larger in the conventionally sintered samples. The smaller increase in freezing range with the microwave sintering process (for TiO<sub>2</sub> reinforced solders) may reduce some manufacturing problems experienced during the soldering process [48]. The nucleation undercooling for the initial solidification reaction can be measured by  $T_{\text{onset heating}} - T_{\text{onset cooling}}$ . Microwave sintering increases the undercooling in alloys free of TiO<sub>2</sub> which may relate to the dissolution of nuclei. There is very little difference between the nucleation undercooling in TiO<sub>2</sub> containing samples.

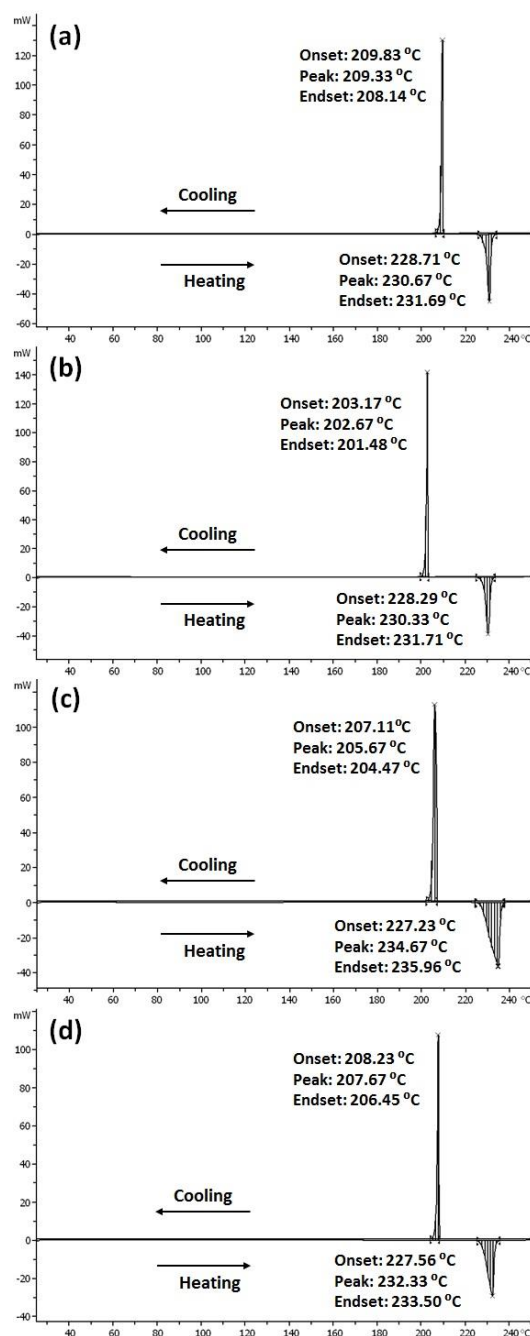


Figure 3: Differential scanning calorimetry curve of (a) conventional sintered Sn-Cu-Ni, (b) microwave sintered Sn-Cu-Ni, (c) conventional sintered Sn-Cu-Ni with TiO<sub>2</sub> and (d) microwave sintered Sn-Cu-Ni with TiO<sub>2</sub>.

Table 3: Thermal properties of microwave and conventional sintered Sn-Cu-Ni with TiO<sub>2</sub> nano-composite solder.

	<b>Coefficient of Thermal Expansion at 150 °C (10<sup>-6</sup>/K)</b>	<b>Liquidus Temperature (T<sub>endset heating</sub>) (°C)</b>	<b>Freezing Range (T<sub>endset heating</sub>- T<sub>onset heating</sub>) (°C)</b>	<b>Undercooling (T<sub>onset heating</sub>- T<sub>onset cooling</sub>) (°C)</b>
Conventional Sintered Sn-Cu-Ni	17.78	231.69	2.98	18.88
Microwave Sintered Sn- Cu-Ni	9.33	231.71	3.42	25.12
Conventional Sintered Sn-Cu-Ni+TiO <sub>2</sub>	20.14	235.96	8.73	20.12
Microwave Sintered Sn- Cu-Ni+TiO <sub>2</sub>	21.33	233.50	5.94	19.33

### 3.2 Microhardness and density

The microhardness results shown in Figure 4 and Table 4, show a trend of higher hardness values in microwave sintered samples for both TiO<sub>2</sub> containing and TiO<sub>2</sub> free samples. While TiO<sub>2</sub> increased the hardness of microwave sintered samples significantly, it had little or a slight softening effect in the conventionally sintered samples. There was no significant difference in the hardness result when comparing conventionally sintered TiO<sub>2</sub> containing and TiO<sub>2</sub> free samples. The hardest samples were the microwave sintered Sn-Cu-Ni with TiO<sub>2</sub> which had an average microhardness value of 16.64 Hv. These results show that additions of TiO<sub>2</sub> reinforcement to the Sn-Cu-Ni solder matrix have dramatically increased the hardness values in microwave sintered samples. From SEM micrographs as in Figure 5e, it is suggested that microwave sintering of TiO<sub>2</sub> reinforced samples may increase the rate of intermetallic formation and could also restrict the growth resulting in a uniform distribution of fine (Cu,Ni)<sub>6</sub>Sn<sub>5</sub>. Fine distributed intermetallics could enhance the pinning effect of the sample and hence increases the hardness. On the other hand, slightly coarser and smaller amounts of (Cu,Ni)<sub>6</sub>Sn<sub>5</sub> intermetallics were observed in conventional sintered

samples which may relate to the long sintering time in comparison to the rapid times involved in microwave sintering.

The density of samples was characterised for unsintered as well as conventionally and microwave sintered. Compared to the theoretical density of  $7.272 \text{ g/cm}^3$ , the density of unsintered, conventionally and microwave sintered  $\text{TiO}_2$  containing samples was  $7.081 \text{ g/cm}^3$ ,  $7.095 \text{ g/cm}^3$  and  $7.113 \text{ g/cm}^3$  respectively. Microwave sintered  $\text{TiO}_2$  containing sample resulted in the highest density which suggests that the microwave process had enhanced the sintering and slightly reduced the porosity of sample.

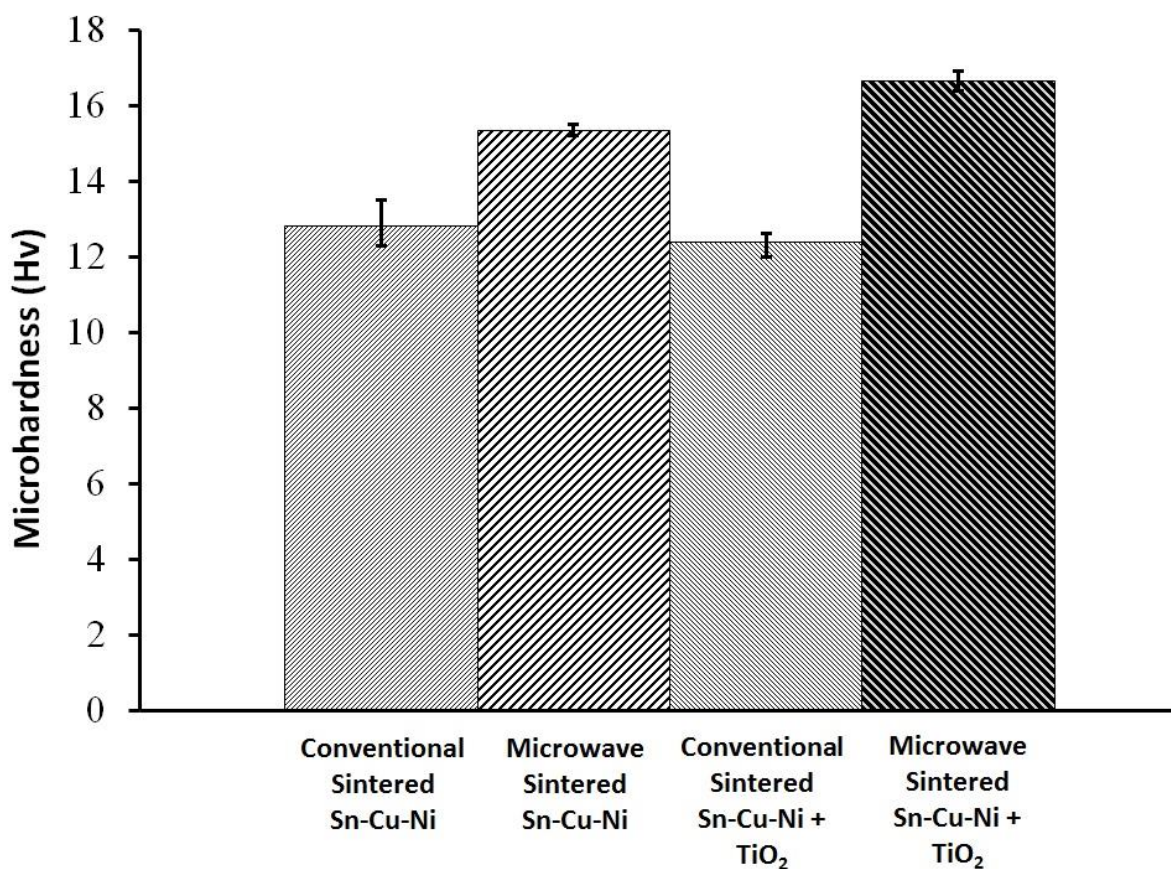


Figure 4: Microhardness of sintered samples.

Table 4: Average microhardness of microwave sintered and conventional sintered Sn-Cu-Ni with/without TiO<sub>2</sub>.

	Average Microhardness (Hv)
Conventional Sintered Sn-Cu-Ni	12.80
Microwave Sintered Sn-Cu-Ni	15.32
Conventional Sintered Sn-Cu-Ni+TiO <sub>2</sub>	12.36
Microwave Sintered Sn-Cu-Ni+TiO <sub>2</sub>	16.64

### 3.3 Microstructure Characterization

Samples of Sn-Cu-Ni with/without TiO<sub>2</sub> along with cross-sectioned as supplied Sn-Cu-Ni powder and un-sintered Sn-Cu-Ni samples were chemically micro-etched and observed using SEM as indicated in Figure 5. On all samples, the majority of eutectic and primary  $\beta$ -Sn phases were observed with (Cu,Ni)<sub>6</sub>Sn<sub>5</sub> intermetallics formed as precipitates along crystal grain boundaries. These fine (Cu,Ni)<sub>6</sub>Sn<sub>5</sub> intermetallics were observed on as supplied (Figure 1b) and un-sintered Sn-Cu-Ni samples (Figure 5a) and exhibit slight growth in the sintered samples. Distributions of (Cu,Ni)<sub>6</sub>Sn<sub>5</sub> intermetallics are slightly different between conventional sintered and microwave sintered samples where a higher number of fine (Cu,Ni)<sub>6</sub>Sn<sub>5</sub> intermetallics observed in microwave sintered samples. By comparing microwave sintered samples without and with TiO<sub>2</sub> (Figure 5c and Figure 5e respectively), the TiO<sub>2</sub> microwave sintered samples are shown to contain a higher amount of fine columnar distributed (Cu,Ni)<sub>6</sub>Sn<sub>5</sub> intermetallics. This higher number of fine columnar distributed (Cu,Ni)<sub>6</sub>Sn<sub>5</sub> intermetallics formed may be related to the rapid heating experienced during microwave heating and this may increases the hardness of the material. In addition there are likely to be TiO<sub>2</sub> particles located along the Sn-Cu-Ni particle grain boundary which appear as the more defined grain boundaries in Figure 5 (d) and (e) compared to (b) and (c).



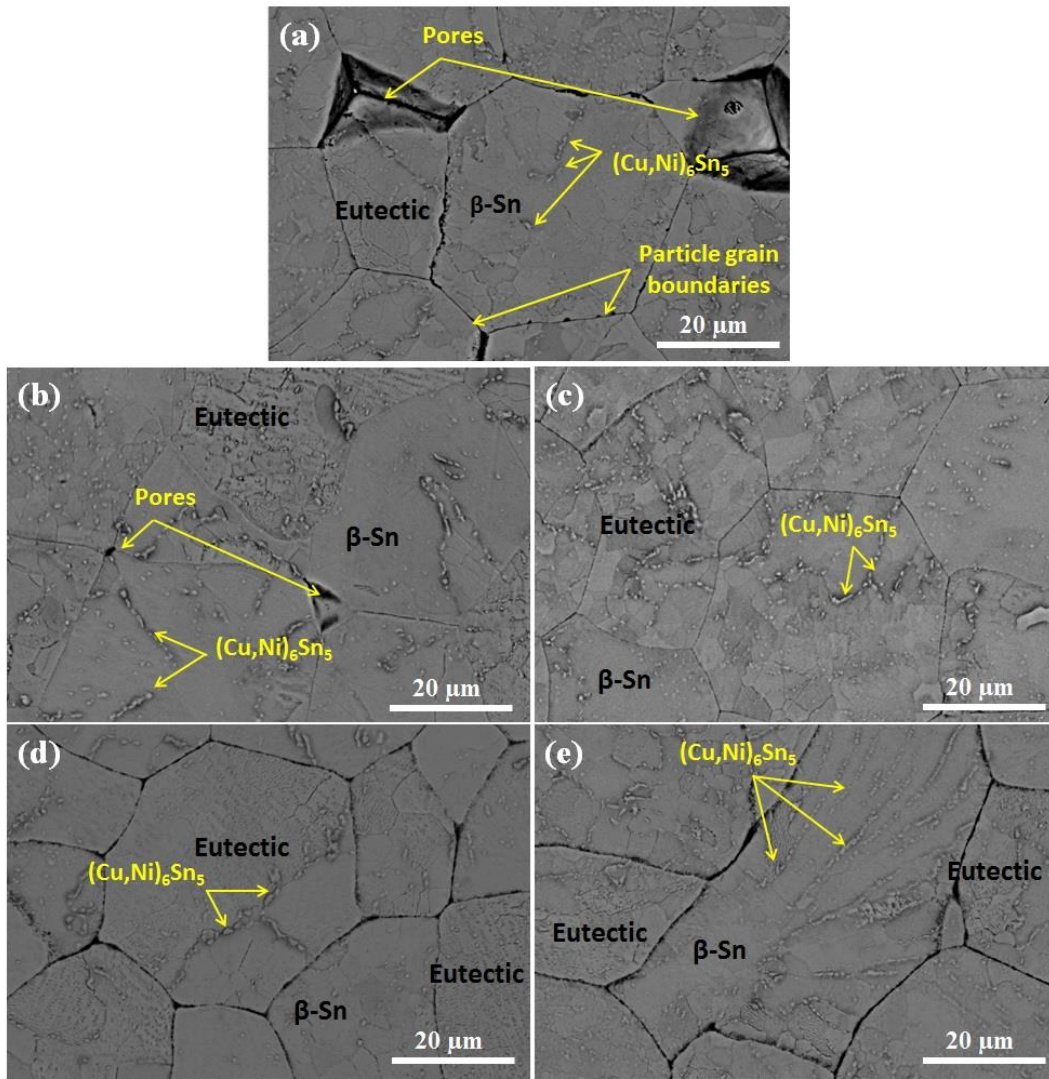


Figure 5: Backscattered electron images of (a) un-sintered Sn-Cu-Ni, (b) conventionally sintered Sn-Cu-Ni, (c) microwave sintered Sn-Cu-Ni, (d) conventionally sintered Sn-Cu-Ni with TiO<sub>2</sub> and (e) microwave sintered Sn-Cu-Ni with TiO<sub>2</sub>.

In order to investigate the distribution and any potential segregation of TiO<sub>2</sub> samples of conventional sintered and microwave sintered Sn-Cu-Ni with TiO<sub>2</sub> were further analyzed and compared using synchrotron micro-XRF mapping. Figure 6 and Figure 7 show the results of micro-XRF mapping in Sn-Cu-Ni with TiO<sub>2</sub> with microwave and conventional sintering respectively, showing that the Ti is mostly located within the particle grain boundaries in both samples. However, interestingly, a small amount of fine Ti can be observed inside the grains of microwave sintered Sn-Cu-Ni with TiO<sub>2</sub> (Figure 6b) while Cu and Ni elements are found distributed throughout the grain and are likely to be (Cu,Ni)<sub>6</sub>Sn<sub>5</sub> intermetallics) (Figure 6c and 6d). Spot analysis was conducted on selected areas of the mapping results. From these results, microwave technology can be a significant assistant in the sintering process since heat is generating within the materials and can produce homogeneous bulk heating

rates in small time frames and alter the distribution of elements in comparison to conventional sintering [37, 49].

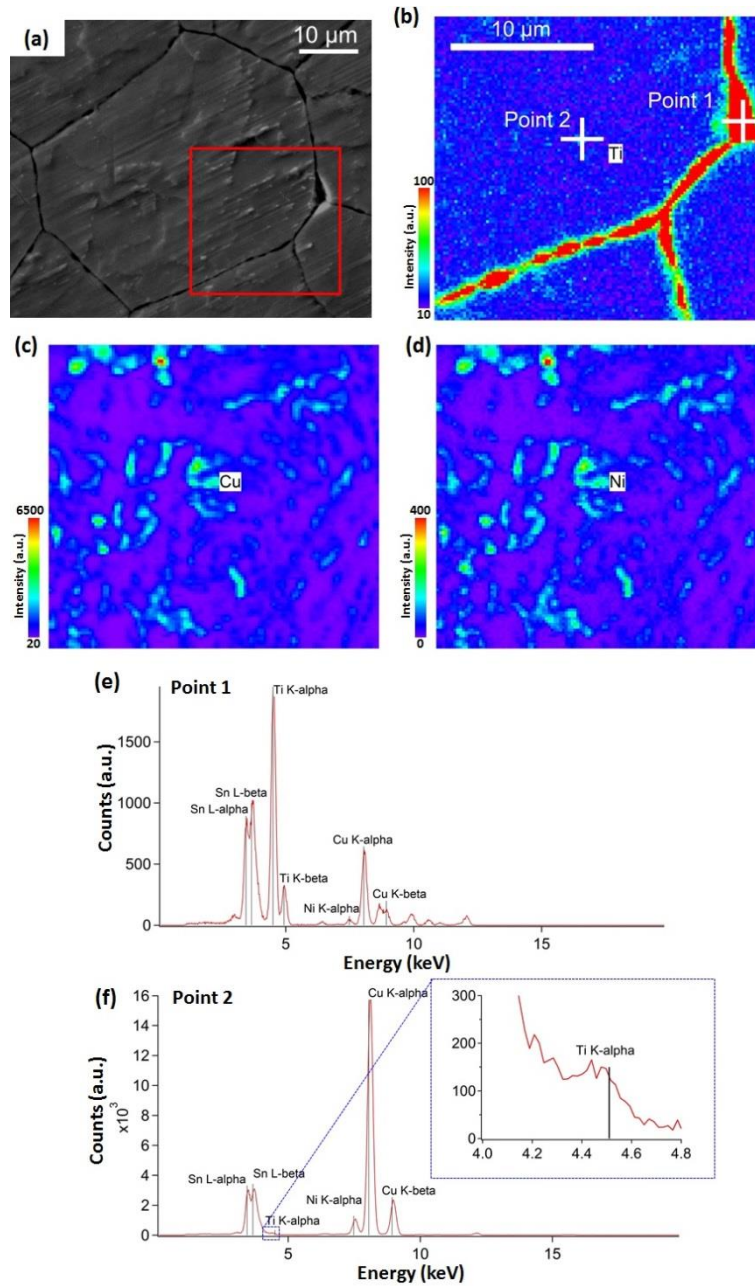


Figure 6: (a) SEM image of micro-XRF mapping area of microwave sintered Sn-Cu-Ni with  $\text{TiO}_2$  (b) Ti element mapping distributions, (c) Cu element mapping distributions, (d) Ni element mapping distributions, (e) point analysis spectrum at point 1 and (f) point analysis spectrum at point 2.

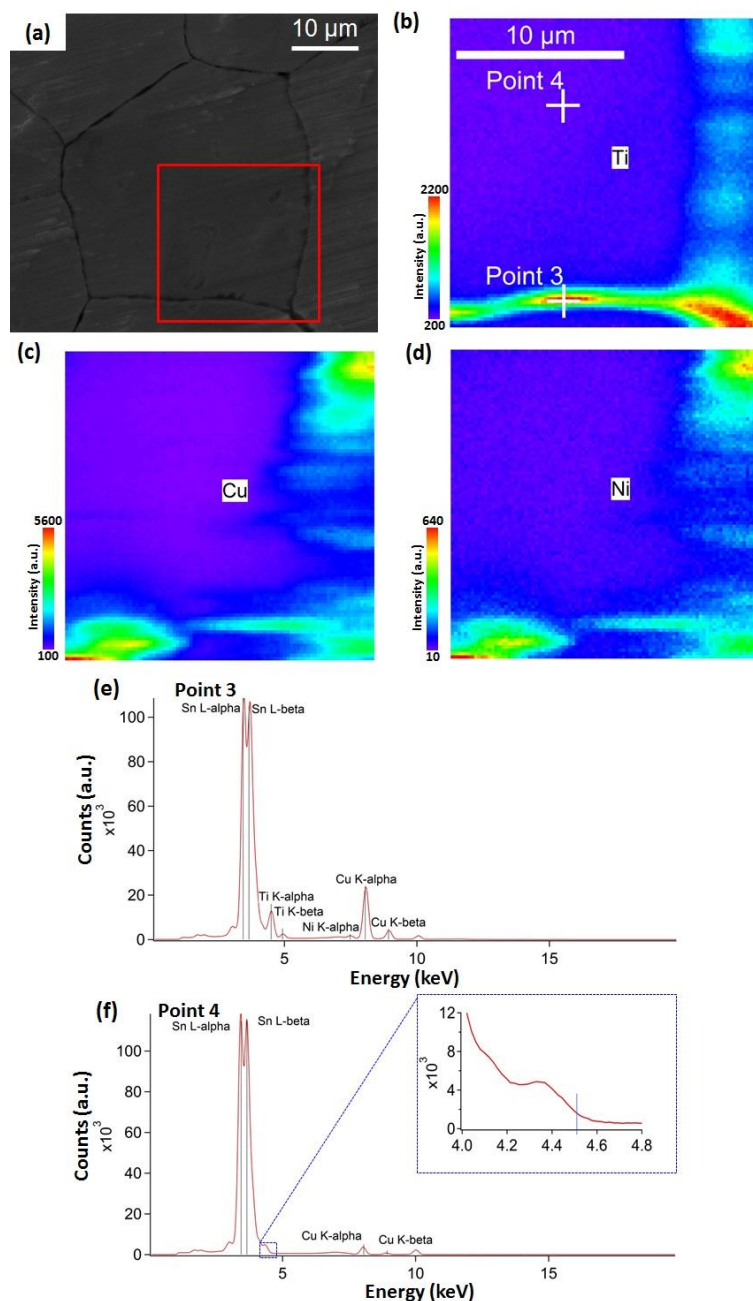


Figure 7: (a) SEM image of micro-XRF mapping area of conventional sintered Sn-Cu-Ni with  $\text{TiO}_2$  (b) Ti element mapping distributions, (c) Cu element mapping distributions, (d) Ni element mapping distributions, (e) point analysis spectrum at point 3 and (e) point analysis spectrum at point 4.

Results of synchrotron micro-XRF on conventional and microwave sintered samples of Sn-Cu-Ni with  $\text{TiO}_2$  were further analyzed using TEM. To eliminate any possibility of contamination of sample damage, samples were prepared using FIB (Figure 8a and 9a). Areas of interest are indicated as red box in the FIB sample cut images. From the TEM analysis results, particles of nano-size  $\text{TiO}_2$  can be clearly observed located along the particle grain boundaries on both conventional and microwave sintered samples as in Figure

8a and 9a respectively. In conventionally sintered Sn-Cu-Ni with  $\text{TiO}_2$  samples, a small amount of  $\text{TiO}_2$  particles were observed within the Sn matrix (Figure 8b and 8d). It is believed that these  $\text{TiO}_2$  particles had migrated during the semi-solid/liquid state regions of the Sn matrix during conventional sintering. In the microwave sintered  $\text{TiO}_2$  containing sample the HRTEM image and SADP of the Sn region as in Figure 9b contains many small nano-scale crystalline areas. These small crystals (indicated with a white dotted line around the perimeter) may have formed due the migration of Ti ions which may occur due to the rapid microwave heating and the presence of microwave induced vibrations [50, 51]. Different lattice planes were observed for both Sn and nano crystals in the HRTEM images. It is believed that Schottky disorder could happen to  $\text{TiO}_2$  at  $<580^\circ\text{C}$  where pairs of Ti ion vacancy and oxide ion vacancy are formed and that this could be accelerated by rapid microwave heating [52]. In addition, with the interaction of multiple valence states of Sn and Ti may result in the possibility of substitution between Sn and Ti [52].



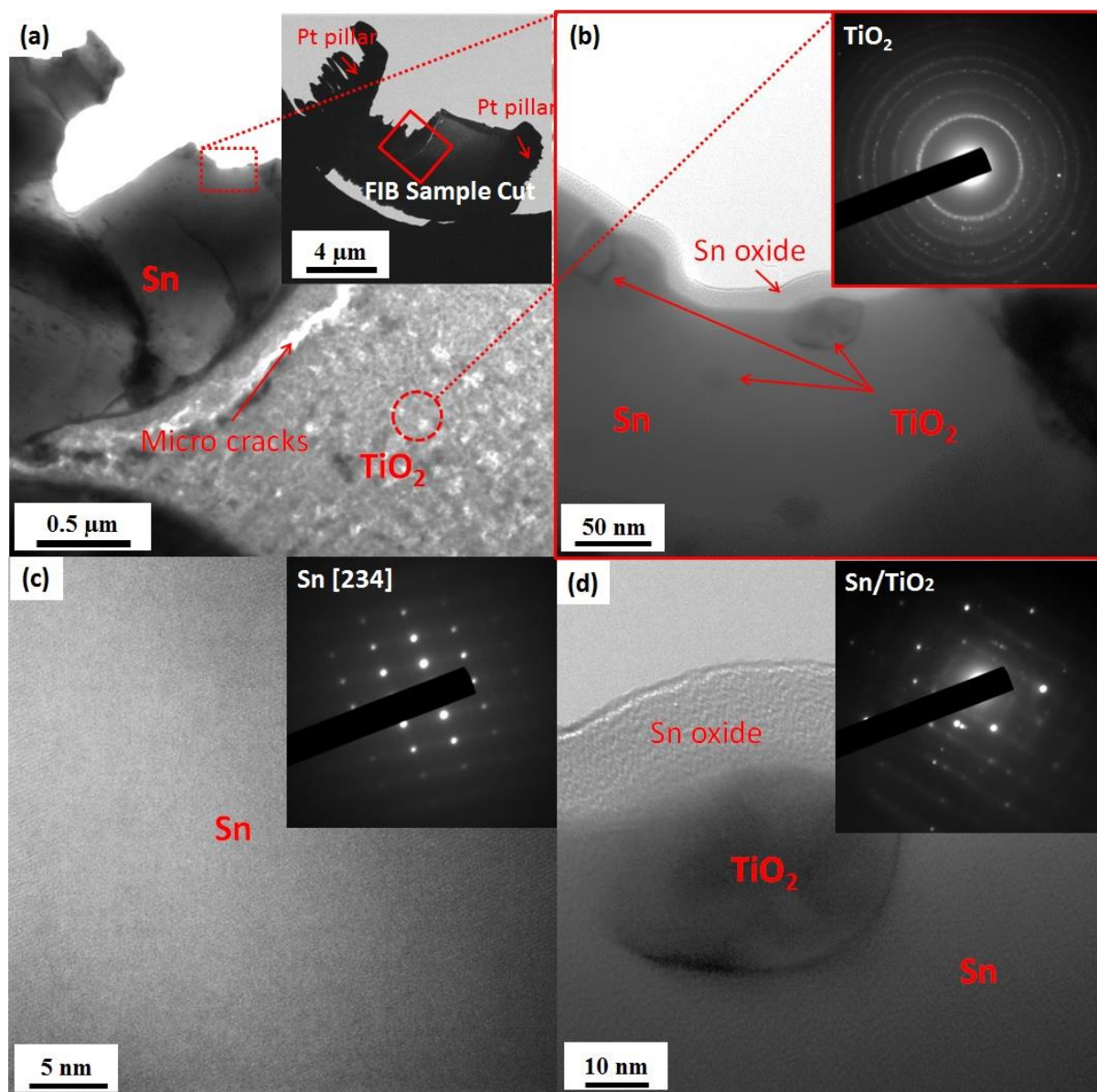


Figure 8: TEM images of conventional sintered Sn-Cu-Ni with  $\text{TiO}_2$  samples: (a) Focus ion beam milled sample; Bright field high resolution TEM image and SADP of (b) Sn region with  $\text{TiO}_2$  particles; (c) Sn area; (d) higher magnification of  $\text{TiO}_2$  particles in the Sn region.

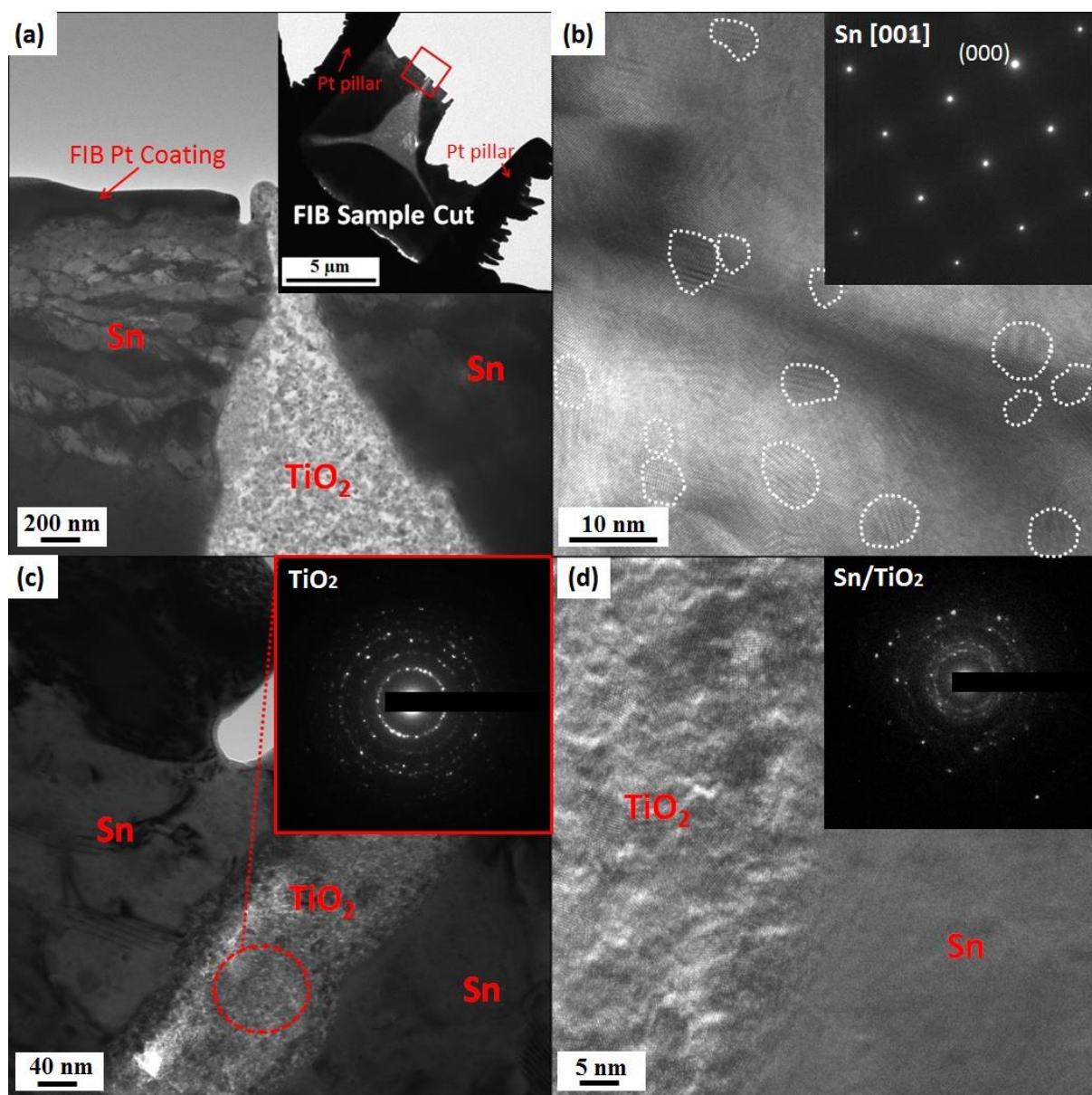


Figure 9: TEM images of microwave sintered Sn-Cu-Ni with TiO<sub>2</sub> samples: (a) Focus ion beam milled sample; Bright field high resolution TEM image and selected area diffraction pattern (SADP) of (b) Sn region; (c) TiO<sub>2</sub> region; (d) Sn/TiO<sub>2</sub> interface area.

Based on XPS result of microwave sintered Sn-Cu-Ni with TiO<sub>2</sub> (Figure 10a, 10b and 10c) and conventionally sintered Sn-Cu-Ni with TiO<sub>2</sub> (Figure 10d, 10e and 10f), the binding energy of species on the surface can be evaluated. Samples were firstly ion milled using a soft X-ray to etch away oxide layers and contamination formed on the sample surface. From Figure 10b and 10e, the energy binding spectrum result of Ti 2p on microwave sintered and conventional sintered samples respectively shows that besides TiO<sub>2</sub> (Ti<sup>4+</sup>) particles, it is likely other forms of Ti compounds exists containing Ti<sup>+</sup>, Ti<sup>2+</sup>, and Ti<sup>3+</sup>. Based on Table 5, a fraction of Ti<sup>4+</sup> of about 48% was obtained on conventional sintering while about 45% was present in microwave sintered samples. Moreover, as shown in Figure 10b on microwave

sintered samples, the fraction of  $\text{Ti}^{2+}$  has significantly increased to about 18% compared to conventionally sintered sample (Figure 10c) with about a 5% fraction whereas  $\text{Ti}^{3+}$  decreases to about 24% on microwave sintered samples compared to conventionally sintered samples with about a 35% fraction.  $\text{Ti}^+$  remains relatively unchanged with no significant fraction difference. Hence, these XPS results coupled with synchrotron micro-XRF mapping (Figure 6) and TEM analysis (Figure 9) suggest the possibility that, during microwave sintering with rapid heating and the presence of a high energy microwave,  $\text{TiO}_2$  particles could dissociate and form other Ti compounds majorly associated with  $\text{Ti}^{2+}$ . On the other hand, with the dissociation of  $\text{TiO}_2$  and the interaction of Sn from the Sn-Cu-Ni solder, the possibility of substitution between Sn and Ti could result in the formation of a new compound [52]. With a very small fraction of migrated Ti and the possibility of a new compound forming, it is impossible to obtaining meaningful analysis using conventional bulk material characterization techniques such as X-ray diffraction (XRD). Thus, to confirm an exact mechanism, investigations using other advanced characterization techniques such as synchrotron X-ray absorption fine structure (XAFS) are required and proposed for future research. The results from XPS analysis as shown in Figure 10, could also be affected by argon-ion etching artifacts during sample preparation. Hence, the relative fractions of  $\text{Ti}^+$ ,  $\text{Ti}^{2+}$ ,  $\text{Ti}^{3+}$  and  $\text{Ti}^{4+}$  are thought to be meaningful but not necessarily absolute.

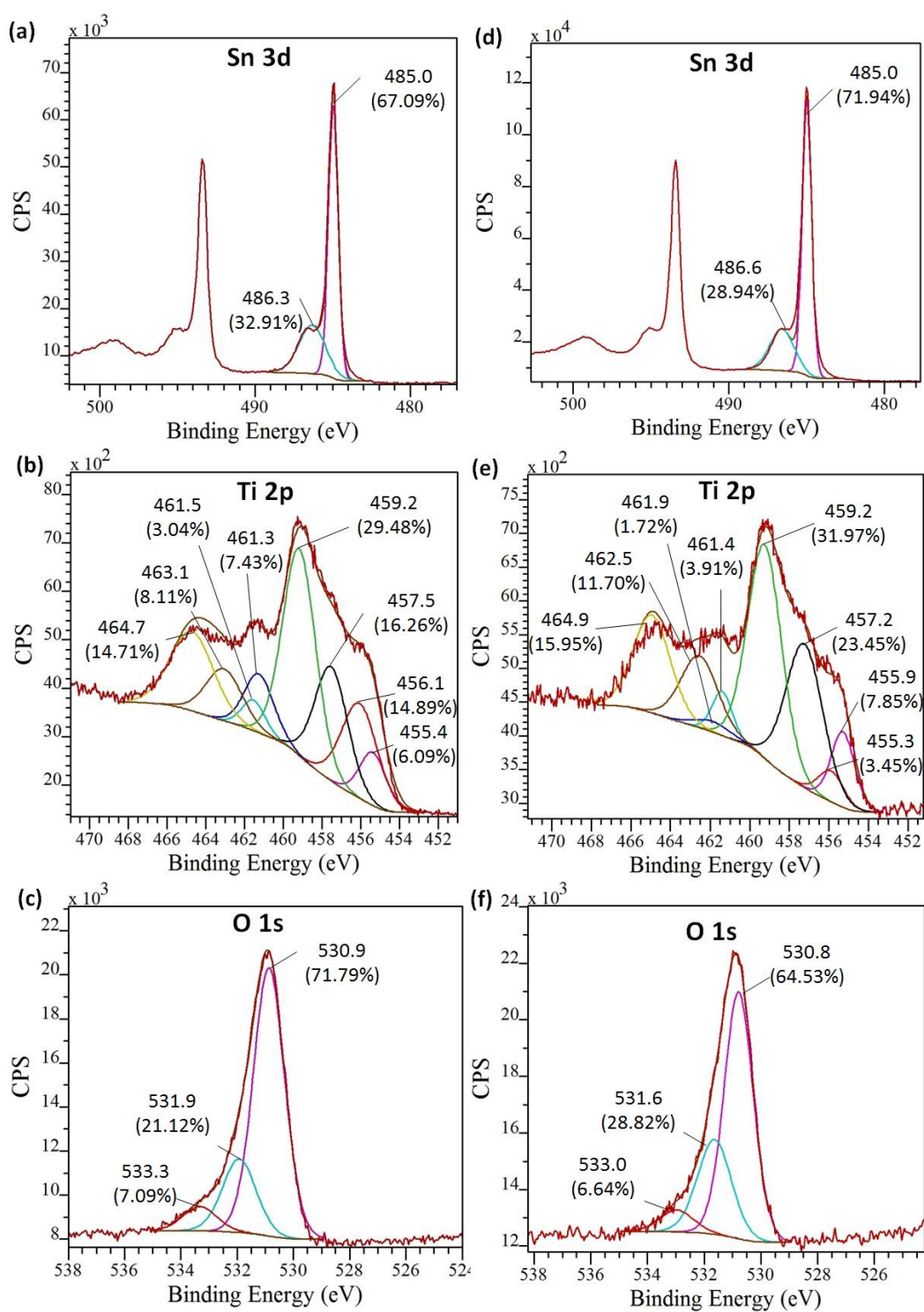


Figure 10: XPS spectra of microwave sintered Sn-Cu-Ni with TiO<sub>2</sub> for (a) Sn 3d, (b) Ti 2p, (c) O 1s and conventionally sintered Sn-Cu-Ni with TiO<sub>2</sub> for (d) Sn 3d, (e) Ti 2p, (f) O 1s.



Table 5: Binding energy of Ti 2p and concentrations of  $Ti^+$ ,  $Ti^{2+}$ ,  $Ti^{3+}$  and  $Ti^{4+}$  on microwave sintered and conventionally sintered Sn-Cu-Ni with  $TiO_2$ .

	Element	Ti 2p 3/2 (eV)	Ti 2p 1/2 (eV)	Concentration (%)
Microwave Sintered Sn- Cu-Ni + $TiO_2$	$Ti^+$	455.4	461.3	13.52
	$Ti^{2+}$	456.1	461.5	17.93
	$Ti^{3+}$	457.5	463.1	24.37
	$Ti^{4+}$	459.2	464.7	44.19
Conventionally Sintered Sn- Cu-Ni + $TiO_2$	$Ti^+$	455.9	461.4	11.76
	$Ti^{2+}$	455.3	461.9	5.17
	$Ti^{3+}$	457.2	462.5	35.15
	$Ti^{4+}$	459.2	464.9	47.92

#### 4. Conclusions

Microwave sintering has a unique heating characteristic that could potentially be a viable fabrication method for composite solder development. By comparing microwave sintered and conventionally sintered samples of Sn-Cu-Ni samples containing  $TiO_2$  additions, the following conclusions can be made:

- Additions of  $TiO_2$  reinforcement to the Sn-Cu-Ni solder matrix have dramatically increased the hardness values in microwave sintered samples where the microstructures indicates fine and homogenously distributed  $(Cu,Ni)_6Sn_5$  intermetallics form within the particle grains.
- Density of microwave sintered  $TiO_2$  containing sample resulted with slightly higher density with  $7.113 \text{ g/cm}^3$  compared to conventional and unsintered sample with  $7.095 \text{ g/cm}^3$  and  $7.081 \text{ g/cm}^3$  respectively.
- The CTE mismatch of microwave sintered,  $TiO_2$  containing samples with Cu at  $150^\circ\text{C}$  was the lowest of all alloys tested and would result in minimization of expansion and contraction during operating temperature.

- d) Microwave sintered  $\text{TiO}_2$  containing samples were characterised by a decreased freezing range of  $5.94^\circ\text{C}$  and a liquidus temperature of  $233.50^\circ\text{C}$ . This is an acceptable freezing range and liquidus temperature for most soldering application and the increased hardness of these samples can contribute to improved reliability.
- e) It is possible microwave sintering with rapid heating may assist  $\text{TiO}_2$  particles to dissociate and form other Ti compounds associated with  $\text{Ti}^{2+}$ .

## **5. Acknowledgements**

The authors would like to gratefully acknowledge financial support from the University of Queensland (UQ)-Nihon Superior (NS) collaborative research program. Synchrotron micro XRF experiments were performed at the SPring-8 BL37XU (Project ID: 2013B1524 and 2014A1360) while SEM, TEM and XPS was performed at the Centre for Microscopy and Microanalysis (CMM) under the Australian Microscopy and Microanalysis Research Facility (AMMRF). Authors would like to acknowledge Dr. Barry J. Wood for his advices on the XPS analysis. DSC analysis was performed using the facility of Australian National Fabrication Facility (ANMF) at the University of Queensland. Mohd Salleh is financially supported for his study by the Malaysian Education Ministry and Universiti Malaysia Perlis.

## Reference

- [1] Abtew M, Selvaduray G. Lead-free Solders in Microelectronics. *Materials Science and Engineering: R: Reports* 2000;27:95-141.
- [2] Zeng K, Tu KN. Six cases of reliability study of Pb-free solder joints in electronic packaging technology. *Materials Science and Engineering: R: Reports* 2002;38:55-105.
- [3] Xin T. Diffusion of Lead-free Soldering in Electronics Industry in China. *China Population, Resources and Environment* 2007;17:66-71.
- [4] Yarime M. Eco-innovation through university-industry collaboration network: co-evolution of technology and institution for the development of lead-free solders. *DRUID Summer Conference 2009*. Denmark: Copenhagen Business School; 2009.
- [5] Bell H. Surface tension and load-carrying capacities of solder. *SMT Magazine*. Seaside, OR: BR Publishing; 2013. p. 18-29.
- [6] Shangguan D. Lead-free solder : interconnect reliability. Materials Park, Ohio: ASM International; 2005.
- [7] Gary Delserro PE. Lead-Free Reliability Issues and Test Methods. *Delserro Engineering Solutions*. Easton, PA EE Evaluation Engineering; 2006.
- [8] Mohd Salleh MAA, Bakri AMMA, Zan@Hazizi MH, Somidin F, Mohd Alui NF, Ahmad ZA. Mechanical properties of Sn–0.7Cu/Si<sub>3</sub>N<sub>4</sub> lead-free composite solder. *Materials Science and Engineering: A* 2012;556:633-7.
- [9] Mohd Salleh MAA, McDonald S, Nogita K. Non-Metal Reinforced Lead-Free Composite Solder Fabrication Methods and its Reinforcing Effects to the Suppression of Intermetallic Formation: Short Review. *Applied Mechanics and Materials* 2013;421:260-6.
- [10] Tsao LC, Wu RW, Cheng T-H, Fan K-H, Chen RS. Effects of nano-Al<sub>2</sub>O<sub>3</sub> particles on microstructure and mechanical properties of Sn<sub>3.5</sub>Ag<sub>0.5</sub>Cu composite solder ball grid array joints on Sn/Cu pads. *Materials & Design* 2013;50:774-81.
- [11] Tsai T-N. Improving the fine-pitch stencil printing capability using the taguchi method and taguchi fuzzy-based model. *Robotics and Computer-Integrated Manufacturing* 2011;27:808-17.
- [12] Yang F, Meguid SA. Efficient multi-level modeling technique for determining effective board drop reliability of PCB assembly. *Microelectronics Reliability* 2013;53:975-84.
- [13] Nai SML, Wei J, Gupta M. Influence of ceramic reinforcements on the wettability and mechanical properties of novel lead-free solder composites. *Thin Solid Films* 2006;504:401-4.

- [14] Guo F. Composite lead-free electronic solders. *Journal of Materials Science: Materials in Electronics* 2007;18:129-45.
- [15] Shen J, Chan YC. Research advances in nano-composite solders. *Microelectronic Reliability* 2009;49:223-34.
- [16] Mohd Salleh MAA, Hazizi M.H Z, A.M MAB, Noriman NZ, Mayapan R, Ahmad ZA. Research advances of composite solder materials fabricated via powder metallurgy route. *Advanced Materials Research* 2013;626:791-6.
- [17] Gupta M, Wong WLE. Enhancing overall mechanical performance of metallic materials using two-directional microwave assisted rapid sintering. *Scripta Materialia* 2005;52:479-83.
- [18] El-Daly AA, Desoky WM, Elmosalami TA, El-Shaarawy MG, Abdraboh AM. Microstructural modifications and properties of SiC nanoparticles-reinforced Sn–3.0Ag–0.5Cu solder alloy. *Materials & Design* 2015;65:1196-204.
- [19] Wang X, Liu YC, Wei C, Gao HX, Jiang P, Yu LM. Strengthening mechanism of SiC-particulate reinforced Sn–3.7Ag–0.9Zn lead-free solder. *Journal of Alloys and Compounds* 2009;480:662-5.
- [20] El-Daly AA, Al-Ganainy GS, Fawzy A, Younis MJ. Structural characterization and creep resistance of nano-silicon carbide reinforced Sn–1.0Ag–0.5Cu lead-free solder alloy. *Materials & Design* 2014;55:837-45.
- [21] Tsao LC, Chang SY, Lee CI, Sun WH, Huang CH. Effects of nano-Al<sub>2</sub>O<sub>3</sub> additions on microstructure development and hardness of Sn<sub>3.5</sub>Ag<sub>0.5</sub>Cu solder. *Materials & Design* 2010;31:4831-5.
- [22] Geranmayeh AR, Mahmudi R, Kangooie M. High-temperature shear strength of lead-free Sn–Sb–Ag/Al<sub>2</sub>O<sub>3</sub> composite solder. *Materials Science and Engineering: A* 2011;528:3967-72.
- [23] Gain AK, Chan YC, Yung WKC. Effect of additions of ZrO<sub>2</sub> nano-particles on the microstructure and shear strength of Sn–Ag–Cu solder on Au/Ni metallized Cu pads. *Microelectronics Reliability* 2011;51:2306-13.
- [24] Shen J, Chan YC. Effects of ZrO<sub>2</sub> nanoparticles on the mechanical properties of Sn–Zn solder joints on Au/Ni/Cu pads. *Journal of Alloys and Compounds* 2009;477:552-9.
- [25] Gain AK, Chan YC. Growth mechanism of intermetallic compounds and damping properties of Sn–Ag–Cu-1wt% nano-ZrO<sub>2</sub> composite solders. *Microelectronics Reliability* 2014;54:945-55.
- [26] Gain AK, Fouzder T, Chan YC, Yung WKC. Microstructure, kinetic analysis and hardness of Sn–Ag–Cu-1wt% nano-ZrO<sub>2</sub> composite solder on OSP-Cu pads. *Journal of Alloys and Compounds* 2011;509:3319-25.

- [27] Hu X, Xu S, Yang Y, Chen Z, Chan YC. Effect of TiO<sub>2</sub> nanoparticle addition on electroless Ni–P under bump metallization for lead-free solder interconnection. *Materials Science and Engineering: A* 2014;600:67-75.
- [28] Tang Y, Li GY, Pan YC. Effects of TiO<sub>2</sub> nanoparticles addition on microstructure, microhardness and tensile properties of Sn–3.0Ag–0.5Cu–xTiO<sub>2</sub> composite solder. *Materials & Design* 2014;55:574-82.
- [29] Tsao LC, Huang CH, Chung CH, Chen RS. Influence of TiO<sub>2</sub> nanoparticles addition on the microstructural and mechanical properties of Sn<sub>0.7</sub>Cu nano-composite solder. *Materials Science and Engineering: A* 2012;545:194-200.
- [30] Tang Y, Li GY, Pan YC. Influence of TiO<sub>2</sub> nanoparticles on IMC growth in Sn–3.0Ag–0.5Cu–xTiO<sub>2</sub> solder joints in reflow process. *Journal of Alloys and Compounds* 2013;554:195-203.
- [31] Tsao LC. An investigation of microstructure and mechanical properties of novel Sn<sub>3.5</sub>Ag<sub>0.5</sub>Cu–XTiO<sub>2</sub> composite solders as functions of alloy composition and cooling rate. *Materials Science and Engineering: A* 2011;529:41-8.
- [32] Tsao LC. Suppressing effect of 0.5wt.% nano-TiO<sub>2</sub> addition into Sn–3.5Ag–0.5Cu solder alloy on the intermetallic growth with Cu substrate during isothermal aging. *Journal of Alloys and Compounds* 2011;509:8441-8.
- [33] M.A.A MS, Bakri AMMA, Kamarudin H, Bnhussain M, M.H ZH, Somidin F. Solderability of Sn-0.7Cu/Si<sub>3</sub>N<sub>4</sub> lead-free composite solder on Cu-substrate. *Physics Procedia* 2011;22:299-304.
- [34] El-Daly AA, Fawzy A, Mansour SF, Younis MJ. Novel SiC nanoparticles-containing Sn–1.0Ag–0.5Cu solder with good drop impact performance. *Materials Science and Engineering: A* 2013;578:62-71.
- [35] Alam ME, Nai SML, Gupta M. Development of high strength Sn–Cu solder using copper particles at nanolength scale. *Journal of Alloys and Compounds* 2009;476:199-206.
- [36] Nai SML, Wei J, Gupta M. Improving the performance of lead-free solder reinforced with multi-walled carbon nanotubes. *Materials Science and Engineering: A* 2006;423:166-9.
- [37] Mohd Salleh MAA, Al Bakri AMM, Somidin F, Hussien K. Recent development of novel lead-free composite solders using microwave-assisted sintering powder metallurgy route. *International Review of Mechanical Engineering IREME* 2013;7:53-9.
- [38] Mohd Salleh MAA, Zan@Hazizi MH, Al Bakri MAM, Noriman NZ, Mayapan R, Ahmad ZA. Research advances of composite solder material fabricated via powder metallurgy route. *Advanced Materials Research* 2013;626:791-6.

- [39] Gupta M, Wai Leong EW. Microwave Heating. *Microwaves and Metals*: John Wiley & Sons (Asia) Pte Ltd; 2007. p. 43-63.
- [40] German RM, Messing GL, Cornwall RG. *Sintering Technology*: Marcel Dekker 1996.
- [41] Babaghorbani P, Nai SML, Gupta M. Reinforcements at nanometer length scale and the electrical resistivity of lead-free solders. *Journal of Alloys and Compounds* 2009;478:458-61.
- [42] Oghbaei M, Mirzaee O. Microwave versus conventional sintering: A review of fundamentals, advantages and applications. *Journal of Alloys and Compounds* 2010;494:175-89.
- [43] Dillon CT. Synchrotron radiation spectroscopic techniques as tools for the medical chemist: microprobe X-Ray fluorescence imaging, X-Ray absorption, and infrared microspectroscopy. *Australian Journal of Chemistry: an international journal for chemical science* 2012;65:204-17.
- [44] Nogita K, Yasuda H, Yoshida K, Uesugi K, Takeuchi A, Suzuki Y, et al. Determination of strontium segregation in modified hypoeutectic Al–Si alloy by micro X-ray fluorescence analysis. *Scripta Materialia* 2006;55:787-90.
- [45] Nogita K, Yasuda H, Yoshiya M, McDonald SD, Uesugi K, Takeuchi A, et al. The role of trace element segregation in the eutectic modification of hypoeutectic Al–Si alloys. *Journal of Alloys and Compounds* 2010;489:415-20.
- [46] Zeng G, McDonald SD, Gu Q, Terada Y, Uesugi K, Yasuda H, et al. The influence of Ni and Zn additions on microstructure and phase transformations in Sn–0.7Cu/Cu solder joints. *Acta Materialia* 2015;83:357-71.
- [47] Shabadi R, Avettand-Fènoël MN, Simar A, Taillard R, Jain PK, Johnson R. Thermal conductivity in yttria dispersed copper. *Materials & Design* 2015;65:869-77.
- [48] El-Daly AA, Hammad AE. Enhancement of creep resistance and thermal behavior of eutectic Sn–Cu lead-free solder alloy by Ag and In-additions. *Materials & Design* 2012;40:292-8.
- [49] Rybakov KI, Oleysky EA, Krikun EV. Microwave sintering: Fundamentals and modeling. *Journal of the American Ceramic Society* 2013;96:1003-20.
- [50] Geiß PL, Klingen J. *Adhesive Bonding: Materials, Applications and Technology*: Wiley-VCH GmbH & Co; 2005.
- [51] Stuerger D. *Microwave-Material Interactions and Dielectric Properties, Key Ingredients for Mastery of Chemical Microwave Processes. Microwaves in Organic Synthesis*: Wiley-VCH Verlag GmbH; 2008. p. 1-61.

[52] Knauth P. Point Defects in 3D and 1D Nanomaterials: The Model Case of Titanium Dioxide. IOP Conference Series: Materials Science and Engineering 2010;15:012004.

## **Paper 2: In-situ soldering process technique by synchrotron X-ray imaging**

Mohd Arif Anuar Mohd Salleh, Stuart D. McDonald, Hideyuki Yasuda, Akira  
Sugiyama, Kazuhiro Nogita

**Applied Mechanics and Materials**, 754-755 (2015) 508-512.



# In-situ Soldering Process Technique by Synchrotron X-ray Imaging

M. A. A. Mohd Salleh<sup>1,2,a</sup>, A. Sugiyama<sup>3,b</sup>, H. Yasuda<sup>4,c</sup>, S. D. McDonald<sup>1,d</sup> and K. Nogita<sup>1,e</sup>

<sup>1</sup>Nihon Superior Centre for the Manufacture of Electronic Materials (NS CMEM), School of Mechanical and Mining Engineering, University of Queensland, 4072 St Lucia, Queensland, Australia.

<sup>2</sup>Centre of Excellence Geopolymer and Green Technology, School of Materials Engineering, Universiti Malaysia Perlis (UniMAP), Taman Muhibbah 02600, Jejawi, Arau, Perlis, Malaysia

<sup>3</sup>Department of Mechanical Engineering for Transportation, Osaka Sangyo University, Daito, Osaka 574-8530, Japan.

<sup>4</sup>Department of Materials Science and Engineering, Kyoto University, Sakyo-ku, Kyoto 606-8501, Japan.

E-mail: [aarifanuar@unimap.edu.my](mailto:aarifanuar@unimap.edu.my), [sugiyama@tm.osaka-sandai.ac.jp](mailto:sugiyama@tm.osaka-sandai.ac.jp),  
[yasuda.hideyuki.6s@kyoto-u.ac.jp](mailto:yasuda.hideyuki.6s@kyoto-u.ac.jp), [s.mcdonald1@uq.edu.au](mailto:s.mcdonald1@uq.edu.au) and [k.nogita@uq.edu.au](mailto:k.nogita@uq.edu.au)

**Keywords:** Lead-free Solder, Synchrotron, Imaging, Intermetallic

**Abstract.** This paper demonstrates the development of an experimental technique of in-situ observation for soldering of Sn-0.7wt%Cu lead-free solder on a Cu substrate which was achieved for the first time by synchrotron X-ray imaging. Reactions between liquid solder and Cu substrate during a soldering process were able to be recorded in real-time. Individual stages of the soldering process consisted of flux activation in removal of Cu oxide, solder melting and contact with the Cu substrate (wetting) and intermetallic compound (IMC) and void formation between the solder and Cu substrate. The technique development which includes experimental setup with calculated optimum beam energy in the range of 20 – 30 keV appears to result in a clear observation of real-time X-ray imaging of the soldering process. This technique provides a key method to understand the mechanism of formation of micro-electronic inter-connects for future electronic packaging applications.

## Introduction

A synchrotron is a particle accelerator that produces very bright light of electromagnetic waves where these X-rays produced by synchrotron are  $10^8$  higher than conventional lab X-ray tubes [1]. This result in better and higher resolution for imaging techniques compared to conventional lab X-ray machines. At a synchrotron, to produce the electromagnetic waves, electrons are firstly fired by an electron gun into a linear accelerator, which then rapidly increases the speed of the electrons. A booster ring then helps to accelerate the electrons further (up to 8GeV for the SPring-8 Japan Synchrotron). This booster ring then transfers the accelerated electrons to storage rings which contain bending magnets, wigglers and undulators that cause the electrons to accelerate and to release very intense electromagnetic waves [1]. From the storage rings, the high intense electromagnetic waves are then emitted through beamlines and used on each experimental hutch for experiments, for example for imaging [1]. With high brilliance and high coherency monochromatized X-ray, synchrotron X-ray imaging is capable in obtaining high time resolution, high spatial resolution and good contrast in its transmission images results.

Advances in synchrotron analysis have provided the opportunity for using synchrotron X-rays in observing the solidification process including microstructure formation and defect formation in metals [2-12]. By using hard X-rays in the synchrotron facility, the microstructure of metallic alloys can be observed in transmission images using monochromatic light. Limited studies have been conducted in real-time to observe solder joint behaviour, particularly the growth of intermetallics at later stage however at early stage during initial formation of the intermetallics at the moment of liquid solder wetting on a particular substrate have not been studied [13-15]. In attempts to understand solder joint reliability, most researchers in the field of solder materials have concentrated their researches on the growth of the intermetallic compounds (IMCs) and several models of IMC formation have been developed [16-22]. However, the formation of IMCs at the early stage during solder wetting is rather a rapid process which is difficult to observe using conventional microstructure observation techniques. The technique of real time in-situ imaging of the full soldering process which consists of a full observation of soldering stage at solid-liquid-solid transition would give further understanding on the early stages of IMC formation during solder wetting and its actual evolution during soldering. This process observation has not been conducted in previous studies. In this study, for the first time, synchrotron X-ray real time in-situ imaging of a full soldering process of a Sn-0.7wt%Cu alloy on a copper substrate was performed. The experiment setup used is as in Figure 1 (a). To mimic a real solder joint condition, rosin based flux and similar real reflow soldering process temperature profiles

were used. This paper focuses on the development of the experimental procedure that enabled the in-situ soldering process of Sn-0.7wt%Cu solder on a Cu substrate to be observed by synchrotron X-ray imaging.

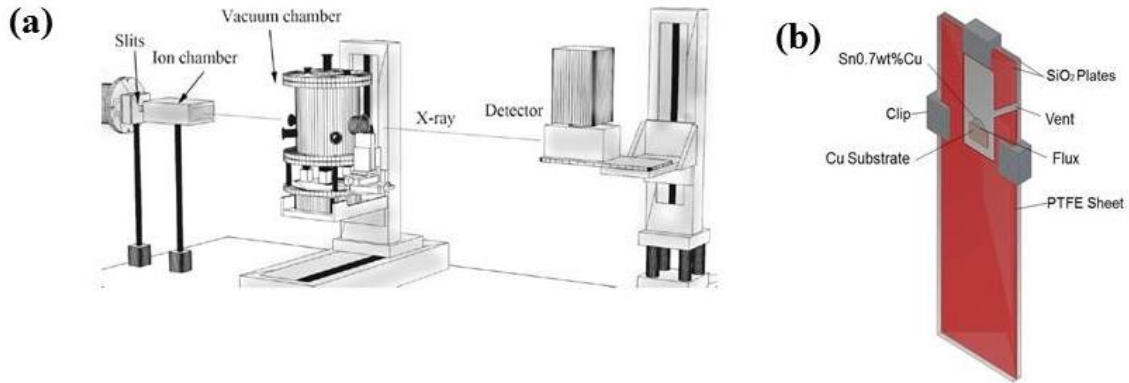


Figure 1: (a) Synchrotron beamline for X-ray imaging at SPring-8, Osaka, Japan [2] and (b) sample cell setup for in-situ soldering process.

## Experimental Procedure

**Materials.** Sn-0.7wt%Cu solder alloy and oxygen-free high thermal conductivity Cu substrate (100  $\mu\text{m}$  thick) were used for the in-situ soldering experiment. To mimic the real reflow soldering process, rosin-based flux JO-1301007 supplied by Nihon Superior Co., Ltd. was used.

**Sample Preparation.** A bulk Sn-0.7wt%Cu solder alloy ingot was sliced using Struers Accutum-50 precision cutter to about 2 mm thick. Samples were then placed on a jig for further fine grinding until reaches a thickness of around 100  $\mu\text{m}$ .

**Sample Cell Setup.** Thin Sn-0.7wt%Cu solder alloy, Cu substrate and rosin-based flux were placed vertically and sandwiched between two SiO<sub>2</sub> plates as shown in Figure 1 (b). A 100  $\mu\text{m}$  thick polytetrafluoroethylene (PTFE) sheet was placed in between the SiO<sub>2</sub> plates (as indicated in the red colour in Figure 2) with a vent provided for flux outgassing purposes.

**Experiment Process.** The real time observation experiment was performed at BL20B2 and BL20XU beamlines at the SPring-8 synchrotron, with an energy of 23 keV using an in-situ synchrotron X-ray real time solidification observation setup (Figure 1a) developed from previous research [3, 4]. A planar undulator was used as a light source and the radiation was monochromatized with Si double crystal monochromators. An experimental hutch was located at 206m from the X-ray source point. With a high degree of coherence, absorption contrast and phase contrast which enhances boundaries in the sample are observed on

transmitted images. An image detector which collects image signals is located 2.5 - 3.0 m from the sample. These image signals are then converted into a digital format of 2000 X 2000 pixels and 16-bit resolution. A charged couple device (CCD) camera with exposure time of 1 s per frame was used to capture the images. To mimic the process of reflow soldering, a furnace with graphite heating elements where heat is transferred through radiation in an enclosed sample chamber was used. The samples were set to be heated from room temperature to approximately 250°C at 10°C/min and cooled down at 20°C/min.

### Beam Energy Selection

Suitable photon energy which is normally referred to as X-ray energy is essential for obtaining a good contrast image. In determining the acceptable energy range, the Beer-Lambert equation as in equation (1) can be applied [23]. From the Beer-Lambert equation, the intensity transmission of the X-ray could be determined.

$$I = I_0 \exp^{-\left(\frac{\mu}{\rho}\right)\rho t} \quad (1)$$

Where  $I_0$  and  $I$  are the X-ray beam intensities at incident and transmission through a material,  $\left[\frac{\mu}{\rho}\right]$  is the mas-attenuation coefficient,  $\rho$  is the density of material and  $t$  is the thickness of material.

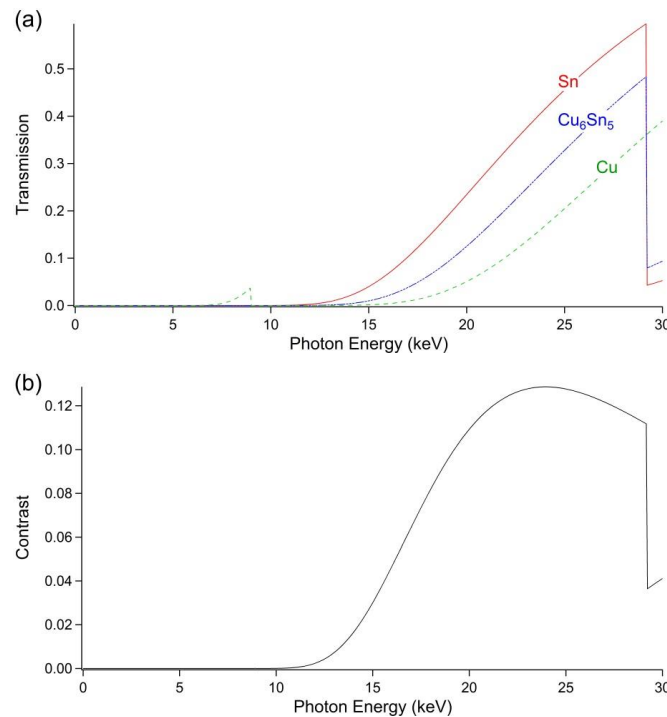


Figure 3: Influence of photon energy on (a) intensity transmission of the X-ray on Sn, Cu<sub>6</sub>Sn<sub>5</sub> and Cu and (b) contrast values between Sn and Cu<sub>6</sub>Sn<sub>5</sub> phases.

Since Sn, Cu and  $\text{Cu}_6\text{Sn}_5$  phases are the main phases for this in-situ observation, the values of intensity transmission of Sn, Cu and  $\text{Cu}_6\text{Sn}_5$  were obtained [24] based on density values of the phases [25] and were plotted as a function of photon energy (Figure 3a) to determine the beam energy range for obtaining a sufficient contrast between different phases for the in-situ imaging results. Since  $\text{Cu}_6\text{Sn}_5$  interfacial IMCs are located on the solder side between the solder and Cu, on the difference of intensity transmission values of Sn and  $\text{Cu}_6\text{Sn}_5$ . Based on Figure 3b, it is suggested that the optimum beam energy for  $\text{Cu}_6\text{Sn}_5$  observation is in the range of 20 – 30 keV.

### **In-situ Soldering Observation**

At BL20B2 beamline, the image signals are converted into a digital format of 2000 X 2000 pixels representing a 5 mm X 5 mm area obtaining a 2.5  $\mu\text{m}$  per pixel resolution ratio. This lower resolution in-situ imaging technique was used to observe the full soldering process formation at a larger image scale. This allowed observation of more on the material interactions in a full reflow soldering process. Using this technique, the flux activation process, solder void formation and solder wetting reaction were able to be observed. As in Figure 4a, at a full soldering process at 911 s, bulk and interfacial solder void formation were able to be observed clearly. At a low magnification image, using the BL20B2 beamline the IMC formation was able to be observed in-situ at the moment the liquid solder flows on the Cu substrate during solder wetting and subsequent IMC growth. In order to observe the IMC formation in detail, the BL20XU beamline was used for the in-situ soldering process where the higher magnification of images can be obtained. In the BL20XU beamline experiment which has a higher strength beam, image signals are converted into a digital format of 2000 X 2000 pixels at 1 mm X 1 mm giving a higher resolution of 0.5  $\mu\text{m}$  per pixel. Clear observations of IMC formation were obtained (Figure 4b) where further detail analyses of IMC formation and growth mechanism were possible.

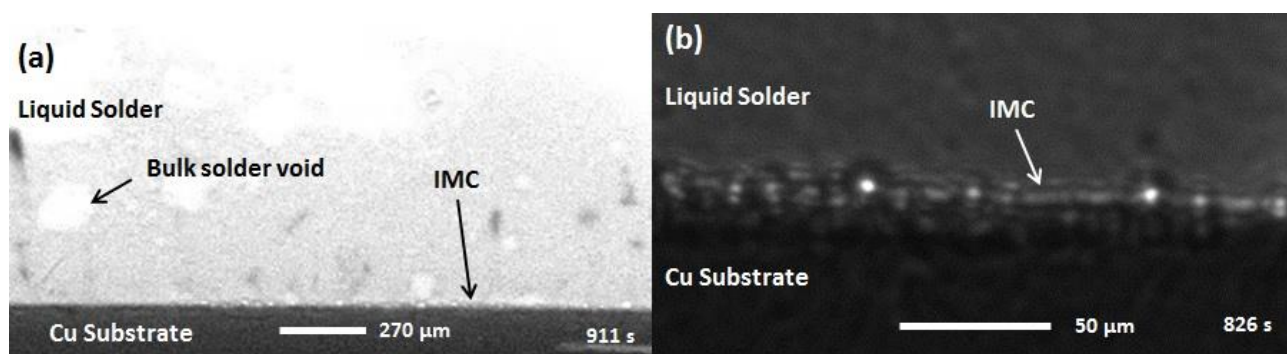


Figure 4: Image of the in-situ soldering process of Sn0.7wt%Cu on a Cu Substrate at (a) low magnification observation experiment at 911 s performed at beamline BL20B2 and (b) high magnification observation experiment at 826 s performed at beamline BL20XU.

## Conclusion

A full soldering process was successfully observed by synchrotron X-ray real-time in-situ imaging for the first time. Using this experiment technique, material interactions in a real soldering process was able to be observed in-situ. This allowed capture of events which have been difficult to observe such as the initial IMC formation at the early stages of soldering during solder wetting. This technique development provides a key method to understanding the initial growth mechanisms of the IMC. This technique will be used as the basis for future research on understanding the growth mechanism and controlling the formation and growth of IMCs of various solder materials during soldering.

## Acknowledgment

The authors would like to gratefully acknowledge financial support from the University of Queensland (UQ)-Nihon Superior (NS) collaborative research program. The authors thank Dr. K. Uesugi of SPring-8 beamline scientist and support staff and students from the Department of Materials Science and Engineering, Kyoto University, the Department of Adaptive Machine Systems, Osaka University for experimental assistance. In-situ observation experiments were performed at the SPring-8 BL20B2 and BL20XU (Project ID: 2014A1540, 2014A1541 and 2014A1114). This work is also supported in part by a Grant-in-Aid for Scientific Research (S) (Project ID: 24226018) from JSPS, Japan and with the International Synchrotron Access Program Fund (AS/IA142/8198). M. A. A. Mohd Salleh is financially supported for his study by the Malaysian Education Ministry and Universiti Malaysia Perlis (UniMAP).

## References

- [1] E. Donnelly, in: Synchrotron Investigation, Australian School Innovation in Science, Technology and Mathematics, The University of Western Australia.
- [2] H. Yasuda, T. Nagira, M. Yoshiya, M. Uesugi, N. Nakatsuka, M. Kiire, A. Sugiyama, K. Uesugi, K. Umetani, IOP Conference Series: Materials Science and Engineering, 27 (2012).
- [3] K. Nogita, H. Yasuda, A. Prasad, S.D. McDonald, T. Nagira, N. Nakatsuka, K. Uesugi, D.H. StJohn, Materials Characterization, 85 (2013) 134-140.
- [4] H. Yasuda, I. Ohnaka, K. Kawasaki, A. Sugiyama, T. Ohmichi, J. Iwane, K. Umetani, Journal of Crystal Growth, 262 (2004) 645-652.
- [5] A. Bogno, H. Nguyen-Thi, N. Bergeon, N. Mangelinck-Noël, T. Schenk, B. Billia, E. Boller, J. Baruchel, Nuclear Instruments and Methods in Physics Research Section B: Beam Interactions with Materials and Atoms, 268 (2010) 394-398.
- [6] Y. Chen, A.-A. Bogno, N.M. Xiao, B. Billia, X.H. Kang, H. Nguyen-Thi, X.H. Luo, D.Z. Li, Acta Materialia, 60 (2012) 199-207.
- [7] F.-g. Li, Q. Dong, J. Zhang, Y.-b. Dai, Y.-n. Fu, H.-l. Xie, F.-c. Yin, B.-d. Sun, Transactions of Nonferrous Metals Society of China, 24 (2014) 2112-2116.
- [8] F. Mao, F. Chen, Q. Han, J. Han, Z. Cao, T. Wang, T. Li, Journal of Alloys and Compounds, 608 (2014) 343-351.
- [9] H. Nguyen-Thi, L. Salvo, R.H. Mathiesen, L. Arnberg, B. Billia, M. Suery, G. Reinhart, Comptes Rendus Physique, 13 (2012) 237-245.
- [10] C.M. Gourlay, K. Nogita, A.K. Dahle, Y. Yamamoto, K. Uesugi, T. Nagira, M. Yoshiya, H. Yasuda, Acta Materialia, 59 (2011) 4043-4054.
- [11] T. Nagira, C.M. Gourlay, A. Sugiyama, M. Uesugi, Y. Kanzawa, M. Yoshiya, K. Uesugi, K. Umetani, H. Yasuda, Scripta Materialia, 64 (2011) 1129-1132.
- [12] H. Yasuda, I. Ohnaka, S. Fujimoto, N. Takezawa, A. Tsuchiyama, T. Nakano, K. Uesugi, Scripta Materialia, 54 (2006) 527-532.
- [13] L. Qu, N. Zhao, H.J. Zhao, M.L. Huang, H.T. Ma, Scripta Materialia, 72–73 (2014) 43-46.
- [14] H.T. Ma, L. Qu, M.L. Huang, L.Y. Gu, N. Zhao, L. Wang, Journal of Alloys and Compounds, 537 (2012) 286-290.
- [15] J. Bertheau, P. Bleuët, F. Hodaj, P. Cloetens, N. Martin, J. Charbonnier, N. Hotellier, Microelectronic Engineering, 113 (2014) 123-129.
- [16] K.N. Tu, Solder Joint Technology: Materials, Properties, and Reliability, Springer, 2007.
- [17] B. Chao, S.-H. Chae, X. Zhang, K.-H. Lu, J. Im, P.S. Ho, Acta Materialia, 55 (2007) 2805-2814.

- [18] M. He, Z. Chen, G. Qi, *Acta Materialia*, 52 (2004) 2047-2056.
- [19] J.F. Li, S.H. Mannan, M.P. Clode, D.C. Whalley, D.A. Hutt, *Acta Materialia*, 54 (2006) 2907-2922.
- [20] M.S. Park, R. Arróyave, *Acta Materialia*, 58 (2010) 4900-4910.
- [21] B.-J. Lee, N.M. Hwang, H.M. Lee, *Acta Materialia*, 45 (1997) 1867-1874.
- [22] M. Schaefer, R. Fournelle, J. Liang, *Journal of Electronic Materials*, 27 (1998) 1167-1176.
- [23] J.L. Glover, C.T. Chantler, Z. Barnea, N.A. Rae, C.Q. Tran, *Journal of Physics B: Atomic, Molecular and Optical Physics*, 43 (2010) 085001.
- [24] B.L. Henke, E.M. Gullikson, J.C. Davis, in: *Atomic Data and Nuclear Data Tables*, 1993, pp. 181-342.
- [25] M.-H. Lu, K.-C. Hsieh, *Journal of Electronic Materials*, 36 (2007) 1448-1454.



## **Chapter 4 Interfacial intermetallic compound (IMC) layer formation in Sn-Cu solders in early stages of soldering and phase transformation.**

This chapter focuses on the interfacial IMC layer formation in Sn-Cu solders on a copper substrate in early stage of soldering and the phase transformation mechanisms during heating. Paper 3 of this thesis, titled “Rapid  $\text{Cu}_6\text{Sn}_5$  growth at liquid Sn/solid Cu interfaces” reveals the initial formation of interfacial IMCs during early stages of reactive wetting. In situ soldering experiments were conducted on Sn-0.7Cu and Cu substrates using the SXRI technique. The initial formation of interfacial  $\text{Cu}_6\text{Sn}_5$  intermetallic layer of Sn-0.7Cu during soldering on Cu and its structure transformation during soldering were revealed. This included characterising the kinetics of growth of the interfacial IMC during soldering. Sn-0.7Cu solders can be considered amongst the class of ‘intrinsically’ reinforced solders with  $\text{Cu}_6\text{Sn}_5$  the reinforcement material. This alloy was used as nominal base materials to be compared to other extrinsically reinforced solders.

Paper 4 of the thesis titled “In-situ TEM observations of  $\text{Cu}_6\text{Sn}_5$  polymorphic transformations in reaction layers between Sn-0.7Cu solders and Cu substrates” reveals the transformation mechanism of the  $\text{Cu}_6\text{Sn}_5$  interfacial layer. Direct evidence of the relationship between the polymorphic phase transformation from monoclinic  $\text{Cu}_6\text{Sn}_5$  to hexagonal  $\text{Cu}_6\text{Sn}_5$  and stress accumulation/release in  $\text{Cu}_6\text{Sn}_5$  formed at the interfacial layer has been obtained. The challenging phenomena was observed by UHV-TEM of thick Cu/ $\text{Cu}_3\text{Sn}$ / $\text{Cu}_6\text{Sn}_5$ /Sn-0.7Cu samples during heating and isothermal holding. Stress creation and release events associated with the polymorphic transformation of the  $\text{Cu}_6\text{Sn}_5$  phase were accompanied by bend contours as discussed in the paper.

The results of both of these papers (Paper 3 and Paper 4) provide a deep understanding of interfacial  $\text{Cu}_6\text{Sn}_5$  in Sn-0.7Cu/Cu solder joints during soldering and subsequent heating.

## **Paper 3: Rapid $\text{Cu}_6\text{Sn}_5$ growth at liquid Sn/solid Cu interfaces**

Mohd Arif Anuar Mohd Salleh, Stuart D. McDonald, Hideyuki Yasuda, Akira Sugiyama, Kazuhiro Nogita

**Scripta Materialia**, 100 (2015), 17-20.

## Rapid Cu<sub>6</sub>Sn<sub>5</sub> growth at liquid Sn/solid Cu interfaces

M. A. A. Mohd Salleh<sup>1,2\*</sup>, S. D. McDonald<sup>1</sup>, H. Yasuda<sup>3</sup>, A. Sugiyama<sup>4</sup>, K. Nogita<sup>1</sup>

<sup>1</sup>Nihon Superior Centre for the Manufacture of Electronic Materials (NS CMEM), School of Mechanical and Mining Engineering, University of Queensland, 4072 St Lucia, Queensland, Australia.

<sup>2</sup>Centre of Excellence Geopolymer and Green Technology, School of Materials Engineering, Universiti Malaysia Perlis (UniMAP), Taman Muhibbah 02600, Jejawi, Arau, Perlis, Malaysia.

<sup>3</sup>Department of Materials Science and Engineering, Kyoto University, Sakyo-ku, Kyoto 606-8501, Japan.

<sup>4</sup>Department of Mechanical Engineering for Transportation, Osaka Sangyo University, Daito, Osaka 574-8530, Japan.

\*Corresponding author: Room 634, 49 Jocks Rd., St Lucia, Brisbane, QLD 4072, Australia

Email: m.mohdsalleh@uq.edu.au / arifanuar@unimap.edu.my

Tel: +61 435 946 670

### Abstract

In-situ observations of the reaction between solid Cu in contact with molten Sn-0.7wt%Cu were achieved using a synchrotron X-ray imaging technique. It is found that upon wetting, the rapid dissolution of Cu adjacent the solid-liquid interface was followed by near-instantaneous interfacial intermetallic compounds (IMCs) formation. The kinetics of IMC formation were also elucidated. Results provide direct experimental evidence on the sequence of events in the dissolution reaction and subsequent diffusion, in particular on the growth mechanisms of the IMC layer.

**Keywords:** Soldering, synchrotron radiation, intermetallic compounds, phase transformations, kinetics.

During the liquid-solid interaction of molten solder and Cu substrates, it had been believed a rapid dissolution of Cu into molten solder with a lower Cu concentration occurs immediately after the Cu oxide film has been removed by the actions of the flux. This rapid direct dissolution of Cu occurs until the conditions become favourable for the nucleation and growth of intermetallic compounds (IMCs) such as  $\eta$ -Cu<sub>6</sub>Sn<sub>5</sub> and  $\epsilon$ -Cu<sub>3</sub>Sn [1-3]. The rapid dissolution of Cu into the molten solder is important in understanding the evolution of IMC formation particularly during the soldering process as the size and morphology of the IMC has been associated with joint reliability. Among commercially available lead-free solders, those based on the near eutectic composition of Sn-0.7wt%Cu with trace level elemental additions such as Ni find applications in soldering due to their availability and low-cost as well as their association with minimal dissolution of Cu substrates [4, 5]. On the other hand, without trace element additions, Sn-0.7wt%Cu has poor mechanical properties and is prone to brittle intermetallic compound (IMC) growth and the formation of a thick interfacial IMC layer consisting of  $\eta$ -Cu<sub>6</sub>Sn<sub>5</sub> and  $\epsilon$ -Cu<sub>3</sub>Sn, that can lead to serious reliability concerns[6]. In an attempt to improve solder joint reliability, many researchers have investigated the growth behaviour of interfacial IMCs and several models have been developed to describe IMC growth during solder wetting reactions and solid-state ageing [1, 2, 7-13]. In understanding the IMC growth mechanisms, recent kinetic studies of IMC growth have focussed on solid state ageing effects rather than the wetting reaction during the liquid-solid interaction. This solid state ageing is more favourable for laboratory examinations as the kinetic processes are much slower compared to the wetting reaction [14]. Existing IMC growth models are largely based on predictions of a sequence of reactions and to-date, lack validation, especially at the early stages of IMC formation during wetting.

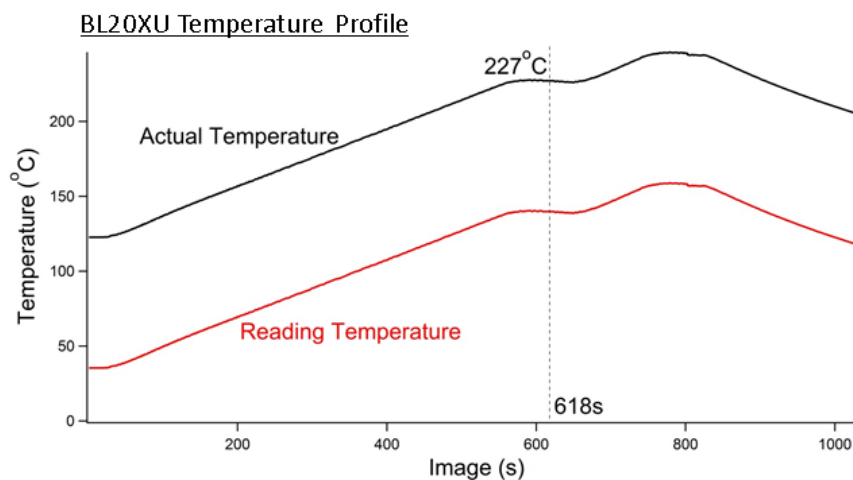


Figure 1: BL20XU beamline soldering temperature profile.

Recent in-situ real time imaging of IMC and solder void growth by Qu et al.[15-17] and Huang et al.[18] was conducted to understand the growth of interfacial IMCs. However, due to the experimental difficulty, real time in-situ imaging observations of molten solder alloy in contact with a solid substrate and studies of the kinetics of IMC formation at the early stages of soldering have not been achieved. In this study, X-ray real time in-situ imaging of the soldering process of a Sn-0.7wt%Cu solder alloy on a Cu substrate was performed focusing on the IMC growth mechanism during the initial liquid-solid interaction.

The experiments were performed at BL20XU beamline in the SPring-8 synchrotron using an in-situ X-ray real time solidification observation setup developed from previous research [4, 19-22]. With a high degree of coherence, absorption contrast and phase contrast are observed on transmitted images with enhanced boundaries. The collected signals are then converted into a digital format of 2000 x 2000 pixels. This area represents a 1 mm x 1 mm area on the BL20XU experiments (giving a resolution of 0.5  $\mu\text{m}$  per pixel). A planar undulator was used as a light source and the radiation was monochromatized with Si double crystal monochromators. An exposure time of 1s per frame to capture the images was used. To mimic the process of reflow soldering, a furnace with graphite heating elements where heat is transferred through radiation in an enclosed sample chamber was used. A 100  $\mu\text{m}$  thickness of both Sn-0.7wt%Cu and the Cu sheet were used and a small amount of rosin-based flux was used in between the solder and Cu substrate. The sample was then placed in a sample cell where an observation window area of 10 x 10 mm<sup>2</sup> with a vent for flux outgassing was made by using a 100  $\mu\text{m}$  thickness poly-tetrafluoroethylene (PTFE) sheet placed between two SiO<sub>2</sub> plates. Samples were set to be heated from room temperature to approximately 250 °C at 0.17 °C/s and cooled down at 0.33 °C/s. There is a temperature difference between the actual temperature of the sample and the thermocouple reading due to the positioning of the thermocouple. The sample temperature was calculated by calibrating with the relative difference between the furnace temperature at the observation of melting to the melting point of Sn-0.7wt%Cu determined by differential scanning calorimetry result. The temperature profile for the BL20XU beamline experiment shows the difference between the thermocouple reading and actual temperatures (Figure 1). The average thickness of the IMC layer at a specific reaction time was determined by dividing the total IMC layer area with the total IMC layer length, both of which were measured using ImageJ software. After real-time observation experiments were completed, the samples were observed using a JEOL 6610 scanning electron microscope (SEM) in backscattered electron imaging mode at an accelerating voltage of 25 kV.

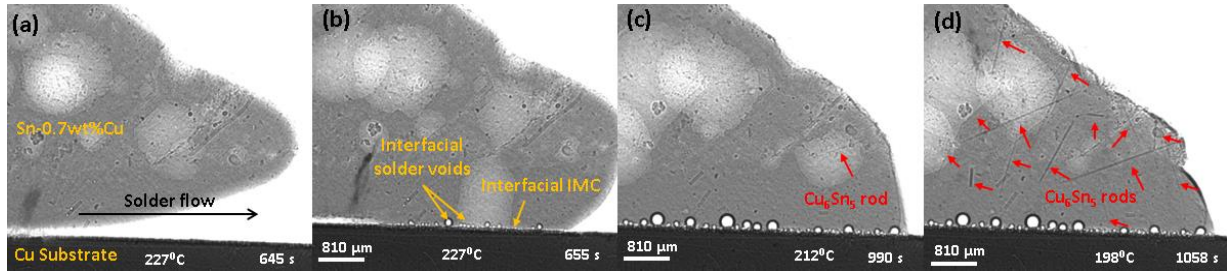


Figure 2: In-situ real time imaging observations of reactions between Sn-0.7wt%Cu and the Cu substrate interface at experimental times of (a) 645 s, (b) 655 s, (c) 990 s, and (d) 1058 s.

The moment of interfacial IMC formation during solder wetting and subsequent IMC growth was observed by the in-situ real time imaging technique. Figure 2 (a-d) shows snapshots of the soldering process. In addition, the soldering process has been recorded as a video and can be found in the supplemental material (Video S1). From Figure 2b, it can be observed that at the moment of molten solder contacting the solid Cu an instant planar (within the resolution of the imaging) IMC layer of significant thickness forms while molten solder flows on the Cu substrate. Subsequently, the IMC layer develops a scalloped interface and the rapid formation of interfacial solder voids is observed. The intermetallic  $\eta$ - $\text{Cu}_6\text{Sn}_5$  is known to dominate the interfacial structure during these initial stages of intermetallic growth. The formation of the initial IMC plays an important role in the kinetics of the diffusion process as the layer of  $\eta$ - $\text{Cu}_6\text{Sn}_5$  formed at the interface reduces the Cu dissolution rate by altering the paths for Cu atoms to diffuse [1, 23]. Based on Figure 2c at 212°C (990s of soldering time), it is observed that large rod-shaped  $\text{Cu}_6\text{Sn}_5$  intermetallics tend to nucleate and subsequently rapidly grow (Figure 2d) during cooling. These large intermetallics tend to form in the solder matrix far from the solder/substrate interface since Sn and Cu are consumed at the interface to form the interfacial IMC in the early stages of soldering [24].

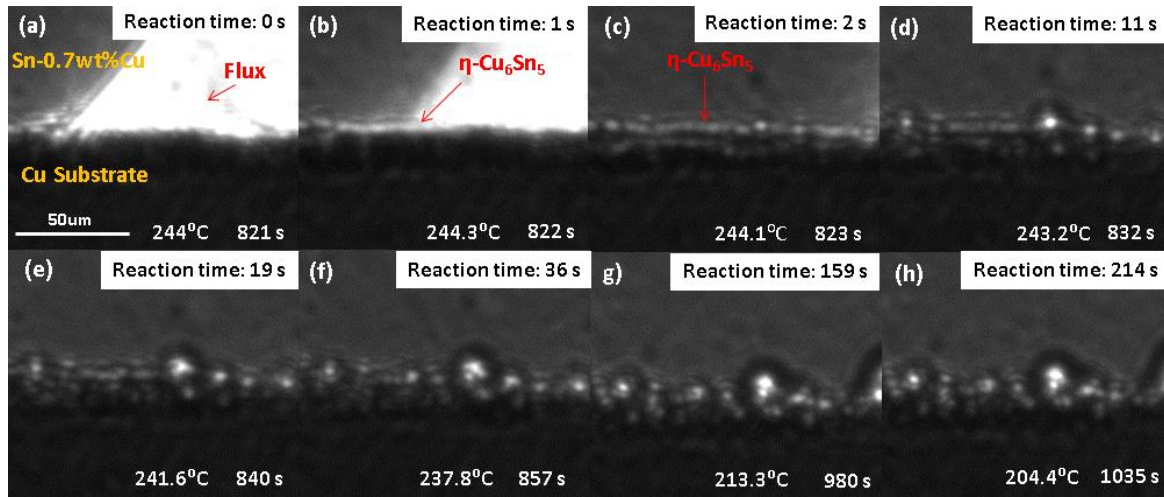


Figure 3: Zoom in of in-situ real time imaging observations of solder voids and intermetallic compound (IMC) formation between Sn-0.7wt%Cu and Cu substrate interface at (a) 821 s, (b) 822 s, (c) 823 s, (d) 832 s, (e) 840 s, (f) 857 s, (g) 980 s, and (h) 1035 s of experiment time. The reaction time shown as an inset in the figures is relative to the initial observation of wetting.

To further study IMC formation mechanisms a zoom-in of the in-situ real time imaging was conducted with the results shown in Figure 3a-3h. It can be observed that within one second of the Sn-0.7wt%Cu wetting the substrate, a planar IMC ( $\eta$ -phase  $\text{Cu}_6\text{Sn}_5$ ) phase forms. The wetting reaction commenced when the liquid solder reached a temperature of 244 °C. At the moment of solder wetting, the dissolution of Cu into the molten solder encourages the rapid precipitation of a significant  $\eta$ - $\text{Cu}_6\text{Sn}_5$  layer as in Figure 3b. This rapid formation of  $\eta$ - $\text{Cu}_6\text{Sn}_5$  is in agreement with a simulation model by Huh et al.[25], which predicts formation of  $\eta$ - $\text{Cu}_6\text{Sn}_5$  in a few milliseconds followed by further IMC growth after several seconds. Due to a higher driving force for precipitation at the metastable solder/substrate interface, this planar  $\eta$ - $\text{Cu}_6\text{Sn}_5$  layer tends to form during the early stages of soldering compared to  $\epsilon$ - $\text{Cu}_3\text{Sn}$  formation which forms at a later stage in a subsequent reaction[26].

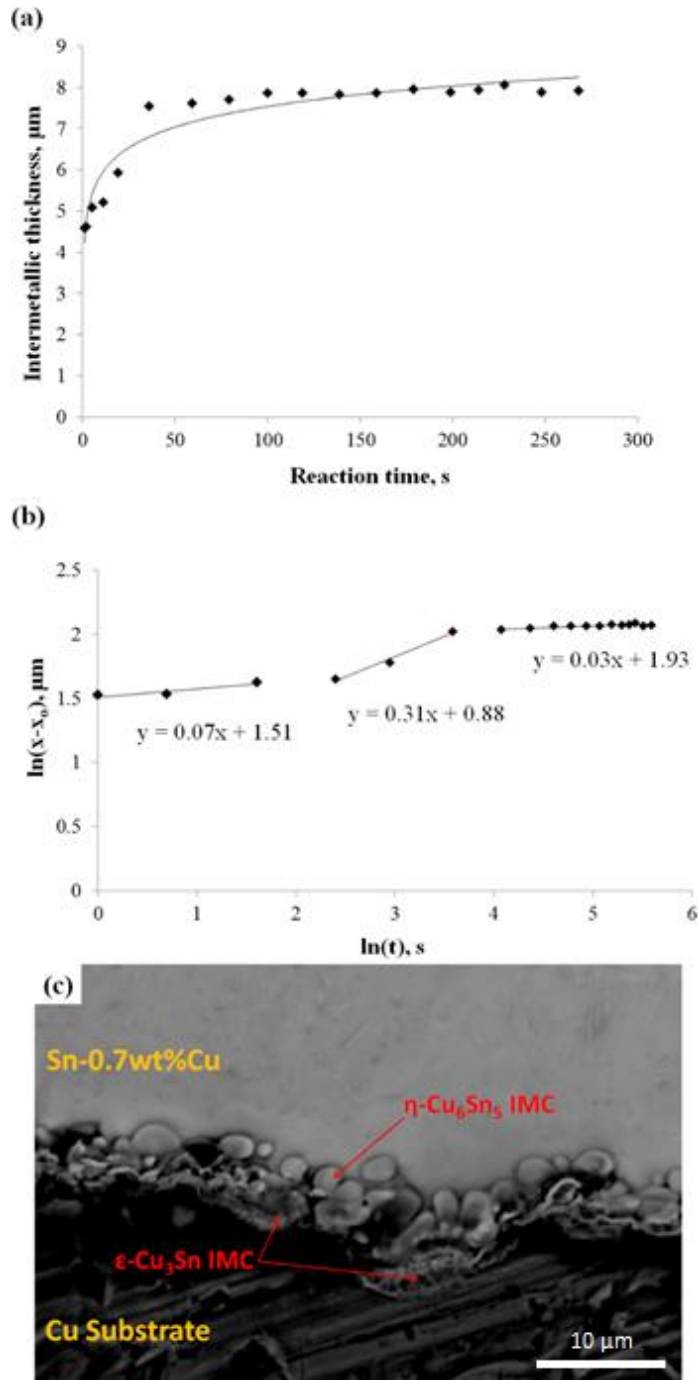


Figure 4: (a) Evolution of average total IMC thickness in the early stages of soldering, (b)  $\ln$  plots of IMC growth and (c) a scanning electron microscopy image of the interfacial microstructure taken subsequent to the synchrotron experiments.

To further investigate the mechanisms of IMC growth, the thickness is plotted against the reaction time in Figure 4(a). The measured layer thickness,  $x$ , versus time,  $t$ , can be modelled with an empirical power law relationship [27, 28]:

$$x = x_0 + A(t)^n \quad (1)$$



where  $x_0$  is the thickness of the IMC layer at  $t=0$ ,  $A$  is the growth constant and  $n$  is the time exponent. Values of the time exponent,  $n$  can be obtained by multivariable linear regression analysis [28]:

$$\ln(x - x_0) = \ln A + n \ln t \quad (2)$$

where the time exponent values are obtained from the slope of  $\ln(x - x_0)$  and  $\ln(t)$  plot as in Figure 4(b). From 4(b) it can be seen that three time exponents can be used to characterise the measured growth data where the correlation of the experimental data. This implies three different growth mechanism have occurred with  $n=0.07$  at 1 to 10 s of reaction time,  $n=0.31$  at 10 to 50 s of reaction time and  $n=0.03$  at 50 to 270 s of reaction time. This finding is somewhat in agreement with that of Lee and Kim[29], where two different time exponents were observed for the reaction between Sn-37wt%Pb on a Cu substrate during soldering at 230 °C and 250 °C with a time exponent  $n=0.15$  for the first few seconds of reaction time followed by a time exponent  $n=0.32$  for remaining growth. At the early stages of molten Sn-0.7wt%Cu reacting with solid Cu, the liquid solder results in dissolution of Cu from the substrate. This dissolution reaction of Cu into liquid solder happens until the solder becomes supersaturated with Cu at the Cu/liquid solder interface with respect to the  $\eta$ -Cu<sub>6</sub>Sn<sub>5</sub> phase[13, 30]. Since Sn-0.7wt%Cu is a near eutectic alloy, little change in composition is required for liquid solder at the Cu/liquid interface to become supersaturated and a significant thickness of planar  $\eta$ -Cu<sub>6</sub>Sn<sub>5</sub> intermetallic forms rapidly as observed in Figure 3(b). It is proposed that the intermetallic thickness that forms initially corresponds to the distance that Cu manages to diffuse in excess of the eutectic point, before  $\eta$ -Cu<sub>6</sub>Sn<sub>5</sub> nucleation becomes possible. However, the Cu concentration of the liquid at the interface will then progress through a transient stage when Cu atoms are depositing back to the Cu substrate surface to form the initial IMC layer[30]. From Figure 4(b), it is believed that at 1-10 s of reaction time with a time exponent  $n=0.065$ , this transient is occurring and the growth rate is lowered. From 10 – 40 s of reaction time the time exponent is  $n=0.315$  similar to the value of  $n=0.33$  found by Gong et al.[31] between 100 s to 1,600 s of reaction time. It is known that during this stage of the reaction, intermetallic growth is dominated by grain boundary diffusion[30]. This growth mechanism can be observed in Figure 3(d)-(f). Small  $\eta$ -Cu<sub>6</sub>Sn<sub>5</sub> grains are observed and the boundaries of these grains are likely to provide a fast diffusion path for Cu atoms to move to the liquid solder. After a few seconds of reaction time, at above 40 s with time exponent  $n=0.026$ , the rate of intermetallic growth has slowed. It is believed that this is due to a reduction in the temperature providing a barrier to diffusion. From the results obtained throughout this in-situ observation, it is expected that the

intermetallic formation and growth mechanisms of Sn-0.7wt%Cu solder during soldering are controlled by both the nucleation barrier to  $\text{Cu}_6\text{Sn}_5$  and the solubility of Cu in the liquid Sn-0.7wt%Cu followed by the grain boundary diffusion of Cu to the molten Sn-0.7wt%Cu solder. Subsequent to the in-situ observation, samples were taken out from the experiment sample cell and observed using SEM as in Figure 4(c). It was observed that the total thickness of the intermetallic layer ( $\eta\text{-Cu}_6\text{Sn}_5 + \varepsilon\text{-Cu}_3\text{Sn}$ ) is of the order of 8  $\mu\text{m}$  with a relatively small contribution from the  $\varepsilon\text{-Cu}_3\text{Sn}$  layer.

In conclusion, we have successfully obtained evidence of the mechanisms occurring during the reaction of Sn-0.7wt%Cu solder with solid Cu. The initial interfacial IMC formation at the moment of solder wetting was able to be observed in real time where a significant thickness of instant planar  $\eta\text{-Cu}_6\text{Sn}_5$  was formed before further growth resulted in a subsequent scallop shaped interface in the  $\eta\text{-Cu}_6\text{Sn}_5$ . The thickness and morphology of the intermetallic layer after soldering is believed to be determined by the nucleation barrier to  $\text{Cu}_6\text{Sn}_5$  and the rate of the dissolution of Cu followed by the diffusion of Cu through the IMC layer into the Sn-0.7wt%Cu liquid. In addition, large rod shape  $\text{Cu}_6\text{Sn}_5$  intermetallics were found to form during cooling. The techniques outlined in this work and the findings will be used as the basis for future research into controlling the formation and growth of IMCs during soldering. This work will include a wider range of compositions of both solder and substrate.

The authors would like to gratefully acknowledge financial support from the University of Queensland (UQ)-Nihon Superior (NS) collaborative research program. The authors thank Dr. K. Uesugi of SPring-8 beamline scientist and support staff and students from the Department of Materials Science and Engineering, Kyoto University, the Department of Adaptive Machine Systems, Osaka University for experimental assistance. In-situ observation experiments were performed at the SPring-8 BL20XU (Project ID: 2014A1540, 2014A1541 and 2014A1114) while SEM imaging was performed at the Centre for Microscopy and Microanalysis (CMM) University of Queensland. This work is also supported in part by a Grant-in-Aid for Scientific Research (S) (Project ID: 24226018) from JSPS, Japan and with the International Synchrotron Access Program Fund (AS/IA142/8198). M. A. A. Mohd Salleh is financially supported by the Malaysian Education Ministry and Universiti Malaysia Perlis (UniMAP).

## References

- [1] S. Mannan, M.P. Clode, *Soldering & Surface Mount Technology*, 16 (2004) 31-33.
- [2] G. Izuta, T. Tanabe, K. Suganuma, *Soldering & Surface Mount Technology*, 19 (2007) 4-11.
- [3] L. Snugovsky, M.A. Ruggiero, D.D. Perovic, J.W. Rutter, *Materials Science and Technology* 19 (2003) 866-874.
- [4] C.M. Gourlay, K. Nogita, A.K. Dahle, Y. Yamamoto, K. Uesugi, T. Nagira, M. Yoshiya, H. Yasuda, *Acta Materialia*, 59 (2011) 4043-4054.
- [5] T. Ventura, C. Gourlay, K. Nogita, T. Nishimura, M. Rappaz, A. Dahle, *Journal of Electronic Materials*, 37 (2008) 32-39.
- [6] P.E. Gary Delserro, in: *Delserro Engineering Solutions, EE Evaluation Engineering*, Easton, PA 2006.
- [7] K.N. Tu, *Solder Joint Technology: Materials, Properties, and Reliability*, Springer, 2007.
- [8] B. Chao, S.-H. Chae, X. Zhang, K.-H. Lu, J. Im, P.S. Ho, *Acta Materialia*, 55 (2007) 2805-2814.
- [9] M. He, Z. Chen, G. Qi, *Acta Materialia*, 52 (2004) 2047-2056.
- [10] J.F. Li, S.H. Mannan, M.P. Clode, D.C. Whalley, D.A. Hutt, *Acta Materialia*, 54 (2006) 2907-2922.
- [11] M.S. Park, R. Arróyave, *Acta Materialia*, 58 (2010) 4900-4910.
- [12] B.-J. Lee, N.M. Hwang, H.M. Lee, *Acta Materialia*, 45 (1997) 1867-1874.
- [13] M. Schaefer, R. Fournelle, J. Liang, *Journal of Electronic Materials*, 27 (1998) 1167-1176.
- [14] K.N. Tu, T.Y. Lee, J.W. Jang, L. Li, D.R. Frear, K. Zeng, J.K. Kivilahti, *Journal of Applied Physics*, 89 (2001) 4843-4849.
- [15] L. Qu, H.T. Ma, H.J. Zhao, A. Kunwar, N. Zhao, *Applied Surface Science*, 305 (2014) 133-138.
- [16] L. Qu, N. Zhao, H.J. Zhao, M.L. Huang, H.T. Ma, *Scripta Materialia*, 72–73 (2014) 43-46.
- [17] L. Qu, N. Zhao, H. Ma, H. Zhao, M. Huang, *Journal of Applied Physics*, 115 (2014) -.
- [18] M.L. Huang, Z.J. Zhang, N. Zhao, Q. Zhou, *Scripta Materialia*, 68 (2013) 853-856.
- [19] H. Yasuda, I. Ohnaka, K. Kawasaki, A. Sugiyama, T. Ohmichi, J. Iwane, K. Umetani, *Journal of Crystal Growth*, 262 (2004) 645-652.
- [20] K. Nogita, H. Yasuda, A. Prasad, S.D. McDonald, T. Nagira, N. Nakatsuka, K. Uesugi, D.H. StJohn, *Materials Characterization*, 85 (2013) 134-140.

- [21] T. Nagira, C.M. Gourlay, A. Sugiyama, M. Uesugi, Y. Kanzawa, M. Yoshiya, K. Uesugi, K. Umetani, H. Yasuda, *Scripta Materialia*, 64 (2011) 1129-1132.
- [22] H. Yasuda, I. Ohnaka, S. Fujimoto, N. Takezawa, A. Tsuchiyama, T. Nakano, K. Uesugi, *Scripta Materialia*, 54 (2006) 527-532.
- [23] D.D. Maio, C.P. Hunt, *Soldering & Surface Mount Technology*, 21 (2009) 24-31.
- [24] J.W. Jang, D.R. Frear, T.Y. Lee, K.N. Tu, *Journal of Applied Physics*, 88 (2000) 6359-6363.
- [25] J.Y. Huh, K.K. Hong, Y.B. Kim, K.T. Kim, *Journal of Electronic Materials*, 33 (2004) 1161-1170.
- [26] Q. Li, Y.C. Chan, *Journal of Alloys and Compounds*, 567 (2013) 47-53.
- [27] D. Shangguan, *Lead-free solder : interconnect reliability*, ASM International, Materials Park, Ohio, 2005.
- [28] J. Shen, M. Zhao, P. He, Y. Pu, *Journal of Alloys and Compounds*, 574 (2013) 451-458.
- [29] J.-H. Lee, Y.-S. Kim, *Journal of Electronic Materials*, 31 (2002) 576-583.
- [30] T. Laurila, V. Vuorinen, J.K. Kivilahti, *Materials Science and Engineering: R: Reports*, 49 (2005) 1-60.
- [31] J. Gong, C. Liu, P.P. Conway, V.V. Silberschmidt, *Acta Materialia*, 56 (2008) 4291-4297.

**Paper 4: In-situ TEM observations of  $\text{Cu}_6\text{Sn}_5$   
polymorphic transformations in reaction layers  
between Sn-0.7Cu solder and Cu substrate**

Kazuhiro Nogita, Mohd Arif Anuar Mohd Salleh, Eishi Tanaka, Guang Zeng,  
Stuart D. McDonald, Syo Matsumura

**JOM** (2016). Accepted on the 25<sup>th</sup> May 2016.

# **In-situ TEM observations of Cu<sub>6</sub>Sn<sub>5</sub> polymorphic transformations in reaction layers between Sn-0.7Cu solders and Cu substrates**

K. Nogita<sup>1\*</sup>, M. A. A. Mohd Salleh<sup>1,2</sup>, E. Tanaka<sup>3</sup>, G. Zeng<sup>1</sup>, S. D. McDonald<sup>1</sup>, S. Matsumura<sup>3,4</sup>

<sup>1</sup>Nihon Superior Centre for the Manufacture of Electronic Materials (NS CMEM), School of Mechanical and Mining Engineering, The University of Queensland, 4072 St Lucia, Queensland, Australia.

<sup>2</sup>Centre of Excellence Geopolymer and Green Technology, School of Materials Engineering, Universiti Malaysia Perlis (UniMAP), Taman Muhibbah 02600, Jejawi, Arau, Perlis, Malaysia.

<sup>3</sup>The Ultramicroscopy Research Center, and <sup>4</sup>Department of Applied Quantum Physics and Nuclear Engineering, Kyushu University, Fukuoka, Japan

\*Corresponding author: Room 644, 49 Jocks Rd., St Lucia, Brisbane, QLD 4072, Australia

Email: k.nogita@uq.edu.au ; Tel: +61 7 3365 3919

## **Summary**

Direct evidence of the relationship between the polymorphic phase transformation from monoclinic Cu<sub>6</sub>Sn<sub>5</sub> to hexagonal Cu<sub>6</sub>Sn<sub>5</sub> and stress accumulation/release in Cu<sub>6</sub>Sn<sub>5</sub> formed at the interface between Sn-0.7Cu lead free solder and their Cu substrates, has been obtained. To explore this challenging phenomena, we developed an in-situ heating/isothermal observation technique in ultra-high voltage transmission electron microscopy (UHV-TEM) that enables the observation of thick samples (around 0.5μm) for solder joints including Cu/Cu<sub>3</sub>Sn/Cu<sub>6</sub>Sn<sub>5</sub>/Sn-0.7Cu solder interfaces prepared by a focused ion beam milling (FIB) technique. The results show evidence of stress creation and release events by imaging bend contours that may arise due to the polymorphic transformations of the Cu<sub>6</sub>Sn<sub>5</sub> phase and the associated volumetric change.

## INTRODUCTION

During the transition from traditional to lead-free soldering, there has been a simultaneous increase in the complexity and spatial density of electrical packages (combined circuitry/chips/solder etc.). This miniaturisation of circuitry has resulted in proportionally smaller volumes of solder at electrical interconnects <sup>1</sup>. In the past a solder joint would retain a significant layer of the original Sn-alloy solder (Sn–0.7wt%Cu for example). The drive towards miniaturisation has resulted in a relative increase in the volume fraction of intermetallic compounds (IMCs) in the microstructure of solder joints and in some cases, a solder joint may consist almost entirely of  $\text{Cu}_6\text{Sn}_5$  and  $\text{Cu}_3\text{Sn}$  <sup>2</sup> with different mechanical, physical properties and co-efficient of thermal expansion (CTE) <sup>3</sup>. Therefore, the current understanding of the ‘bulk’ properties of solder joints mainly consisting of the  $\beta$ -Sn phase (which is already limited for many alloy/substrate combinations) is not always relevant when designing high performance 3D IC electrical packages. For this reason, there is a strong and urgent need to understand (i) the growth crystallography, morphology and anisotropic thermo-mechanical properties of intermetallic joints, and (ii) the impact these factors have on the integrity of solder joints for micro-electronics applications, and to use this information to develop interconnects with IMCs optimized for crack resistance.

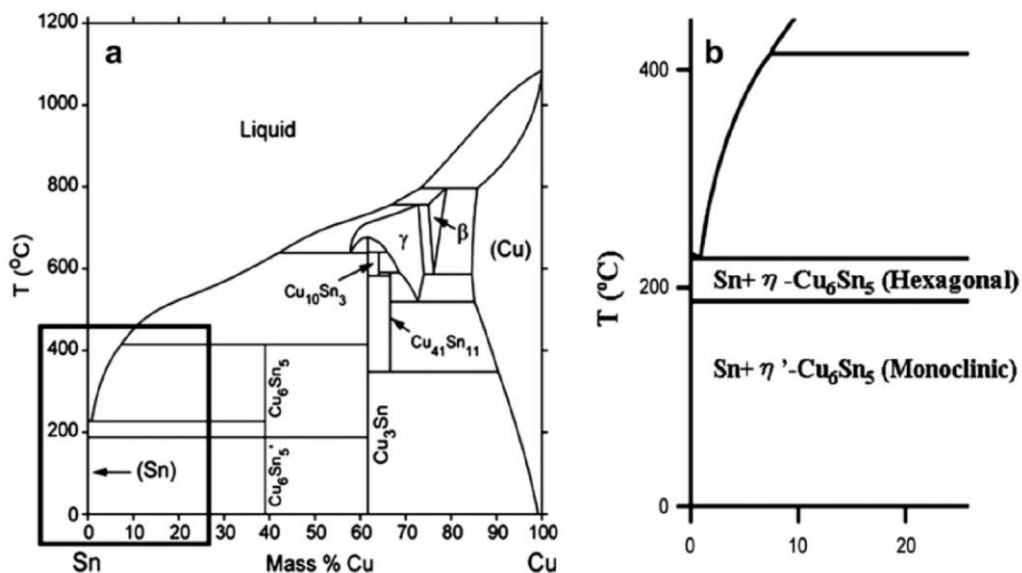


Fig. 1. (a) Sn–Cu phase diagram and (b) magnified from Sn-rich corner of (a), adapted from <sup>4,5</sup>.

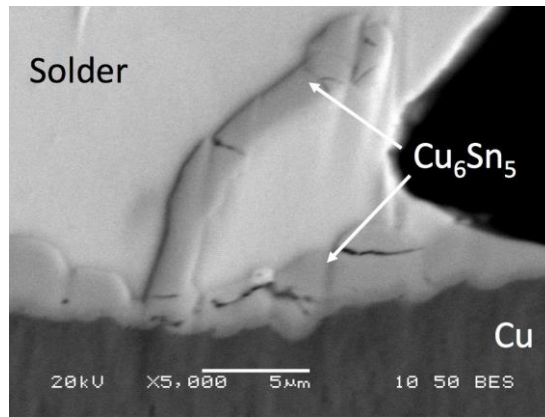


Fig. 2. A typical cross-sectioned ball grid array (Sn-0.7wt%Cu solder) on Cu substrate, adapted from <sup>10</sup>.

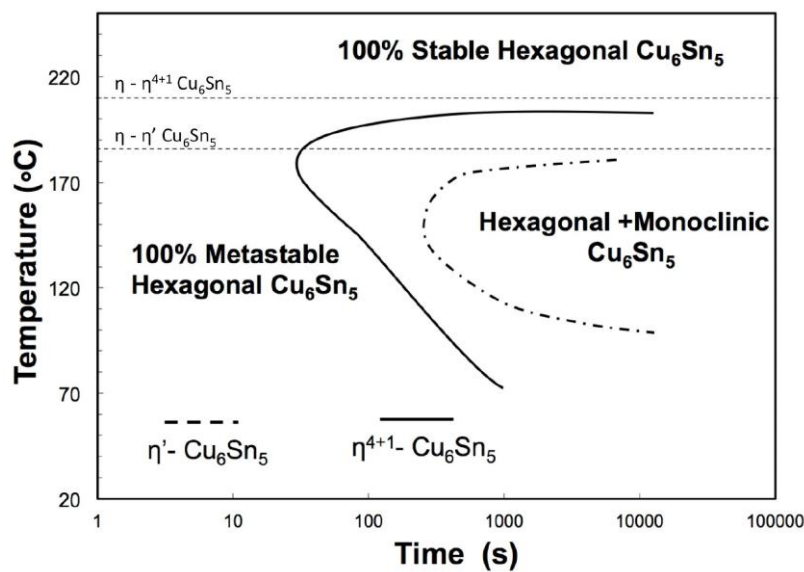


Fig. 3. Schematic TTT diagrams of hexagonal to monoclinic transformations in  $\text{Cu}_6\text{Sn}_5$  intermetallics, adapted from <sup>11,12</sup>.

The reaction products in solder joints are typically the IMCs  $\text{Cu}_6\text{Sn}_5$  and  $\text{Cu}_3\text{Sn}$ , often of complex crystal structures and including trace elements from both the substrate and the solder. Although conventional Sn-Cu binary phase diagrams (**Figure 1**)<sup>4,5</sup>, shows two polymorphs of  $\text{Cu}_6\text{Sn}_5$ , up to five variants have now been identified ( $\eta$ ,  $\eta'$ ,  $\eta^6$ ,  $\eta^8$  and  $\eta^{4+1}$ )<sup>6,7</sup> but very limited information exists for these structures, particularly the latter three. It has been shown that a polymorphic transformation from hexagonal  $\eta$ - $\text{Cu}_6\text{Sn}_5$  to monoclinic  $\eta'$ - $\text{Cu}_6\text{Sn}_5$  occurs as the temperature falls below 186°C. We have previously shown<sup>5,8,9</sup> that the faceted eutectic  $(\text{Cu},\text{Ni})_6\text{Sn}_5$  intermetallics containing Ni remain stable as the hexagonal  $\eta$  phase at room temperature when, in contrast, identically cooled binary  $\text{Cu}_6\text{Sn}_5$  transform into the low temperature monoclinic  $\eta'$  phase. This is an important discovery as the



transformation is associated with a volumetric change and this has been hypothesized to be a cause of internal stress generation in soldered joints during real-world applications, and research has already led to improvements in the performance of this IMC layer<sup>3</sup>. Nogita et. al.<sup>10</sup> shows an example of a ball grid array (BGA) soldered joint (see **Figure 2**), commonly used in mobile phones and e-tablets, on an electronic circuit board produced using a slightly hypo-eutectic lead-free solder alloy (Sn-0.7Cu), which has a microstructure consisting of Sn primary dendrites and Sn-Cu<sub>6</sub>Sn<sub>5</sub> eutectic. The cross section of the IMC layer between the solder ball and Cu substrate, contains crystals of Cu<sub>6</sub>Sn<sub>5</sub>, and within these crystals are a number of cracks and voids that are generated during solidification and cooling to room temperature<sup>10</sup>. These cracks compromise the reliability and diminish the shock resistance of the final microelectronic devices. By adding trace Ni additions to this solder, we demonstrated that the Cu<sub>6</sub>Sn<sub>5</sub> layer becomes stabilised in the hexagonal polymorph, undergoes less cracking and the growth texture of the layer is altered <sup>10</sup>. However, direct evidence between the polymorphic phase transformations and the generation of stress has yet to be provided. Additionally, although time-temperature-transformation (TTT) diagrams of monoclinic to hexagonal transformations have been developed (see **Figure 3**)<sup>11,12</sup>, detailed mechanisms of the polymorphic phase transformation, such as nucleation and growth of monoclinic to hexagonal Cu<sub>6</sub>Sn<sub>5</sub>, in real solder joints (Cu/Cu<sub>3</sub>Sn/Cu<sub>6</sub>Sn<sub>5</sub>/Sn-0.7Cu solder) is not known.

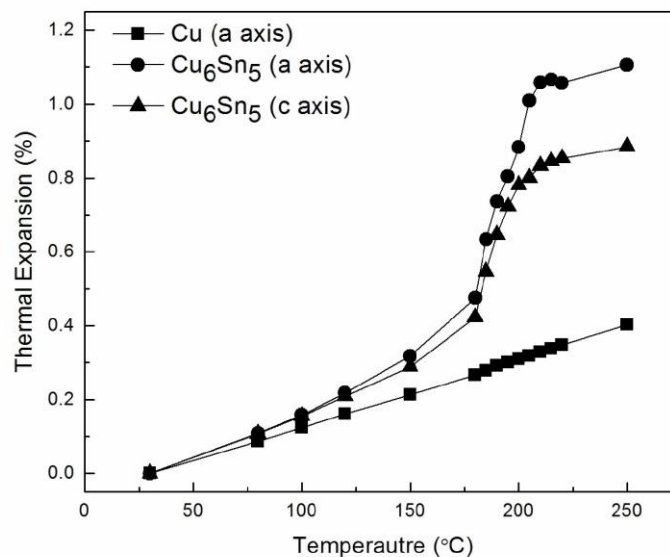


Fig. 4. Whole-pattern profile fitting method to determine thermal expansion behavior of interfacial Cu<sub>6</sub>Sn<sub>5</sub> and Cu substrate. The variation in lattice parameters of Cu<sub>6</sub>Sn<sub>5</sub> and Cu in the temperature range 30–250 °C, adapted from <sup>20</sup>.

A significant challenge in research on the link between phase transformation and crack formation has been the difficulty of proving the cracking mechanisms and, therefore, the mechanisms have long been the subject of questions. As the results, so far we proposed three possible hypotheses for the cause of cracking of  $\text{Cu}_6\text{Sn}_5$ <sup>10</sup> as (1) polymorphic transformations and associated stresses<sup>5,8,9</sup>, (2) mismatch of mechanical properties, such as hardness and elastic modulus between interfacial structures<sup>13-15</sup>, and (3) growth orientations associated with anisotropy of mechanical properties<sup>15-19</sup>. This lack of fundamental understanding is reflected in many solder alloys and hampers the further rational development of alloys for increased reliability and use in emerging and demanding applications such as 3D ICs.

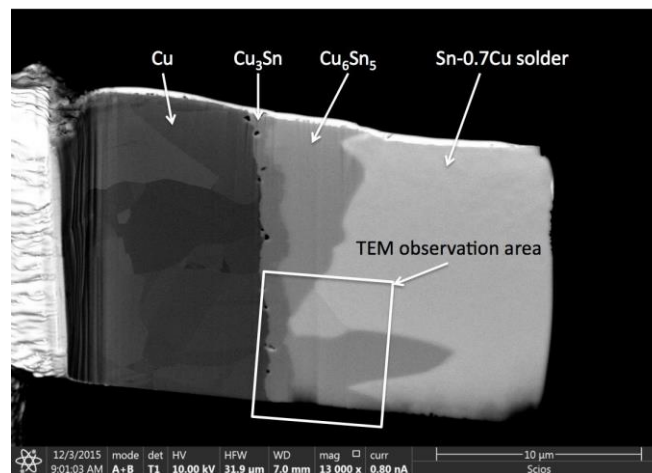


Fig. 5. SEM image of the sample. Area showing in the image corresponds to the in-situ observation with heating and isothermal.

As shown in **Figure 4**, we have performed in-situ XRD heating experiments<sup>20</sup> to determine the thermal expansion behavior of interfacial  $\text{Cu}_6\text{Sn}_5$  and Cu substrates with Sn-0.7wt%Cu solder. In addition to the difference of the thermal expansion between  $\text{Cu}_6\text{Sn}_5$  and Cu, there is a large discontinuity between them at around 180°C, which corresponds to the volume change due to the polymorphic transformation from monoclinic  $\text{Cu}_6\text{Sn}_5$ . In-situ transmission electron microscopy (TEM) is an established experimental technique that permits direct observation of the dynamics and mechanisms of deformation behavior. In this paper we report on direct evidence for the relationship between the polymorphic phase transformation and stress accumulations/release in  $\text{Cu}_6\text{Sn}_5$  using ultra-high voltage transmission electron microscopy (UHV-TEM) with controlled temperature in-situ observations.

## EXPERIMENTAL PROCEDURES

### BGA-sample preparation

Sn-0.7wt%Cu bulk alloy was firstly prepared by casting a mixture of Sn and Cu. The solidified bulk sample was then cut into thin sheets and its composition was confirmed using energy dispersive X-ray spectroscopy (EDS) to be in the range of 99.3 wt% Sn and 0.7 wt% Cu. Sn-0.7wt%Cu solder sheets were further rolled at room temperature to approximately 0.02 mm thickness. The thinned sheets were then punched into 2.5mm diameter discs and were further heated on a Pyrex plate to 250°C with the aid of N<sub>2</sub> gas flow to form a ball shape. The fabricated solder balls were then sieved to achieve spheres of 500 - 600 µm. The solder balls, with a small amount of rosin mildly activated (RMA) flux were then soldered onto a Cu with organic soldering preservative surface finish (Cu-OSP) printed circuit board (PCB) with a 600 µm ball pitch using a tabletop reflow oven with a maximum 250°C reflow temperature and 127 s reflow time with N<sub>2</sub> gas flow. The solder joint samples were then further annealed for 500 hours at 150 °C.

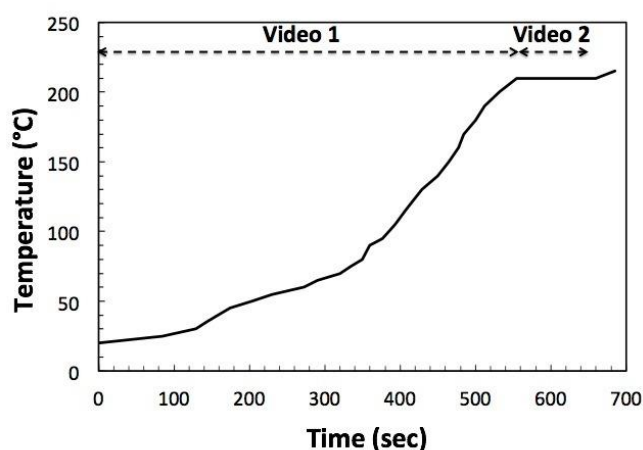


Fig. 6. The temperature profile for the in-situ observation of the sample.

### UHV-TEM sample preparations

Annealed samples were cross-sectioned and fine polished perpendicular to the solder/Cu interface. UHV-TEM samples were then prepared using a FEI SCIOS focus ion beam (FIB) dual beam system. This system was used with the electron and ion column mounted at 52 degrees to each other on a 21 port specimen chamber and a 7mm working distance, the featured area perpendicular to the solder/Cu interface were deposited with a Pt protective layer approximately 1.5 micrometers thick. Using a 30nA and 15nA beam, two cross-sections were milled in serial mode to provide a 2 µm lamella. By using the Easylift needle

tip, the lamella cross-sectioned sample was transferred and welded using Pt deposition on a Cu TEM grid. Finally to provide a smooth cross-section area for UHV-TEM observation, the welded samples were thinned to about 0.5  $\mu\text{m}$  thickness using 0.5nA beam current. **Figure 5** shows SEM images of the sample, which clearly shows the cross-sectioned Cu/Cu<sub>3</sub>Sn/Cu<sub>6</sub>Sn<sub>5</sub>/Sn-0.7Cu solder. The area shown in **Figure 5** corresponds to the in-situ observation area.

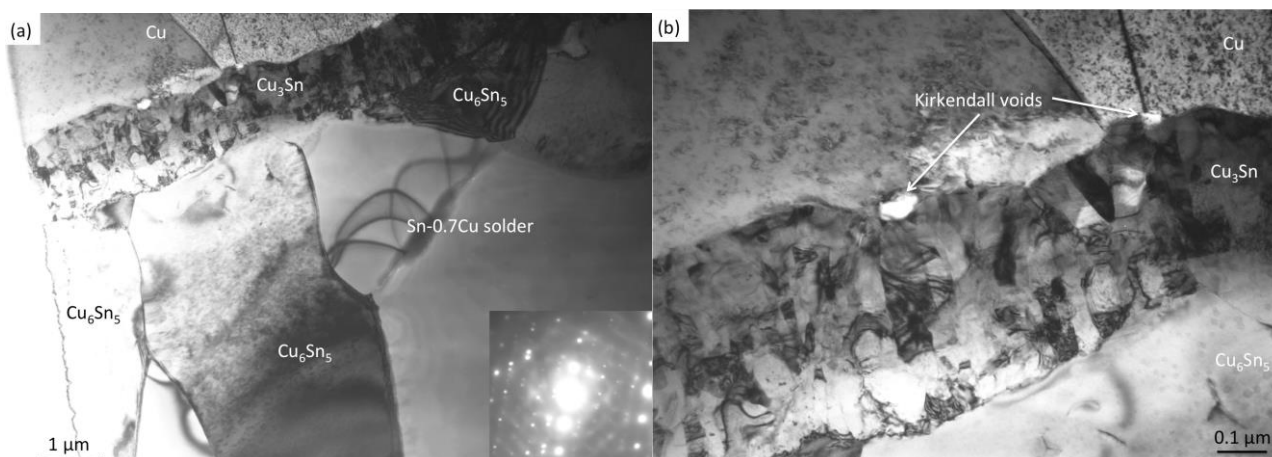


Fig. 7. (a) Low magnification bright field image of solder joint with selected area electron diffraction from Cu<sub>6</sub>Sn<sub>5</sub>, (b) higher magnification bright field image of Cu/Cu<sub>3</sub>Sn/Cu<sub>6</sub>Sn<sub>5</sub> interface.

### In-situ Synchrotron XRD characterization

For XRD experiments, Sn-0.7Cu/Cu solder joints were prepared by dipping Cu plates (C1220P) of 10 mm×30 mm×0.3 mm with flux into the molten solder in a solder bath at 270°C. Samples were etched after being annealed for 500 hours at 150°C in a solution of ortho-nitrophenol (35 g) and NaOH (50 g) in 1 L of water at 80°C to completely remove the Sn phase from the solder alloys. XRD data were obtained from the prepared dipped Sn-0.7Cu/Cu samples at 30°C, 150°C and 250°C, in flat-plate asymmetric reflection geometry with sample heater at the powder diffraction beamline of the Australian Synchrotron using an X-ray energy of 18keV. The Wavelength (0.689Å) and 2 $\theta$  zero-error were determined from a standard 0.3 mm capillary of a LaB<sub>6</sub>/Si mixture using transmission geometry. The angle between the X-ray beam and the sample surface was fixed at 5°. Indexing of XRD patterns was conducted using TOPAS 4.2 software. A Fundamental parameter (FP) approach was employed in TOPAS<sup>21</sup>.

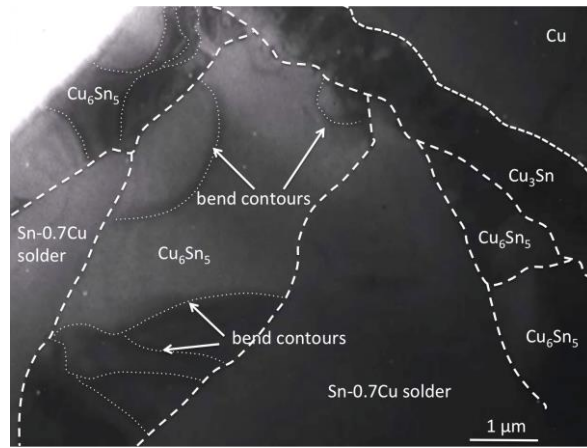


Fig. 8. A still frame TEM images from in-situ video of an interface in Cu/Cu<sub>3</sub>Sn/Cu<sub>6</sub>Sn<sub>5</sub>/Sn taken at 210°C.

### In-situ UHV-TEM observations

In-situ UHV-TEM observations were performed using a JEM-1000 (JEOL, Japan) at an acceleration voltage of 1,000 kV with an EM-HSTH (JEOL, Japan) heating holder and high resolution video recorder. **Figure 6** shows the temperature profile for the in-situ observation of the sample. A sample was measured at room temperature, then heated from 25 to 210°C with heating a heating rate of approximately 20°C/min following isothermal observations at 210°C. The beam-induced heating remains small at the acceleration voltage of 1,000kV, allowing for proper observations of the phase transformation.

## RESULTS AND DISCUSSION

### UHV-TEM bright field image of solder joint Cu/Cu<sub>3</sub>Sn/Cu<sub>6</sub>Sn<sub>5</sub>/Sn-0.7Cu solder

**Figure 7a and 7b** shows a bright field image of solder joint and selected area electron diffraction from Cu<sub>6</sub>Sn<sub>5</sub>. Multiple small grains a few submicron size of Cu<sub>3</sub>Sn can be seen on the Cu substrate with a columnar morphology, with Kirkendall voids between the Cu<sub>3</sub>Sn and Cu substrate. It is expected that the relatively thick Cu<sub>3</sub>Sn layer with Kirkendall voids was formed during annealing for 500 hours at 150°C<sup>20</sup>. The Cu<sub>6</sub>Sn<sub>5</sub> layer is typical scalloped morphology and a single crystal grain was observed during in-situ heating experiments. According to the reported TTT diagram based on annealing for 500 hours at 150°C, Cu<sub>6</sub>Sn<sub>5</sub> will be a stable monoclinic phase. However, it is difficult to determine whether this monoclinic phase is  $\eta'$  or  $\eta^{4+1}$  from the electron diffraction pattern obtained from Cu<sub>6</sub>Sn<sub>5</sub>. The Sn phase also exists at outer areas of the Cu<sub>6</sub>Sn<sub>5</sub>, and interdiffusion with Cu<sub>6</sub>Sn<sub>5</sub> can be expected during heating in the in-situ observation experiments. In Figure 7 (a) and Figure 8 taken from the still frame in-situ video at 20°C, no lattice defects, such as dislocations, stacking

faults or twining were recognised in  $\text{Cu}_6\text{Sn}_5$  grains by bright field imaging at several tilting conditions. However, some wide and dark banded contrast patterns within  $\text{Cu}_6\text{Sn}_5$  were found. This contrasting is likely to be bend contours<sup>22</sup> but not thickness fringes since the sample is flat with thickness of around 0.5  $\mu\text{m}$ , prepared by parallel ion beam milling. Note thickness fringes only appear when the sample is not flat<sup>22</sup>.

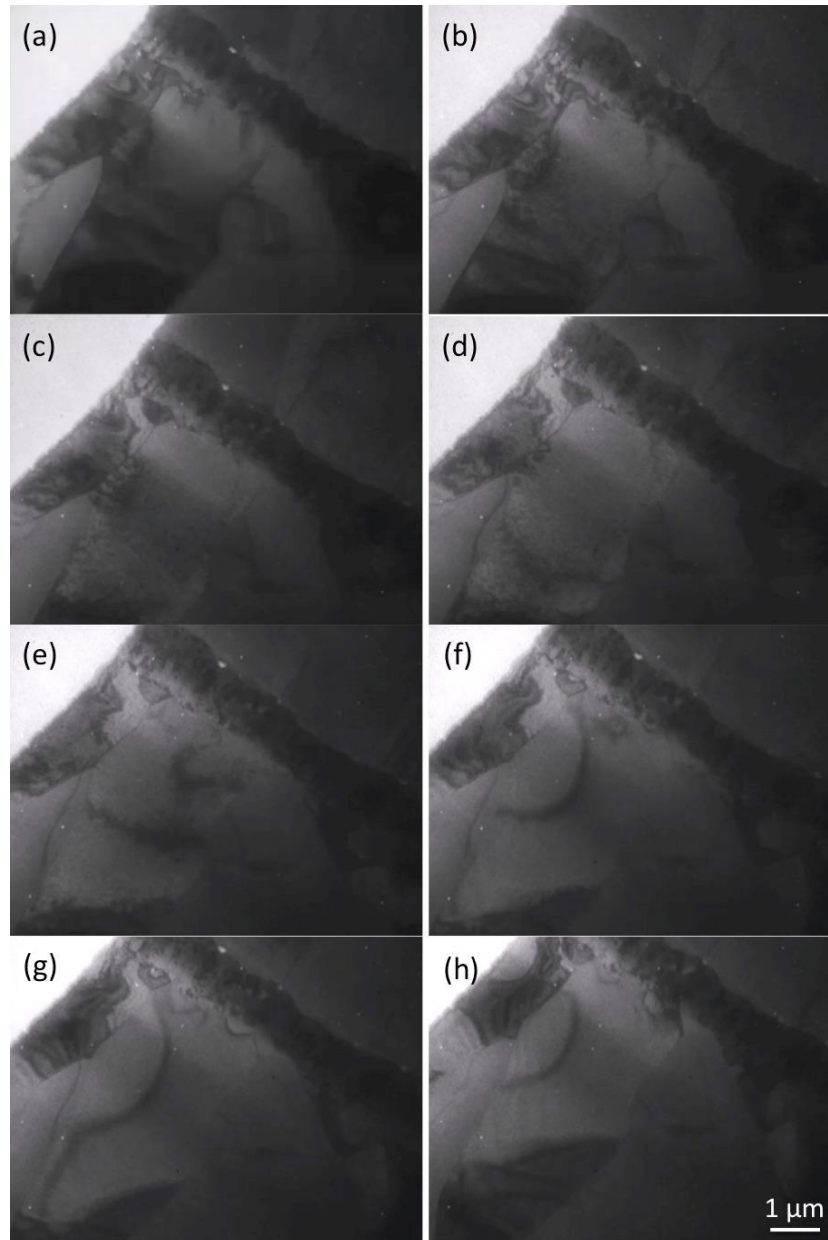


Fig. 9. Selected still frame TEM images from in-situ video of high voltage TEM of an interface in Cu/ $\text{Cu}_3\text{Sn}$ / $\text{Cu}_6\text{Sn}_5$ /Sn taken at (a) 20°C, (b) 60°C, (c) 120°C, (d) 150°C, (e) 180°C, (f) 190°C, (g) 200°C, and (h) 210°C.

In Figure 8, the thick dotted lines correspond to grain boundaries of Cu,  $\text{Cu}_3\text{Sn}$ ,  $\text{Cu}_6\text{Sn}_5$  and Sn-0.7wt%Cu solder, and the thin dotted lines within  $\text{Cu}_6\text{Sn}_5$  may be bend contours. Bend



contours are a diffraction phenomenon that arises from the change in orientation of particular sets of planes within the sample relative to the electron beam <sup>22</sup> and indicate that there is strain in the grains. In this instance the patterns appear in a temperature range which is likely to correspond to the polymorphic transformation of Cu<sub>6</sub>Sn<sub>5</sub> and may be indicative of transformation related stresses.

### In-situ heating observations from room temperature to 210°C

**Figure 9 (a)-(h)** are selected still frame TEM images from the in-situ video of UHV-TEM of an interface in Cu/Cu<sub>3</sub>Sn/Cu<sub>6</sub>Sn<sub>5</sub>/Sn-0.7Cu solder taken at (a) 20°C, (b) 60°C, (c) 120°C, (d) 150°C, (e) 180°C, (f) 190°C, (g) 200°C, and (h) 210°C. As shown in **Figure 8** and **Figure 9(a)**, in Cu<sub>6</sub>Sn<sub>5</sub>, there are contrast patterns. Note the sample thickness is around 0.5 μm and flat due to the FIB for parallel cutting, so the thickness fringe, if any, should be straight but not curved. Contributions from thermal expansion are estimated at approximately 1.8% volume expansion from unit cell volume measurements by synchrotron XRD <sup>14</sup>. At around 180°C, the contrast patterns moved from the left side of the Cu<sub>6</sub>Sn<sub>5</sub> toward the right of the Cu<sub>6</sub>Sn<sub>5</sub> grain, then disappeared and the new contrast patterns were created from the left side of the grain. There are potentially two different monoclinic variants, η' and η<sup>4+1</sup>. The former transformation temperature is reported at 186°C and the latter at 210°C. This TEM experiments involve a heating rate of 20°C /min to reach 210°C, then isothermal holding. It is possible if monoclinic is η', due to the relatively slow kinetics for the phase transformation from monoclinic η'-Cu<sub>6</sub>Sn<sub>5</sub> to hexagonal η-Cu<sub>6</sub>Sn<sub>5</sub>, a phase transformation is observed at 210°C. Or alternatively if this monoclinic variant is η<sup>4+1</sup>, a phase transformation occurring at 210°C is expected. However, it is difficult to determine whether this monoclinic phase is η' or η<sup>4+1</sup> from the electron diffraction pattern obtained from Cu<sub>6</sub>Sn<sub>5</sub>.

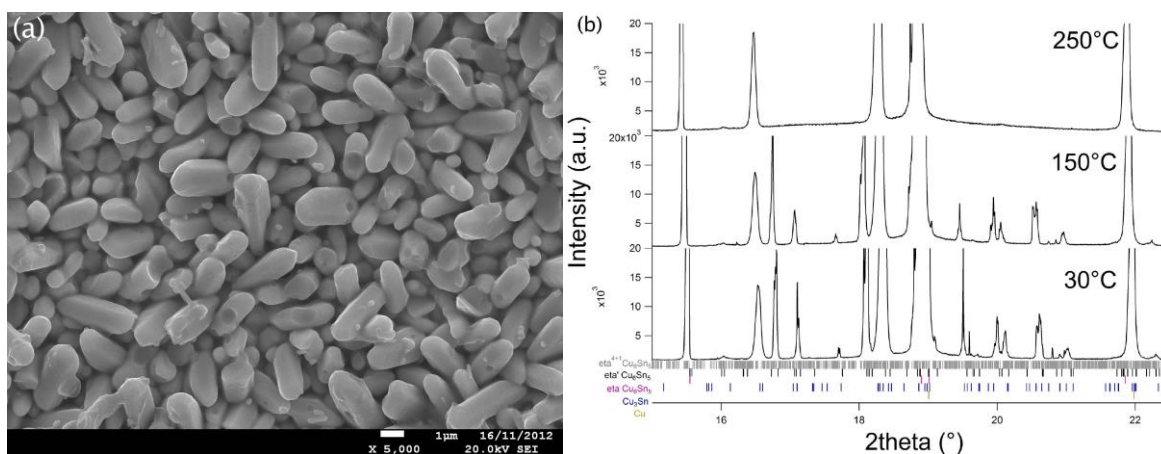


Fig. 10. (a) SEM image of the sample used for XRD, (b) The XRD patterns from the

interfacial IMCs in Sn-0.7Cu/Cu show an  $\eta'/\eta^{4+1}$   $\text{Cu}_6\text{Sn}_5$  crystal structure at 30°C and 150°C, and an  $\eta$   $\text{Cu}_6\text{Sn}_5$  structure at 250°C.

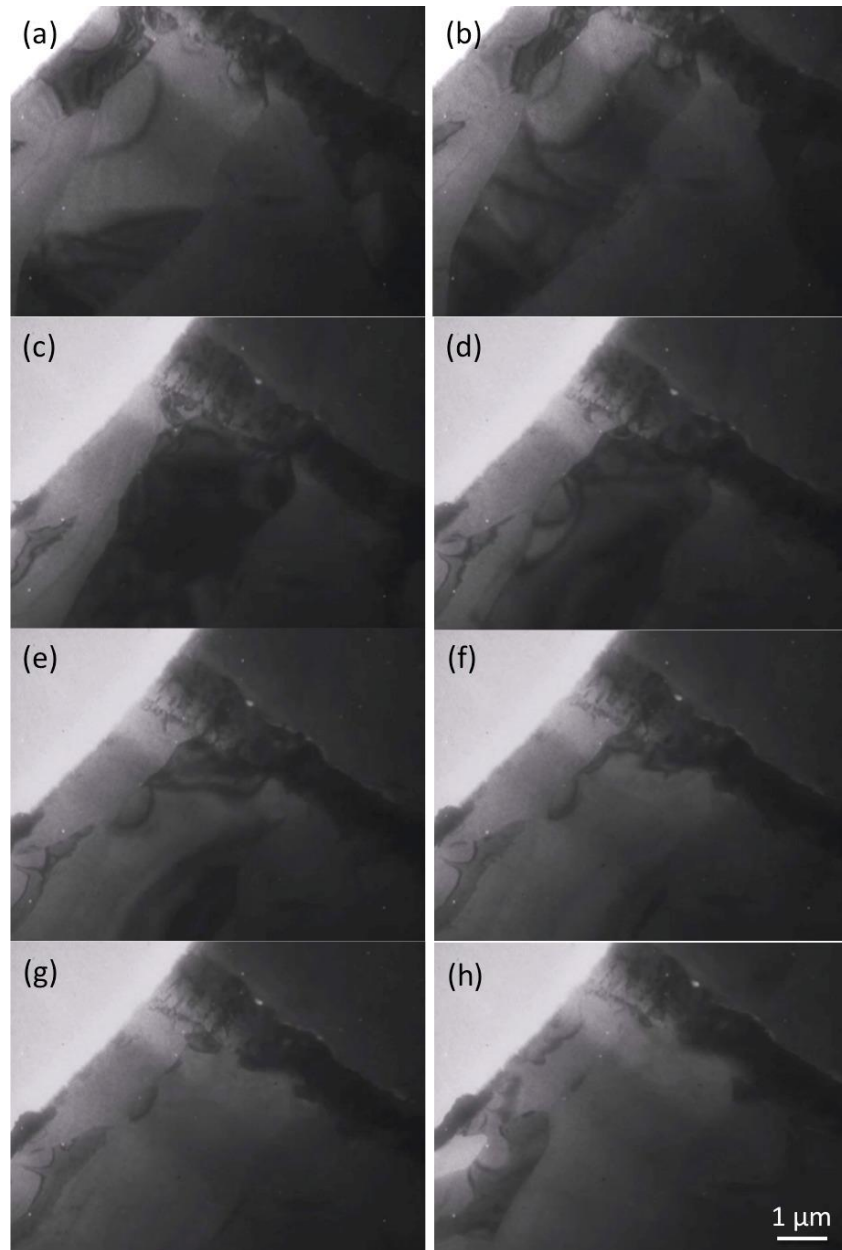


Fig. 11. Selected still frame TEM images from in-situ video of an interface in Cu/Cu<sub>3</sub>Sn/Cu<sub>6</sub>Sn<sub>5</sub>/Sn taken at 210°C isothermally for (a) 0 sec, (b) 15 sec, (c) 45 sec, (d) 75 sec, (e) 85 sec, (f) 95 sec, (g) 105 sec, and (h) 130 sec followed by heating to 210°C.

Figure 10 (a) shows an SEM image of the sample surface after removed Sn by etching. As shown in **Figure 10 (b)** after being annealed at 500h (identical to TEM samples in this study), the interfacial IMCs in Sn-0.7Cu/Cu show an  $\eta'/\eta^{4+1}$   $\text{Cu}_6\text{Sn}_5$  crystal structure at 30°C and 150°C conditions. As they are heated the peaks gradually shifted to low  $2\theta$  angle because of thermal expansion. The XRD pattern at 250 °C became relatively flat and can be indexed



as hexagonal eta  $\text{Cu}_6\text{Sn}_5$ ,  $\text{Cu}_3\text{Sn}$  and Cu, which indicates that polymorphic phase transformation of  $\text{Cu}_6\text{Sn}_5$  has completed. In-situ XRD patterns on identical samples to the TEM study therefore revealed a polymorphic transformation of  $\text{Cu}_6\text{Sn}_5$ .

### In-situ isothermal observations at 210°C

To eliminate the effects of thermal expansion, isothermal in-situ observations were made immediately after the temperature reached 210°C as shown in the experimental temperature profile in **Figure 6**. **Figure 11 (a)-(h)** are selected still frame TEM images from in-situ videos of the interface in Cu/ $\text{Cu}_3\text{Sn}$ / $\text{Cu}_6\text{Sn}_5$ /Sn-0.7Cu solder taken at 210°C isothermally for (a) 0 sec, (b) 15 sec, (c) 45 sec, (d) 75 sec, (e) 85 sec, (f) 95 sec, (g) 105 sec, and (h) 130 sec followed by heating to 210°C. During early stages of the observation in **Figure 11(a)-(d)**, contrast patterns moved from the grain boundary to the center of the grain. Then after 105 sec in **Figure 11(g)**, all contrast patterns disappeared. In **Figure 11(g) and (h)**, there is no contrast patterns in the  $\text{Cu}_6\text{Sn}_5$ .

According to the review by Laurila et al<sup>23</sup>, during soldering and subsequent cooling the time available for the transformation into the low temperature monoclinic structure is not sufficient and the high temperature hexagonal  $\text{Cu}_6\text{Sn}_5$  remains as a metastable phase. However, in our case, the sample had been annealed for 500hours at 150°C, the transformation to monoclinic is expected to occur, evidenced by TTT diagram shown in **Figure 3**. The expected volume change if  $\text{Cu}_6\text{Sn}_5$  transforms from the  $\eta'$ -monoclinic phase to the  $\eta$ -hexagonal phase during service is a 2.15% shrinkage based on the ambient temperature theoretical densities of monoclinic and hexagonal  $\text{Cu}_6\text{Sn}_5$ : 8.270 g/cm<sup>3</sup> and 8.448 g/cm<sup>3</sup>, respectively<sup>24</sup>. A 2% volume shrinkage would conceivably be accompanied by significant stress in the IMC layer. For our in-situ experiments, no crack propagation was observed but contrast patterns formation and movement. This is expected due to the sample thickness (0.5 $\mu\text{m}$ ) being insufficient to accumulate the strain for initiation of cracking.

### Conclusion

We observed two phenomena, namely, the polymorphic transformation of monoclinic to hexagonal  $\text{Cu}_6\text{Sn}_5$  and strain of the  $\text{Cu}_6\text{Sn}_5$  IMC layer formed at the interface of Cu/ $\text{Cu}_3\text{Sn}$ / $\text{Cu}_6\text{Sn}_5$ /Sn-0.7Cu solder joints by in-situ heating/isothermal while observing thick solder joint samples by high voltage transmission electron microscopy. Due to the polymorphic transformation from monoclinic to hexagonal, the strain has been accumulated

by volume changes that initiated at the grain boundary of the  $\text{Cu}_6\text{Sn}_5/\text{Sn}$  interface. This strain is a likely source of cracking of the  $\text{Cu}_6\text{Sn}_5$  in samples that cycle through this critical temperature range.

## **Acknowledgments**

This research has been conducted under an international cooperative research program between the University of Queensland, Australia, Kyushu University, and Nihon Superior Company Ltd., Japan. K. Nogita has been supported by the “UQ-KU Project”, which assists research collaborations between the University of Queensland and Kyushu University, during his visit at Kyushu University for high voltage TEM experiments. PXRD experiments were performed at the Australian Synchrotron Powder Diffraction Beamline (AS132/PD/5784). The authors greatly thank Dr. Qinfen Gu of Australian Synchrotron for technical assistance.

## References

1. M. Waldrop, *Nature* 530, 144-147 (2016).
2. H.-Y. Hsiao, C.-M. Liu, H.-w. Lin, T.-C. Liu, C.-L. Lu, Y.-S. Huang, C. Chen & K. N. Tu, *Science*, 336, 1007-1010 (2012).
3. D. Mu, S. D. McDonald, J. Read, H. Huang & K. Nogita, *Current Opinion in Solid State & Materials Science*, 20, 55-76 (2016).
4. H. Okamoto. Phase Diagrams of Dilute Binary Alloys. (ASM International, 2002).
5. K. Nogita, *Intermetallics*, 18, 145-149 (2010).
6. A.-K. Larsson, L. Stenberg & S. Lidin, *Acta Crystallographica*, B50, 636-643 (1994).
7. Y. Q. Wu, J. C. Barry, Y. T. Q. F. Gu, S. D. McDonald, S. Matsumura, H. Huang & K. Nogita, *Acta Mater.*, 60, 6581–6591 (2012).
8. K. Nogita & T. Nishimura, *Scripta Mater.*, 59, 191-194 (2008).
9. U. Schwingenschlögl, C. d. Paola, K. Nogita & C. M. Gourlay, *Appl. Phys. Lett.*, 96, 061908 (2010).
10. K. Nogita, C. M. Gourlay & T. Nishimura, *JOM*, 61, 45-51 (2009).
11. K. Nogita, C. M. Gourlay, S. D. McDonald, Y. Q. Wu, J. Read & Q. F. Gu, *Scripta Mater.*, 65, 922-925 (2011).
12. G. Zeng, S. D. McDonald, J. J. Read, Q. F. Gu & K. Nogita, *Acta Mater.*, 69, 135–148 (2014).
13. D. Mu, H. Tsukamoto, H. Huang & K. Nogita, *Mater. Sci. Forum*, 654-656, 2450-2454 (2010).
14. D. Mu, J. Read, Y.-F. Yang & K. Nogita, *J. Mater. Res.*, 26, 2660 - 2664 (2011).
15. D. Mu, H. Huang & K. Nogita, *Mater. Lett.*, 86, 46-49 (2012).
16. H. Tsukamoto, T. Nishimura & K. Nogita, *Mater. Lett.*, 63, 2687-2690 (2009).
17. D. Mu, H. Yasuda, H. Huang & K. Nogita, *J. Alloys Compd.*, 536, 38-46 (2012).
18. D. Mu, H. Huang, S. D. McDonald & K. Nogita, *J. Electron. Mater.*, 42, 304-311 (2013).
19. D. Mu, H. Huang, S. D. McDonald, J. Read & K. Nogita, *Mater. Sci. Eng., A*, 566, 126-133 (2013).
20. G. Zeng, S. D. McDonald, Q. F. Gu, Y. Terada, K. Uesugi, H. Yasuda & K. Nogita, *Acta Mater.*, 83, 357–371 (2015).
21. R. W. Cheary & A. Coelho, *J. Appl. Crystallogr.*, 25, 109-121 (1992).
22. E. A. Stach, T. Freeman, A. M. Minor, D. K. Owen, J. Cumings, M. A. Wall, T. Chraska, R. Hull, J. J.W. Morris, A. Zettl & U. Dahmen, *Microsc. Microanal.*, 7, 507-517 (2001).

23. T. Laurila, V. Vuorinen & J. K. Kivilahti, *Materials Science and Engineering R*, 49, 1-60 (2005).
24. G. Ghosh & M. Asta, *J. Mater. Res.*, 20, 3102-3117 (2005).

## Authors

**K. Nogita** is an associate professor and director of Nihon Superior Centre for the Manufacturing of Electronic Materials (NS CMEM) in the School of Mechanical and Mining Engineering at the University of Queensland (UQ), Australia and an invited professor at Kyushu University (KU), Japan. **M. A. A. Mohd Salleh** is a lecturer at Universiti Malaysia Perlis (UniMAP) and a PhD student at UQ. **E. Tanaka** is a senior research fellow at KU. **G. Zeng** was a PhD student at UQ and now is a Research Associate at the Department of Materials, Imperial College London, UK. **S. D. McDonald** is senior research fellow at UQ. **S. Matsumura** is a professor of Department of Applied Quantum Physics and Nuclear Engineering and director of The Ultramicroscopy Research Center, KU. **K. Nogita** can be reached at [k.nogita@uq.edu.au](mailto:k.nogita@uq.edu.au).

## **Chapter 5 Nucleation and growth behavior of primary intermetallics as an intrinsic reinforcing material in solder joints.**

This chapter focuses on the nucleation and growth behavior of primary intermetallics that form in the solder matrix. As primary  $\text{Cu}_6\text{Sn}_5$  crystals can be considered an intrinsic reinforcing material variations in their nucleation and growth behaviour in different solder alloys (Sn-0.7Cu and Sn-3.0Ag-0.5Cu) with and without the presence of Ni additions were analysed. In Paper 5 titled “In situ imaging of microstructure formation in electronic interconnections” the formation of primary  $\text{Cu}_6\text{Sn}_5$  in the solidification of Sn-0.7Cu and Sn-3.0Ag-0.5Cu was studied. Outstanding questions on how the solder joint microstructure develops in real soldering applications that are difficult to conclusively answer with post mortem studies were revealed by the in situ SXRI technique. This included the nucleation and growth of flux voids in soldering and the interaction of solder paste and the substrate, initial rapid wetting and nucleation of the interfacial  $\text{Cu}_6\text{Sn}_5$  intermetallics and interfacial voids during early soldering, nucleation location of time and nucleation growth rate of primary  $\text{Cu}_6\text{Sn}_5$  intermetallics in a solder joint during soldering and Sn dendrite nucleation during soldering solidification.

Paper 6 titled “Effect of Ni on the formation and growth of primary  $\text{Cu}_6\text{Sn}_5$  intermetallics in Sn-0.7wt%Cu solder pastes on Cu substrates during the soldering process” investigates the effect of 0.05 wt% Ni on the formation and growth of primary  $\text{Cu}_6\text{Sn}_5$  in Sn-0.7Cu solder paste soldered on a Cu substrate using a real-time synchrotron imaging technique. It was found that small additions of Ni significantly alter the formation and growth of the primary  $\text{Cu}_6\text{Sn}_5$  primary intermetallics making them smaller. In contrast, without Ni, primary  $\text{Cu}_6\text{Sn}_5$  primary intermetallics tend to continue growth throughout solidification and end up much larger and coarser. The effect of the Ni addition appears to be in promoting the nucleation of a larger number of small  $\text{Cu}_6\text{Sn}_5$  crystals. The results provide direct evidence of the sequence of events in the reaction of Ni containing Sn-0.7Cu solder pastes with a Cu substrate, and in particular the formation and growth of the primary  $\text{Cu}_6\text{Sn}_5$  intermetallic.

## **Paper 5: In situ imaging of microstructure formation in electronic interconnects**

Mohd Arif Anuar Mohd Salleh, Christopher M. Gurlay, Jing Wei Xian, Sergey A. Belyakov, Hideyuki Yasuda, Stuart D. McDonald, Kazuhiro Nogita

(Submitted to **Scientific Report** on the 5<sup>th</sup> June 2016 and currently under review)

## **In situ imaging of microstructure formation in electronic interconnections**

M.A.A. Mohd Salleh<sup>1,2,3\*</sup>, C.M. Gurlay<sup>3</sup>, J.W. Xian<sup>3</sup>, S.A. Belyakov<sup>3</sup>, H. Yasuda<sup>4</sup>, S.D.

McDonald<sup>1</sup>, K. Nogita<sup>1</sup>

<sup>1</sup>*Nihon Superior Centre for the Manufacture of Electronic Materials (NS CMEM), School of Mechanical and Mining Engineering, The University of Queensland, 4072 St Lucia, Queensland, Australia.*

<sup>2</sup>*Centre of Excellence Geopolymer and Green Technology, School of Materials Engineering, Universiti Malaysia Perlis (UniMAP), Taman Muhibbah 02600, Jejawi, Arau, Perlis, Malaysia.*

<sup>3</sup>*Department of Materials, Imperial College, London SW7 2AZ, United Kingdom.*

<sup>4</sup>*Department of Materials Science and Engineering, Kyoto University, Sakyo-ku, Kyoto 606-8501, Japan.*

## **Abstract**

The development of microstructure during melting, reactive wetting and solidification of solder pastes on Cu-plated printed circuit boards has been studied by synchrotron radiography. Using Sn-3.0Ag-0.5Cu/Cu and Sn-0.7Cu/Cu as examples, we show that the interfacial  $\text{Cu}_6\text{Sn}_5$  layer is present within 0.05 s of wetting, and explore the kinetics of flux void formation at the interface between the liquid and the  $\text{Cu}_6\text{Sn}_5$  layer. Quantification of the nucleation locations and anisotropic growth kinetics of primary  $\text{Cu}_6\text{Sn}_5$  crystals reveals a competition between the nucleation of  $\text{Cu}_6\text{Sn}_5$  in the liquid versus growth of  $\text{Cu}_6\text{Sn}_5$  from the existing  $\text{Cu}_6\text{Sn}_5$  layer. Direct imaging confirms that the  $\beta$ -Sn nucleates at/near the  $\text{Cu}_6\text{Sn}_5$  layer in Sn-3.0Ag-0.5Cu/Cu joints.



## Introduction

Microstructures are an important link between materials processing and performance, and microstructure control is essential for any materials processing route where the microstructure plays a major role in determining the properties<sup>1</sup>. In the application of electrical and electronic devices, Sn alloys are used widely as solder materials, joining one electrical connection to another. The interconnection microstructure can strongly affect the performance of a joint including the fatigue life during thermal cycling<sup>2</sup>, the tolerance to drop impacts<sup>3</sup> and the resistance to electromigration<sup>4</sup>. Hence, microstructure formation in solder joints is an important area of research<sup>5,6</sup> particularly considering the need to develop more advanced electronic joining technologies while meeting the global environmental demands required of Pb-free solder joints<sup>7,8</sup>.

In the last decades, characterization techniques for understanding microstructure development in a solidification process have advanced significantly with the development of 3rd generation synchrotron X-ray imaging techniques. This has enabled studies of Sn alloy solidification related to columnar and equiaxed dendritic growth, eutectic solidification, intermetallic growth behaviour and stresses and strain induced by phase transformations<sup>9-16</sup>. Furthermore, several studies have focussed on X-ray imaging of solder solidification during a solder reaction with a substrate such as Cu. In our previous study<sup>17,18</sup>, we reported on the formation of the  $\text{Cu}_6\text{Sn}_5$  interfacial layer at the liquid/Cu interface during the early stages of soldering and the effect of Ni on the growth of primary  $(\text{Cu,Ni})_6\text{Sn}_5$  in Sn-0.7Cu/Cu joints. In synchrotron studies of soldering solidification (with a substrate), Ma et al.<sup>19</sup> and Huang et al.<sup>20</sup> reported the observation of a morphology change of large  $\text{Ag}_3\text{Sn}$  plates in Sn-3.5Ag/Cu joints. In addition, Qu et al.<sup>21</sup> investigated thick interfacial  $\text{Cu}_6\text{Sn}_5$  layer growth at a late stage of soldering at 350 °C. Qu et al.<sup>22</sup> in another study investigated interfacial flux void formation in pure Sn and Sn-3.5Ag foils soldered on Cu. However, from existing synchrotron studies of solder reactions, the solder joint experiments were conducted at low frame rates (above 0.5 s per frame) and fast reactions during the soldering process, especially in the early stages of reactive wetting and subsequent solidification, were unable to be investigated. Previous synchrotron soldering experiments also used large volumes of solder and Cu foils as substrates, and small volumes of solder paste and substrates with a surface finish similar to industrial soldering have not been reported.

Although there have been many studies of microstructure formation in Pb-free solder joints by post mortem methods<sup>23-26</sup>, outstanding questions remain on how solder joint

microstructures develop in the soldering process that are difficult to conclusively answer using these techniques. For example, the nucleation and growth of flux voids in the solder paste during activation and early wetting and their interaction with solidification reactions during soldering are not well understood. There is limited information on the nucleation time of the interfacial  $\text{Cu}_6\text{Sn}_5$  intermetallic layer and interfacial voids, of the kinetics of primary  $\text{Cu}_6\text{Sn}_5$  solidification in solder joints, and of the  $\beta$ -Sn dendrite nucleation location in joints.

Here we conduct a synchrotron radiography investigation on the reflow of commercial solder pastes on FR-4 type printed circuit boards (PCBs), with Cu-plating and organic soldering preservative (OSP) surface finish, that mimics the solder reaction and solidification processes that occur in electronics manufacturing. This approach enables the direct observation and quantification of flux activation, solder paste melting, reactive wetting and flux void formation during heating to the peak temperature and then the nucleation and growth of primary intermetallic compounds (IMCs) and the point of  $\beta$ -Sn nucleation during solidification. We use Sn-3.0Ag-0.5Cu and Sn-0.7Cu (wt.%) solder pastes as case studies with a particular focus on quantifying the nucleation and growth kinetics of flux voids and primary  $\text{Cu}_6\text{Sn}_5$  crystals, understanding their formation mechanisms, and identifying the location of  $\beta$ -Sn nucleation.

## Results

**Reactive wetting and flux void development.** A typical example of the first moments of solder wetting and spreading is shown in Figure 1a-g for molten Sn-0.7Cu on Cu. Initially, in Figure 1a, the liquid is not in contact with the Cu substrate and, between the frames in Figure 1a and b, the liquid spreads from left to right over the Cu. Within 0.05 s of solder wetting, the dissolution of Cu from the substrate caused the formation of a  $\eta$ - $\text{Cu}_6\text{Sn}_5$  layer. Together with the formation of interfacial layer, interfacial voids were also present (Figure 1b). Subsequently, the layer develops a scalloped interface and the growth of interfacial solder voids is observed. Figure 1h is a post-mortem scanning electron microscopy image of the same sample which shows the interfacial  $\text{Cu}_6\text{Sn}_5$  layer and interfacial voids which formed during reactive wetting.

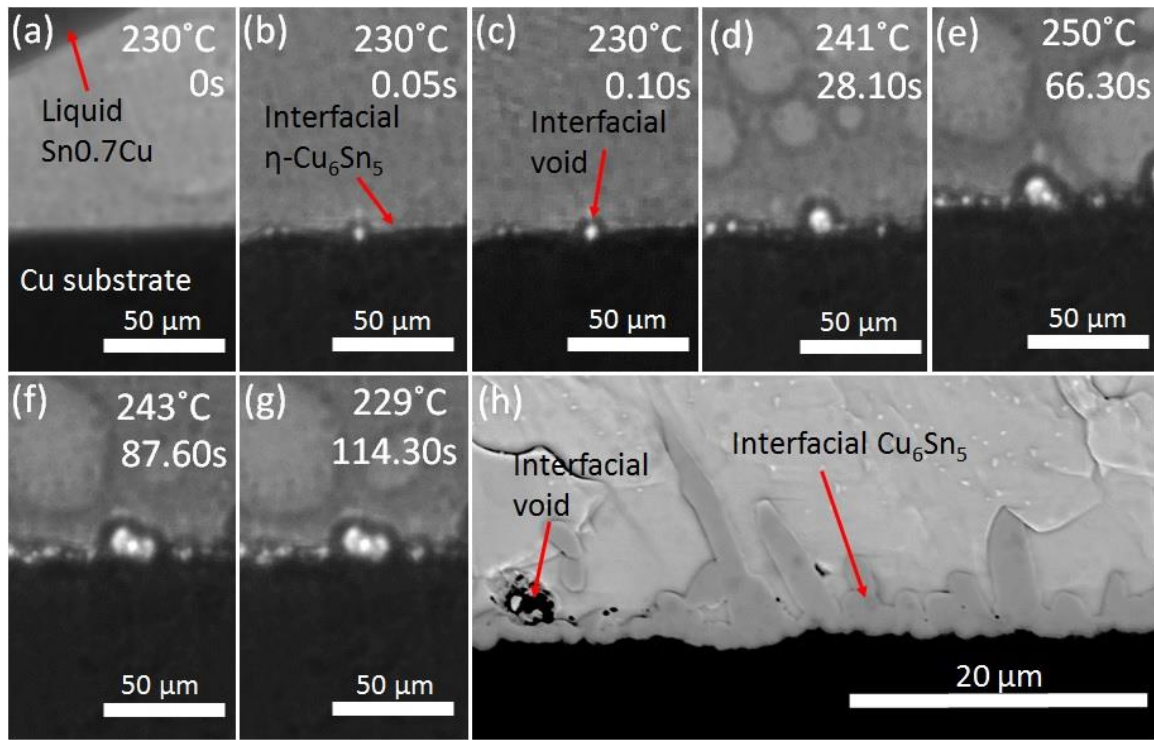


Figure 1: In situ real time imaging observations of interfacial  $\text{Cu}_6\text{Sn}_5$  formation during early wetting reactions between liquid Sn-0.7Cu and the Cu substrate interface at (a) 0 s, (b) 0.05 s, (c) 0.10 s, (d) 28.10 s, (e) 66.30 s, (f) 87.60 s and (g) 114.30 s times after wetting: (h) a post mortem backscattered electron scanning electron microscopy (SEM) image of the solidified sample.

Figure 2a shows the solder paste on the Cu-plated PCB at the first moment of solder melting. The individual  $\sim 35\mu\text{m}$  grains of solder powder can be seen suspended in flux. Figure 2a shows the first moment of melting. There are a number of voids/bubbles in the paste and at the paste-Cu interface which exist from the first moments of melting. These are mostly caused by flux outgassing<sup>17,24</sup>. At the stage shown in Figure 2a, the voids have an irregular shape and are present between the solid solder grains. As the solder paste fully melts in Figure 2a,b and c, the voids develop into a spherical shape to minimise their interfacial area with the molten solder. Figure 2b is a snapshot during solder paste melting where both liquid solder and unmelted solder powder coexist. In the first few seconds after melting (Figure 2b-d), many flux voids first become more spherical and then float up and out of the solder ball due to buoyancy. However, comparing Figure 2b-f, it can be seen that the flux voids at the solder-substrate interface do not float upwards despite being significantly less dense than the liquid solder.

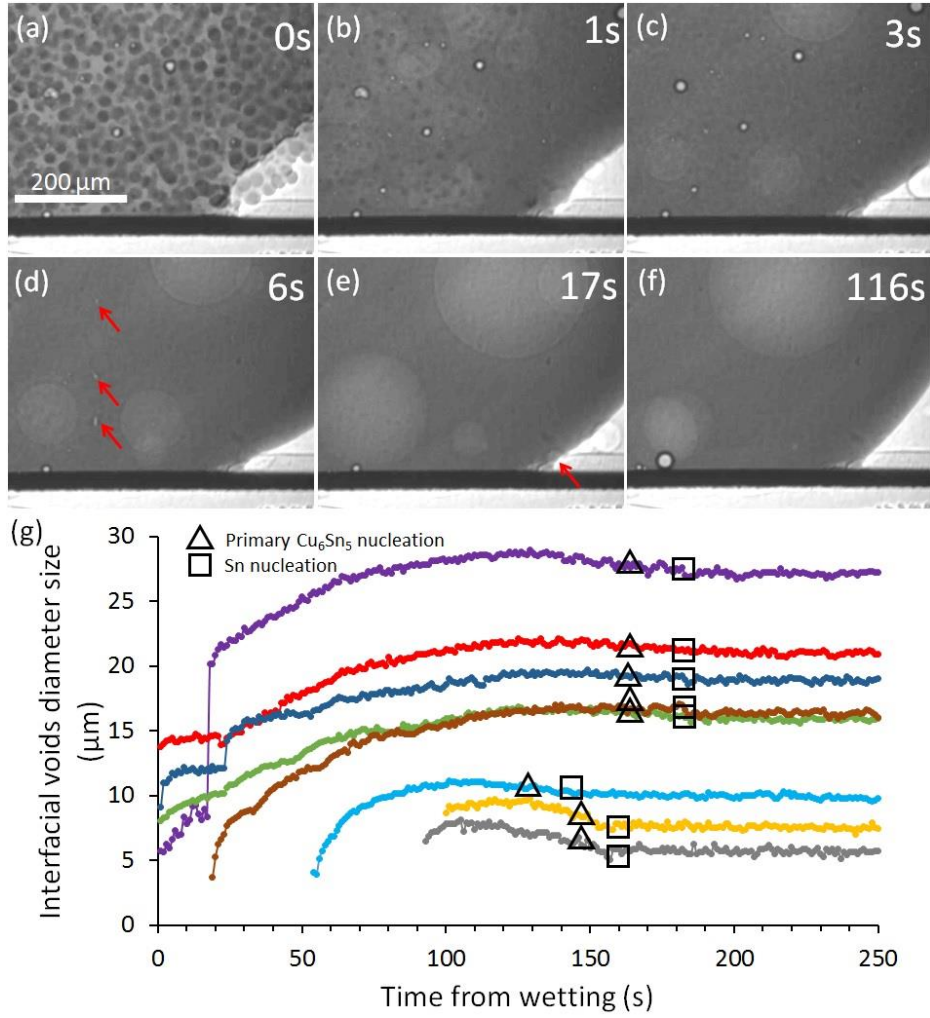


Figure 2: (a-f) Synchrotron image sequence of the flux void formation during early wetting of Sn-0.7Cu paste on a Cu substrate and (g) quantification of interfacial voids size (diameter) formation and growth in Sn-0.7Cu paste during soldering from synchrotron image sequences (compilation from several experiments where different colours indicates different flux voids).

A bubble is expected to remain attached to the Cu<sub>6</sub>Sn<sub>5</sub> layer if the balance of interfacial energies satisfies the following inequality (assuming for simplicity that there is only a small contact area between the bubble and interfacial intermetallic compound (IMC) so that the bubble shape is unchanged):

$$\gamma_{IMC-g} < \gamma_{L-g} + \gamma_{IMC-L} \quad (1)$$

Where  $\gamma$  is the interfacial Gibbs energy per unit area (IMC-g refers to intermetallic compound layer and flux void interface, L-g refers to liquid solder and flux void interface and IMC-L refers to intermetallic compound layer and liquid solder interface). This inequality is likely to

be met given the relatively high interfacial energy between liquid Sn and  $\text{Cu}_6\text{Sn}_5$ . The total interfacial energy would be even lower if bubbles were located in the grooves between the  $\text{Cu}_6\text{Sn}_5$  scallops. Therefore, they would be partially stabilised against a buoyancy force in these locations. This appears to be the origin of the difficulty of removing flux voids from the solder-substrate interface. It can also be seen in Figure 2e-f, that the size of the interfacial flux voids increases with time and that new voids nucleate and grow at the  $\text{Cu}_6\text{Sn}_5$ -L interface between 17 and 116 s after the onset of melting. Figure 2g is a compilation plot showing the diameter of interfacial flux voids as a function of the time from wetting. Note that the measurements were gathered from several Sn-0.7Cu/Cu synchrotron imaging experiments. From this plot, it can be seen that some interfacial flux voids of 5-15  $\mu\text{m}$  were observed from the moment of wetting and that further flux voids nucleate later as the joint is heated towards the peak reflow temperature. All observable interfacial voids grow rapidly to a size of at least 4  $\mu\text{m}$  in diameter and then continue to expand (maximum expansion near peak temperature  $\sim 250^\circ\text{C}$ ) and then contract during cooling. Towards the end of contracting, a sudden slight increase (approximately 1%) in their size was observed coinciding with the  $\beta$ -Sn nucleation event, which is associated with solidification shrinkage as the undercooled liquid solidifies within a few frames. Subsequently, it can be seen that the flux void sizes remain constant after  $\beta$ -Sn nucleation when they are surrounded by solid.

Similar interfacial flux voids formed in all experiments, as can be seen in Figures 1, 3 and 4. In some experiments, bubbles of evaporated flux continuously formed near the air-solder-substrate triple points, were transported upwards along the sides of the solder ball and then floated away. Examples of this are highlighted with arrows in Figure 2e. Note that the large round features near the centre of the solder balls in Figures 1-4 are shallow bubbles between the sample and the quartz confining sheets. These are artifacts of the experiment and form even without flux and will not be discussed further.

**Nucleation and growth of primary  $\text{Cu}_6\text{Sn}_5$  crystals.** Figure 3a-3e and Figure 4a-4e, show the development of primary  $\text{Cu}_6\text{Sn}_5$  during continuous cooling from the peak temperature of  $250^\circ\text{C}$  in Sn-3.0Ag-0.5Cu/Cu and Sn-0.7Cu/Cu respectively. On both figures, the central round features are shallow bubbles (artifacts) while the round features at the Sn/ $\text{Cu}_6\text{Sn}_5$ /Cu interface are flux voids. The dark rods in the solder ball are primary  $\text{Cu}_6\text{Sn}_5$  and the tin liquid is slightly brighter. Figure 3f and 4f are processed images where each  $\text{Cu}_6\text{Sn}_5$  crystal has been segmented and colored by its nucleation time to visualise the sequence of nucleation events. In Sn-3.0Ag-0.5Cu/Cu, many  $\text{Cu}_6\text{Sn}_5$  grew from the edge (the side surface) of the

solder ball into the liquid as observed in Figure 3a-c and in Figure 3f (dark blue). Other  $\text{Cu}_6\text{Sn}_5$  crystals appear to nucleate in the bulk liquid but note that there are also solder surfaces perpendicular to the x-ray beam. The  $\text{Cu}_6\text{Sn}_5$  nucleation location can be inferred from the observation that the crystals did not move under gravity despite being significantly denser than liquid Sn ( $8,082$  vs  $6,967 \text{ kg/m}^3$  at  $250^\circ\text{C}$ <sup>27,28</sup>). This suggests that the  $\text{Cu}_6\text{Sn}_5$  crystals nucleated on the surface or on particles attached to the surface (possibly on the oxide where the SnO-L interfacial energy is relatively high) in both Sn-3.0Ag-0.5Cu/Cu and Sn-0.7Cu/Cu joints. Also it can be observed from the colour maps in Figure 3f and 4f that the nucleation sequence of primary  $\text{Cu}_6\text{Sn}_5$  in both materials bears no detectable relationship to the small temperature gradient of  $\sim 1 \text{ K}$  (from the top to bottom of the field of view) and nucleation events do not follow an isotherm sweeping through the sample.

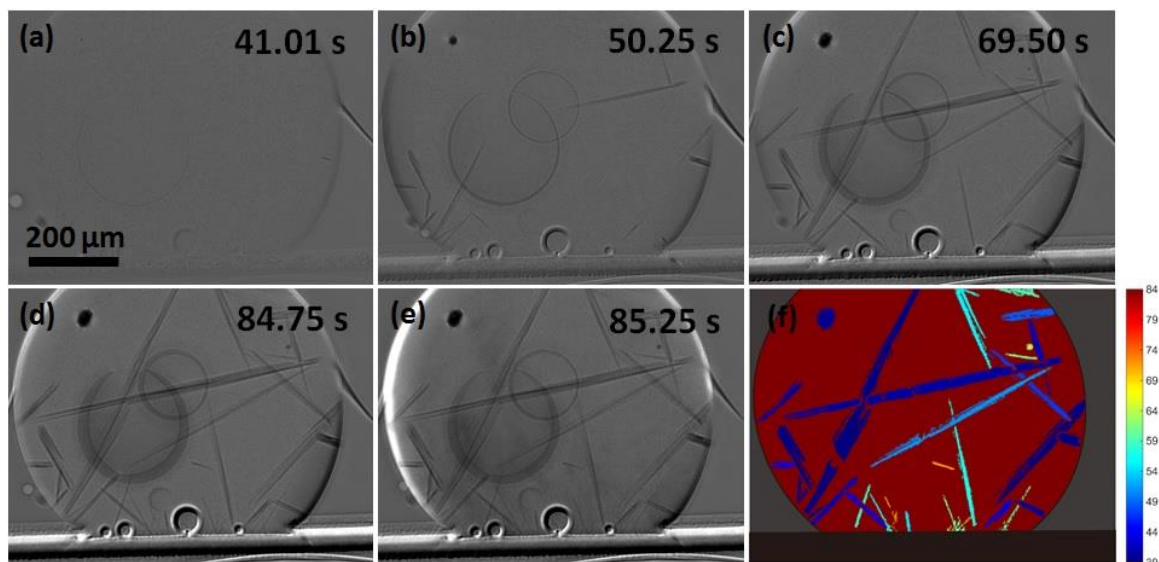


Figure 3: Synchrotron image sequence of the nucleation and growth of primary  $\text{Cu}_6\text{Sn}_5$  in a Sn-3.0Ag-0.5Cu/Cu joint. Images have been normalised against a frame shortly before that in (a).  $\text{Cu}_6\text{Sn}_5$  are dark. The two central round features are bubbles. The round features at the  $\text{Cu}_6\text{Sn}_5$  interfacial layer are flux voids. (f) a processed image with each  $\text{Cu}_6\text{Sn}_5$  segmented and coloured by its nucleation time in s.  $t=0$  is the onset of cooling from the peak temperature of  $250^\circ\text{C}$ .



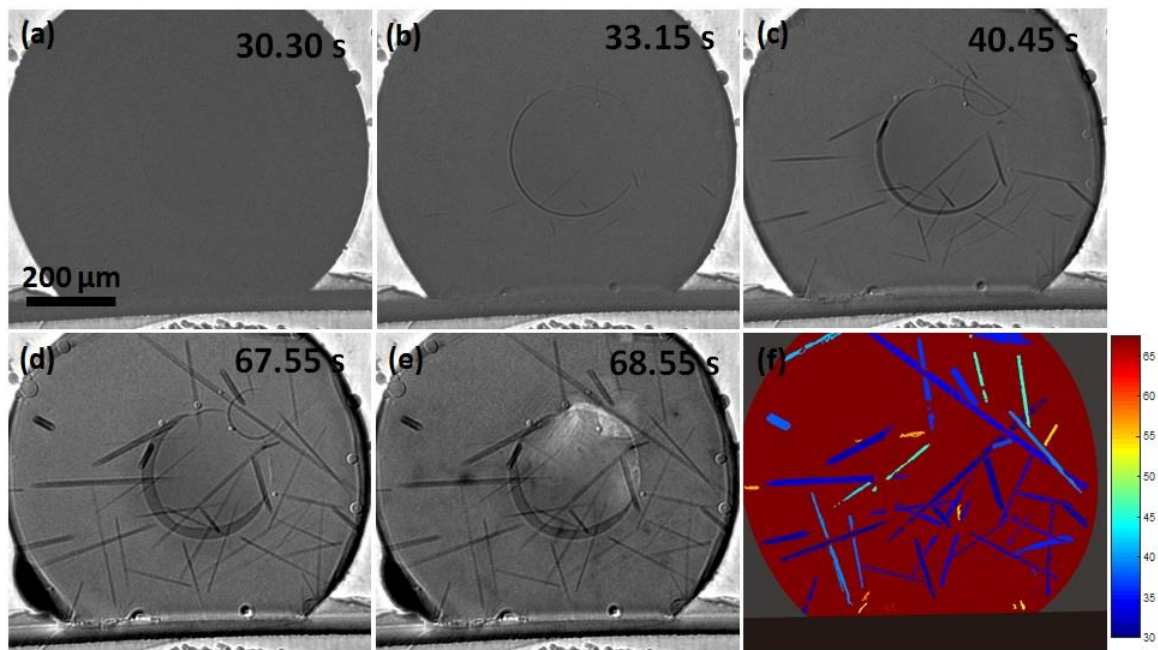


Figure 4: Synchrotron image sequence of the nucleation and growth of primary  $\text{Cu}_6\text{Sn}_5$  in a Sn-0.7Cu/Cu joint. Images have been normalised against a frame shortly before that in (a).  $\text{Cu}_6\text{Sn}_5$  are dark. The central round feature is a bubble. The round features at the  $\text{Cu}_6\text{Sn}_5$  interfacial layer are flux voids. (f) is a processed image with each  $\text{Cu}_6\text{Sn}_5$  segmented and coloured by its nucleation time in s.  $t=0$  is the onset of cooling from the peak temperature of 250°C.

The solidification kinetics of all primary  $\text{Cu}_6\text{Sn}_5$  crystals in a joint of Sn-3.0Ag-0.5Cu/Cu and Sn-0.7Cu/Cu are quantified in Figure 5. Since the primary  $\text{Cu}_6\text{Sn}_5$  crystals grew as faceted rods without branching, their growth could be quantified by a single vector. Figure 5a and 5d are plots of  $\text{Cu}_6\text{Sn}_5$  growth vectors and Figure 5b and 5e are similar plots using a single origin. They show that there is no preferred  $\text{Cu}_6\text{Sn}_5$  growth direction which is consistent with growth from randomly oriented nucleation sites.

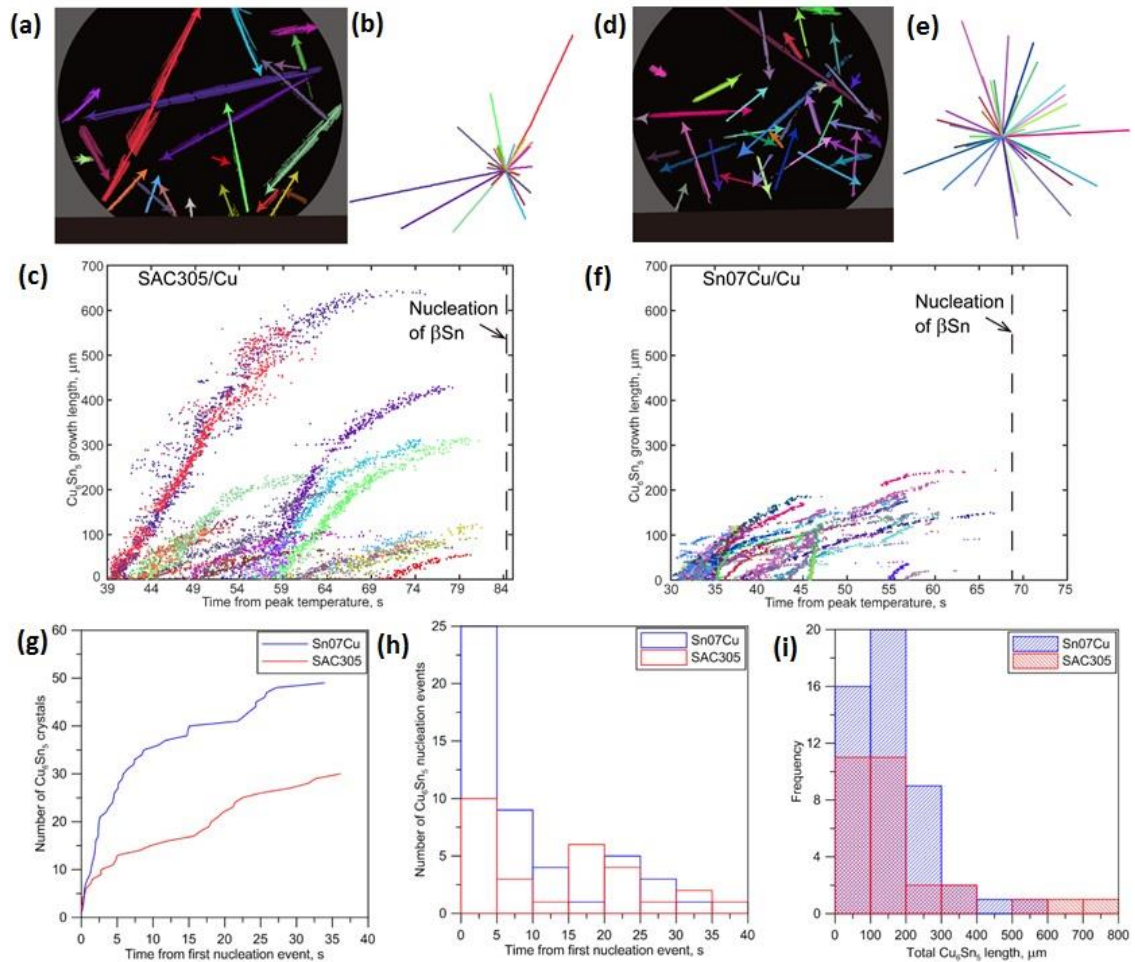


Figure 5: Quantification of the solidification kinetics of primary  $\text{Cu}_6\text{Sn}_5$  crystals from the synchrotron image sequences in Figures 3 and 4. (a)-(c) Sn-3.0Ag-0.5Cu/Cu. (d)-(f) Sn-0.7Cu/Cu. (a) and (d):  $\text{Cu}_6\text{Sn}_5$  growth vectors. (b) and (e): the same vectors with a common origin showing the growth orientation distribution. (c) and (f): the growth tip position versus time for most  $\text{Cu}_6\text{Sn}_5$  crystals in each sample. (g) total number of  $\text{Cu}_6\text{Sn}_5$  crystals versus time for each joint. (h) histogram of the number of  $\text{Cu}_6\text{Sn}_5$  nucleation events with time. (i) size distribution of the primary  $\text{Cu}_6\text{Sn}_5$  crystals at the end of solidification in both joints.

Figure 5c and 5f are plots of the growth length of primary  $\text{Cu}_6\text{Sn}_5$  crystals as a function of time, where Figure 5a, b and c have a common  $\text{Cu}_6\text{Sn}_5$  colour scale as do Figure 5d, e and f. Here, 'growth length' is the distance from the nucleation point to the growth tip along the main [0001] growth direction. In the Sn-3.0Ag-0.5Cu/Cu joint, the first two  $\text{Cu}_6\text{Sn}_5$  crystals grew with a near-constant tip velocity of  $9.8 \mu\text{m/s}$  for  $\sim 600 \mu\text{m}$  before slowing down due to solute field interaction with surrounding growing  $\text{Cu}_6\text{Sn}_5$  crystals. Most other  $\text{Cu}_6\text{Sn}_5$  crystals in Figure 5c exhibited nonlinear growth from immediately after nucleation because the existing  $\text{Cu}_6\text{Sn}_5$  led to overlapping solute fields reducing the tip undercooling. In the Sn-



0.7Cu/Cu joint, there was little linear growth (Figure 5f) because crystals nucleated in close proximity and solute fields overlapped early during growth.

Figure 5g shows the number of  $\text{Cu}_6\text{Sn}_5$  crystals versus time, Figure 5h is a plot of the number of  $\text{Cu}_6\text{Sn}_5$  nucleation events versus time, and Figure 5i shows the distribution of final lengths of  $\text{Cu}_6\text{Sn}_5$  crystals for both joints. Combining Figure 5g-i, it is clear that  $\text{Cu}_6\text{Sn}_5$  rods are more numerous and, generally, shorter in Sn-0.7Cu/Cu joints than in Sn-3.0Ag-0.5Cu/Cu joints. Some understanding of the origin of more primary  $\text{Cu}_6\text{Sn}_5$  nucleation events in Sn-0.7Cu/Cu can be gained from the predicted solidification path in Figure 6, which assumes that dissolution of the substrate occurs until the liquid solder is uniformly saturated in Cu. It can be seen that a slightly higher fraction of primary  $\text{Cu}_6\text{Sn}_5$  is predicted to form in Sn-3.0Ag-0.5Cu/Cu than in Sn-0.7Cu/Cu for the same  $\beta$ -Sn nucleation undercooling. The growth restriction factor (GRF)<sup>29</sup> can be deduced directly from the T vs  $f_s$  plots because it can be expressed as  $-\left(\frac{\partial T}{\partial f_s}\right)_{f_s \rightarrow 0}$  (2). Since the T vs  $f_s$  slope is slightly steeper near  $f_s=0$  in Sn-0.7Cu/Cu, it can be seen that the GRF is higher for this joint. Thus, a given level of constitutional supercooling develops in a shorter  $\text{Cu}_6\text{Sn}_5$  growth distance in Sn-0.7Cu/Cu compared with Sn-3.0Ag-0.5Cu/Cu which would enable nucleation events to occur closer together in Sn-0.7Cu/Cu.

Note that the only primary intermetallic phase observed in this work was  $\text{Cu}_6\text{Sn}_5$  (i.e.  $\text{Ag}_3\text{Sn}$  primary crystals were never observed in Sn-3.0Ag-0.5Cu/Cu joints). This can be understood from the predicted solidification path in Figure 6: primary  $\text{Ag}_3\text{Sn}$  are not predicted to form until below  $\sim 198^\circ\text{C}$  ( $\Delta T_{\text{nuc}} \sim 19\text{K}$ ). For joints of the size studied in this work soldered to Cu, it is common for the nucleation undercooling for  $\beta$ -Sn to be less than  $19\text{K}$ <sup>30</sup>. This interpretation was confirmed in our laboratory studies in which primary  $\text{Ag}_3\text{Sn}$  only formed in Sn-3.0Ag-0.5Cu/Cu joints at undercoolings higher than  $20\text{K}$  (refer to supplementary data).

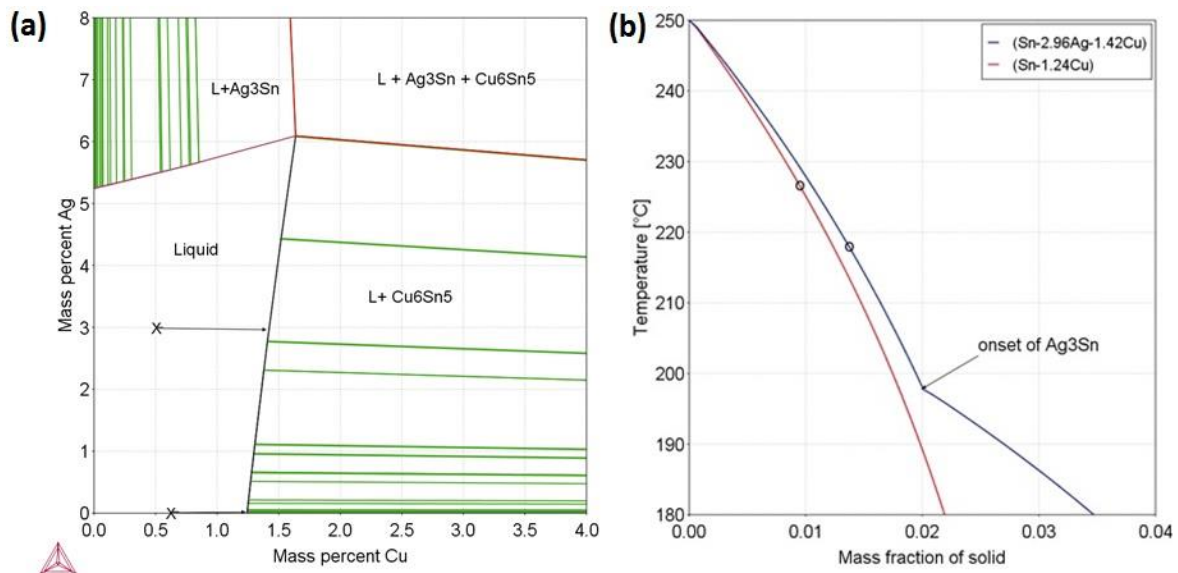


Figure 6: (a) Sn-Ag-Cu 250°C isothermal section based on Thermocalc<sup>29</sup>. Crosses mark the initial solder compositions and the arrows show the change in liquid composition due to Cu substrate dissolution (up to the solubility limit). (b) Predicted development of primary IMC during cooling from 250°C in Sn-3.0Ag-0.5Cu/Cu and Sn-0.7Cu/Cu joints, assuming the liquid was saturated in Cu at 250°C. The circles show the equilibrium eutectic onset temperatures and, below these temperatures, primary Cu<sub>6</sub>Sn<sub>5</sub> only continues to grow if  $\beta$ -Sn fails to nucleate. Note that, in Sn-3.0Ag-0.5Cu/Cu, primary Ag<sub>3</sub>Sn crystals are not predicted to form until  $\sim 198^\circ\text{C}$  ( $\Delta T_{\text{nuc}} \sim 19\text{K}$ ).

In Figure 5h, the highest nucleation rate occurs at the beginning of primary Cu<sub>6</sub>Sn<sub>5</sub> solidification. However, in both joints, the number of Cu<sub>6</sub>Sn<sub>5</sub> crystals continuously increases during cooling from the peak temperature almost until the nucleation of  $\beta$ -Sn. That is to say, nucleation occurred continuously during cooling and did not only occur in the first stages of cooling as commonly occurs in the solidification of alloys<sup>31</sup>. One reason for this appears to be the highly anisotropic faceted growth mechanism of Cu<sub>6</sub>Sn<sub>5</sub>, where this crystal only grows along [0001] and does not branch (under the conditions of the paper). Thus, Cu<sub>6</sub>Sn<sub>5</sub> cannot grow into liquid regions that are not in the [0001] growth path and constitutional supercooling builds up in these liquid regions until it exceeds the required nucleation undercooling for Cu<sub>6</sub>Sn<sub>5</sub>, when a new nucleation event is triggered. This effect is compounded by the high GRF of Cu<sub>6</sub>Sn<sub>5</sub> in Sn-rich compositions which causes a large constitutional supercooling to develop in a relatively short growth distance. Thus, due to the combined high growth anisotropy and GRF, it is easier for new Cu<sub>6</sub>Sn<sub>5</sub> crystals to nucleate in the liquid than it is for existing Cu<sub>6</sub>Sn<sub>5</sub> to branch during growth, which causes continuous nucleation during cooling in a near-uniform thermal field.

In some samples, some primary  $\text{Cu}_6\text{Sn}_5$  also grew from the pre-existing  $\text{Cu}_6\text{Sn}_5$  reaction layer as shown in Figure 7c-g for Sn-3.0Ag-0.5Cu/Cu. This shows that there is competition between primary  $\text{Cu}_6\text{Sn}_5$  nucleation in the liquid versus  $\text{Cu}_6\text{Sn}_5$  growth from the  $\text{Cu}_6\text{Sn}_5$  reaction layer. For example, as shown in Figure 3, late during solidification of the Sn-3.0Ag-0.5Cu/Cu between 50.25 s – 84.75 s of cooling time, some  $\text{Cu}_6\text{Sn}_5$  crystals grew upwards from the pre-existing  $\text{Cu}_6\text{Sn}_5$  layer (turquoise and orange crystals in Figure 5(c) and (f)). Note also that other  $\text{Cu}_6\text{Sn}_5$  crystals grew from elsewhere down into the layer in the same time period and, from the post mortem SEM images in Figure 7a and 7b, it is often not possible to deduce whether primary  $\text{Cu}_6\text{Sn}_5$  grew into the layer or grew out from the layer, which highlights the importance of in-situ imaging.

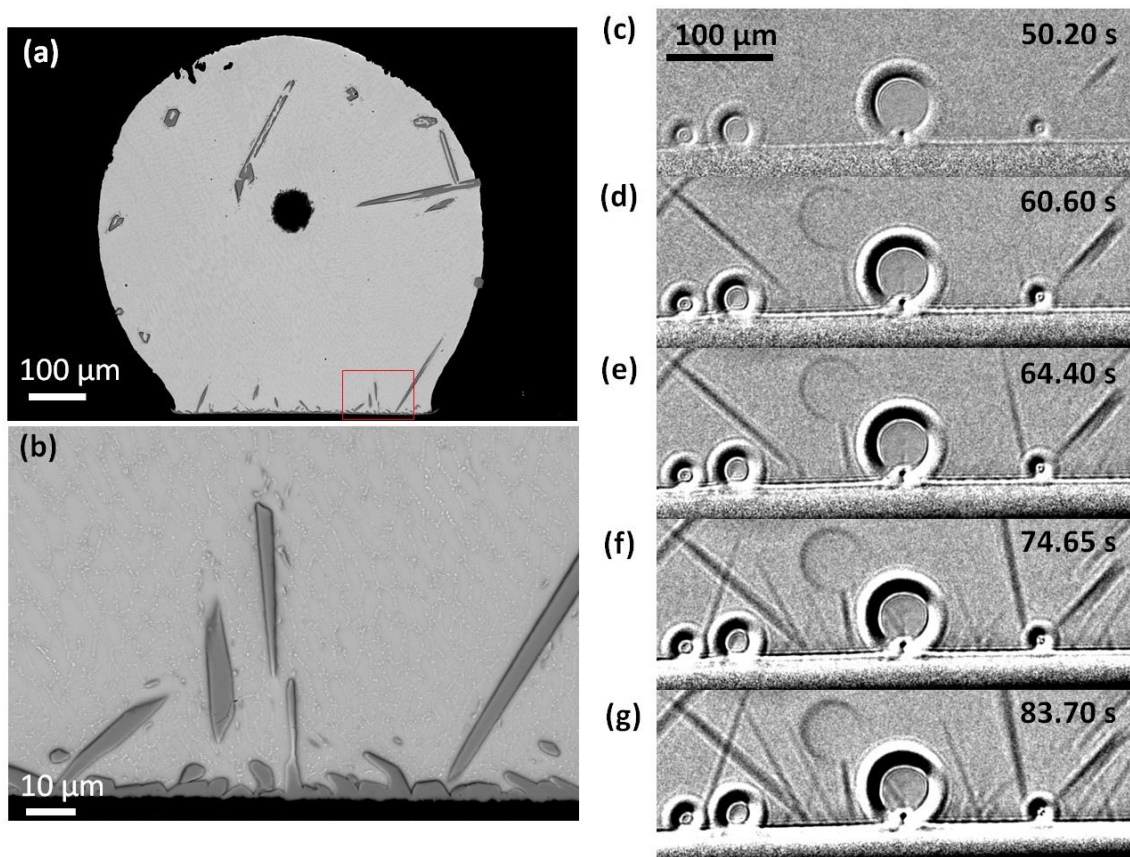


Figure 7: Growth of primary  $\text{Cu}_6\text{Sn}_5$  on Sn-3.0Ag-0.5Cu/Cu near the interfacial intermetallic compound (IMC) layer later during solidification (a)-(b) post-mortem SEM images. (c)-(g) in-situ synchrotron images at five different times.

The growth of  $\text{Cu}_6\text{Sn}_5$  out from the layer produces long IMC protrusions that are undesirable and potentially harmful to reliability. In Sn-Ag-Cu/Cu-OSP solder joints after drop impact testing, Pang<sup>32</sup> reported that the crack path could occur either near the Cu- $\text{Cu}_6\text{Sn}_5$  interface, the Sn-Ag-Cu- $\text{Cu}_6\text{Sn}_5$  interface, or in the middle of the  $\text{Cu}_6\text{Sn}_5$ . After 500 cycles of thermal

cyclic testing, drop impact tests indicated that the dominant cracking was observed in the  $\text{Cu}_6\text{Sn}_5$  interfacial layer<sup>32</sup>. In addition, Tian et al.<sup>33</sup> have proven that long primary  $\text{Cu}_6\text{Sn}_5$  crystals in the bulk solder joint were the crack sources during in-situ tensile tests of Sn-3Ag-0.5Cu/Cu after multiple reflows. Thus, it is important to understand the conditions under which  $\text{Cu}_6\text{Sn}_5$  grows out from the layer and methods to prevent it. It was found that samples where  $\text{Cu}_6\text{Sn}_5$  grew out from the layer usually had a region of open liquid ahead of the layer relatively late during primary  $\text{Cu}_6\text{Sn}_5$  solidification. Open liquid regions remain when no or few primary  $\text{Cu}_6\text{Sn}_5$  rods have their [0001] growth direction oriented towards the IMC layer (e.g. Figure 3). In this situation, new  $\text{Cu}_6\text{Sn}_5$  can only nucleate in the liquid ahead of the layer if the constitutional supercooling in this region exceeds the required nucleation undercooling. This is less likely in the solute field ahead of the growing  $\text{Cu}_6\text{Sn}_5$  layer than in the liquid far from the layer, and becomes even less likely late during cooling when the solute fields of surrounding primary  $\text{Cu}_6\text{Sn}_5$  have impinged on the solute field of the  $\text{Cu}_6\text{Sn}_5$  layer. When the nucleation of new primary  $\text{Cu}_6\text{Sn}_5$  crystals are suppressed in this way, the conditions exist for  $\text{Cu}_6\text{Sn}_5$  to grow out from the existing  $\text{Cu}_6\text{Sn}_5$  layer. The development of open liquid regions ahead of the  $\text{Cu}_6\text{Sn}_5$  layer is more likely when there are few, large  $\text{Cu}_6\text{Sn}_5$  rods (such as in Figure 3) because this increases the chance that a few  $\text{Cu}_6\text{Sn}_5$  rods will have a [0001] direction towards the layer. On the other hand,  $\text{Cu}_6\text{Sn}_5$  can be prevented from growing out from the layer by encouraging numerous small  $\text{Cu}_6\text{Sn}_5$  to nucleate throughout the liquid (with numerous growth directions) so that no large liquid region develops ahead of the interfacial IMC layer into which layer crystals need to grow (e.g. for Sn-0.7Cu/Cu in Figure 4a-f).

**$\beta$ -Sn nucleation and growth.** Although the in-situ imaging technique used here was not optimized for the high interface velocities after  $\beta$ -Sn nucleates, useful information could still be extracted. The nucleation location of  $\beta$ -Sn in Sn-3.0Ag-0.5Cu/Cu joints was observed to be at/near the interfacial  $\text{Cu}_6\text{Sn}_5$  layer as indicated by the red arrow towards the top (Figure 8a-8c). This has been inferred in previous ‘post mortem’ work<sup>30,34</sup> but here we directly prove that  $\beta$ -Sn nucleates on or near the  $\text{Cu}_6\text{Sn}_5$  layer in Sn-3.0Ag-0.5Cu/Cu joints. The subsequent growth of the  $\beta$ -Sn dendrite can be seen by comparing Figure 8a, b and c where the dendrite growth velocity was measured to be around 800  $\mu\text{m/s}$  early during growth. Post-mortem EBSD mapping in Figure 8d shows that there is a single  $\beta$ -Sn crystal in the joint. Comparing the EBSD inverse pole figure (IPF) map with the BSE-SEM image in Figure 8e shows that the dendrite growth direction is close to  $\langle 110 \rangle$ . With the knowledge of the nucleation location (the start of the red arrow in Figure 8a-f), the  $\beta$ -Sn primary dendrite arm



spacing was measured as a function of growth distance. The primary dendrite arm spacing increases from around 10  $\mu\text{m}$  at the nucleation location to 300  $\mu\text{m}$  at the maximum distance from nucleation (Figure 8g), which is consistent with the dendrite tip velocity decreasing during growth into an undercooled melt due to the release of latent heat and consequent decrease in tip growth undercooling<sup>24,35,36</sup>. Previous research has shown that Sn-3.0Ag-0.5Cu/Cu joints usually solidify with one  $\beta$ -Sn orientation or two or three  $\beta$ -Sn orientations that are all related by a twin orientation relationship<sup>30,34,37,38</sup>. The presence of a single  $\beta$ -Sn orientation in Figure 8 is consistent with this.

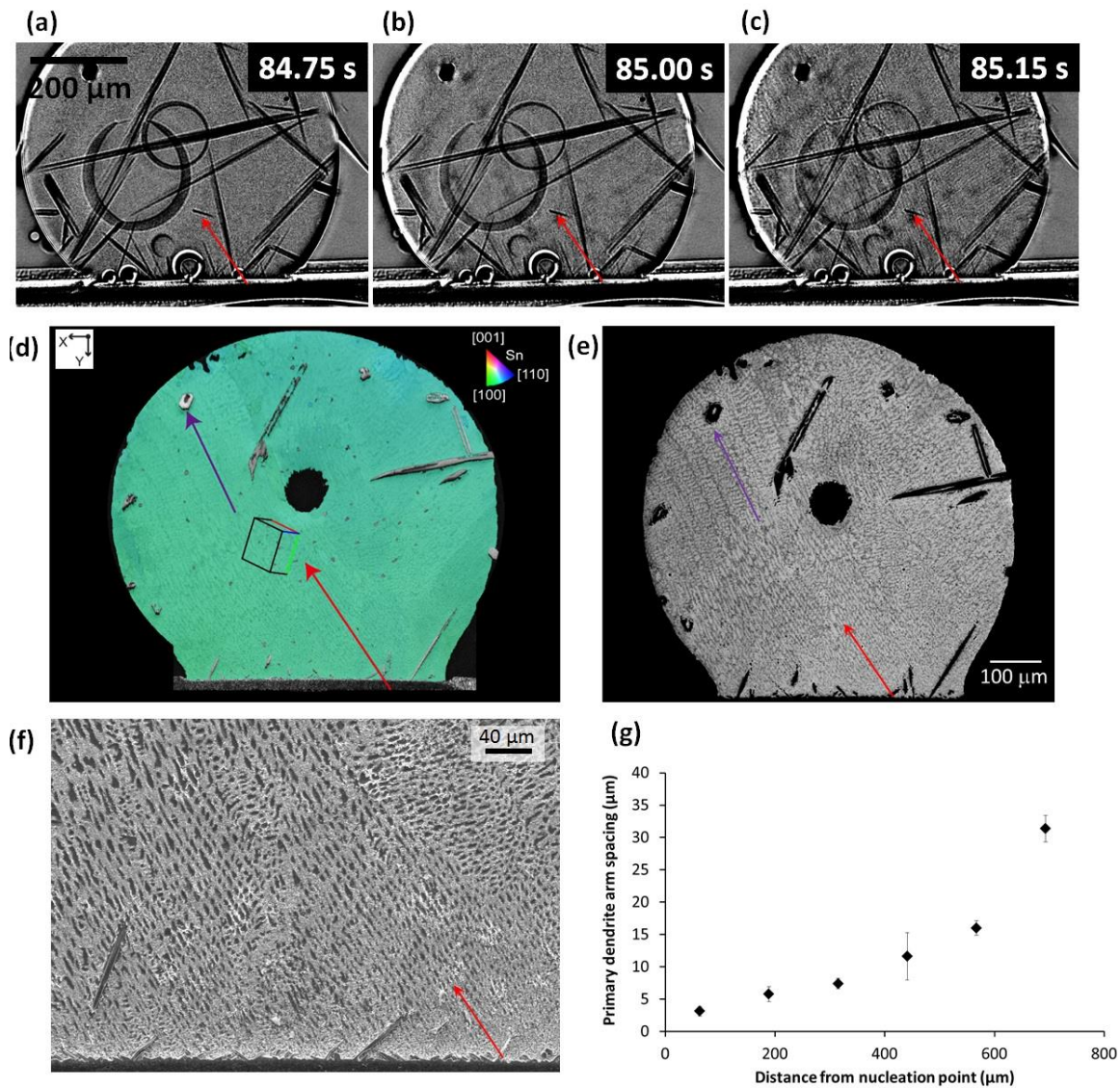


Figure 8: (a) - (c) Synchrotron images of the nucleation and growth of  $\beta$ -Sn in the Sn-3.0Ag-0.5Cu/Cu joint. (d) EBSD inverse pole figure (IPF)-y map of the Sn-3.0Ag-0.5Cu/Cu joint with the unit cell orientation superimposed. (e) BSE-SEM image in which the  $\beta$ -Sn dendrite growth direction can be deduced. Arrows show the growth direction in two regions projected onto the imaging plane. (f) BSE-SEM image of dendrites near the

nucleation site. (g) plot of primary dendrite arm spacing versus distance from the observed nucleation point.

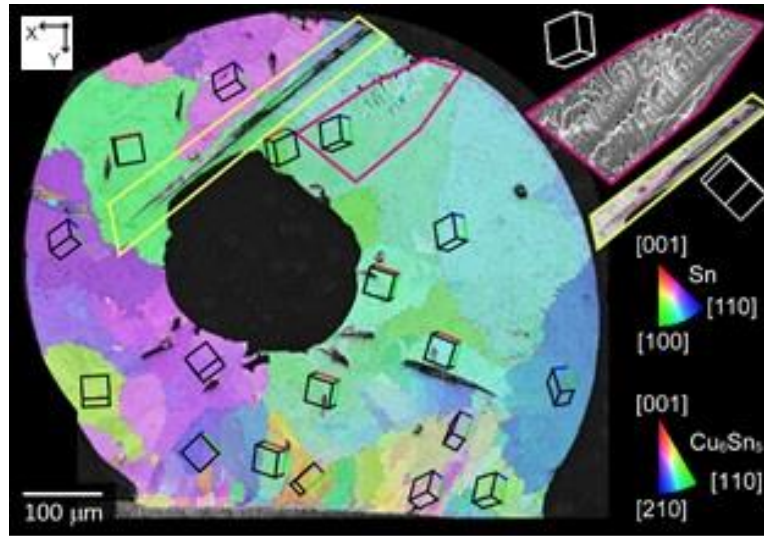


Figure 9: EBSD inverse pole figure (IPF)-y map of the Sn-0.7Cu/Cu joint with unit cell orientations superimposed. The inserts show the  $\beta$ -Sn dendrite morphology relative to its unit cell orientation, and a primary  $\text{Cu}_6\text{Sn}_5$  rod relative to its unit cell orientation.

For the Sn-0.7Cu/Cu joint, EBSD mapping showed multiple  $\beta$ -Sn crystal orientations and no evidence of solidification twinning (Figure 9). A dendrite near the upper surface, highlighted by the insert, is growing almost in the sectioning plane and has a dendrite growth direction close to  $\langle 110 \rangle$ , similar to the Sn-3.0Ag-0.5Cu/Cu joint in Figure 8. The other insert confirms that the  $\text{Cu}_6\text{Sn}_5$  rods are oriented along [0001]. The larger number of  $\beta$ -Sn orientations and wider range of misorientation angles in Figure 9 than Figure 8 is a significant difference between Sn-0.7Cu/Cu and Sn-3.0Ag-0.5Cu/Cu joints, that occurs both in these in-situ experiments and other BGA studies<sup>30,37</sup>.

In summary, using time-resolved synchrotron X-ray radiography adapted to mimic the paste reflow soldering process, nucleation events and microstructure evolution which cannot be deduced from post-mortem methods have been revealed and quantified during soldering solidification. The elucidation of solder joint microstructure development revealed in this study could be used as a basis for the design of an optimized and controlled microstructure in solder joints for future electronic interconnects technology.

## Methods

**Sample preparation.** Sn-0.7Cu and Sn-3.0Ag-0.5Cu (wt.%) solder pastes with 35  $\mu\text{m}$  average solder sphere diameter were used. A Cu plated printed circuit board (Fire retardant-FR-4 type) with 600  $\mu\text{m}$  ball pitch size was cross sectioned to produce a Cu-OSP substrate suitable for radiography with 100  $\mu\text{m}$  thickness and 600  $\mu\text{m}$  wide pitch. A small amount of solder paste (approximately 0.0002 g) was placed on the Cu pad in a cavity within a 100  $\mu\text{m}$  thick polytetrafluoroethylene (PTFE) spacer sheet with an observation window of 10 x 10  $\text{mm}^2$  and a vent for flux outgassing. Finally, the paste, substrate and PTFE were secured between two quartz plates. Further details, including a figure of the materials and sample preparation are given in the Supplementary Figure 2.

**Synchrotron X-ray Imaging.** Experiments were conducted at BL20XU in the SPring-8 synchrotron using the solidification observation setup developed in previous research<sup>14,39</sup> and an X-ray energy of 21 keV. Transmitted images were converted into visible light and recorded in a digital format with 2,000 X 2,000 pixels representing a 1 mm X 1 mm field of view giving a resolution of 0.477  $\mu\text{m}$  per pixel. An exposure time of 120 ms per frame with 20 frames per second was used. A radiation furnace with graphite heating elements applied a reflow profile that heated from room temperature to approximately 250  $^{\circ}\text{C}$  at 0.33  $^{\circ}\text{C}/\text{s}$ , held at this peak temperature for 30 s before cooling down at approximately 0.33  $^{\circ}\text{C}/\text{s}$ .

**X-ray image processing and analysis.** Image sequences were flatfield corrected and normalized against 10 frames shortly before the nucleation of primary intermetallic and flux voids for the primary intermetallic study and void study respectively using Image-Pro Plus v.7.0. For the study of primary intermetallics, a 3x3x5 (x,y,t) median filter was applied and for the study of tin dendrites, a 3x3 (x,y) median filter was applied. To quantify the growth of flux voids, Image-Pro Plus v.7.0 was used for object tracking. To quantify the primary  $\text{Cu}_6\text{Sn}_5$  solidification kinetics, a routine was written in MATLAB 7.1 to identify the time (frame) at which each pixel becomes a solid pixel. First, the transmitted X-ray intensity was smoothed in time to reduce noise using a locally weighted linear regression. The sudden decrease in the intensity associated with a liquid pixel becoming a solid pixel was defined as the intersection of a linear-fit line to the flat region prior to solidification with a linear-fit line through the point with steepest decreasing slope. Crystal growth kinetics were then extracted from the solidification time of each pixel within each  $\text{Cu}_6\text{Sn}_5$  crystal.

**Analytical Scanning Electron Microscopy (SEM).**

Beamline samples were polished for scanning electron microscopy (SEM) and electron backscatter diffraction (EBSD) analysis. For measuring the dendrite arm spacing, polished samples were lightly etched (93% distilled water + 5% sodium hydroxide + 2% 2-nitrophenol). A Zeiss Auriga field emission gun SEM was used, with an Oxford Instruments INCA 80mm<sup>2</sup> x-sight energy dispersive X-ray (EDX) detector and a Bruker EBSD detector. EBSD mapping was conducted at 20kV, scanning at 1  $\mu$ m step per pixel and 50 ms exposure time. Kikuchi patterns were analysed using Bruker Espirit 2.0 software.



## **Acknowledgements**

Real-time observation experiments were performed at the SPring-8 BL20XU beamline (2014B1620 and 2015A1675). This work was financially supported by the University of Queensland (UQ)-Nihon Superior (NS) collaboration research project, Australian Synchrotron International Synchrotron Access Program (AS/IA143/9218 and AS/IA151/9538), ARC Linkage project (LP140100485), Grant-in-Aid for Scientific Research (S) (24226018) from JSPS, Japan, UK EPSRC grant (EP/M002241/1), and a postgraduate scholarship from the Malaysian Higher Education Ministry and University Malaysia Perlis (UniMAP).

Correspondence and requests for materials should be addressed to: M. A. A. Mohd Salleh ([m.mohdsalleh@uq.edu.au](mailto:m.mohdsalleh@uq.edu.au) / [arifanuar@unimap.edu.my](mailto:arifanuar@unimap.edu.my))

## References

- 1 Boettinger, W. J. *et al.* Solidification microstructures: recent developments, future directions. *Acta Materialia* **48**, 43-70, doi:[http://dx.doi.org/10.1016/S1359-6454\(99\)00287-6](http://dx.doi.org/10.1016/S1359-6454(99)00287-6) (2000).
- 2 Arfaei, B. & Cotts, E. Correlations Between the Microstructure and Fatigue Life of Near-Eutectic Sn-Ag-Cu Pb-Free Solders. *Journal of Electronic Materials* **38**, 2617-2627, doi:10.1007/s11664-009-0932-y (2009).
- 3 Liu, W. & Lee, N.-C. The effects of additives to SnAgCu alloys on microstructure and drop impact reliability of solder joints. *JOM* **59**, 26-31, doi:10.1007/s11837-007-0085-5 (2007).
- 4 Lu, M., Shih, D.-Y., Lauro, P., Goldsmith, C. & Henderson, D. W. Effect of Sn grain orientation on electromigration degradation mechanism in high Sn-based Pb-free solders. *Applied Physics Letters* **92**, 211909, doi:<http://dx.doi.org/10.1063/1.2936996> (2008).
- 5 Huang, M. L. & Yang, F. Size effect model on kinetics of interfacial reaction between Sn-xAg-yCu solders and Cu substrate. *Scientific Reports* **4**, 7117, doi:10.1038/srep07117 (2014).
- 6 Frear, D. R. Issues related to the implementation of Pb-free electronic solders in consumer electronics. *Journal of Materials Science: Materials in Electronics* **18**, 319-330, doi:10.1007/s10854-006-9021-7 (2006).
- 7 Waldrop, M. M. The chips are down for Moore's law. *Nature* **530**, 144-147 (2016).
- 8 Hsiao, H.-Y. *et al.* Unidirectional Growth of Microbumps on (111)-Oriented and Nanotwinned Copper. *Science* **336**, 1007-1010, doi:10.1126/science.1216511 (2012).
- 9 Nguyen-Thi, H. *et al.* On the interest of synchrotron X-ray imaging for the study of solidification in metallic alloys. *Comptes Rendus Physique* **13**, 237-245, doi:<http://dx.doi.org/10.1016/j.crhy.2011.11.010> (2012).
- 10 Mathiesen, R. H., Arnberg, L., Mo, F., Weitkamp, T. & Snigirev, A. Time Resolved X-Ray Imaging of Dendritic Growth in Binary Alloys. *Physical Review Letters* **83**, 5062-5065 (1999).
- 11 LI, B., BRODY, H. D. & KAZIMIROV, A. Real Time Synchrotron Microradiography of Dendrite Coarsening in Sn-13 Wt Pct Bi Alloy. *Metall and Mat Trans A* **38**, 599-605, doi:10.1007/s11661-006-9058-5 (2007).
- 12 Zeng, G. *et al.* Solidification of Sn-0.7Cu-0.15Zn Solder: In Situ Observation. *Metall and Mat Trans A* **45**, 918-926, doi:10.1007/s11661-013-2008-0 (2014).

- 13 Yasuda, H. *et al.* Direct observation of stray crystal formation in unidirectional solidification of Sn–Bi alloy by X-ray imaging. *Journal of Crystal Growth* **262**, 645-652, doi:<http://dx.doi.org/10.1016/j.jcrysgro.2003.09.052> (2004).
- 14 Gourlay, C. M. *et al.* In situ investigation of unidirectional solidification in Sn–0.7Cu and Sn–0.7Cu–0.06Ni. *Acta Materialia* **59**, 4043-4054, doi:<http://dx.doi.org/10.1016/j.actamat.2011.03.028> (2011).
- 15 Zhu, J. *et al.* Real time observation of equiaxed growth of Sn–Pb alloy under an applied direct current by synchrotron microradiography. *Materials Letters* **89**, 137-139, doi:<http://dx.doi.org/10.1016/j.matlet.2012.08.094> (2012).
- 16 Zhou, P. *et al.* In situ study on growth behavior of Cu<sub>6</sub>Sn<sub>5</sub> during solidification with an applied DC in RE-doped Sn–Cu solder alloys. *Journal of Materials Science: Materials in Electronics* **25**, 4538-4546, doi:10.1007/s10854-014-2201-y (2014).
- 17 Mohd Salleh, M. A. A., McDonald, S. D., Yasuda, H., Sugiyama, A. & Nogita, K. Rapid Cu<sub>6</sub>Sn<sub>5</sub> growth at liquid Sn/solid Cu interfaces. *Scripta Materialia* **100**, 17-20, doi:<http://dx.doi.org/10.1016/j.scriptamat.2014.11.039> (2015).
- 18 Mohd Salleh, M. A. A. *et al.* Effect of Ni on the Formation and Growth of Primary Cu<sub>6</sub>Sn<sub>5</sub> Intermetallics in Sn-0.7 wt.%Cu Solder Pastes on Cu Substrates During the Soldering Process. *Journal of Electronic Materials* **45**, 154-163, doi:10.1007/s11664-015-4121-x (2015).
- 19 Ma, H. T. *et al.* In-situ study on growth behavior of Ag<sub>3</sub>Sn in Sn–3.5Ag/Cu soldering reaction by synchrotron radiation real-time imaging technology. *Journal of Alloys and Compounds* **537**, 286-290, doi:<http://dx.doi.org/10.1016/j.jallcom.2012.05.055> (2012).
- 20 Huang, M. L., Yang, F., Zhao, N. & Yang, Y. C. Synchrotron radiation real-time in situ study on dissolution and precipitation of Ag<sub>3</sub>Sn plates in sub-50 μm Sn–Ag–Cu solder bumps. *Journal of Alloys and Compounds* **602**, 281-284, doi:<http://dx.doi.org/10.1016/j.jallcom.2014.03.047> (2014).
- 21 Qu, L., Zhao, N., Zhao, H. J., Huang, M. L. & Ma, H. T. In situ study of the real-time growth behavior of Cu<sub>6</sub>Sn<sub>5</sub> at the Sn/Cu interface during the soldering reaction. *Scripta Materialia* **72–73**, 43-46, doi:<http://dx.doi.org/10.1016/j.scriptamat.2013.10.013> (2014).
- 22 Qu, L., Ma, H. T., Zhao, H. J., Kunwar, A. & Zhao, N. In situ study on growth behavior of interfacial bubbles and its effect on interfacial reaction during a soldering process. *Applied Surface Science* **305**, 133-138, doi:<http://dx.doi.org/10.1016/j.apsusc.2014.03.003> (2014).

- 23 Kotadia, H. R., Howes, P. D. & Mannan, S. H. A review: On the development of low melting temperature Pb-free solders. *Microelectronics Reliability* **54**, 1253-1273, doi:<http://dx.doi.org/10.1016/j.microrel.2014.02.025> (2014).
- 24 Lee, T.-K., Bieler, T. R., Kim, C.-U. & Ma, H. in *Fundamentals of lead-free solder interconnect From Microstructure to Reliability* Ch. Microstructure Development: Solidification and Isothermal Aging, 95-96 (Springer, 2015).
- 25 Anderson, I. E. Development of Sn–Ag–Cu and Sn–Ag–Cu–X alloys for Pb-free electronic solder applications. *Journal of Materials Science: Materials in Electronics* **18**, 55-76, doi:10.1007/s10854-006-9011-9 (2007).
- 26 Ho, C. E., Tsai, R. Y., Lin, Y. L. & Kao, C. R. Effect of Cu concentration on the reactions between Sn-Ag-Cu solders and Ni. *Journal of Electronic Materials* **31**, 584-590, doi:10.1007/s11664-002-0129-0 (2002).
- 27 Nogita, K., Mu, D., McDonald, S. D., Read, J. & Wu, Y. Q. Effect of Ni on phase stability and thermal expansion of Cu<sub>6-x</sub>Ni<sub>x</sub>Sn<sub>5</sub> (X = 0, 0.5, 1, 1.5 and 2). *Intermetallics* **26**, 78-85, doi:<http://dx.doi.org/10.1016/j.intermet.2012.03.047> (2012).
- 28 Assael, M. J. *et al.* Reference Data for the Density and Viscosity of Liquid Copper and Liquid Tin. *Journal of Physical and Chemical Reference Data* **39**, 033105, doi:<http://dx.doi.org/10.1063/1.3467496> (2010).
- 29 Thermo-Calc. **TCSLD Database version 3.0** (2015).
- 30 Gourlay, C. M., Belyakov, S. A., Ma, Z. L. & Xian, J. W. Nucleation and Growth of Tin in Pb-Free Solder Joints. *JOM* **67**, 2383-2393, doi:10.1007/s11837-015-1582-6 (2015).
- 31 Kurz, W. & Fisher, D. J. *Fundamentals of solidification*. (Trans Tech Publications, 1992).
- 32 Pang, J. H. L. *Lead Free Solder: Mechanics and Reliability*. (Springer New York, 2011).
- 33 Tian, Y. *et al.* Effect of intermetallic compounds on fracture behaviors of Sn<sub>3.0</sub>Ag<sub>0.5</sub>Cu lead-free solder joints during in situ tensile test. *Journal of Materials Science: Materials in Electronics* **23**, 136-147, doi:10.1007/s10854-011-0538-z (2012).
- 34 Arfaei, B., Kim, N. & Cotts, E. J. Dependence of Sn Grain Morphology of Sn-Ag-Cu Solder on Solidification Temperature. *Journal of Electronic Materials* **41**, 362-374, doi:10.1007/s11664-011-1756-0 (2011).
- 35 Padilla, E., Jakkali, V., Jiang, L. & Chawla, N. Quantifying the effect of porosity on the evolution of deformation and damage in Sn-based solder joints by X-ray

- microtomography and microstructure-based finite element modeling. *Acta Materialia* **60**, 4017-4026, doi:<http://dx.doi.org/10.1016/j.actamat.2012.03.048> (2012).
- 36 Mu, D. K., McDonald, S. D., Read, J., Huang, H. & Nogita, K. Critical properties of Cu<sub>6</sub>Sn<sub>5</sub> in electronic devices: Recent progress and a review. *Current Opinion in Solid State and Materials Science* **20**, 55-76, doi:<http://dx.doi.org/10.1016/j.cossms.2015.08.001> (2016).
- 37 Lehman, L. P., Xing, Y., Bieler, T. R. & Cotts, E. J. Cyclic twin nucleation in tin-based solder alloys. *Acta Materialia* **58**, 3546-3556, doi:<http://dx.doi.org/10.1016/j.actamat.2010.01.030> (2010).
- 38 Yang, S., Tian, Y. & Wang, C. Investigation on Sn grain number and crystal orientation in the Sn–Ag–Cu/Cu solder joints of different sizes. *Journal of Materials Science: Materials in Electronics* **21**, 1174-1180, doi:10.1007/s10854-009-0042-x (2009).
- 39 Mohd Salleh, M. A. A., McDonald, S. D., Yasuda, H., Sugiyama, A. & Nogita, K. Rapid Cu<sub>6</sub>Sn<sub>5</sub> growth at liquid Sn/solid Cu interfaces. *Scripta Mater* **100**, 17-20 (2015).

## Figure Captions

Figure 1: In situ real time imaging observations of interfacial  $\text{Cu}_6\text{Sn}_5$  formation during early wetting reactions between liquid Sn-0.7Cu and the Cu substrate interface at (a) 0 s, (b) 0.05 s, (c) 0.10 s, (d) 28.10 s, (e) 66.30 s, (f) 87.60 s and (g) 114.30 s times after wetting: (h) a post mortem backscattered electron scanning electron microscopy (SEM) image of the solidified sample.

Figure 2: (a-f) Synchrotron image sequence of the flux void formation during early wetting of Sn-0.7Cu paste on a Cu substrate and (g) quantification of interfacial voids size (diameter) formation and growth in Sn-0.7Cu paste during soldering from synchrotron image sequences (compilation from several experiments where different colours indicates different flux voids).

Figure 3: Synchrotron image sequence of the nucleation and growth of primary  $\text{Cu}_6\text{Sn}_5$  in a Sn-3.0Ag-0.5Cu/Cu joint. Images have been normalised against a frame shortly before that in (a).  $\text{Cu}_6\text{Sn}_5$  are dark. The two central round features are bubbles. The round features at the  $\text{Cu}_6\text{Sn}_5$  interfacial layer are flux voids. (f) a processed image with each  $\text{Cu}_6\text{Sn}_5$  segmented and coloured by its nucleation time in s.  $t=0$  is the onset of cooling from the peak temperature of 250°C.

Figure 4: Synchrotron image sequence of the nucleation and growth of primary  $\text{Cu}_6\text{Sn}_5$  in a Sn-0.7Cu/Cu joint. Images have been normalised against a frame shortly before that in (a).  $\text{Cu}_6\text{Sn}_5$  are dark. The central round feature is a bubble. The round features at the  $\text{Cu}_6\text{Sn}_5$  interfacial layer are flux voids. (f) is a processed image with each  $\text{Cu}_6\text{Sn}_5$  segmented and coloured by its nucleation time in s.  $t=0$  is the onset of cooling from the peak temperature of 250°C.

Figure 5: Quantification of the solidification kinetics of primary  $\text{Cu}_6\text{Sn}_5$  crystals from the synchrotron image sequences in Figures 3 and 4. (a)-(c) Sn-3.0Ag-0.5Cu/Cu. (d)-(f) Sn-0.7Cu/Cu. (a) and (d):  $\text{Cu}_6\text{Sn}_5$  growth vectors. (b) and (e): the same vectors with a common origin showing the growth orientation distribution. (c) and (f): the growth tip position versus time for most  $\text{Cu}_6\text{Sn}_5$  crystals in each sample. (g) total number of  $\text{Cu}_6\text{Sn}_5$  crystals versus time for each joint. (h) histogram of the number of  $\text{Cu}_6\text{Sn}_5$  nucleation events with time. (i) size distribution of the primary  $\text{Cu}_6\text{Sn}_5$  crystals at the end of solidification in both joints.

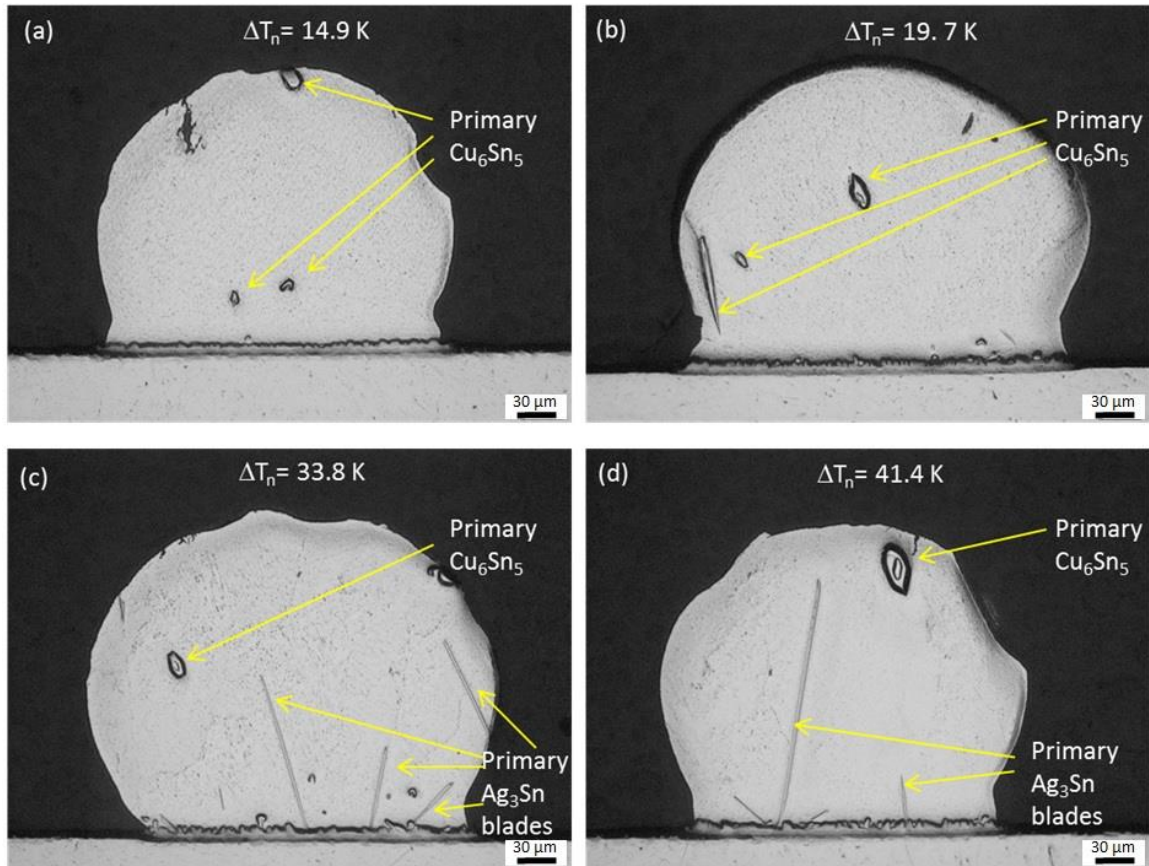
Figure 6: (a) Sn-Ag-Cu 250°C isothermal section based on Thermocalc<sup>29</sup>. Crosses mark the initial solder compositions and the arrows show the change in liquid composition due to Cu substrate dissolution (up to the solubility limit). (b) Predicted development of primary IMC during cooling from 250°C in *Sn-3.0Ag-0.5Cu/Cu* and *Sn-0.7Cu/Cu* joints, assuming the liquid was saturated in Cu at 250°C. The circles show the equilibrium eutectic onset temperatures and, below these temperatures, primary Cu<sub>6</sub>Sn<sub>5</sub> only continues to grow if β-Sn fails to nucleate. Note that, in *Sn-3.0Ag-0.5Cu/Cu*, primary Ag<sub>3</sub>Sn crystals are not predicted to form until ~198°C ( $\Delta T_{\text{nuc}} \sim 19\text{K}$ ).

Figure 7: Growth of primary Cu<sub>6</sub>Sn<sub>5</sub> on *Sn-3.0Ag-0.5Cu/Cu* near the interfacial intermetallic compound (IMC) layer later during solidification (a)-(b) post-mortem SEM images. (c)-(g) in-situ synchrotron images at five different times.

Figure 8: (a) - (c) Synchrotron images of the nucleation and growth of β-Sn in the *Sn-3.0Ag-0.5Cu/Cu* joint. (d) EBSD inverse pole figure (IPF)-y map of the *Sn-3.0Ag-0.5Cu/Cu* joint with the unit cell orientation superimposed. (e) BSE-SEM image in which the β-Sn dendrite growth direction can be deduced. Arrows show the growth direction in two regions projected onto the imaging plane. (f) BSE-SEM image of dendrites near the nucleation site. (g) plot of primary dendrite arm spacing versus distance from the observed nucleation point.

Figure 9: EBSD inverse pole figure (IPF)-y map of the *Sn-0.7Cu/Cu* joint with unit cell orientations superimposed. The inserts show the β-Sn dendrite morphology relative to its unit cell orientation, and a primary Cu<sub>6</sub>Sn<sub>5</sub> rod relative to its unit cell orientation.

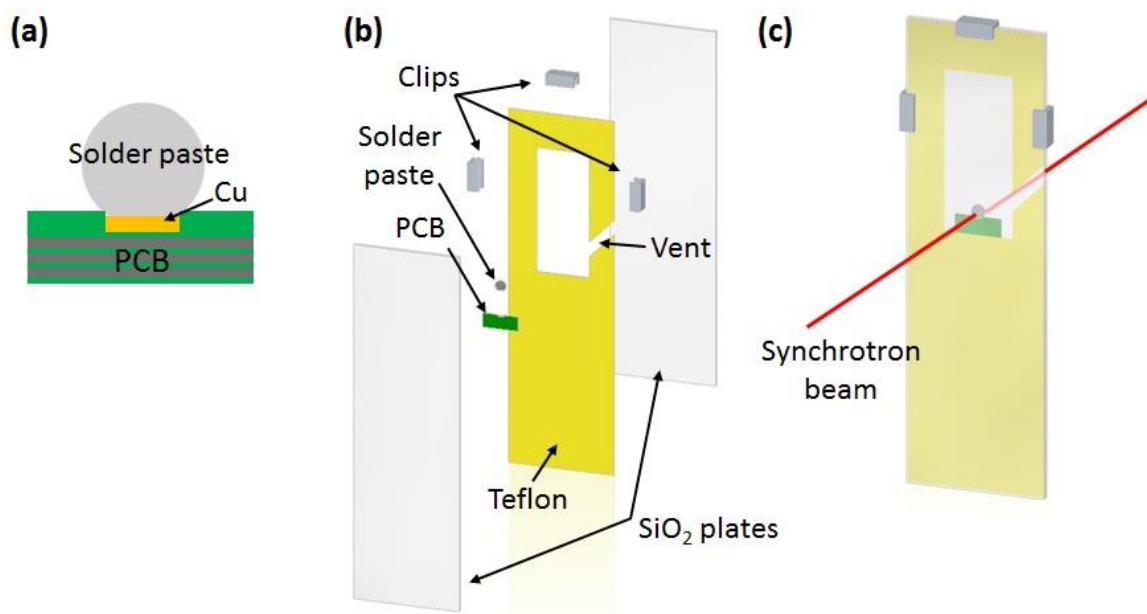
## Supplementary Data



Supplementary Figure 1: SEM-BSE images of Sn-3.0Ag-0.5Cu/Cu joints at undercooling of (a) 14.9 K, (b) 19.7 K, (c) 33.8 K and (d) 41.4 K, indicating primary  $\text{Ag}_3\text{Sn}$  blades only formed in the joints at undercoolings higher than 20 K.



## Supplementary Methods



Supplementary Figure 2: Schematic diagram of in situ soldering observation experiment sample cell setup. (a) sample of solder paste on Cu PCB (b) parts of sample cell and (c) assembled parts of sample cell. Note that image is not to scale.

Solder pastes with 35  $\mu\text{m}$  average solder sphere diameter were used with similar weight (approximately 0.0002 g) were used throughout the experiments. A Cu plated with organic soldering preservative (OSP) surface finish printed circuit board (Fire retardant FR-4 type) with 600  $\mu\text{m}$  ball pitch size was cross sectioned to produce a Cu-OSP substrate suitable for radiography with 100  $\mu\text{m}$  thickness. A small amount of solder paste was placed on the Cu pad (Supplementary Figure 2a). As in Supplementary Figure 2b and 2c, samples were placed in a cavity within a 100  $\mu\text{m}$  thick polytetrafluoroethylene (PTFE) spacer sheet with an observation window of 10 x 10  $\text{mm}^2$  and a vent for flux outgassing. Finally, the paste, substrate and PTFE were secured between two quartz plates.

## Author contributions:

**Mr. M. A. A. Mohd Salleh** ([m.mohdsalleh@uq.edu.au](mailto:m.mohdsalleh@uq.edu.au)/ [arifanuar@unimap.edu.my](mailto:arifanuar@unimap.edu.my)) is a PhD student of the Nihon Superior Centre for the Manufacture of Electronic Materials, School of Mechanical and Mining Engineering, The University of Queensland. He is also a lecturer of Universiti Malaysia Perlis (UniMAP), Malaysia. He is the first author of this article and contributed to the planning of all experiments, data analysis, participating SEM and EBSD experiments and writing the article.

**Dr. Christopher M. Gourlay** ([c.gourlay@imperial.ac.uk](mailto:c.gourlay@imperial.ac.uk)) is a Senior Lecturer in the Department of Materials, Imperial College London. He is the second author of this article and contributed to the interpretation including Thermocalc and EBSD analysis, discussions, and writing the article.

**Mr. Jing Wei Xian** ([jingwei.xian11@imperial.ac.uk](mailto:jingwei.xian11@imperial.ac.uk)) is a PhD student in the Department of Materials, Imperial College London. He is the third author of this article and contributed to the discussion and conducted EBSD experiments and synchrotron imaging data analysis.

**Dr. Sergey A. Belyakov** ([s.belyakov@imperial.ac.uk](mailto:s.belyakov@imperial.ac.uk)) is a postdoc fellow in the Department of Materials, Imperial College London. He is the fourth author of this article and contributed to the discussion, conducted SEM sample preparation and analysis.

**Dr. Hideyuki Yasuda** ([yasuda.hideyuki.6s@kyoto-u.ac.jp](mailto:yasuda.hideyuki.6s@kyoto-u.ac.jp)) is a Professor of the Department of Materials Science and Engineering, Kyoto University. He is the fifth author of this article and contributed to the planning and the setup of synchrotron imaging experiment.

**Dr. Stuart D. McDonald** ([s.mcdonald1@uq.edu.au](mailto:s.mcdonald1@uq.edu.au)) is a Senior Research Fellow of the Nihon Superior Centre for the Manufacture of Electronic Materials, School of Mechanical and Mining Engineering, The University of Queensland. He is the sixth author of this article and contributed to the planning of all experiments, discussion, and writing the article.

**Dr. Kazuhiro Nogita** ([k.nogita@uq.edu.au](mailto:k.nogita@uq.edu.au)) is a visiting Professor of the School of Materials Engineering, Universiti Malaysia Perlis (UniMAP), and also Associate Professor and Director of the Nihon Superior Centre for the Manufacture of Electronic Materials,

School of Mechanical and Mining Engineering, The University of Queensland. He is the last author of this article and contributed to the planning of all experiments, discussion, and writing the article.

All authors reviewed the manuscript.

#### **Additional Information:**

##### **Competing financial interests**

The author(s) declare no competing financial interests.

**Paper 6: Effect of Ni on the formation and growth  
of primary  $\text{Cu}_6\text{Sn}_5$  intermetallics in Sn-0.7wt%Cu  
solder paste on Cu substrates during the  
soldering process**

Mohd Arif Anuar Mohd Salleh, Stuart D. McDonald, Christopher M. Gourlay,  
Sergey A. Belyakov, Hideyuki Yasuda, Kazuhiro Nogita

**Journal of Electronic Materials**, Vol 45 No 1 (2016)

**Effect of Ni on the formation and growth of primary Cu<sub>6</sub>Sn<sub>5</sub> intermetallics in Sn-0.7wt%Cu solder pastes on Cu substrates during the soldering process**

M. A. A. Mohd Salleh<sup>a,b\*</sup>, S. D. McDonald<sup>a</sup>, C.M. Gourlay<sup>c</sup>, S.A. Belyakov<sup>c</sup>, H. Yasuda<sup>d</sup>, K. Nogita<sup>a</sup>

<sup>a</sup>Nihon Superior Centre for the Manufacture of Electronic Materials (NS CMEM), School of Mechanical and Mining Engineering, The University of Queensland, 4072 St Lucia, Queensland, Australia.

<sup>b</sup>Centre of Excellence Geopolymer and Green Technology, School of Materials Engineering, Universiti Malaysia Perlis (UniMAP), Taman Muhibbah 02600, Jejawi, Arau, Perlis, Malaysia.

<sup>c</sup>Department of Materials, Imperial College, London SW7 2AZ, United Kingdom.

<sup>d</sup>Department of Materials Science and Engineering, Kyoto University, Sakyo-ku, Kyoto 606-8501, Japan.

\*Corresponding author: Room 634, 49 Jocks Rd., St Lucia, Brisbane, QLD 4072, Australia

Email: m.mohdsalleh@uq.edu.au / arifanuar@unimap.edu.my ;

Tel: +61 435 946 670

## ABSTRACT

This paper investigates the effect of 0.05wt%Ni on the formation and growth of primary  $\text{Cu}_6\text{Sn}_5$  in Sn-0.7wt%Cu solder paste soldered on a Cu substrate using a real-time synchrotron imaging technique. It was found that small additions of Ni significantly alter the formation and growth of the primary  $\text{Cu}_6\text{Sn}_5$  primary intermetallics making them small. In contrast, without Ni primary  $\text{Cu}_6\text{Sn}_5$  primary intermetallics tend to continue growth throughout solidification and end up much larger and coarser. The primary effect of the Ni addition appears to be in promoting the nucleation of a larger amount of small  $\text{Cu}_6\text{Sn}_5$ . The results provide direct evidence of the sequence of events in the reaction of Ni containing Sn-0.7wt%Cu solder paste with a Cu substrate, and in particular the formation and growth of the primary  $\text{Cu}_6\text{Sn}_5$  intermetallic.

Keyword: Synchrotron imaging, solder paste, intermetallic, solidification.

## INTRODUCTION

Electric and electronic devices have rapidly become more advanced and denser necessitating stronger and higher reliability interconnects and advances in solder materials. Among commercially available lead-free solders, Sn-0.7wt%Cu solder systems were widely used in wave soldering due to their availability and low cost [1, 2]. However, Sn-0.7wt%Cu has poor mechanical properties, is prone to brittle intermetallic compound (IMC) growth and formation of large primary  $\eta\text{-Cu}_6\text{Sn}_5$  in the solder matrix and a thick interfacial IMC layer consisting of  $\eta\text{-Cu}_6\text{Sn}_5$  and  $\epsilon\text{-Cu}_3\text{Sn}$ , that can lead to serious reliability concerns [3]. Due to this disadvantage, research has been undertaken on the micro-alloying effects of several elements in the Sn-Cu solder system including Ni [4-8], Zn [6], Bi [9], In [10] and Al [11, 12]. These micro-alloying studies have been made to improve the mechanical properties of a solder joint. Within the range of alloys developed, the near eutectic composition of Sn-0.7wt%Cu with ~0.05 wt% Ni has been used in industry since 1999 [13]. Yoon et al. [14] investigated the growth of interfacial  $\text{Cu}_6\text{Sn}_5$  in Sn-Cu-Ni solders after thermal ageing and identified that the interfacial intermetallic compound (IMC) activation energy was considered low compared to the activation energy of interfacial IMC in binary Sn-Cu solders. In another study, Yang et al. [7] reported that with Ni additions to Sn-0.7wt%Cu the growth of  $\text{Cu}_3\text{Sn}$  interfacial IMC was suppressed which also resulted in the formation of fine needle-like  $(\text{Cu,Ni})_6\text{Sn}_5$  at the solder/substrate interface. In addition, the reported effects of small additions of Ni in Sn-0.7wt%Cu solder alloys have included better fluidity [15], alterations to

the eutectic composition and promotion of a near eutectic Sn-Cu<sub>6</sub>Sn<sub>5</sub> microstructure [16], stabilisation of the hexagonal high temperature phase of Cu<sub>6</sub>Sn<sub>5</sub> [17], and suppression of cracking in Cu<sub>6</sub>Sn<sub>5</sub> solder joints formed between Sn-0.7wt%Cu solders and Cu substrates [18]. However, most of these investigations on IMC formation in Sn-Cu and Sn-Cu-Ni solder systems were ex-situ experiments and focused on the interfacial IMC rather than the primary IMC that forms in the solder matrix prior to  $\beta$ -Sn nucleation.

Previous research has used synchrotron radiography to directly image (i) the solidification of primary Cu<sub>6</sub>Sn<sub>5</sub> intermetallics in bulk solders (without a substrate) [19] [11] [20] and (ii) the intermetallic reaction layer [21]. Recently, we have successfully developed [22] a synchrotron based in-situ method to observe, in real time, the entire soldering process of a solder paste on a Cu substrate, including the solid-liquid-solid transition to provide an understanding on the real-time primary intermetallic growth. In this study, we use this technique to observe the soldering of Sn-0.7wt%Cu and Sn-0.7wt%Cu-0.05wt%Ni solder paste on a Cu substrate in order to investigate the influence of Ni additions on the formation and growth of the primary Cu<sub>6</sub>Sn<sub>5</sub> intermetallic.

## EXPERIMENTAL PROCEDURE

Real time observation experiments were performed at the BL20XU beamline in the SPring-8 synchrotron using the solidification observation setup developed in previous research [22-24]. The parameters were chosen to allow a high degree of coherence, absorption contrast and phase contrast enabling boundaries in the sample to be observed on transmitted images. These image signals collected were then converted into a digital format of 2000 X 2000 pixels at 1 mm X 1 mm field of view giving a resolution of 0.477  $\mu$ m per pixel. A planar undulator was used as a light source and the radiation was monochromatized with Si double crystal monochromators. An exposure time of 1 s per frame to capture the images was used. To mimic the process of reflow soldering, a furnace with graphite heating elements where heat is transferred through radiation in an enclosed sample chamber was used (Figure 1a). The sample position and sample cell configuration is shown in Figure 1b, and each sample of either Sn-0.7wt%Cu or Sn-0.7wt%Cu-0.05wt%Ni solder paste supplied by Nihon Superior Co Ltd had an average solder spheres sizes of 35  $\mu$ m and was placed vertically on a thin 100  $\mu$ m Cu substrate. The observation window area of 10 x 10 mm<sup>2</sup> with a vent for flux outgassing was made by using a 100  $\mu$ m thickness poly-tetrafluoroethylene (PTFE) sheet placed between two SiO<sub>2</sub> plates. Samples were set to be heated from room

temperature to approximately 250 °C at 0.33 °C/s and held for 30 s before cooling down at approximately 0.33 °C/s. The soldering temperature profiles for the experiments are shown in Figure 1c. Experimental time from 0 s was determined from the point of solder melting at 227 °C.

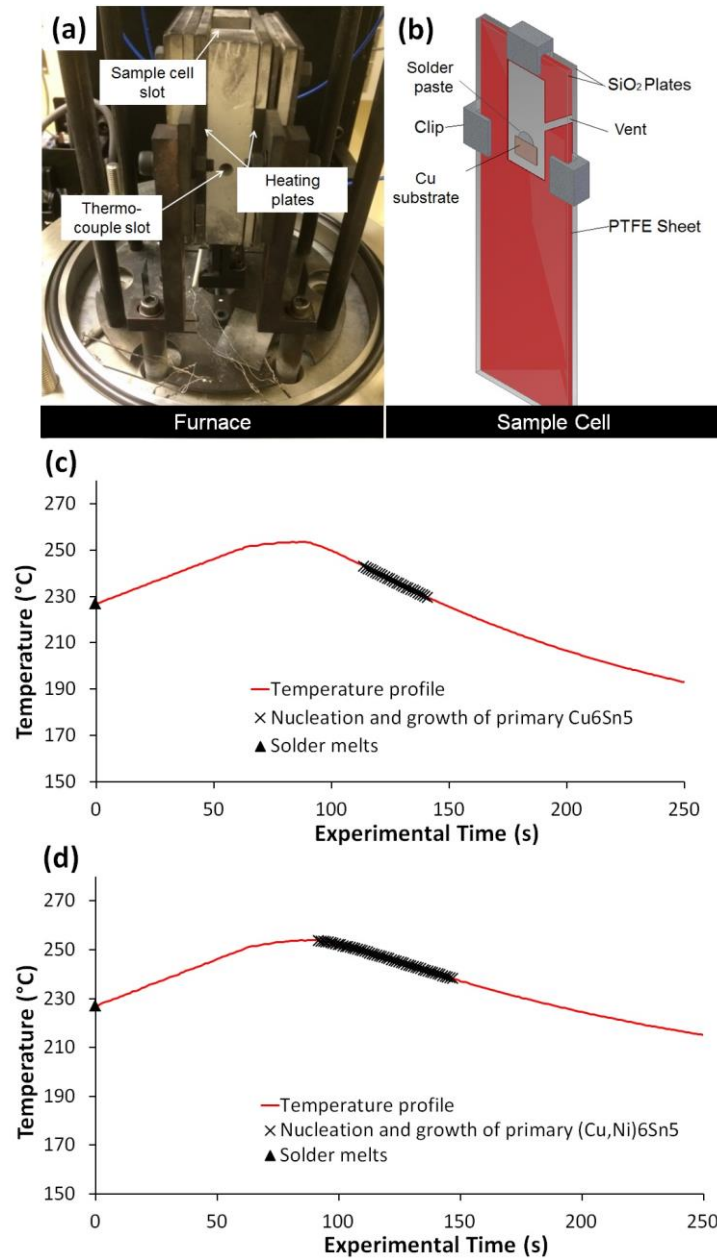


Figure 1: (a) Synchrotron real-time in-situ observation heating furnace setup, (b) soldering sample cell setup, and (c) temperature profile of Sn-0.7wt%Cu/Cu and (d) temperature profile of Sn-0.7wt%Cu-0.05wt%Ni/Cu.



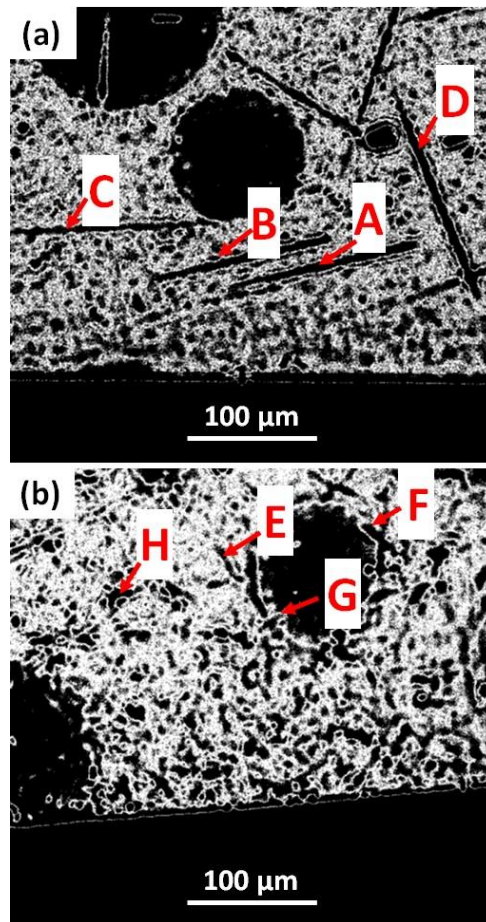


Figure 2: Threshold X-ray synchrotron images for measuring primary intermetallic compounds (IMC) of (a)  $\text{Cu}_6\text{Sn}_5$  on Sn-0.7wt%Cu and (b)  $(\text{Cu,Ni})_6\text{Sn}_5$  on Sn-0.7wt%Cu-0.05wt%Ni. Individual primary  $\text{Cu}_6\text{Sn}_5$  particles are labeled with letters corresponding to the particles shown in Figure 3(i) and Figure 4(i).

The size of primary intermetallics on Sn-0.7wt%Cu and Sn-0.7wt%Cu-0.05wt%Ni solder pastes on Cu substrates was measured using ImageJ software. Synchrotron radiography images were then processed by using a threshold method [25] to obtain an accurate measurement. Several primary intermetallics of each solder alloy were chosen for measurement as indicated in Figure 2. After synchrotron in-situ observation, samples were polished and scanning electron microscopy (SEM) images were obtained using backscattered mode. Electron dispersive X-ray spectroscopy (EDS) point analysis and mapping was conducted to observe the Ni and Cu distribution.

To help with the analysis of the results, an additional experiment was performed to test whether any solid phases are present at the peak temperature of 250°C. Approximately 200 g of Sn-0.7wt%Cu-0.05wt%Ni solder paste was heated to 250°C until all flux was removed. The sample was then poured into a borosilicate glass test tube to produce a cylindrical

sample 18 mm in diameter. This was then held vertically at 250°C for 24 hrs before being abruptly quenched in water. The microstructures of the top and bottom of the sample were then studied to explore whether any particles had settled or floated under gravity at 250°C.

## RESULTS

Figure 3 reveals the real-time observations of reactions between Sn-0.7wt%Cu solder paste and the Cu substrate at nine experimental times. From the observations, Sn-0.7wt%Cu solder paste which contains solder spheres and flux starts to transform to a more viscous suspension (Figure 3a) at approximately 227°C and the solder spheres contained in the suspension fully melt after a few seconds as seen in Figure 3b. The liquid Sn-0.7wt%Cu then immediately wets the Cu substrate followed by the formation of interfacial  $\text{Cu}_6\text{Sn}_5$  IMC. From Figure 3c, it can be seen that at the moment the molten solder contacts the solid Cu an intermetallic layer of significant thickness forms, while molten solder flows onto the Cu substrate. During the reflow soldering process, solder voids can be observed as in Figure 3 and 4 due to the flux outgassing process. After a peak temperature of 250°C for 30 s, the solder then was cooled down. During cooling (Figure 3d-3i), primary rod-shaped  $\text{Cu}_6\text{Sn}_5$  intermetallics nucleated at 110 – 120 s of the experimental time at approximately 244 – 240°C. The large primary rod-shaped  $\text{Cu}_6\text{Sn}_5$  continue to grow during cooling before solidification is complete.

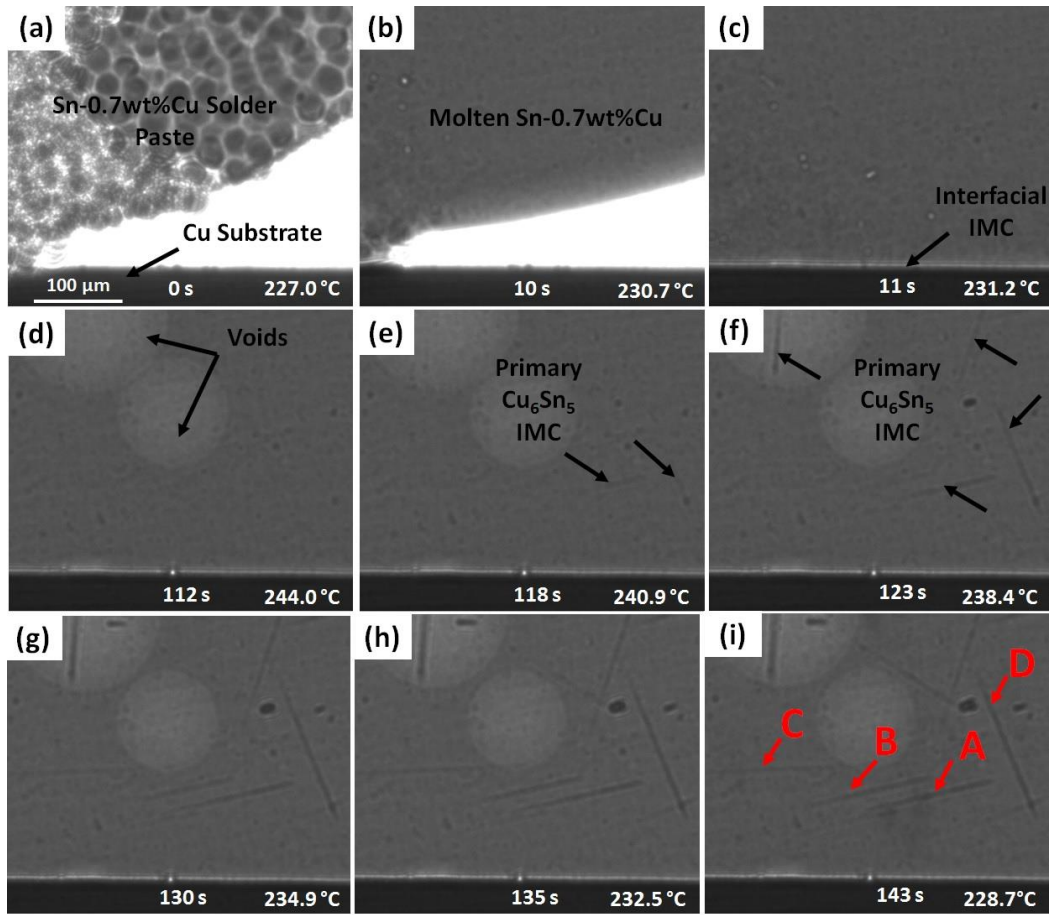


Figure 3: Real-time observations of reactions between Sn-0.7wt%Cu solder paste and the Cu substrate at experimental times of (a) 0 s, (b) 10 s, (c) 11 s, (d) 112 s, (e) 118 s, (f) 123 s, (g) 130 s, (h) 135 s and (i) 143 s.

Figure 4 reveals the real-time observation of the reaction between Sn-0.7wt%Cu-0.05wt%Ni solder paste and the Cu substrate at an experimental time of (a) 0 s, (b) 4 s, (c) 22 s, (d) 34 s, (e) 119 s, (f) 123 s, (g) 132 s, (h) 141 s and (i) 147 s. From the observations, the solder spheres and flux starts to transform to a more viscous suspension (Figure 4a) at approximately 227°C and the solder spheres contained in suspension tend to fully melt after a few seconds. The liquid Sn-0.7wt%Cu-0.05wt%Ni then immediately wets the Cu substrate and interfacial  $\text{Cu}_6\text{Sn}_5$  IMC formation occurs (Figure 4c). From the synchrotron image sequences, small pre-existing primary  $(\text{Cu},\text{Ni})_6\text{Sn}_5$  particles approximately 8  $\mu\text{m}$  in length were observed before the peak temperature during heating. For example, at 34 s of the experimental time at 239.9°C in Figure 4d. Within the resolution of imaging, the pre-existing  $(\text{Cu},\text{Ni})_6\text{Sn}_5$  could only be clearly observed when they were being pushed by an adjacent void and it is not possible to conclude on whether these pre-existing particles completely melted or not from the imaging. Later in this section, it will be shown that  $(\text{Cu},\text{Ni})_6\text{Sn}_5$

particles are stable at 250°C in Sn-0.7wt%Cu-0.05wt%Ni. During cooling from the peak temperature (Figure 4e-4i), new primary  $(\text{Cu,Ni})_6\text{Sn}_5$  intermetallics nucleate and grow to a scale of a few tens of  $\mu\text{m}$  in length at 92 – 147 s of the experimental time at approximately 250 – 238°C. Note that primary  $\text{Cu}_6\text{Sn}_5$  form earlier (at higher temperature) in Sn-0.7wt%Cu-0.05wt%Ni/Cu joints than in Sn-0.7wt%Cu/Cu joints as shown in Figure 1c and d. Similar to the large  $\text{Cu}_6\text{Sn}_5$  rods observed on Sn-0.7wt%Cu/Cu, the new primary  $(\text{Cu,Ni})_6\text{Sn}_5$  intermetallics tend to nucleate and grow with increasing time during cooling before tin nucleation. Due to the density difference with the liquid, these small  $(\text{Cu,Ni})_6\text{Sn}_5$  intermetallics tend to settle down at the interface between the molten solder and Cu substrate. However it is clear that these particles do not form at the substrate but in the bulk of the solder.

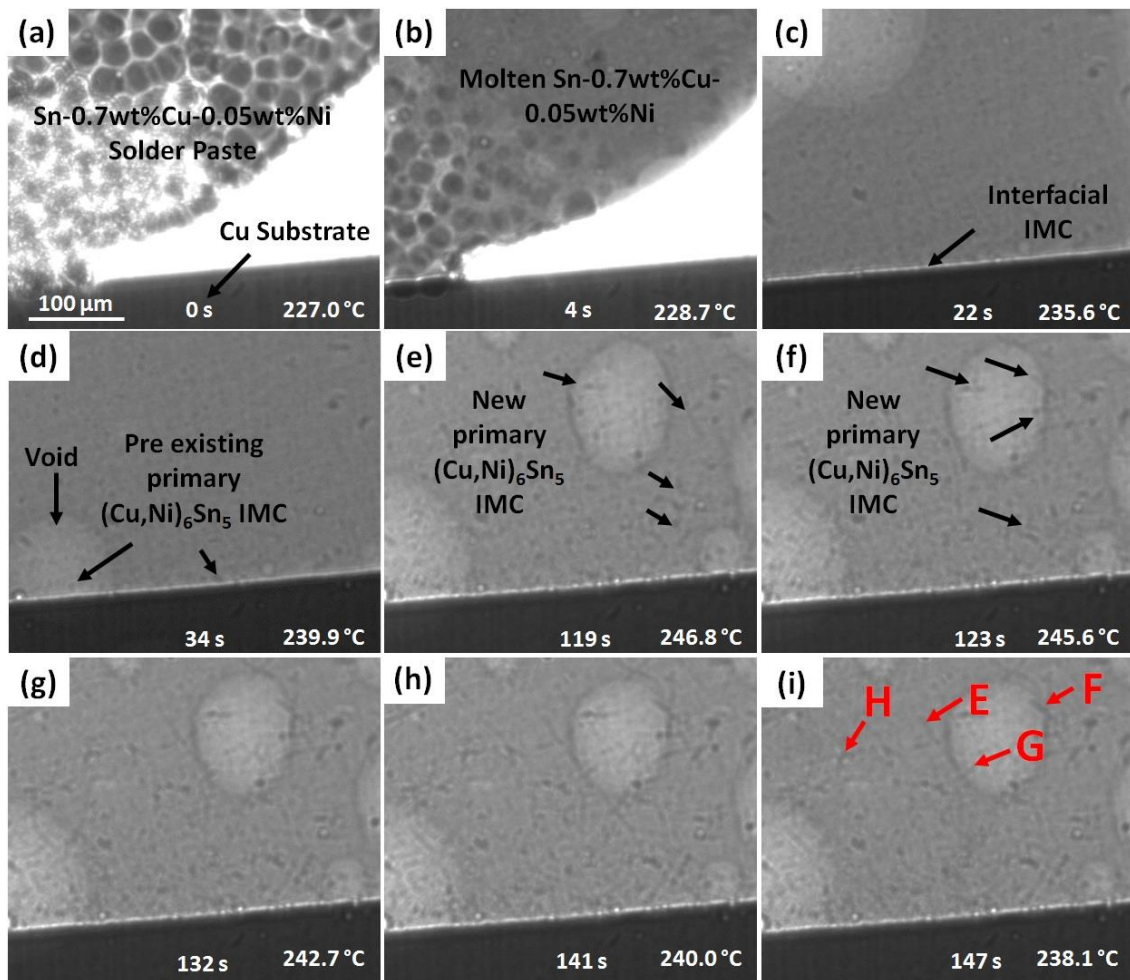


Figure 4: Real-time observations of reactions between Sn-0.7wt%Cu-0.05wt%Ni solder paste and the Cu substrate at experimental times of (a) 0 s, (b) 4 s, (c) 22 s, (d) 34 s, (e) 119 s, (f) 123 s, (g) 132 s, (h) 141 s and (i) 147 s.

A key finding in this work is that the primary  $\text{Cu}_6\text{Sn}_5$  are significantly smaller and more numerous in Sn-0.7wt%Cu-0.05wt%Ni/Cu than in Sn-0.7wt%Cu/Cu, as can be seen by comparing Figure 3 and 4. Within the field of imaging as in Figure 3 and 4, approximately 15 large  $\text{Cu}_6\text{Sn}_5$  and more than 100 small  $(\text{Cu,Ni})_6\text{Sn}_5$  primary intermetallics were observed on Sn-0.7wt%Cu/Cu and Sn-0.7wt%Cu-0.05wt%Ni/Cu respectively. For the primary  $\text{Cu}_6\text{Sn}_5$  growth investigations of both solder alloys, four typical individual intermetallic  $\text{Cu}_6\text{Sn}_5$  particles were chosen and measured which are indicated as A, B, C, and D for Sn-0.7wt%Cu and E, F, G and H for Sn-0.7wt%Cu-0.05wt%Ni (Figure 2, Figure 3i and Figure 4i). In Figure 5, the evolution of primary  $\text{Cu}_6\text{Sn}_5$  intermetallics in Sn-0.7wt%Cu and Sn-0.7wt%Cu-0.05wt%Ni during cooling are plotted. Noting the different axis limits, it is obvious that the sizes of primary  $\text{Cu}_6\text{Sn}_5$  intermetallics in Sn-0.7wt%Cu-0.05wt%Ni are smaller compared to Sn-0.7wt%Cu with approximately  $150 - 350 \mu\text{m}^2$  and  $1300 - 1800 \mu\text{m}^2$  in area size, respectively. As in Figure 5a, the primary  $\text{Cu}_6\text{Sn}_5$  intermetallic in Sn-0.7wt%Cu tends to continue to grow until the tin nucleates while, in Sn-0.7wt%Cu-0.05wt%Ni, the growth of some rods is restricted before tin nucleates. Several studies have shown that a smaller size of primary IMCs in the matrix could strengthen the solder mechanically by pinning dislocation glide [26, 27]. In contrast, larger brittle primary IMCs could promote crack initiation in a solder joint [27].

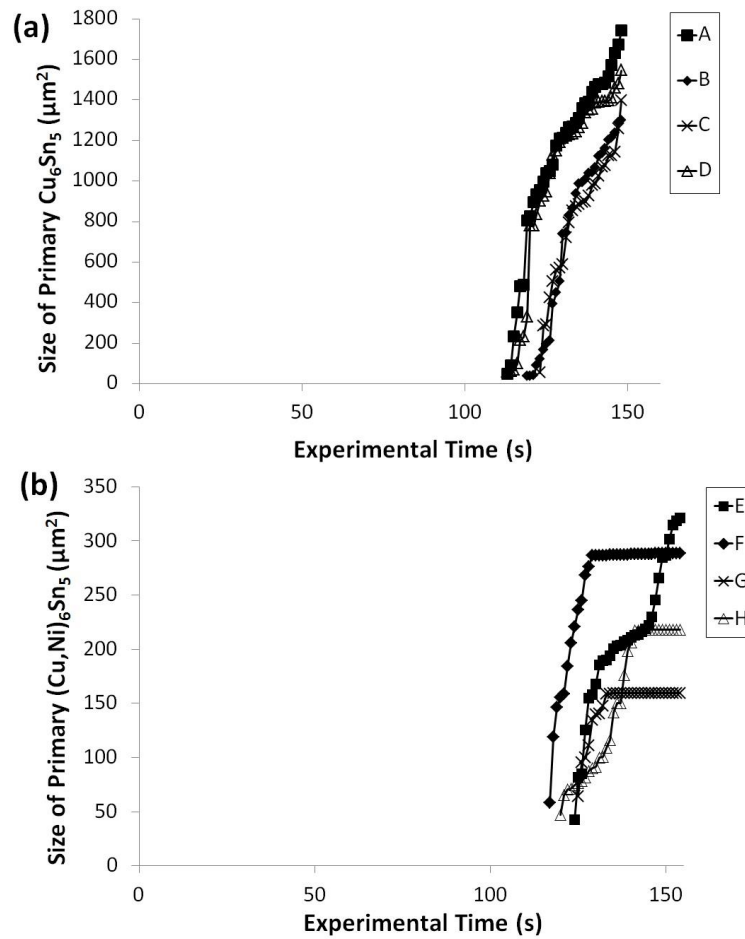


Figure 5: Evolution of primary intermetallic growth of (a) Sn-0.7wt%Cu/Cu and (b) Sn-0.7wt%Cu-0.05wt%Ni/Cu joints, during cooling. A, B, C, D, E, F, G and H are typical individual primary intermetallics chosen for measurements in this study.

Subsequent to the in-situ observation, samples were taken out from the experiment sample cell and prepared for further metallographic observations including SEM coupled with electron dispersive x-ray spectroscopy (EDS). Figure 6 shows the Sn L and Cu K maps of regions containing primary and interfacial  $\text{Cu}_6\text{Sn}_5$  in Sn-0.7wt%Cu/Cu. It can be clearly observed that the Cu K distributions are associated primarily with the large rod-shape primary  $\text{Cu}_6\text{Sn}_5$  and the interfacial IMC layer of Sn-0.7wt%Cu. Figure 7 shows the distribution of Sn L, Ni K and Cu K of Sn-0.7wt%Cu-0.05wt%Ni/Cu which shows that Ni is present in the  $\text{Cu}_6\text{Sn}_5$  reaction layer as  $(\text{Cu,Ni})_6\text{Sn}_5$ . It is not clear if there is any Ni in the primary  $\text{Cu}_6\text{Sn}_5$  from the EDS mapping, but EDS point analysis in Table I confirms that Ni is present in both the primary  $\text{Cu}_6\text{Sn}_5$  and interfacial  $\text{Cu}_6\text{Sn}_5$  with ~2 at% Ni and ~3 at% Ni respectively.



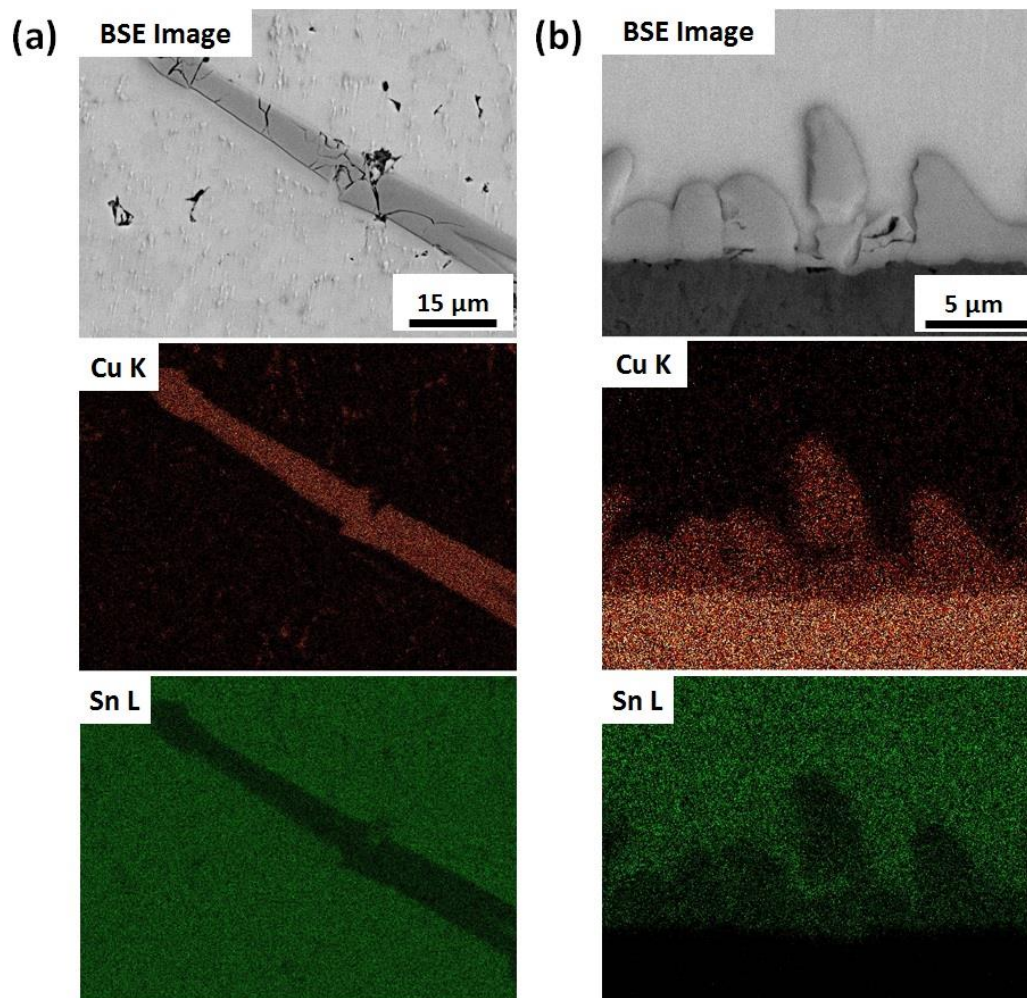


Figure 6: Backscattered SEM image and EDS mapping images of (a) primary  $\text{Cu}_6\text{Sn}_5$  IMC and (b) interfacial  $\text{Cu}_6\text{Sn}_5$  IMC layer and of Sn-0.7wt%Cu/Cu taken subsequent to the synchrotron experiments.

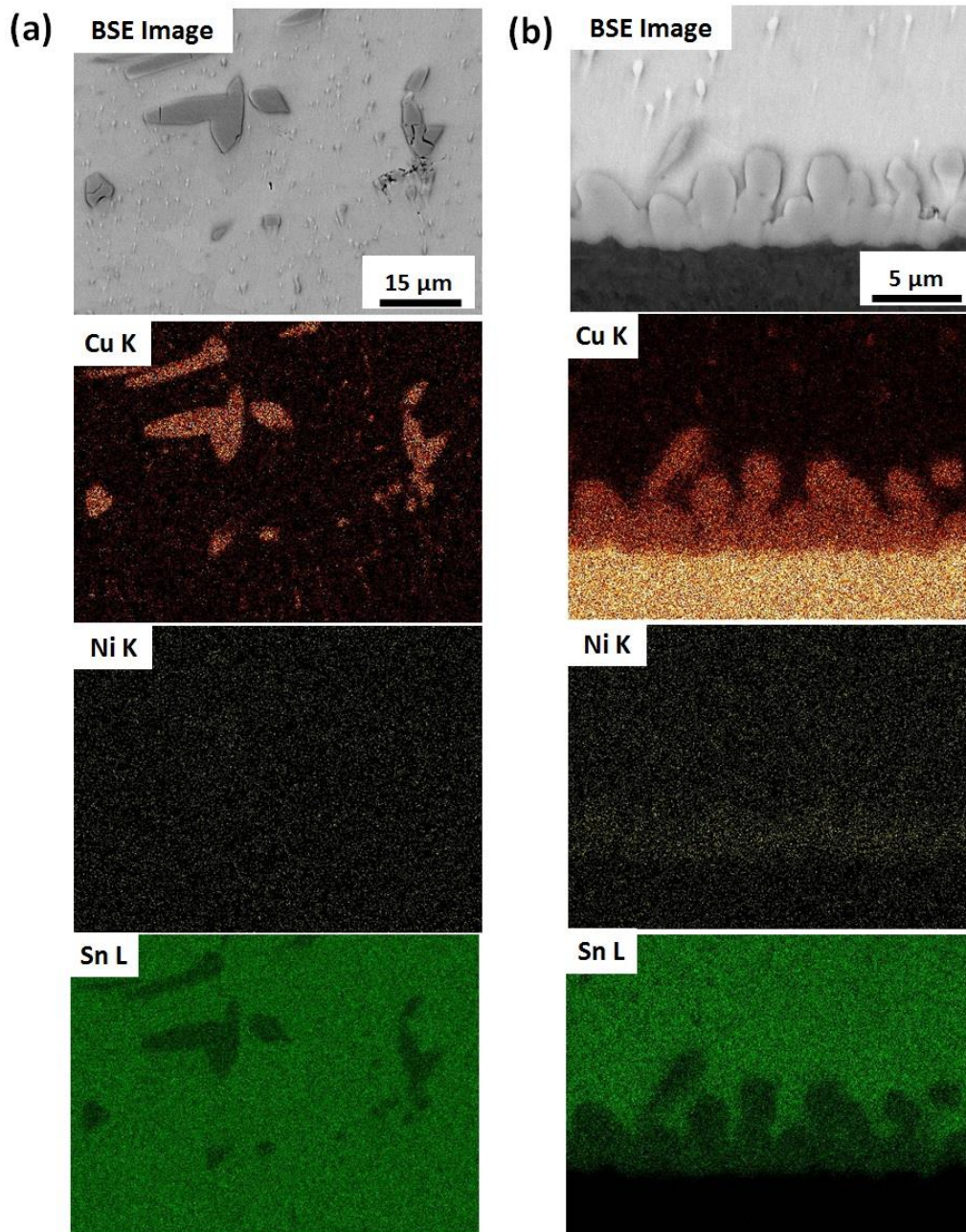


Figure 7: Backscattered SEM image and EDS mapping images of (a) primary  $\text{Cu}_6\text{Sn}_5$  IMC and (b) interfacial  $\text{Cu}_6\text{Sn}_5$  IMC layer and of Sn-0.7wt%Cu-0.05wt%Ni/Cu taken subsequent to the synchrotron experiments.



Table I: SEM-EDS results of the  $(\text{Cu,Ni})_6\text{Sn}_5$  composition in Sn-0.7wt%Cu-0.05wt%Ni for the primary  $\text{Cu}_6\text{Sn}_5$  and interfacial  $\text{Cu}_6\text{Sn}_5$  layer in Sn-0.7wt%Cu-0.05wt%Ni/Cu joints, as well as bulk samples held at 250°C for 24 hours. # = number of points/particles studied.

Mean compositions are shown with standard deviations in brackets.

Number of points/particles studied	#	Sn (at%)	Cu (at%)	Ni (at %)
Primary $\text{Cu}_6\text{Sn}_5$ in joint on Cu	15	48.4 (1.4)	49.7 (1.6)	1.9 (1.3)
Interfacial $\text{Cu}_6\text{Sn}_5$ in joint on Cu	10	48.4 (2.2)	48.4 (2.2)	3.2 (1.1)
Primary $\text{Cu}_6\text{Sn}_5$ in bulk solder	22	49.4 (2.5)	35.8 (1.9)	14.8 (1.9)

To further investigate the pre-existing  $(\text{Cu,Ni})_6\text{Sn}_5$  primary phase observed on heating near the peak reflow temperature in Sn-0.7wt%Cu-0.05wt%Ni/Cu joints (e.g. Figure 4d), an experiment was conducted holding the molten solder at 250°C for 24 hours and subsequently quenching the sample in water. Figure 8 shows the bottom of a quenched sample after 24 hours at 250°C. A layer of particles can be seen clearly and these were found to be  $(\text{Cu,Ni})_6\text{Sn}_5$  containing ~15 at% Ni by EDS analysis (Table I). At 250°C, the density of  $(\text{Cu,Ni})_6\text{Sn}_5$  is ~8180 kg.m<sup>-3</sup> [28] and that of liquid tin is 6980 kg.m<sup>-3</sup> [29], and gravity has concentrated the  $(\text{Cu,Ni})_6\text{Sn}_5$  particles in a layer at the bottom. Note that the whole sample is approximately 8 times taller than the region shown and that the volume fraction of  $(\text{Cu,Ni})_6\text{Sn}_5$  particles at 250°C is actually very low. This result is in reasonable agreement with the Thermo-Calc prediction using the TCSSL v.3 database [30]. It predicts that, at equilibrium at 250°C, Sn-0.7wt%Cu-0.05wt%Ni should consist of 99.16 mass% liquid and 0.84 mass%  $(\text{Cu,Ni})_6\text{Sn}_5$  (0.74 vol%  $(\text{Cu,Ni})_6\text{Sn}_5$ ). This result is also consistent with our past work that has shown Sn-0.7wt%Cu-0.05wt%Ni to be a hypereutectic composition in the  $(\text{Cu,Ni})_6\text{Sn}_5$  primary phase field in contrast to Sn-0.7Cu which is hypoeutectic (in the  $\beta\text{Sn}$  primary phase field) [16] [19].

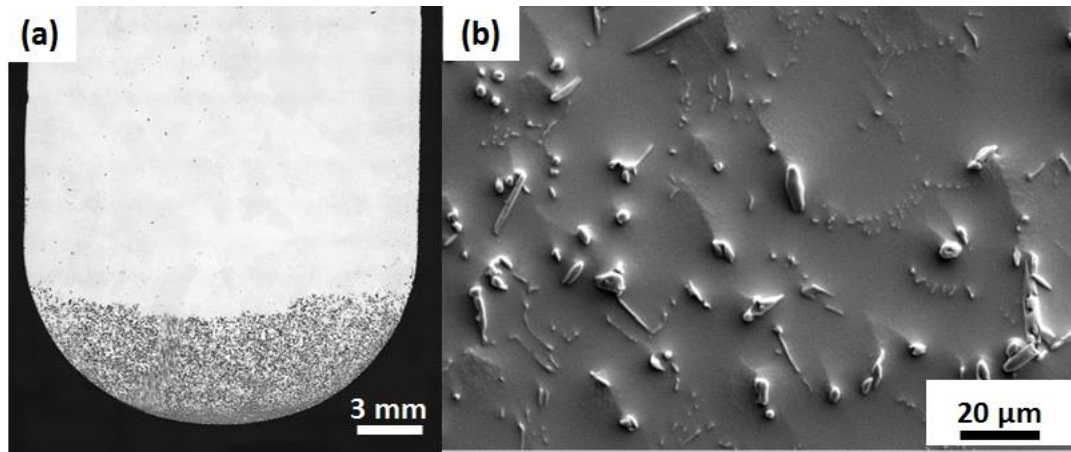


Figure 8: (a) Optical micrograph of Sn-0.7wt%Cu-0.05wt%Ni held at 250°C for 24 hours.  
(b) SEM image of  $(\text{Cu,Ni})_6\text{Sn}_5$  observed in the same sample.

## DISCUSSION

A key finding in this work is that primary  $\text{Cu}_6\text{Sn}_5$  form at higher temperature and are significantly smaller and more numerous in Sn-0.7wt%Cu-0.05wt%Ni /Cu joints than in Sn-0.7wt%Cu /Cu joints.

In both samples at the early stages of molten solder reacting with the Cu substrate, there is a rapid reaction with the Cu substrate and the quick formation of an interfacial IMC layer. The formation of  $\eta\text{-Cu}_6\text{Sn}_5$  interfacial IMC becomes possible after the Cu substrate/liquid solder interface becomes supersaturated in Cu. For Sn-0.7wt%Cu this requires Cu dissolution to the binary liquidus composition at  $T=250^\circ\text{C}$  which is  $\sim 1.2 \text{ wt\% Cu}$  [30]. In contrast, Sn-0.7wt%Cu-0.05wt%Ni is already saturated in Cu at  $250^\circ\text{C}$ , as demonstrated in Figure 8, which is most likely the reason for the earlier formation of primary  $\text{Cu}_6\text{Sn}_5$  in Sn-0.7wt%Cu-0.05wt%Ni/Cu joints.

Figure 8 shows that Sn-0.7wt%Cu-0.05wt%Ni (without a Cu substrate) is a mixture of liquid and  $(\text{Cu,Ni})_6\text{Sn}_5$  at  $250^\circ\text{C}$ . Therefore, primary  $(\text{Cu,Ni})_6\text{Sn}_5$  is not expected to fully melt during reflow soldering, which is consistent with the observations. For example, Figure 4d shows that some pre-existing primary  $(\text{Cu,Ni})_6\text{Sn}_5$  exists before the peak temperature at  $250^\circ\text{C}$ . On cooling, some new primary  $(\text{Cu,Ni})_6\text{Sn}_5$  probably grow from these pre-existing  $(\text{Cu,Ni})_6\text{Sn}_5$  particles rather than nucleating from the liquid. This indicates that the size of primary  $(\text{Cu,Ni})_6\text{Sn}_5$  particles in the original paste will affect the size of primary  $(\text{Cu,Ni})_6\text{Sn}_5$  during

solidification on cooling from the peak temperature. Since the powder in solder paste is made by atomization (at a high cooling rate), the primary  $(\text{Cu,Ni})_6\text{Sn}_5$  in the powder is small and is probably one reason that primary  $(\text{Cu,Ni})_6\text{Sn}_5$  particles in Sn-0.7wt%Cu-0.05wt%Ni/Cu joints are smaller than in Sn-0.7wt%Cu/Cu joints where all primary  $\text{Cu}_6\text{Sn}_5$  must nucleate from the liquid.

A further factor that is expected to affect the size of primary  $\text{Cu}_6\text{Sn}_5$  in joints is the influence of dilute Ni additions on the shape of the Sn-Cu-Ni phase diagram. During soldering to Cu substrates, Cu dissolution will increase the Cu content of the liquid to a composition where the liquid is in equilibrium with the  $\text{Cu}_6\text{Sn}_5$  interfacial reaction layer. For binary Sn-0.7wt%Cu/Cu joints, this is the liquidus composition at  $T=250^\circ\text{C}$  which is  $\sim 1.2$  wt% Cu [30]. For Sn-0.7wt%Cu-0.05wt%Ni/Cu joints, Figure 8 shows that the liquid composition is already in equilibrium with  $(\text{Cu,Ni})_6\text{Sn}_5$  at  $250^\circ\text{C}$ , but further Cu dissolution is expected which will feed the growing IMC layer, enrich the liquid in Cu (as the liquid follows the  $(\text{Cu,Ni})_6\text{Sn}_5$  liquidus contour at  $250^\circ\text{C}$ ), and decrease the Ni content of the  $(\text{Cu,Ni})_6\text{Sn}_5$ . This is consistent with the SEM-EDS results in Table I where the mean composition of the  $(\text{Cu,Ni})_6\text{Sn}_5$  interfacial layer is about 3 at% Ni and the primary  $(\text{Cu,Ni})_6\text{Sn}_5$  is about 2 at% Ni, which is significantly lower than the  $\sim 15$  at% Ni in the primary  $(\text{Cu,Ni})_6\text{Sn}_5$  in Sn-0.7wt%Cu-0.05wt%Ni without a Cu substrate (Table I). Primary  $\text{Cu}_6\text{Sn}_5$  crystals are therefore expected to be forming from liquid of  $\sim \text{Sn-1.2wt\%Cu}$  in Sn-0.7wt%Cu/Cu joints and from hypereutectic liquid containing somewhat less than 0.05 wt% Ni in Sn-0.7Cu-0.05Ni/Cu joints. Thermo-Calc predictions show that even very dilute Ni additions steepen the  $\text{Cu}_6\text{Sn}_5$  liquidus surface significantly compared with the binary  $\text{Cu}_6\text{Sn}_5$  liquidus line [30]. Previous work has shown that composition changes that significantly increase the liquidus slope (while keeping the partition coefficient near-constant) lead to grain refinement [31] [32]. In particular, grain refinement occurs when the growth restriction factor,  $Q = \left( \frac{\partial(\Delta T_s)}{\partial f_s} \right)_{f_s \rightarrow 0}$  or  $Q = - \left( \frac{\partial T}{\partial f_s} \right)_{f_s \rightarrow 0}$ , is increased (where  $\Delta T_s$  is the solute undercooling,  $T$  is the liquidus temperature and  $f_s$  is the fraction of solid) [33, 34]. A higher  $Q$  requires a larger amount of heat to be removed per increment of solid fraction developed in the early stages of growth which restricts crystal growth and also increases the degree of constitutional supercooling in the liquid ahead of the  $\text{Cu}_6\text{Sn}_5$  crystals in which further nucleation events can occur. Thus, the steepening of the  $\text{Cu}_6\text{Sn}_5$  liquidus surface due to dilute Ni additions is

likely to be a factor in the observed grain refinement of primary  $\text{Cu}_6\text{Sn}_5$  in Sn-0.7wt%Cu-0.05wt%Ni/Cu compared with Sn-0.7wt%Cu/Cu joints.

It is possible that differences in the diffusion of Cu into the liquid also play a role. In the Sn-0.7wt%Cu-0.05wt%Ni solders, the interfacial  $\text{Cu}_6\text{Sn}_5$  are a finer needle-like shaped  $\eta$ - $\text{Cu}_6\text{Sn}_5$  [7] with a larger grain boundary area and provide a large area of molten solder in contact with the initial interfacial IMC (e.g. compare Figure 6b and 7b). This contrasts with Sn-0.7wt%Cu solder where scallop shaped  $\eta$ - $\text{Cu}_6\text{Sn}_5$  interfacial IMCs are known to form [7] with a smaller grain boundary area in contact with molten solder. With a larger grain boundary area in contact with the molten solder, Cu atoms diffuse faster. As a result, the Cu concentration from the solder matrix and a faster Cu atom diffusion from the Cu substrate is likely play some role in allowing the primary  $\text{Cu}_6\text{Sn}_5$  intermetallic in the Sn-0.7wt%Cu-0.05wt%Ni/Cu joint to form earlier compared to the Sn-0.7wt%Cu/Cu joint (Figure 1).

Finally, it is natural to consider whether Ni introduces nucleation sites for  $\text{Cu}_6\text{Sn}_5$  to the melt, but we found no evidence for any additional phases and it seems that grain refinement of primary  $\text{Cu}_6\text{Sn}_5$  is mostly due to the effect of Ni on the Sn-Cu-Ni phase diagram.

## CONCLUSIONS

The entire soldering process of solder pastes on Cu substrates was directly observed using a real-time synchrotron imaging technique to investigate the formation and growth of primary  $\text{Cu}_6\text{Sn}_5$  intermetallic in the solder matrix of Sn-0.7wt%Cu/Cu and Sn-0.7wt%Cu-0.05wt%Ni/Cu solder joints. With a 0.05 wt% Ni addition to Sn-0.7wt%Cu, the nucleation and growth of the primary  $\text{Cu}_6\text{Sn}_5$  intermetallic was significantly altered. Primary  $\text{Cu}_6\text{Sn}_5$  formed at higher temperature and were significantly smaller and more numerous in Sn-0.7wt%Cu-0.05wt%Ni/Cu joints than in Sn-0.7wt%Cu/Cu joints. The morphologies of primary  $\text{Cu}_6\text{Sn}_5$  intermetallic are observed to be large and rod shaped in Sn-0.7wt%Cu solder paste while smaller  $\text{Cu}_6\text{Sn}_5$  particles were observed in Sn-0.7wt%Cu-0.05wt%Ni solder paste.

## ACKNOWLEDGEMENTS

The authors gratefully acknowledge financial support from the University of Queensland (UQ)-Nihon Superior (NS) collaboration research project, ARC Linkage project (LP140100485) and Grant-in-Aid for Scientific Research (S) (24226018) from JSPS, Japan. The authors thank Dr. K. Uesugi and Dr. A. Takeuchi of SPring-8, Professor A. Sugiyama

from the Osaka Sangyo University, Dr. T. Nagira from Osaka University and students from the Department of Materials Science and Engineering, Kyoto University. Real-time observation experiments were performed at the SPring-8 BL20XU (2014B1620 and 2015A1675). We acknowledge travel funding provided by the Australian Synchrotron International Synchrotron Access Program (AS/IA143/9218 and AS/IA151/9538) managed by the Australian Synchrotron and funded by the Australian government. Mohd Salleh is financially supported by the Malaysian Education Ministry and University Malaysia Perlis (UniMAP).

## REFERENCES

1. Xianfen Li, Fei Zhang, Fangqiu Zu, Xue Lv, Zhenxing Zhao and Dongdong Yang, *J. Alloys Compd.* 2010, vol. 505, pp. 472-475.
2. Hongqin Wang, Fengjiang Wang, Feng Gao, Xin Ma and Yiyu Qian, *J. Alloys Compd.* 2007, vol. 433, pp. 302-305.
3. P.E. Gary Delserro, In *Delserro Engineering Solutions*, (EE Evaluation Engineering: Easton, PA 2006).
4. A. E. Hammad, *Mater. Des.* 2013, vol. 50, pp. 108-116.
5. Fangjie Cheng, Hiroshi Nishikawa and Tadashi Takemoto, *J. Mater. Sci.* 2008, vol. 43, pp. 3643-3648.
6. Guang Zeng, Stuart D. McDonald, Qinfen Gu, Yasuko Terada, Kentaro Uesugi, Hideyuki Yasuda and Kazuhiro Nogita, *Acta Mater.* 2015, vol. 83, pp. 357-371.
7. Chaoran Yang, Fubin Song and S. W. Ricky Lee, *Microelectronics Reliability* 2014, vol. 54, pp. 435-446.
8. Bismarck Luiz Silva, Noé Cheung, Amauri Garcia and José Eduardo Spinelli, *J. Alloys Compd.* 2015, vol. 632, pp. 274-285.
9. Xiaowu Hu, Ke Li and Zhixian Min, *J. Alloys Compd.* 2013, vol. 566, pp. 239-245.
10. Mustafa Kamal and Tarek El-Ashram, *Mater. Sci. Eng., A* 2007, vol. 456, pp. 1-4.
11. S. McDonald, K. Nogita, J. Read, T. Ventura and T. Nishimura, *J. Electron. Mater.* 2013, vol. 42, pp. 256-262.
12. J. W. Xian, S. A. Belyakov, T. B. Britton and C. M. Gourlay, *J. Alloys Compd.* 2015, vol. 619, pp. 345-355.
13. Randy Schueller, Nathan Blattau, Joelle Arnold and Craig Hillman, *SMTA Journal* 2010, vol. 23, pp. 18-26.
14. Jeong-Won Yoon, Young-Ho Lee, Dae-Gon Kim, Han-Byul Kang, Su-Jeong Suh, Cheol-Woong Yang, Chang-Bae Lee, Jong-Man Jung, Choong-Sik Yoo and Seung-Boo Jung, *J. Alloys Compd.* 2004, vol. 381, pp. 151-157.
15. T. Ventura, C. M. Gourlay, K. Nogita, T. Nishimura, M. Rappaz and A. K. Dahle, *J. Electron. Mater.* 2008, vol. 37, pp. 32-39.
16. C. M. Gourlay, K. Nogita, J. Read and A. K. Dahle, *J. Electron. Mater.* 2010, vol. 39, pp. 56-69.
17. K. Nogita, *Intermetallics* 2010, vol. 18, pp. 145-149.
18. K. Nogita, C. M. Gourlay and T. Nishimura, *JOM* 2009, vol. 61, pp. 45-51.
19. C. M. Gourlay, K. Nogita, A. K. Dahle, Y. Yamamoto, K. Uesugi, T. Nagira, M. Yoshiya and H. Yasuda, *Acta Mater.* 2011, vol. 59, pp. 4043-4054.

20. Tongmin Wang, Peng Zhou, Fei Cao, Huijun Kang, Zongning Chen, Yanan Fu, Tiqiao Xiao, Wanxia Huang and Qingxi Yuan, *Intermetallics* 2015, vol. 58, pp. 84-90.
21. L. Qu, N. Zhao, H. J. Zhao, M. L. Huang and H. T. Ma, *Scripta Mater.* 2014, vol. 72-73, pp. 43-46.
22. M. A. A. Mohd Salleh, S. D. McDonald, H. Yasuda, A. Sugiyama and K. Nogita, *Scripta Mater.* 2015, vol. 100, pp. 17-20.
23. Hideyuki Yasuda, Itsuo Ohnaka, Koichi Kawasaki, Akira Sugiyama, Tetsutaro Ohmichi, Jun Iwane and Keiji Umetani, *J. Cryst. Growth* 2004, vol. 262, pp. 645-652.
24. Kazuhiro Nogita, Hideyuki Yasuda, Arvind Prasad, Stuart D. McDonald, Tomoya Nagira, Noriaki Nakatsuka, Kentaro Uesugi and David H. StJohn, *Mater. Charact.* 2013, vol. 85, pp. 134-140.
25. Ryosuke Tajima and Yoichiro Kato, *Field Crops Research* 2011, vol. 121, pp. 460-463.
26. J. S. Karppinen, T. Laurila, T. T. Mattila and M. Paulasto-Kröckel, *J. Electron. Mater.* 2012, vol. 41, pp. 3232-3246.
27. Mingna Wang, Jianqiu Wang, Hao Feng and Wei Ke, *Mater. Sci. Eng., A* 2012, vol. 558, pp. 649-655.
28. K. Nogita, D. Mu, S. D. McDonald, J. Read and Y. Q. Wu, *Intermetallics* 2012, vol. 26, pp. 78-85.
29. Marc J Assael, Konstantinos Kakosimos, R Michael Banish, Jürgen Brillo, Ivan Egry, Robert Brooks, Peter N Quested, Kenneth C Mills, Akira Nagashima and Yuzuru Sato, *Journal of Physical and Chemical Reference Data* 2006, vol. 35, pp. 285-300.
30. 2015, vol. TCSLD Database version 3.0.
31. M. J. Bermingham, S. D. McDonald, K. Nogita, D. H. St. John and M. S. Dargusch, *Scripta Mater.* 2008, vol. 59, pp. 538-541.
32. Mark Easton and David StJohn, *Metallurgical and Materials Transaction A* 1999, vol. 30, pp. 1625-1633.
33. T. E. Quested, A. T. Dinsdale and A. L. Greer, *Acta Mater.* 2005, vol. 53, pp. 1323-1334.
34. R. Schmid-Fetzer and A. Kozlov, *Acta Mater.* 2011, vol. 59, pp. 6133-6144.

## **Chapter 6 Assembly processing and operating conditions: the effects of intrinsic and extrinsic reinforcement of solder joints.**

This chapter focuses on the effect of processing and operating conditions on the microstructure and properties of intrinsic and extrinsic reinforced solder joints. The microstructure of the reinforced solder joints, particularly differences in the interfacial intermetallic layer thickness caused by the extrinsic reinforcing particles during multiple reflow soldering and isothermal annealing was investigated. Solder joint strength was then investigated as an indicator of the performance of the reinforced solder.

In Paper 7 of the thesis titled “Suppression of  $\text{Cu}_6\text{Sn}_5$  in  $\text{TiO}_2$  reinforced solder joints after multiple reflow cycles” the effects of multiple reflow cycles on  $\text{TiO}_2$  reinforced Sn-0.7Cu solder fabricated by a powder metallurgy microwave sintering technique was investigated. In an electronic assembly, with complex 3D packaging and multiple layer substrates, solder joints are often subjected to multiple heating cycles. Hence it is important to understand the effects of multiple reflow cycles in solder joints. Compared to  $\text{TiO}_2$ -free equivalents, a relative suppression of the  $\text{Cu}_6\text{Sn}_5$  phase, both as primary crystals and as an interfacial layer was observed. The likely mechanism of  $\text{Cu}_6\text{Sn}_5$  layer suppression relates to the accumulation of  $\text{TiO}_2$  at the interfacial  $\text{Cu}_6\text{Sn}_5$  layer hindering the diffusion and dissolution pathways of Cu from the substrate into the molten solder. The suppression of  $\text{Cu}_6\text{Sn}_5$  results in  $\text{TiO}_2$  reinforced solder joints having a higher shear strength after multiple reflow cycles compared to Sn-0.7Cu solder joints.

In Paper 8, titled “Effects of Ni and  $\text{TiO}_2$  additions in as-reflowed and annealed Sn0.7Cu solders on Cu substrates” reports the effect of Ni,  $\text{TiO}_2$  and a combination of both additions on the suppression of interfacial  $\text{Cu}_6\text{Sn}_5$  and  $\text{Cu}_3\text{Sn}$  in Sn-0.7Cu after isothermal annealing. The solder joint strength of the fabricated samples was also studied. In this paper, microstructure analysis reveals the combination of both additions (Ni and  $\text{TiO}_2$ ) resulted in the suppression of the  $\text{Cu}_6\text{Sn}_5$  and  $\text{Cu}_3\text{Sn}$  interfacial layers. Using a high speed shear solder ball tester, the solder joint strength, total fracture energy and fracture modes were analysed. It was found a combination of Ni and  $\text{TiO}_2$  additions to Sn-0.7Cu resulted in a superior shear strength and fracture energy of the solder joints as a result of the interfacial layer suppression after isothermal annealing.



## **Paper 7: Suppression of $\text{Cu}_6\text{Sn}_5$ in $\text{TiO}_2$ reinforced solder joints after multiple reflow cycles**

Mohd Arif Anuar Mohd Salleh, Stuart D. McDonald, Christopher M. Gourlay,  
Hideyuki Yasuda, Kazuhiro Nogita

**Materials & Design**, 108 (2016), 418-428

## **Suppression of Cu<sub>6</sub>Sn<sub>5</sub> in TiO<sub>2</sub> reinforced solder joints after multiple reflow cycles**

M. A. A. Mohd Salleh<sup>a,b,\*</sup>, S. D. McDonald<sup>a</sup>, C.M. Gourlay<sup>c</sup>, H. Yasuda<sup>d</sup>, K. Nogita<sup>a</sup>

<sup>a</sup>Nihon Superior Centre for the Manufacture of Electronic Materials (NS CMEM), School of Mechanical and Mining Engineering, The University of Queensland, 4072 St Lucia, Queensland, Australia.

<sup>b</sup>Centre of Excellence Geopolymer and Green Technology, School of Materials Engineering, Universiti Malaysia Perlis (UniMAP), Taman Muhibbah 02600, Jejawi, Arau, Perlis, Malaysia.

<sup>c</sup>Department of Materials, Imperial College, London SW7 2AZ, United Kingdom.

<sup>d</sup>Department of Materials Science and Engineering, Kyoto University, Sakyo-ku, Kyoto 606-8501, Japan.

\*Corresponding author: Room 634, 49 Jocks Rd., St Lucia, Brisbane, QLD 4072, Australia

Email: m.mohdsalleh@uq.edu.au / arifanuar@unimap.edu.my ; Tel: +61 435 946 670

## Abstract

In the current generation of 3D electronic packaging, multiple reflows are often required during soldering. In addition, electronic packages may be subjected to additional solder rework or other heating processes. This paper investigates the effects of multiple reflow cycles on  $\text{TiO}_2$  reinforced Sn-0.7Cu solder fabricated by a powder metallurgy microwave sintering technique. Compared to  $\text{TiO}_2$ -free equivalents, a relative suppression of the  $\text{Cu}_6\text{Sn}_5$  phase, both as primary crystals and as an interfacial layer was observed. The likely mechanism relates to the  $\text{TiO}_2$  nanoparticles promoting nucleation and decreasing the amount of time that liquid is in contact with the interfacial layer. The  $\text{TiO}_2$  particles appear to stabilise the interfacial  $\text{Cu}_6\text{Sn}_5$  layer and result in a more planar morphology. The suppression of  $\text{Cu}_6\text{Sn}_5$  results in  $\text{TiO}_2$  reinforced solder joints having a higher shear strength after multiple reflow cycles compared to Sn-0.7Cu solder joints.

Keywords: Lead-free solder, intermetallic compound, synchrotron, multiple reflow, shear strength.

## 1.0 Introduction

Solder alloys play a crucial role in determining performance and reliability in the assembly and interconnection of electronic products and have electrical, thermal and mechanical functions [1, 2]. The relative importance of solder alloy properties has increased due to continued miniaturization of microelectronic circuitry and the use of finer pitch interconnects. Higher functional densities in printed circuit boards (PCB) have been made possible by surface mount technology (SMT) using reflow soldering, often with multiple reflow cycles. Other heating cycles can be present in manufacturing such as additional solder rework [3]. One challenge associated with current generation Pb-free solder alloys is that during multiple thermal cycles, the joint strength may degrade due to the rapid growth of the interfacial layer of intermetallic compounds [4-12]. In a typical Pb-free solder joint,  $\text{Cu}_6\text{Sn}_5$ , which may form either as primary crystals or an interfacial layer during soldering can play a determining role in solder joint strength. There is evidence that by suppressing the  $\text{Cu}_6\text{Sn}_5$  interfacial layer, solder joint properties could be improved [13-17] and as such there are benefits associated with controlling the growth of this layer during multiple reflows.

It has recently been reported that additions of reinforcement to a variety of solder matrices, with compounds including silicon carbide (SiC) [18-20], nickel oxide (NiO) [21], alumina ( $\text{Al}_2\text{O}_3$ ) [22-24], zirconia ( $\text{ZrO}_2$ ) [25-28], titanium oxide ( $\text{TiO}_2$ ) [29-34] and silicon nitride ( $\text{Si}_3\text{N}_4$ ) [35, 36] result in suppression of the growth of the interfacial layer during soldering [37]. In our recent study [38], we developed a method of fabricating a reinforced solder using a powder metallurgy microwave sintering method that results in a homogeneous distribution of  $\text{TiO}_2$  in the solder material and an improvement in the bulk solder material thermal and mechanical properties. However, properties related to the solder joint strength after multiple reflows of this reinforced solder are yet to be explored.

This paper investigates the effects of multiple reflow cycles on the  $\text{TiO}_2$  reinforced Sn-0.7Cu solder joint by comparing it with a base Sn0.7wt%Cu (unreinforced) solder joint. This includes investigating the evolution of  $\text{Cu}_6\text{Sn}_5$  intermetallics both as a primary phase in the bulk solder and as an interfacial compound layer during multiple reflow and its effect on the solder joint strength. Since it is impossible to investigate the evolution of primary  $\text{Cu}_6\text{Sn}_5$  in real time using conventional methods, advanced real time experimental techniques including synchrotron X-ray imaging were used.

## **2.0 Experimental**

### **2.1 Sample Fabrication**

In this study, Sn-0.7Cu solder powders of spherical morphology with an average particle size of 45  $\mu\text{m}$  were supplied by Nihon Superior Co. Ltd. and used for the base matrix material, along with 99.7% purity  $\text{TiO}_2$  anatase powder supplied by Sigma Aldrich, which had an average particle size of <50 nm. To fabricate the Sn-Cu containing  $\text{TiO}_2$  nano-composite solder, 1wt% of  $\text{TiO}_2$  particles were incorporated into the Sn-0.7Cu solder matrix using a powder metallurgy route similar to previous research [38]. The composite solder materials were homogeneously mixed with the base matrix powder in an airtight container using a tubular mixer for 1 hour. The solder mixtures were uniaxially compacted in a 12-mm diameter mold at 120 bar, and the compacted discs were microwave sintered in an inert argon atmosphere. The cycle involved approximately 3 minutes of microwave sintering at 1000W to achieve a sintering temperature of 185  $^{\circ}\text{C}$  ( $\sim 0.8T_m$ ). For comparing with the base material, a Sn0.7Cu alloy was prepared by compacting the Sn0.7wt%Cu solder powder and sintering using the same method as the composite solder without the addition of  $\text{TiO}_2$  particles. Sintered samples were then cold rolled to produce thin solder sheets for solder ball fabrication. Thin solder sheets of approximately 100  $\mu\text{m}$  thickness were used for synchrotron x-ray imaging experiment while thinner sheets (approximately 23  $\mu\text{m}$ ) were used for solder ball fabrication as subsequently described.

### **2.2 Solder ball fabrication**

Solder balls of approximately 600  $\mu\text{m}$  diameter size were prepared by punching the thin (23  $\mu\text{m}$ ) solder sheet using a 2.5 mm diameter metal punch. The punched solder sheets were then dipped in a rosin mildly activated (RMA) flux and placed on a Pyrex sheet. Using a controlled heating temperature, the 2.5 mm diameter solder discs were melted using a reflow oven at 250  $^{\circ}\text{C}$  maximum temperature with  $\text{N}_2$  gas flow. The solder discs adopted a spherical morphology under the action of surface tension during melting, resulting in solder balls of approximately 600  $\mu\text{m}$  in diameter. To ensure uniformity of size the solder balls were passed through a series of sieves eliminating balls that were substantially bigger or smaller than 600  $\mu\text{m}$ . In making solder joints, the fabricated balls were reflowed at 127s of reflow time (time above 227 $^{\circ}\text{C}$ ) on a 600  $\mu\text{m}$  ball pitch size of Cu substrate printed circuit board (PCB) with organic soldering preservative (OSP) surface finish with the aid of small amount of RMA flux using a desktop reflow oven with  $\text{N}_2$  gas flow (reflow temperature profile shown in Figure 1a).

### **2.3 Thermal Analysis**

To investigate the thermal reactions of a solder joint during soldering and multiple reflow cycles, a Mettler Toledo differential scanning calorimetry (DSC) under a N<sub>2</sub> atmosphere was used. In this experiment, the solder samples underwent a series of reflow cycles in a DSC which was prepared as in Figure 1b. The solder balls were coated with small amount of RMA flux and placed on a 600 µm ball pitch size Cu substrate printed circuit board (PCB) with organic soldering preservative (OSP) surface finish and placed in an encapsulated aluminium pan (substrate side down). A hole was made on the aluminium pan lid for flux outgas venting purposes. Six samples of each of Sn-0.7Cu and Sn-0.7Cu+TiO<sub>2</sub> were heated at 20 °C/min to 250 °C and cooled down at room temperature at 20 °C/min for six cycles. Thermal reactions in each reflow cycle were determined based on the endothermic (heating) and exothermic (cooling) temperature curves.

### **2.4 Synchrotron X-ray Radiography Imaging**

The real time observation experiments were performed at BL20XU beamline in the SPring-8 synchrotron using an in-situ synchrotron X-ray real time solidification observation setup developed in previous research [39-42]. The parameters were chosen to allow a high degree of coherence, absorption contrast and phase contrast enabling boundaries in the sample to be observed on transmitted images. These image signals were then converted into a digital format of 2000 X 2000 pixels at 1 mm X 1 mm giving a resolution of 0.477 µm per pixel. A planar undulator was used as a light source and the radiation was monochromatized with Si double crystal monochromators. An exposure time of 1s per frame to capture the images was used. To mimic the process of reflow soldering, a furnace with graphite heating elements where heat is transferred through radiation in an enclosed sample chamber was used. The approximately 100 µm thin rolled solder foils were cut into 3 x 2 mm<sup>2</sup> pieces and placed vertically on thin 100 µm Cu substrates. The observation window area of 10 x 10 mm<sup>2</sup> with a vent for flux outgassing was made by using a 100 µm thickness polytetrafluoroethylene (PTFE) sheet placed between two SiO<sub>2</sub> plates. Samples were set to be heated from room temperature to approximately 250°C at 20°C /min and cooled down at approximately 20°C/min to 180°C for six cycles. The soldering temperature profiles for the experiments are shown in Figure 1c.

### **2.4 High Speed Shear Solder Joint Test**

The solder joint strength after multiple reflows was tested using a Dage 4000 high speed bond tester at 60 µm shear height. A 50N shear load cartridge was used at 100 mm/s and 2000 mm/s shear speed. The high speed shear test sample positioning is as shown in Figure

1d. The microstructures and X-ray microanalysis of the samples were analysed using a JEOL 6610 scanning electron microscopy (SEM)/energy dispersive X-ray spectroscopy (EDS) in secondary and backscattered electron imaging mode at an accelerating voltage of 20 kV. For a top-down view of the interfacial layer, solder joints were etched using a solution of 2% 2-nitrophenol, 5% sodium hydroxide and 93% of distilled water. Before detailed SEM imaging and X-ray microanalysis were conducted, samples were thoroughly cleaned and rinsed using acetone in an ultrasonic bath.

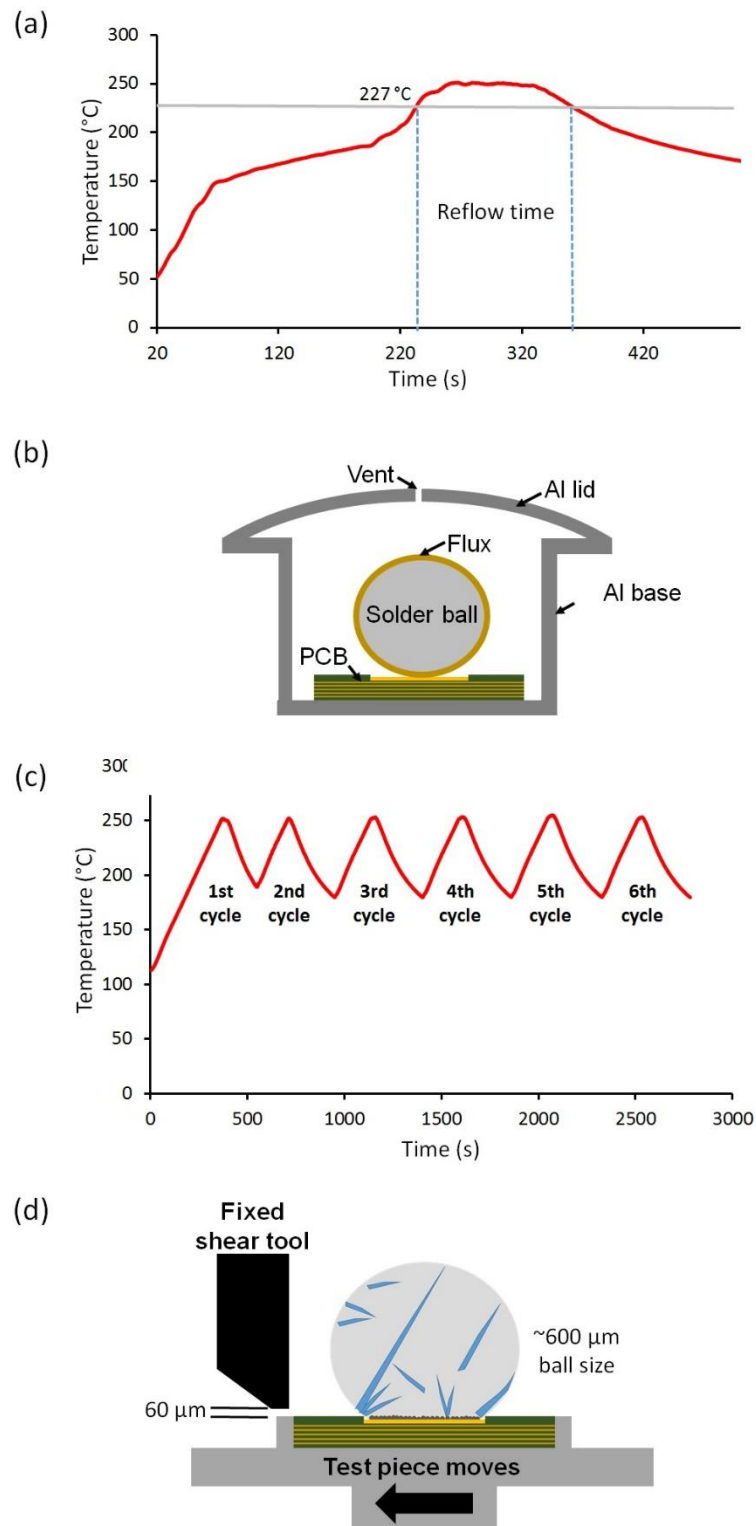


Figure 1: a) Reflow temperature profile using benchtop reflow oven, b) multiple reflow cycle temperature profile for in-situ synchrotron X-ray imaging experiment and c) high speed shear test setup and sample positioning.



### **3.0 Results and Discussion**

#### **3.1 Thermal reactions in solder joints during multiple reflow**

Thermal reactions during heating and cooling of solder joints are important in understanding the reactions of the solid-liquid-solid transition during soldering. Figure 2 shows a differential scanning calorimetry curve of multiple reflow cycles of Sn-0.7Cu with TiO<sub>2</sub> (Figure 1a and 1b) and Sn-0.7Cu during cooling and heating (Figure 1c and 1d). During heating, the endothermic melting peaks, were consistent throughout the multiple cycles for both type of solder joints. However, during cooling the exothermic solidification peak varied with each reflow cycle. From the DSC results, the undercooling (the onset on heating minus the onset on cooling) and liquid contact temperature range (end heating - end cooling) of both solder joints were analysed. It is observed that generally as the number of heating cycles increases, Sn-0.7Cu solder joints displayed a higher undercooling compared to Sn-0.7Cu with TiO<sub>2</sub> as in Figure 3a. In addition, the range of temperatures for which liquid is present in Sn-0.7Cu solder joints is higher compared to Sn-0.7Cu with TiO<sub>2</sub>. In other words, by promoting nucleation earlier, the TiO<sub>2</sub> particles reduce the time of contact between the IMC layer and the liquid phase during solidification. In both solder joints, a trend of increased undercooling was observed as the number of reflow cycles increases. It is likely Cu from the substrate dissolves more into the molten solder with every reflow cycle and increases the Cu content in the solder allowing it to become slightly increasingly hyper eutectic. During reactive dissolution of the Cu substrate during the soldering of Sn-0.7Cu at 250 °C, the liquid will become enriched in Cu to a maximum solubility limit of approximately 1.2wt%Cu [41]. However the small increment in Cu concentration is not able to be detected by DSC as shown in Figure 2.

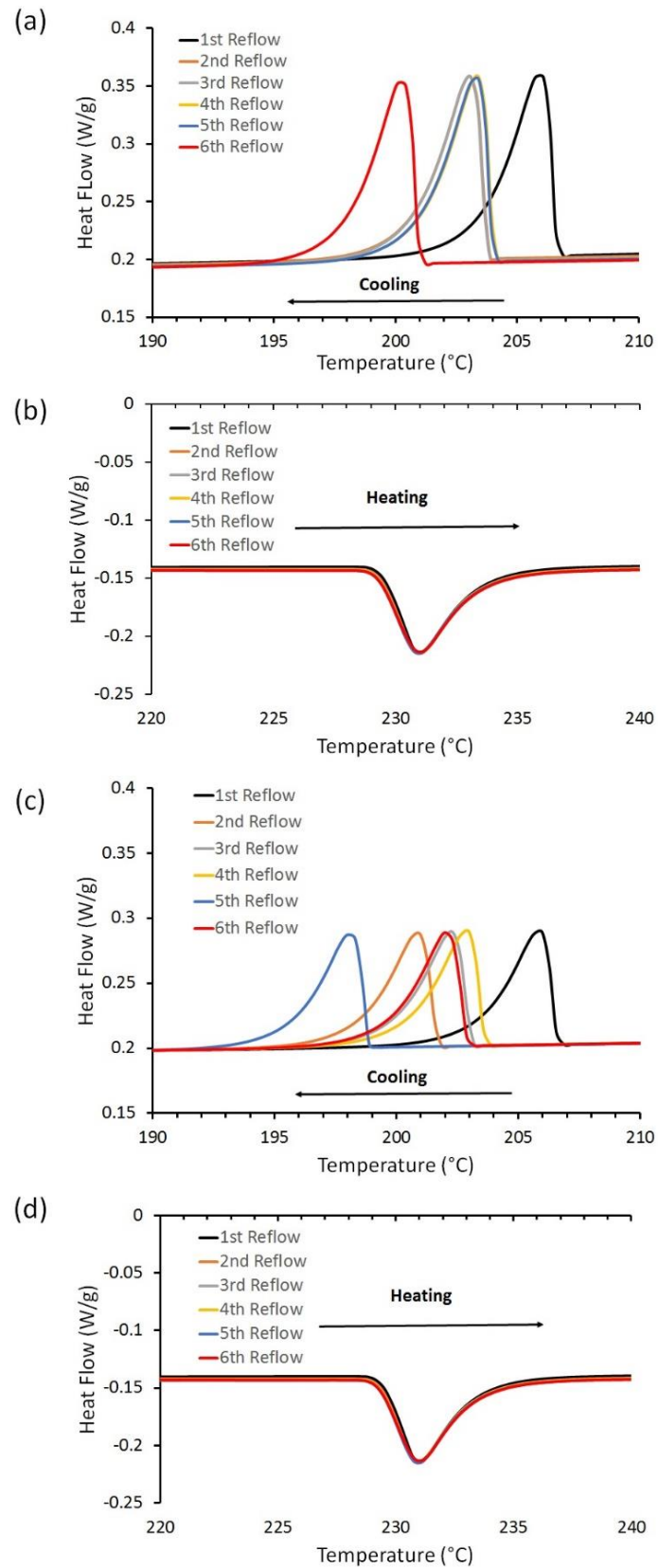


Figure 2: Typical differential scanning calorimetry curve of multiple reflow cycle of Sn-0.7Cu with TiO<sub>2</sub> at (a) cooling (b) heating and Sn-0.7Cu at (c) cooling (d) heating.

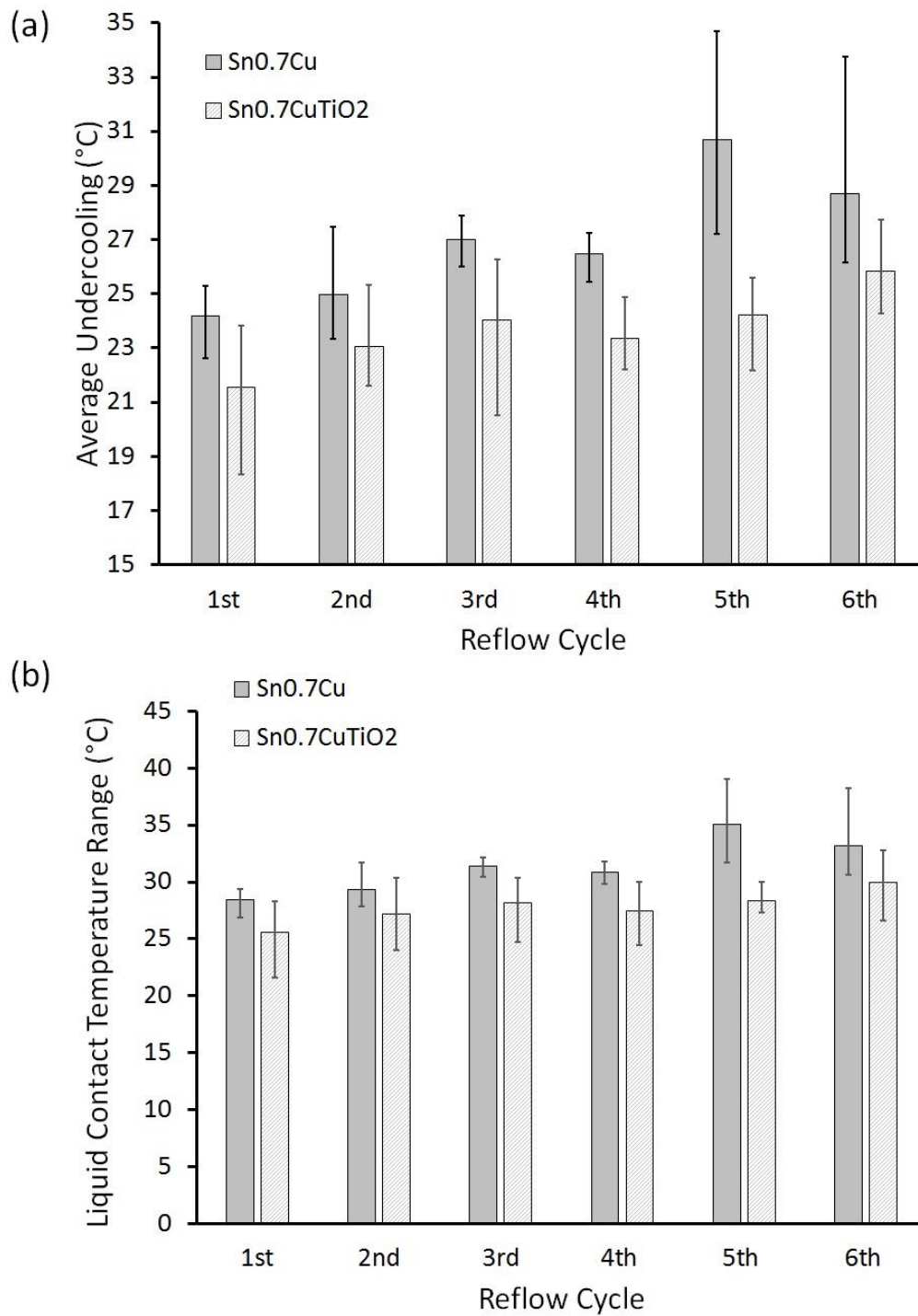


Figure 3: (a) Average undercooling and (b) liquid contact temperature range of Sn-0.7Cu and Sn-0.7Cu with TiO<sub>2</sub> during multiple reflow cycle.

## 3.2 Microstructure analysis

### 3.2.1 *Cu<sub>6</sub>Sn<sub>5</sub> primary growth during multiple reflow*

The nucleation and growth of Cu<sub>6</sub>Sn<sub>5</sub> primary crystals during simulated multiple reflow cycles was observed using in-situ synchrotron X-ray imaging in both Sn-0.7Cu and Sn-0.7Cu with TiO<sub>2</sub>. Figure 4 shows the distribution of Cu<sub>6</sub>Sn<sub>5</sub> primary crystals during solidification just prior to Sn nucleation during each reflow cycle of both solder joints. In order to quantify the nucleation rate and growth of primary Cu<sub>6</sub>Sn<sub>5</sub> during multiple reflow cycles, the apparent numbers and total length of primary Cu<sub>6</sub>Sn<sub>5</sub> primary were measured just prior to Sn nucleation during each reflow cycle. The apparent numbers and length were then divided by the given area resulting in the number density and total length. Figure 5 shows the number density and total length of Cu<sub>6</sub>Sn<sub>5</sub> primary crystals during each reflow cycle in both the Sn-0.7Cu and Sn-0.7Cu with TiO<sub>2</sub> solder joints. Results in Figure 5a indicate that the number density of primary Cu<sub>6</sub>Sn<sub>5</sub> crystals in Sn-0.7Cu containing TiO<sub>2</sub> solder joint is initially higher compared to Sn-0.7Cu and this number reduces after multiple reflow. As shown in Figure 5b, the total length of Cu<sub>6</sub>Sn<sub>5</sub> primary crystals in the reinforced solder is decreased indicating the crystals were able to be suppressed compared to Sn-0.7Cu. It is acknowledged that the numbers and length of primary Cu<sub>6</sub>Sn<sub>5</sub> in TiO<sub>2</sub> containing solder measured using this synchrotron technique may not include small particles of Cu<sub>6</sub>Sn<sub>5</sub> below the resolution limitations of this technique and thus the measured numbers and length were should be considered apparent values. The results indicate that during reflow cycles, TiO<sub>2</sub> reinforcements in the bulk solders may act as nucleation sites to both primary Cu<sub>6</sub>Sn<sub>5</sub> and  $\beta$ -Sn, as also supported by the DSC results (Figure 3).

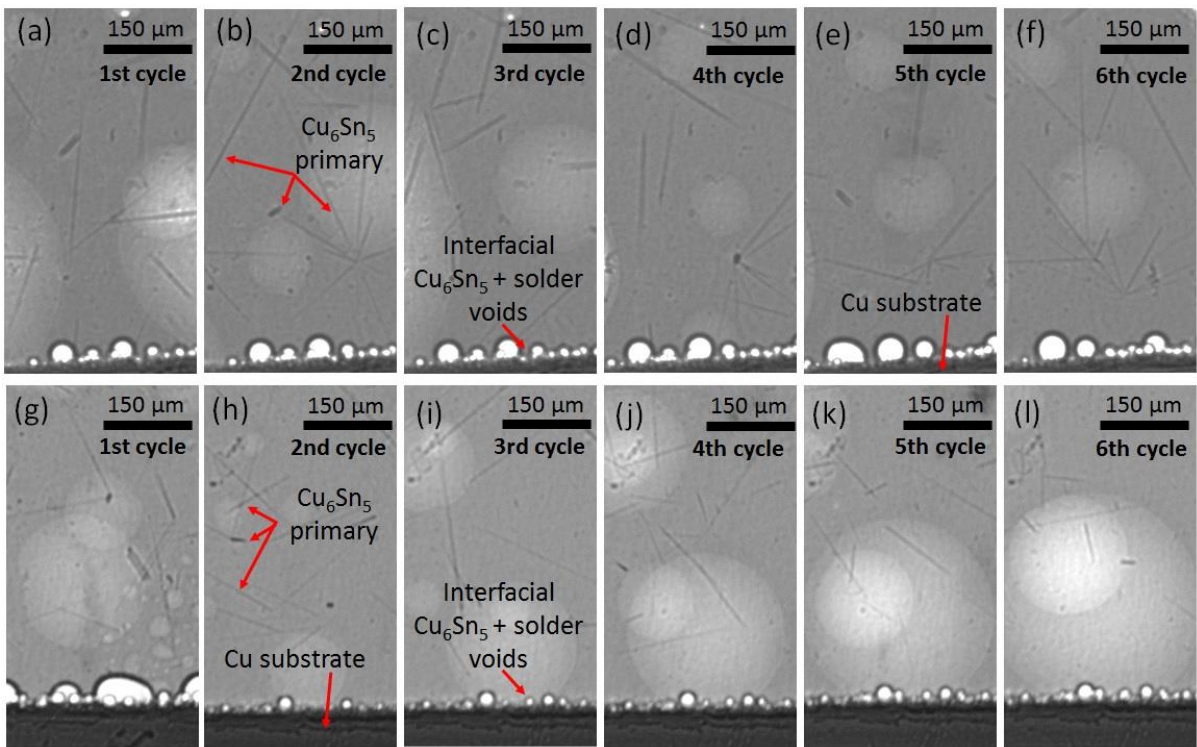


Figure 4: Real-time observations of reactions of (a-f) Sn-0.7Cu solder and (g-l) Sn-0.7Cu solder with TiO<sub>2</sub> between Cu substrate before Sn nucleation during each reflow cycle.

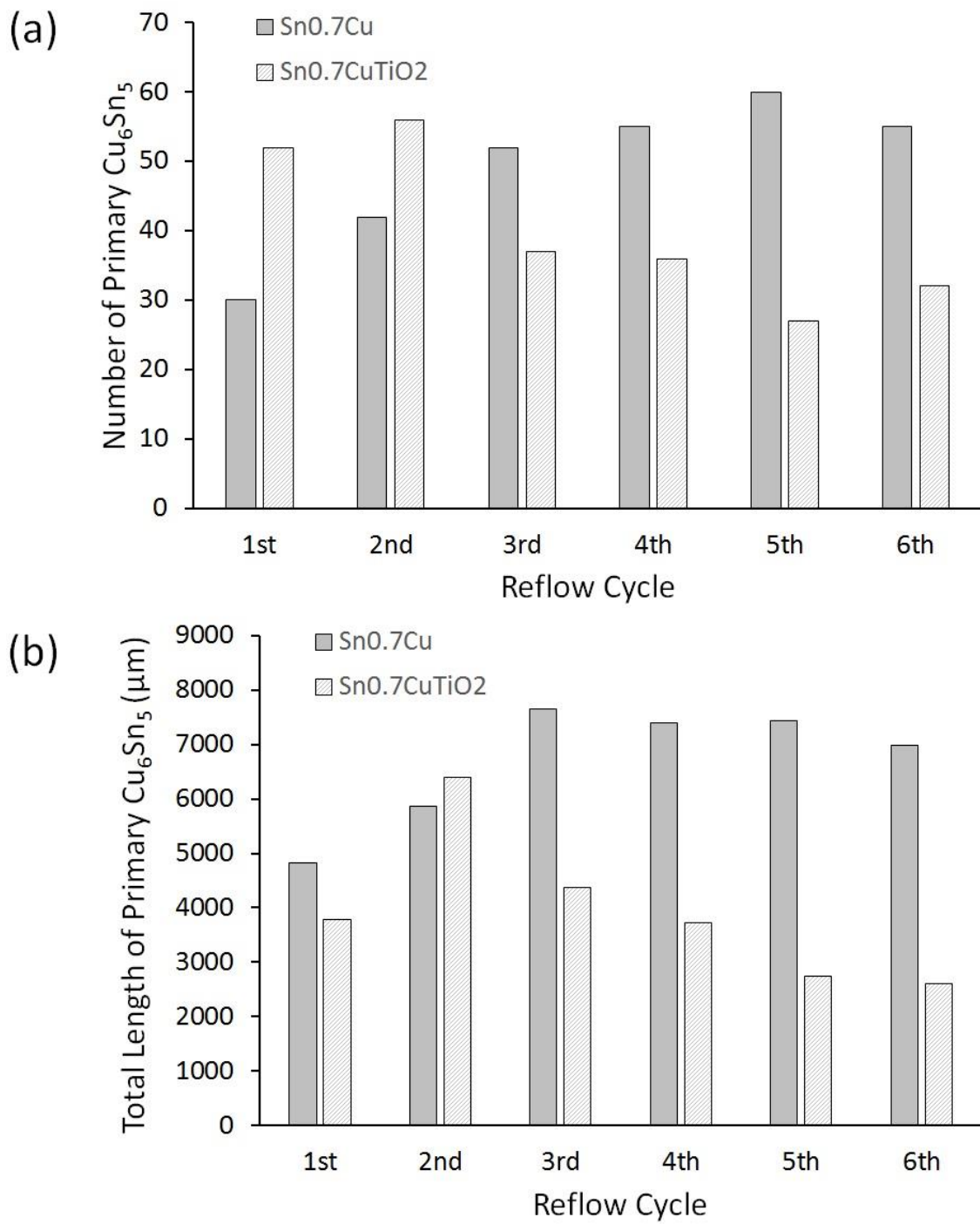


Figure 5: (a) Number and (b) total length of  $\text{Cu}_6\text{Sn}_5$  primary during each reflow cycle in Sn-0.7Cu solder joint and Sn-0.7Cu with  $\text{TiO}_2$  solder joint.

### 3.2.2 Interfacial $\text{Cu}_6\text{Sn}_5$ growth during multiple reflow

As can be observed in Figure 6 and 7, the interfacial  $\text{Cu}_6\text{Sn}_5$  layer present in Sn-0.7Cu/Cu and Sn-0.7Cu+TiO<sub>2</sub>/Cu after multiple reflow cycles respectively, differs significantly. In Sn-0.7wt%Cu/Cu, the interfacial  $\text{Cu}_6\text{Sn}_5$  crystals were more needle-like and scalloped in morphology while in TiO<sub>2</sub> containing solders, the interfacial  $\text{Cu}_6\text{Sn}_5$  were shorter and more faceted. In Sn-0.7Cu, heterogeneous growth of the interfacial layer was observed where the majority of the growth comes from select grains that advance a long way from the interface, which is not observed in TiO<sub>2</sub> containing solder. These  $\text{Cu}_6\text{Sn}_5$  crystals that manage to grow ahead of the interface will reject Sn solute laterally and this will further limit the growth of the neighbouring grains. The TiO<sub>2</sub> particles appear to hinder the growth of advancing grains and the IMC layer appears to be inherently more stable. In addition to cross-section observations, these solder joint samples were etched in to remove the Sn and reveal the morphology of the  $\text{Cu}_6\text{Sn}_5$ . Top-down (viewing direction normal to the substrate) observations of interfacial  $\text{Cu}_6\text{Sn}_5$  layers present in Sn-0.7Cu/Cu and Sn-0.7Cu+TiO<sub>2</sub>/Cu after multiple reflow cycles are shown in Figure 8 and 9 respectively. In the TiO<sub>2</sub> containing solders, a more faceted and flat morphology of the interfacial  $\text{Cu}_6\text{Sn}_5$  was observed as indicated in the red circle in Figure 9f.

To measure the average interfacial  $\text{Cu}_6\text{Sn}_5$  thickness, the total area of the interfacial layer was divided by the total length measured from the cross-sectioned samples. Figure 10a compares the average interfacial layer thickness growth over multiple reflow cycles. For Sn-0.7Cu/Cu, the average interfacial layer grows from ~5.2  $\mu\text{m}$  after the first reflow cycle to a maximum of ~13  $\mu\text{m}$  thickness after multiple reflows. In the Sn-0.7Cu+TiO<sub>2</sub>/Cu, it shows that the growth of the interfacial layer is relatively suppressed and grows from an initial average of ~4.2  $\mu\text{m}$  thickness after the first reflow cycle to a maximum of ~8  $\mu\text{m}$  thickness after multiple reflows.

The thickness of the interfacial layer in diffusion couples can be generally expressed by an empirical power-law equation;

$$\delta = kt^n \quad (1)$$

where  $\delta$  is the average thickness of the interfacial layer,  $k$  is the growth rate constant,  $n$  is the time exponent and  $t$  is the reflow time (time above liquid temperature during reflow). In obtaining the growth rate constant ( $k$ ) and time exponent ( $n$ ), linear fitting results of a log-log graph of interfacial layer thickness of Sn-0.7Cu solder joint and Sn-0.7Cu with TiO<sub>2</sub> solder joint with reflow time were plotted as in Figure 10b. Reflow time is considered to be

the time above 227 °C, and each cycle in this experiment was of 127 s reflow time. Results shows that Sn-0.7Cu has a slightly higher growth rate constant compared to the reinforced solder with values of 0.52 and 0.43  $\mu\text{m/s}$  respectively. Both solder materials displayed a similar time exponent value of approximately 0.5 and this  $t^{\frac{1}{2}}$  dependence indicates that the interfacial layer thickness of both samples is controlled by volume diffusion or chemical reaction [43]. Tang et al. [44] in their recent study of  $\text{TiO}_2$  additions to Sn-3.0Ag-0.5Cu indicated that the time exponent values of both interfacial  $\text{Cu}_6\text{Sn}_5$  and  $\text{Cu}_3\text{Sn}$  are close to 0.5 at 150°C ageing temperature. It is also reported that with 0.1wt%  $\text{TiO}_2$  additions to Sn-3.0Ag-0.5Cu the activation energy of the interfacial layer increases where it majorly effects the  $\text{Cu}_6\text{Sn}_5$  layer and little influence on the  $\text{Cu}_3\text{Sn}$  layer [44].

High magnification, top-down images of the interfacial layer of both materials and EDS on the interfacial layer are shown in Figure 11a-c, and it is observed that agglomerated particles on the  $\text{Cu}_6\text{Sn}_5$  exist at the boundary of the interfacial layer of Sn-0.7Cu+ $\text{TiO}_2$ /Cu after six reflow cycles. This suggests  $\text{TiO}_2$  remains in contact with the interfacial  $\text{Cu}_6\text{Sn}_5$  layer and stabilises the Cu diffusion path into the molten solder. Hsiao et al. [45] in his study on inhibiting the consumption of Cu during multiple reflows of Pb-free solder on Cu substrates concluded that the channels between the  $\text{Cu}_6\text{Sn}_5$  scallops play a critical role in the growth of the Cu-Sn interfacial layer. From the study, it is reported that the channels serve as rapid diffusion and dissolution paths of Cu into the molten solder to facilitate the growth of the interfacial layer. Considering this, it is possible that  $\text{TiO}_2$  particles in intimate contact with the  $\text{Cu}_6\text{Sn}_5$  interfacial stabilises the Cu dissolution path and prevent individual grains from growing further from the interface during reflow cycles. This suppression of the interfacial layer is also promoted by the shorter time of contact between the liquid and the IMC layer in the  $\text{TiO}_2$  containing solders as observed in the DSC results. The DSC results also indicate that the Sn-0.7Cu samples solidify at a larger undercooling and this is well known to be associated with a higher velocity and more unstable interface [46]. This is consistent with our observation in Figure 3a and 10b where the  $\text{TiO}_2$  containing solders grown at lower undercoolings have a lower growth rate for the interfacial layer and a more planar morphology.



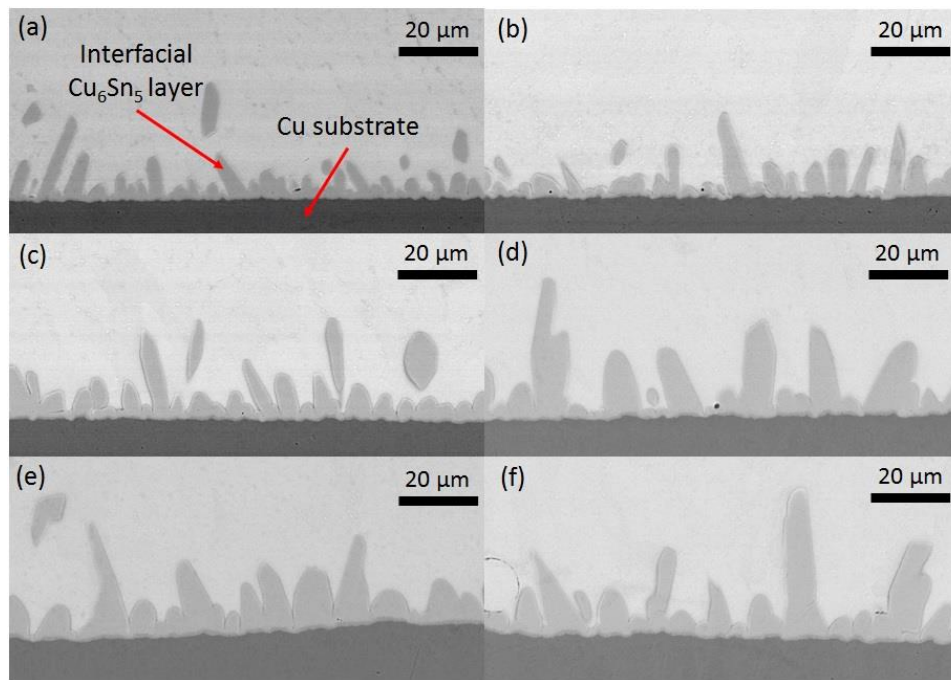


Figure 6: Micrographs of the interfacial  $\text{Cu}_6\text{Sn}_5$  layer of Sn-0.7Cu/Cu after the (a) first, (b) second, (c) third, (d) fourth, (e) fifth, and (f) sixth reflow cycles.

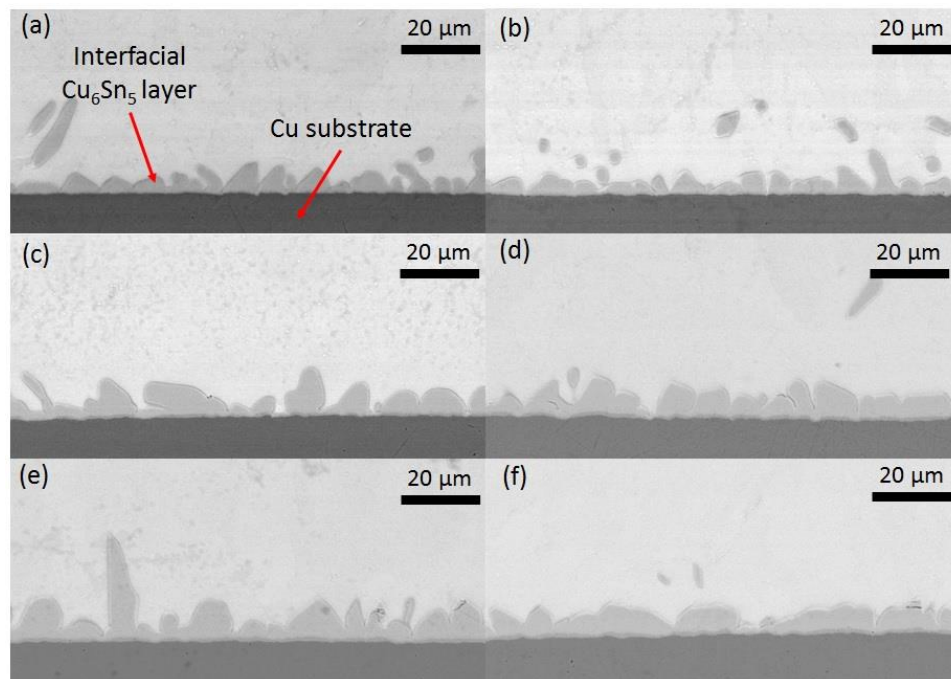


Figure 7: Micrographs of interfacial  $\text{Cu}_6\text{Sn}_5$  layers of Sn-0.7Cu- $\text{TiO}_2$ /Cu after the (a) first, (b) second, (c) third, (d) fourth, (e) fifth, and (f) sixth reflow cycles.

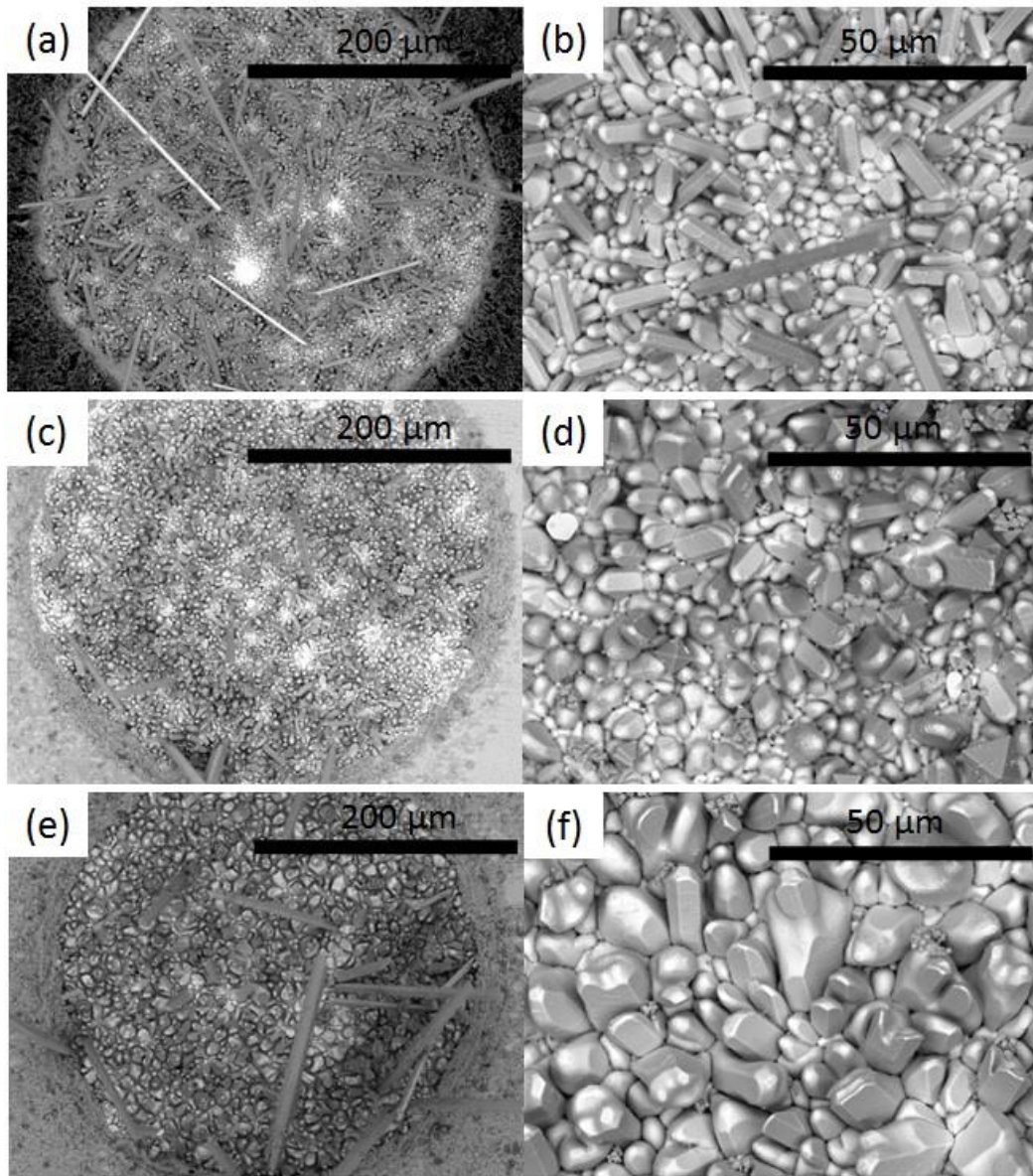


Figure 8: Top-down view of the interfacial  $\text{Cu}_6\text{Sn}_5$  layer of Sn-0.7Cu/Cu after the first reflow cycle at low (a) and high (b) magnification. The third reflow cycle at (c) low and (d) high magnification. The sixth reflow cycle at (e) low and (f) high magnification.

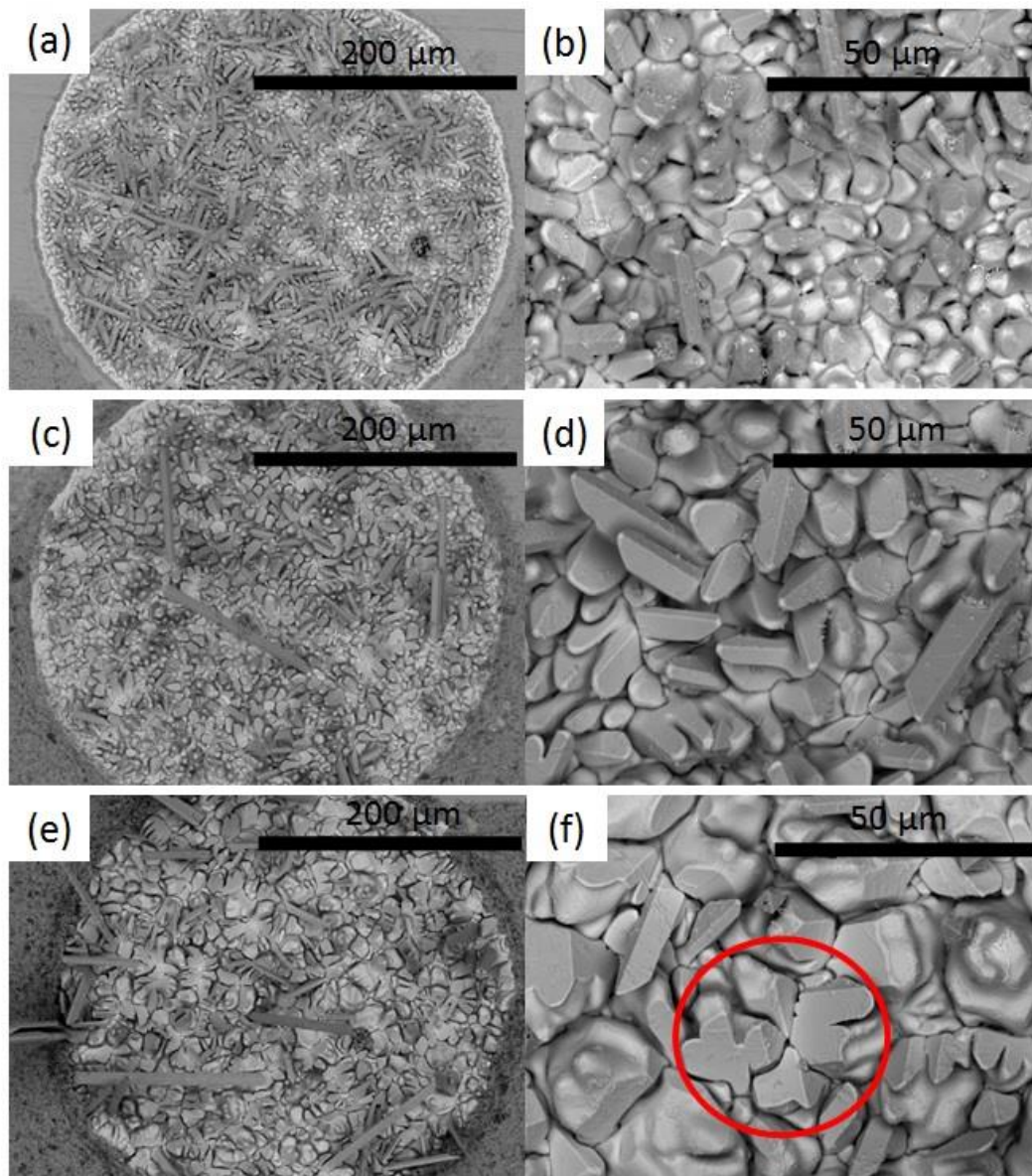


Figure 9: Top-down view of the interfacial  $\text{Cu}_6\text{Sn}_5$  layer of  $\text{Sn-0.7Cu+TiO}_2/\text{Cu}$  after the first reflow cycle at low (a) and high (b) magnification. The third reflow cycle at (c) low and (d) high magnification. The sixth reflow cycle at (e) low and (f) high magnification.



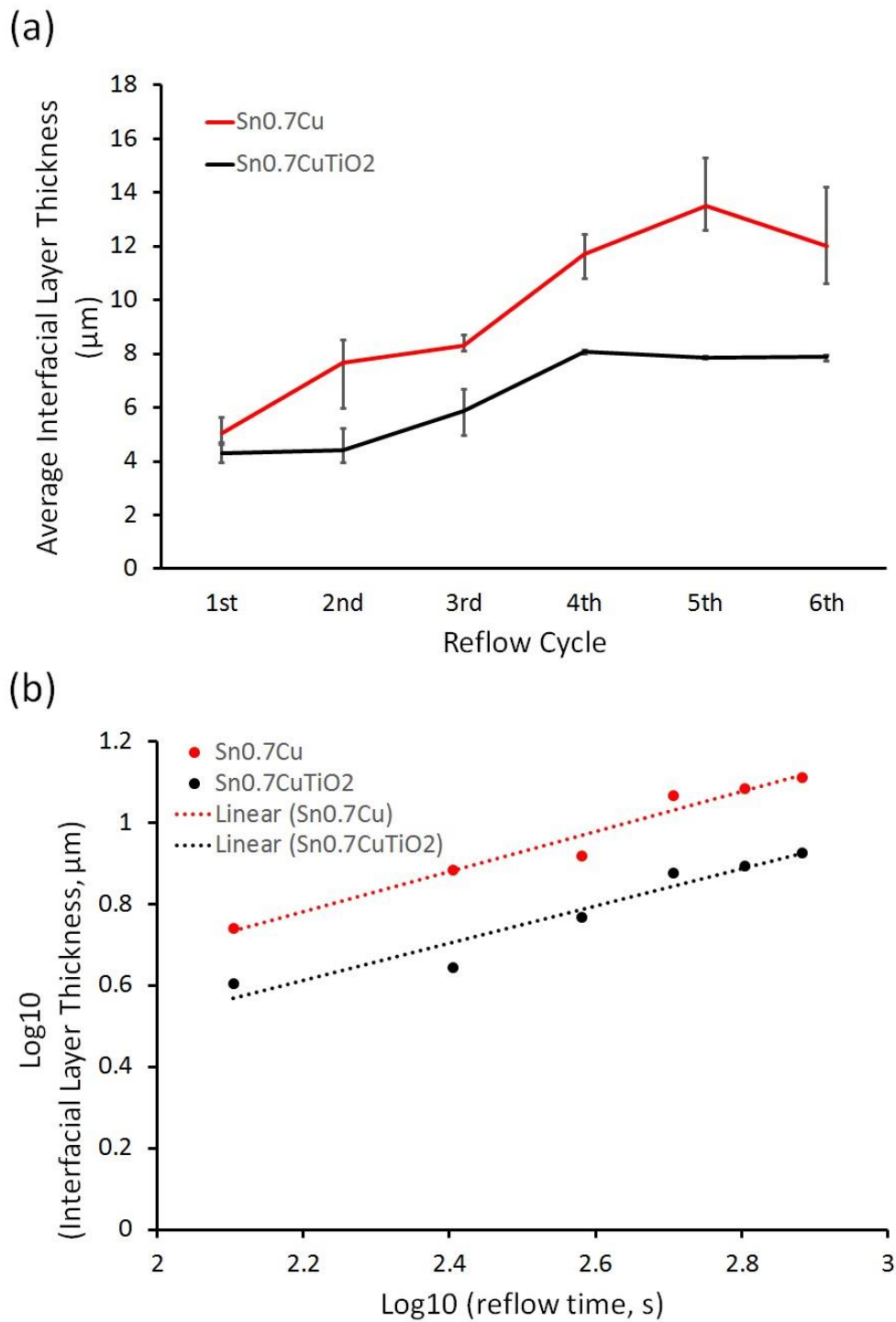


Figure 10: (a) Average interfacial layer thickness of Sn-0.7Cu solder joint and Sn-0.7Cu+TiO<sub>2</sub> solder joint after multiple reflows and (b) log-log graph of the interfacial layer thickness of Sn-0.7Cu solder joint and Sn-0.7Cu+TiO<sub>2</sub> solder joint with reflow time.

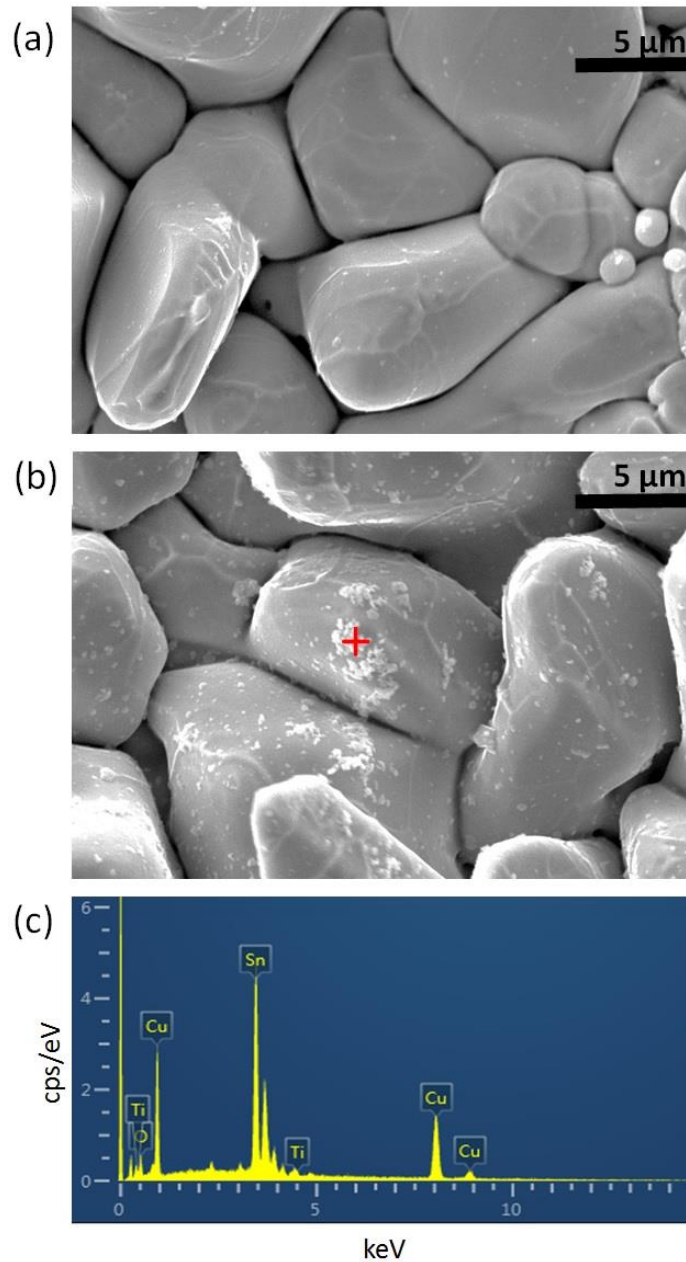


Figure 11: Interfacial  $\text{Cu}_6\text{Sn}_5$  layer of solder joints after six reflow cycles of (a) Sn-0.7Cu/Cu, (b) Sn-0.7Cu+ $\text{TiO}_2$ /Cu and (c) energy dispersive x-ray spectroscopy (EDS) spot analysis (red cross) on the Sn-0.7Cu+ $\text{TiO}_2$ /Cu interfacial layer.

### 3.3 Solder joint strength

The solder joint strength of both solder materials after multiple reflows were evaluated using a high speed shear solder ball machine at 100mm/s and 2000mm/s shear speed. A lower shear speed was chosen to evaluate the bulk solder joint strength while a higher solder speed was used in evaluating the solder joint strength at the interfacial layer [47]. After the shear tests were conducted, samples were examined using SEM to analyse the failure modes of each of the sheared solder joints. Failure was classified as one of four different failure modes including ductile, quasi-ductile, quasi-brittle and brittle as indicated in Figure

12. Figure 13 shows the average shear strength of the Sn-0.7Cu and Sn-0.7Cu+TiO<sub>2</sub> solder joint at 100 mm/s shear speed and the failure mode percentage of Sn-0.7Cu after the first, third and sixth reflow cycles. At both 100mm/s and 2000mm/s shear speeds, the results show that the TiO<sub>2</sub> containing solder joints resulted in a higher shear strength on every reflow cycle compared to Sn-0.7Cu solder joints. After multiple cycles, the shear strength at 100mm/s shear speed of Sn-0.7Cu solder joints decreases, however in TiO<sub>2</sub> containing solder joints, the shear strength is relatively insensitive to the number of reflow cycles and remains around ~14 N. Most of the failure modes for both solders at 100mm/s shear speed were dominated by the quasi-ductile mode.

Figure 14 shows the average shear strength of Sn-0.7Cu and Sn-0.7Cu+TiO<sub>2</sub> solder joints when tested at a 2000 mm/s shear speed and the failure mode percentage of Sn-0.7Cu after the first, third and sixth reflow cycle. Similar to the solder joint strength at 100mm/s, after multiple cycles, the shear strength of Sn-0.7Cu solder joints at a 2000mm/s shear speed significantly decreases, however in TiO<sub>2</sub> containing solder joints, the shear strengths decrease only slightly from ~15N to ~14N. After increasing the shear speed, the brittle and quasi-brittle failure modes were dominant and increasing the reflow cycle increases the percentage of brittle failure modes. The results show that with additions of TiO<sub>2</sub>, both the strength of the bulk solder area and the interfacial layer area were higher compared to Sn-0.7Cu after multiple reflows.

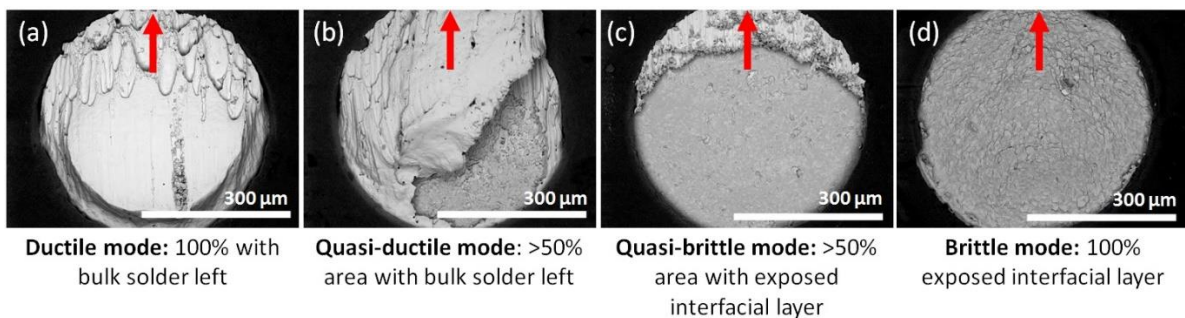


Figure 12: Micrograph of different failure mode of high speed shear fractured samples.

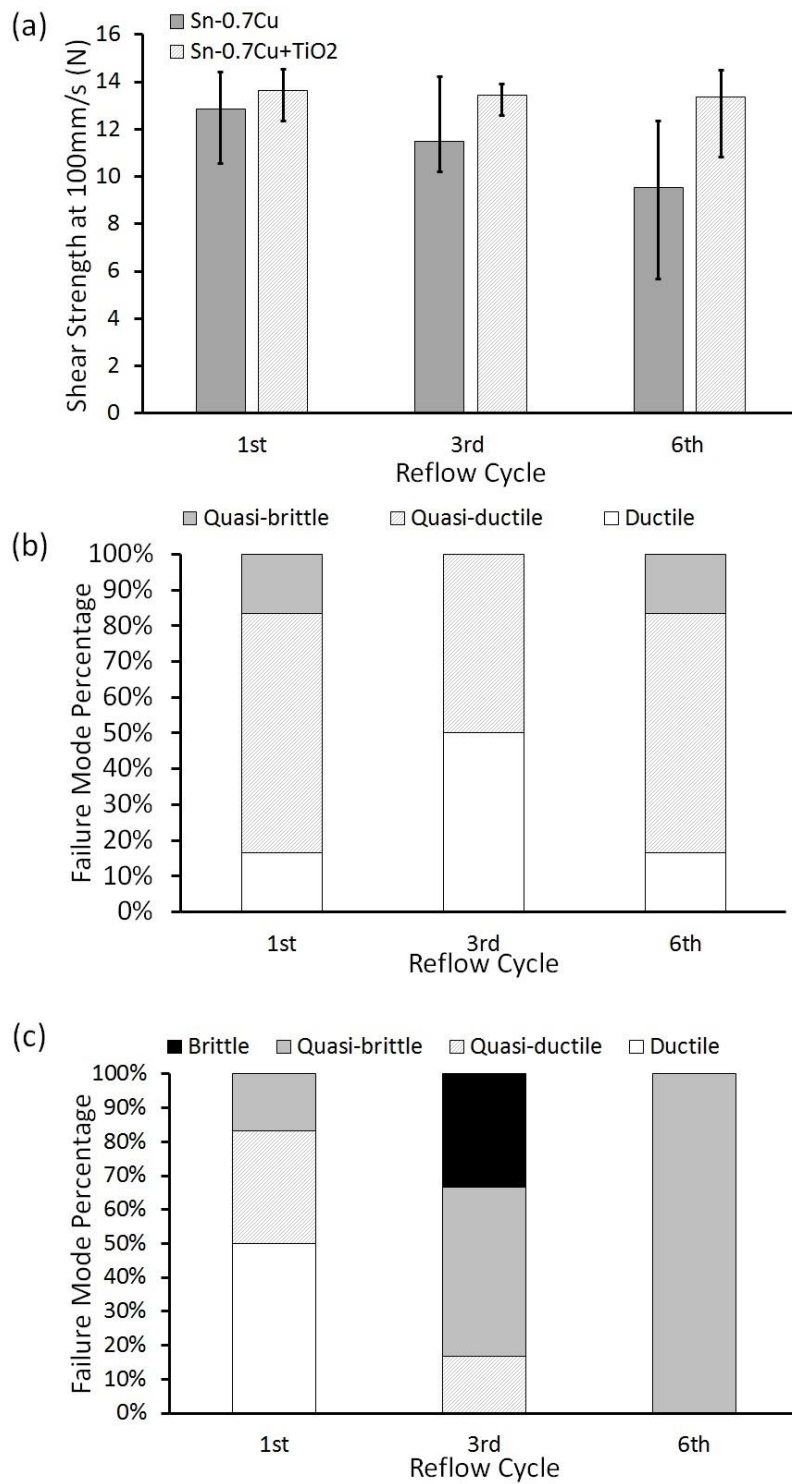


Figure 13: (a) Shear strength of Sn-0.7Cu and Sn-0.7Cu+TiO<sub>2</sub> solder joint at 100 mm/s shear speed, (b) failure mode percentage of Sn-0.7Cu after the first, third and sixth reflow cycle and (c) failure mode percentage of Sn-0.7Cu+TiO<sub>2</sub> after the first, third and sixth reflow cycle.

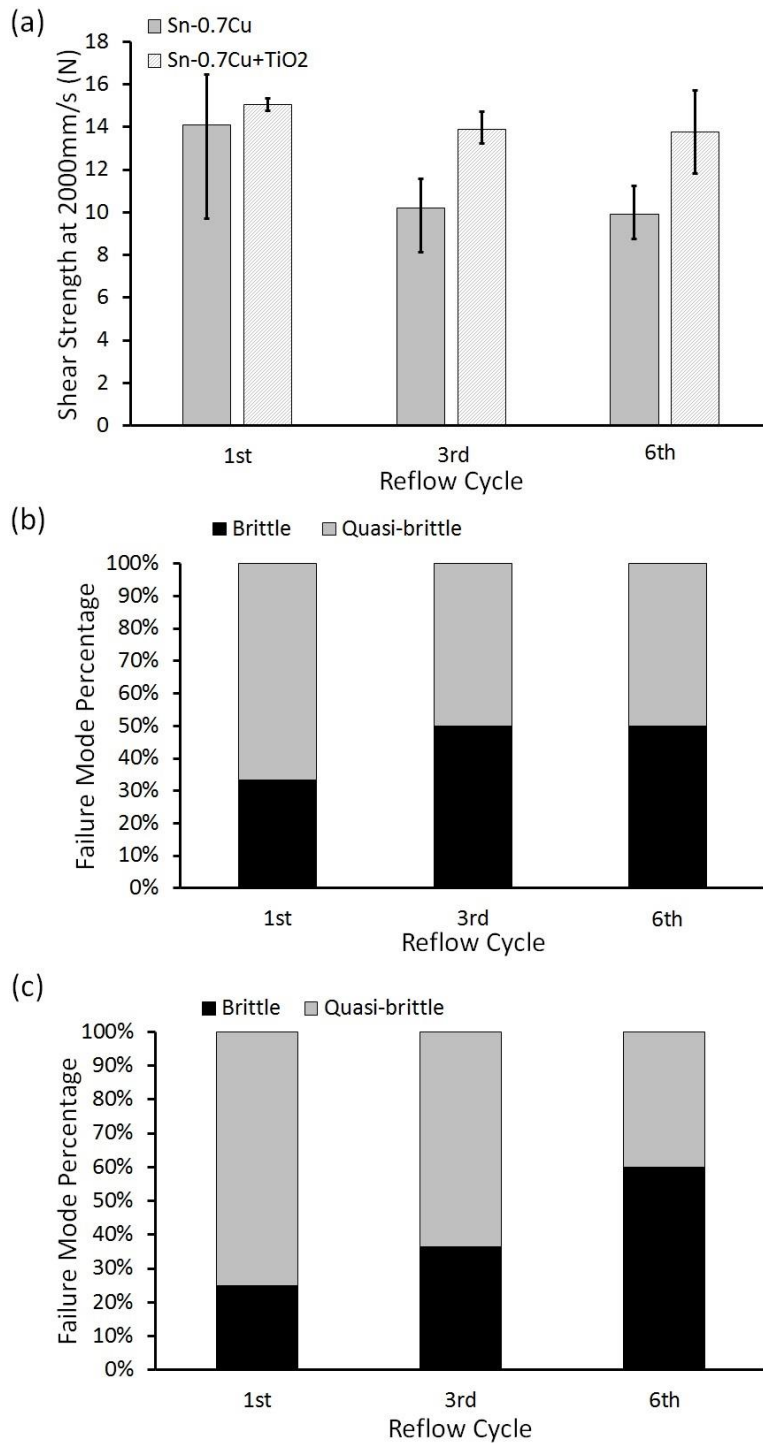


Figure 14: (a) Shear strength of Sn-0.7Cu and Sn-0.7Cu+TiO<sub>2</sub> solder joint at 2000 mm/s shear speed, (b) failure mode percentage of Sn-0.7Cu after first, third and sixth reflow cycle and (c) failure mode percentage of Sn-0.7Cu+TiO<sub>2</sub> after first, third and sixth reflow cycle.



## 4.0 Conclusions

In conclusion, the effect of multiple reflow cycles on the formation of  $\text{Cu}_6\text{Sn}_5$  primary crystals and the interfacial layer in Sn-0.7Cu and Sn-0.7Cu+ $\text{TiO}_2$  solders on copper substrates was investigated. In addition, the effects of the growth of  $\text{Cu}_6\text{Sn}_5$  after multiple reflows on the solder joint strength were evaluated. The following conclusion can be made:

- a) Multiple reflow and  $\text{TiO}_2$  additions to Sn-0.7Cu affect the  $\text{Cu}_6\text{Sn}_5$  primary and interfacial layer growth mechanisms.
- b) Sn-0.7Cu solder joints displayed a higher undercooling and larger temperature (and subsequently time) range over which liquid is present compared to Sn-0.7Cu with  $\text{TiO}_2$ . This primarily occurs due to the role that  $\text{TiO}_2$  particles have in promoting nucleation and earlier solidification.
- c) Additions of  $\text{TiO}_2$  were able to reduce the number density and total length per unit area of primary  $\text{Cu}_6\text{Sn}_5$  particles and suppress the interfacial layer during multiple reflows. It is possible that  $\text{TiO}_2$  particles in intimate contact with the interfacial  $\text{Cu}_6\text{Sn}_5$  stabilise the Cu dissolution path. By reducing the undercooling, additions of  $\text{TiO}_2$  result in a lower average thickness in the interfacial IMC and a more stable growth morphology.
- d) With the suppression of primary and interfacial  $\text{Cu}_6\text{Sn}_5$  in  $\text{TiO}_2$  containing solders, the solder joint strength in the bulk solder area and the interfacial layer area were able to be increased. The strength of  $\text{TiO}_2$  containing solder joints was relatively insensitive to the number of reflow cycles however the strength of Sn-0.7Cu solder joints generally decreased with increasing reflows.

## 5.0 Acknowledgements

Real-time observation experiments were performed at the SPring-8 BL20XU beamline (2014B1620 and 2015A1675) while SEM and DSC was performed at the Centre for Microscopy and Microanalysis (CMM) and Australian National Fabrication facility (ANFF). High speed shear tests were conducted at Nihon Superior Japan. This work was financially supported from the University of Queensland (UQ)-Nihon Superior (NS) collaboration research project, the Australian Synchrotron International Synchrotron Access Program (AS/IA143/9218 and AS/IA151/9538), ARC Linkage project (LP140100485), Grant-in-Aid for Scientific Research (S) (24226018) from the JSPS, Japan and a scholarship from the Malaysian Higher Education Ministry and University Malaysia Perlis (UniMAP).

## References

- [1] Abtew M, Selvaduray G. Lead-free Solders in Microelectronics. *Materials Science and Engineering: R: Reports* 2000;27:95-141.
- [2] Zeng K, Tu KN. Six cases of reliability study of Pb-free solder joints in electronic packaging technology. *Materials Science and Engineering: R: Reports* 2002;38:55-105.
- [3] Zhong WH, Chan YC, Alam MO, Wu BY, Guan JF. Effect of multiple reflow processes on the reliability of ball grid array (BGA) solder joints. *Journal of Alloys and Compounds* 2006;414:123-30.
- [4] Chen H, Tsai Y-L, Chang Y-T, Wu AT. Effect of massive spalling on mechanical strength of solder joints in Pb-free solder reflowed on Co-based surface finishes. *Journal of Alloys and Compounds* 2016;671:100-8.
- [5] Haseeb ASMA, Arafat MM, Johan MR. Stability of molybdenum nanoparticles in Sn–3.8Ag–0.7Cu solder during multiple reflow and their influence on interfacial intermetallic compounds. *Materials Characterization* 2012;64:27-35.
- [6] Ha S-S, Jang J-K, Ha S-O, Yoon J-W, Lee H-J, Joo J-H, et al. Effect of multiple reflows on interfacial reaction and shear strength of Sn–Ag electroplated solder bumps for flip chip package. *Microelectronic Engineering* 2010;87:517-21.
- [7] Liu P, Yao P, Liu J. Effects of multiple reflows on interfacial reaction and shear strength of SnAgCu and SnPb solder joints with different PCB surface finishes. *Journal of Alloys and Compounds* 2009;470:188-94.
- [8] Yao P, Liu P, Liu J. Effects of multiple reflows on intermetallic morphology and shear strength of SnAgCu–xNi composite solder joints on electrolytic Ni/Au metallized substrate. *Journal of Alloys and Compounds* 2008;462:73-9.
- [9] Kim D-G, Kim J-W, Ha S-S, Noh B-I, Koo J-M, Park D-W, et al. Effect of reflow numbers on the interfacial reaction and shear strength of flip chip solder joints. *Journal of Alloys and Compounds* 2008;458:253-60.
- [10] Noh BI, Koo JM, Kim JW, Kim DG, Nam JD, Joo J, et al. Effects of number of reflows on the mechanical and electrical properties of BGA package. *Intermetallics* 2006;14:1375-8.
- [11] Zhang F, Li M, Chum CC, Shao ZC. Effects of substrate metallization of solder/under-bump metallization interfacial reactions in flip-chip packages during multiple reflow cycles. *Journal of Electronic Materials*;32:123-30.
- [12] Sharif A, Chan YC. Interfacial reactions of Sn-3.5% Ag and Sn-3.5% Ag-0.5% Cu solder with electroless Ni/Au metallization during multiple reflow cycles. *Journal of Materials Science: Materials in Electronics*;16:153-8.

- [13] Chen W-Y, Yu C-Y, Duh J-G. Improving the shear strength of Sn–Ag–Cu–Ni/Cu–Zn solder joints via modifying the microstructure and phase stability of Cu–Sn intermetallic compounds. *Intermetallics* 2014;54:181-6.
- [14] Gu Y, Zhao X, Li Y, Liu Y, Wang Y, Li Z. Effect of nano-Fe<sub>2</sub>O<sub>3</sub> additions on wettability and interfacial intermetallic growth of low-Ag content Sn–Ag–Cu solders on Cu substrates. *Journal of Alloys and Compounds* 2015;627:39-47.
- [15] Huang Y, Xiu Z, Wu G, Tian Y, He P, Gu X, et al. Improving shear strength of Sn-3.0Ag-0.5Cu/Cu joints and suppressing intermetallic compounds layer growth by adding graphene nanosheets. *Materials Letters* 2016;169:262-4.
- [16] Xing F, Shang Q, Lu Y, Liang J, Qiu X. Intermetallic compounds growth suppression in ZSCB solder with RE addition on Cu substrate. *Journal of Alloys and Compounds* 2016;666:122-30.
- [17] Xing F, Yao J, Liang J, Qiu X. Influence of intermetallic growth on the mechanical properties of Zn–Sn–Cu–Bi/Cu solder joints. *Journal of Alloys and Compounds* 2015;649:1053-9.
- [18] El-Daly AA, Desoky WM, Elmosalami TA, El-Shaarawy MG, Abdraboh AM. Microstructural modifications and properties of SiC nanoparticles-reinforced Sn–3.0Ag–0.5Cu solder alloy. *Materials & Design* 2015;65:1196-204.
- [19] Wang X, Liu YC, Wei C, Gao HX, Jiang P, Yu LM. Strengthening mechanism of SiC-particulate reinforced Sn–3.7Ag–0.9Zn lead-free solder. *Journal of Alloys and Compounds* 2009;480:662-5.
- [20] El-Daly AA, Al-Ganainy GS, Fawzy A, Younis MJ. Structural characterization and creep resistance of nano-silicon carbide reinforced Sn–1.0Ag–0.5Cu lead-free solder alloy. *Materials & Design* 2014;55:837-45.
- [21] Chellvarajoo S, Abdullah MZ. Microstructure and mechanical properties of Pb-free Sn–3.0Ag–0.5Cu solder pastes added with NiO nanoparticles after reflow soldering process. *Materials & Design* 2016;90:499-507.
- [22] Tsao LC, Chang SY, Lee CI, Sun WH, Huang CH. Effects of nano-Al<sub>2</sub>O<sub>3</sub> additions on microstructure development and hardness of Sn<sub>3.5</sub>Ag<sub>0.5</sub>Cu solder. *Materials & Design* 2010;31:4831-5.
- [23] Tsao LC, Wu RW, Cheng T-H, Fan K-H, Chen RS. Effects of nano-Al<sub>2</sub>O<sub>3</sub> particles on microstructure and mechanical properties of Sn<sub>3.5</sub>Ag<sub>0.5</sub>Cu composite solder ball grid array joints on Sn/Cu pads. *Materials & Design* 2013;50:774-81.

- [24] Geranmayeh AR, Mahmudi R, Kangooie M. High-temperature shear strength of lead-free Sn–Sb–Ag/Al<sub>2</sub>O<sub>3</sub> composite solder. *Materials Science and Engineering: A* 2011;528:3967-72.
- [25] Gain AK, Chan YC, Yung WKC. Effect of additions of ZrO<sub>2</sub> nano-particles on the microstructure and shear strength of Sn–Ag–Cu solder on Au/Ni metallized Cu pads. *Microelectronics Reliability* 2011;51:2306-13.
- [26] Shen J, Chan YC. Effects of ZrO<sub>2</sub> nanoparticles on the mechanical properties of Sn–Zn solder joints on Au/Ni/Cu pads. *Journal of Alloys and Compounds* 2009;477:552-9.
- [27] Gain AK, Chan YC. Growth mechanism of intermetallic compounds and damping properties of Sn–Ag–Cu-1wt% nano-ZrO<sub>2</sub> composite solders. *Microelectronics Reliability* 2014;54:945-55.
- [28] Gain AK, Fouzder T, Chan YC, Yung WKC. Microstructure, kinetic analysis and hardness of Sn–Ag–Cu-1wt% nano-ZrO<sub>2</sub> composite solder on OSP-Cu pads. *Journal of Alloys and Compounds* 2011;509:3319-25.
- [29] Hu X, Xu S, Yang Y, Chen Z, Chan YC. Effect of TiO<sub>2</sub> nanoparticle addition on electroless Ni–P under bump metallization for lead-free solder interconnection. *Materials Science and Engineering: A* 2014;600:67-75.
- [30] Tang Y, Li GY, Pan YC. Effects of TiO<sub>2</sub> nanoparticles addition on microstructure, microhardness and tensile properties of Sn–3.0Ag–0.5Cu–xTiO<sub>2</sub> composite solder. *Materials & Design* 2014;55:574-82.
- [31] Tsao LC, Huang CH, Chung CH, Chen RS. Influence of TiO<sub>2</sub> nanoparticles addition on the microstructural and mechanical properties of Sn<sub>0.7</sub>Cu nano-composite solder. *Materials Science and Engineering: A* 2012;545:194-200.
- [32] Tang Y, Li GY, Pan YC. Influence of TiO<sub>2</sub> nanoparticles on IMC growth in Sn–3.0Ag–0.5Cu–xTiO<sub>2</sub> solder joints in reflow process. *Journal of Alloys and Compounds* 2013;554:195-203.
- [33] Tsao LC. An investigation of microstructure and mechanical properties of novel Sn<sub>3.5</sub>Ag<sub>0.5</sub>Cu–XTiO<sub>2</sub> composite solders as functions of alloy composition and cooling rate. *Materials Science and Engineering: A* 2011;529:41-8.
- [34] Tsao LC. Suppressing effect of 0.5wt.% nano-TiO<sub>2</sub> addition into Sn–3.5Ag–0.5Cu solder alloy on the intermetallic growth with Cu substrate during isothermal aging. *Journal of Alloys and Compounds* 2011;509:8441-8.
- [35] Mohd Salleh MAA, Bakri AMMA, Zan@Hazizi MH, Somidin F, Mohd Alui NF, Ahmad ZA. Mechanical properties of Sn–0.7Cu/Si<sub>3</sub>N<sub>4</sub> lead-free composite solder. *Materials Science and Engineering: A* 2012;556:633-7.

- [36] M.A.A MS, Bakri AMMA, Kamarudin H, Bnhussain M, M.H ZH, Somidin F. Solderability of Sn-0.7Cu/Si<sub>3</sub>N<sub>4</sub> lead-free composite solder on Cu-substrate. *Physics Procedia* 2011;22:299-304.
- [37] Mohd Salleh MAA, McDonald SD, Terada Y, Yasuda H, Nogita K. Development of a microwave sintered TiO<sub>2</sub> reinforced Sn–0.7wt%Cu–0.05wt%Ni alloy. *Materials & Design* 2015;82:136-47.
- [38] Yasuda H, Ohnaka I, Kawasaki K, Sugiyama A, Ohmichi T, Iwane J, et al. Direct observation of stray crystal formation in unidirectional solidification of Sn–Bi alloy by X-ray imaging. *Journal of Crystal Growth* 2004;262:645-52.
- [39] Nogita K, Yasuda H, Prasad A, McDonald SD, Nagira T, Nakatsuka N, et al. Real time synchrotron X-ray observations of solidification in hypoeutectic Al–Si alloys. *Materials Characterization* 2013;85:134-40.
- [40] Salleh MAAM, McDonald SD, Yasuda H, Sugiyama A, Nogita K. Rapid Cu<sub>6</sub>Sn<sub>5</sub> growth at liquid Sn/solid Cu interfaces. *Scripta Materialia* 2015;100:17-20.
- [41] Mohd Salleh MAA, McDonald SD, Gourlay CM, Belyakov SA, Yasuda H, Nogita K. Effect of Ni on the Formation and Growth of Primary Cu<sub>6</sub>Sn<sub>5</sub> Intermetallics in Sn-0.7 wt.%Cu Solder Pastes on Cu Substrates During the Soldering Process. *Journal of Electronic Materials* 2015;45:154-63.
- [42] Shangguan D. Lead-free solder : interconnect reliability. Materials Park, Ohio: ASM International; 2005.
- [43] Hsiao HY, Hu CC, Guo MY, Chen C, Tu KN. Inhibiting the consumption of Cu during multiple reflows of Pb-free solder on Cu. *Scripta Materialia* 2011;65:907-10.
- [44] Flood SC, Hunt JD. Columnar and equiaxed growth. *Journal of Crystal Growth* 1987;82:543-51.
- [45] Tsukamoto H, Nishimura T, Suenaga S, Nogita K. Shear and tensile impact strength of lead-free solder ball grid arrays placed on Ni (P)/Au surface-finished substrates. *Materials Science and Engineering: B* 2010;171:162-71.

## **Paper 8: Effects of Ni and TiO<sub>2</sub> additions in as-reflowed and annealed Sn0.7Cu solders on Cu substrates**

Mohd Arif Anuar Mohd Salleh, Stuart D. McDonald, Kazuhiro Nogita

(Submitted to **Journal of Materials Processing Technology** on the 15<sup>th</sup> June 2016 and currently under review)

# Effects of Ni and TiO<sub>2</sub> additions in as-reflowed and annealed Sn0.7Cu solders on Cu substrates

M. A. A. Mohd Salleh<sup>a,b\*</sup>, S. D. McDonald<sup>a</sup>, K. Nogita<sup>a</sup>

<sup>a</sup>Nihon Superior Centre for the Manufacture of Electronic Materials (NS CMEM), School of Mechanical and Mining Engineering, The University of Queensland, 4072 St Lucia, Queensland, Australia.

<sup>b</sup>Centre of Excellence Geopolymer and Green Technology, School of Materials Engineering, Universiti Malaysia Perlis (UniMAP), Taman Muhibbah 02600, Jejawi, Arau, Perlis, Malaysia.

\*Corresponding author: Room 634, 49 Jocks Rd., St Lucia, Brisbane, QLD 4072, Australia

Email: m.mohdsalleh@uq.edu.au / arifanuar@unimap.edu.my ;

Tel: +61 435 946 670

## Abstract

The growth of Cu<sub>6</sub>Sn<sub>5</sub> and Cu<sub>3</sub>Sn<sub>5</sub> interfacial layers after isothermal annealing and the resultant effect on the solder joint strength are studied in TiO<sub>2</sub> and Ni containing Sn0.7Cu solders. These composite solders were fabricated using a powder metallurgy method and reflow soldered on a Cu substrate printed circuit board (PCB) with an organic soldering preservative (OSP) surface finish. With TiO<sub>2</sub> additions, a more planar scalloped Cu<sub>6</sub>Sn<sub>5</sub> morphology was observed with reduced interfacial boundary grooves while a fine scallop-shaped interfacial (Cu,Ni)<sub>6</sub>Sn<sub>5</sub> layer was observed in Ni containing solder joints. The interfacial layer was further suppressed with a combination of Ni and TiO<sub>2</sub> even after annealing which resulted in superior shear strength and fracture energy.

Keywords: Lead-free solder, Reflow soldering, Microstructure, Intermetallic, Interfacial reaction, Shear strength

## 1.0 Introduction

Intermetallic phases such as  $\text{Cu}_6\text{Sn}_5$  and  $\text{Cu}_3\text{Sn}$  often form at the solder/substrate interface in many Pb-free solder joints. During thermal ageing, the interfacial intermetallic layer may grow and Kirkendall voids often form at the  $\text{Cu}_6\text{Sn}_5/\text{Cu}$  substrate interface. The brittle interfacial intermetallic layer and voids at the solder joint interface can deteriorate the solder joint reliability where cracks may be initiated and propagate. Hence, controlling the thickness of interfacial intermetallics and minimising void formation can improve solder joint reliability.

Ceramic reinforcement of solder matrices with a variety of micrometer or nanometer-size particles such as silicon carbide ( $\text{SiC}$ ), nickel oxide ( $\text{NiO}$ ), alumina ( $\text{Al}_2\text{O}_3$ ), zirconia ( $\text{ZrO}_2$ ), titanium oxide ( $\text{TiO}_2$ ) and silicon nitride ( $\text{Si}_3\text{N}_4$ ) has been proposed by Mohd Salleh et al. (2013) as a method of suppressing the growth of  $\text{Cu}_6\text{Sn}_5$  interfacial intermetallic layers during soldering. Chellvarajoo and Abdullah (2016) showed that additions of 2.5 wt%  $\text{NiO}$  in a  $\text{Sn3.0Ag0.5Cu}$  solder alloy resulted in a reduction of 60% thickness of the intermetallic layer after a single reflow. However, Shen and Chan (2009) reported that additions of  $\text{ZrO}_2$  suppressed the intermetallic layer observed in a  $\text{Sn9Zn/Cu}$  solder joint after five reflow cycles. During single and multiple reflow cycles, Said et al. (2016) reported that the suppression of the intermetallic layer could be more significant during isothermal annealing.

Various hypotheses exist relating to how the interfacial intermetallic layer is suppressed by additions of particle reinforcements. Chuang et al. (2010) hypothesized that the  $\text{Al}_2\text{O}_3$  nanoparticles are absorbed in a liquid nanocomposite solder/ $\text{Cu}$  substrate interface which then suppresses the  $\text{Cu}$  dissolution in the liquid solder and in return reduces the formation of  $\text{Cu}_6\text{Sn}_5$  intermetallic compound (IMC) layer. In addition, El-Daly et al. (2013) hypothesized that  $\text{SiC}$  nanoparticles could act as additional nucleation sites where the rate of solidification of  $\beta\text{-Sn}$  will be faster and limit the time for the  $\text{Ag}_3\text{Sn}$  and  $\text{Cu}_6\text{Sn}_5$  to grow. This mechanism was also reported by Liu et al. (2013) in the reinforcing of  $\text{Sn-Ag-Cu}$  solder alloys with graphene nanosheets which enhanced the thermodynamic resistance to IMC growth and reduced diffusion.

A growing body of research exists relating to the development of  $\text{Sn0.7Cu}$  alloys through reinforcement additions. This includes additions of either metallic or non-metallic particles to the solder. Somidin et al. (2013) investigated the effect of additions of aluminum particles to  $\text{Sn0.7Cu}$  showing both thin  $\text{Cu}_9\text{Al}_4$  and  $\text{Cu}_6\text{Sn}_5$  intermetallic layers were formed. Mohd Salleh et al. (2011) and Mohd Salleh et al. (2012) have concluded that additions of  $\text{Si}_3\text{N}_4$



could enhance the wettability and reduce the  $\text{Cu}_6\text{Sn}_5$  intermetallic layer thickness and have shown that the shear joint strength could be significantly improved. In addition, Tsao et al. (2012) had investigated the mechanical and thermal properties of  $\text{TiO}_2$  reinforced  $\text{Sn0.7Cu}$  bulk solder. In their report, the melting temperature of the reinforced solder was able to be reduced and an improvement of hardness and tensile strength of the bulk solder was achieved. It has also been reported by Zeng et al. (2014) that Ni additions to  $\text{Sn0.7Cu}$  solder alloys suppress the  $\text{Cu}_3\text{Sn}$  layer intermetallic layer which typically forms between the  $\text{Cu}_6\text{Sn}_5/\text{Cu}$  interface as a result of continuous Cu diffusion from the substrate into the  $\text{Cu}_6\text{Sn}_5$  layer. Besides the suppression of the intermetallic layer, Mohd Salleh et al. (2016a) revealed that primary  $\text{Cu}_6\text{Sn}_5$  in the bulk could be significantly refined with Ni additions. In Sn-Ag-Cu solders, additions of Ni was reported by Chuang and Lin (2003) to also effectively suppress the  $\text{Cu}_6\text{Sn}_5$  layer. Shohji et al. (2005) had also proved that additions of Ni to Sn-Ag-Cu solder were able to suppress the layer after annealing and subsequently improve the solder joint shear strength on Cu substrates after annealing for 1000 hours at  $100^\circ\text{C}$ .

This paper investigates the effects of Ni,  $\text{TiO}_2$  and combination of both additions in the suppression of the interfacial intermetallic compound after isothermal annealing and their effects on the solder joint mechanical performance by means of high speed shear testing. This includes investigating the solder joint strength, fracture deformation energy and analysis of the failure mode. In addition, we also seek to understand the presence of  $\text{TiO}_2$  reinforcement in the solder joints and how it suppresses the interfacial intermetallic layer.

## **2.0 Experimental**

### **2.1 Sample and solder ball fabrication**

Chellvarajoo and Abdullah (2016) reported that most of the methods used to fabricate reinforced solders involve mixing reinforcement particles into a solder paste (a mixture of flux and solder spheres) where due to the buoyancy of the flux and outgassing and density differences, reinforcement particles were observed to be concentrated on the surface of the solder joint after being pushed out during the soldering process. Thus, to reduce the possibility of reinforcement push-out by excessive flux in solder pastes and to obtain a homogenous reinforcement of distribution in the solder matrix, Mohd Salleh et al. (2015a) have previously developed a method of fabricating a preform  $\text{TiO}_2$  reinforced solder by a powder metallurgy microwave sintering method. This homogeneous distribution of reinforcement allows the mechanisms of interfacial intermetallic layer suppression to be

investigated with more confidence. In preparing the samples, Sn0.7Cu and Sn0.7Cu0.05Ni solder powders of spherical shape (45  $\mu\text{m}$  average particle size) were supplied by Nihon Superior Co. Ltd. for the base matrix materials, along with 99.7% purity  $\text{TiO}_2$  anatase powder supplied by Sigma Aldrich Co. (<50 nm average particle size). Table 1 and 2 presents the chemical compositions of the solder powders used as base alloys as obtained using optical emission spectroscopy. Four different solder composition were prepared including Sn0.7Cu, Sn0.7Cu0.05Ni, Sn0.7Cu+ $\text{TiO}_2$  and Sn0.7Cu0.05Ni+ $\text{TiO}_2$ . To fabricate the reinforced solders, 1wt% of  $\text{TiO}_2$  particles were incorporated into the base solder matrix using a powder metallurgy route. The  $\text{TiO}_2$  reinforcement was homogeneously mixed with the base matrix powder (Sn0.7Cu alloy and Sn0.7Cu0.05Ni) separately in an airtight container using a tubular mixer for 1 hour. The solder mixtures were uniaxially compacted in a 12-mm diameter mold at 120 bar, and the compacted discs were microwave sintered in an inert argon atmosphere. Using a microwave oven with an output power of 1,000W at full power, approximately 3 minutes of microwave sintering time was taken to achieve the sintering temperature of 185°C ( $\sim 0.8T_m$ ). For comparison the base materials, Sn0.7Cu alloy and Sn0.7Cu0.05Ni alloys were prepared by compacting the Sn0.7Cu and Sn0.7Cu0.05Ni solder powders respectively and sintered using the same method as the reinforced solders. Sintered samples were then cold rolled to produce thin solder sheets of approximately 23  $\mu\text{m}$  thickness.

In fabricating solder balls, thin solder sheets were punched using a 2.5 mm diameter metal punch to form a thin solder discs. The thin solder discs were then dipped in a rosin mildly activated (RMA) flux and placed on a Pyrex sheet. Using a controlled heating temperature, the solder discs were melted using a reflow oven at 250°C maximum temperature with the aid of  $\text{N}_2$  gas flow. Due to the solder melting and the action of surface tension, solder sheets were transformed to solder balls of spherical shape with an approximate diameter of 600  $\mu\text{m}$ . Solder balls were passed through sieves to ensure a uniform size. The fabricated solder balls with small amount of RMA flux were then placed on a Cu substrate printed circuit board (PCB) with an organic soldering preservative (OSP) surface finish and were solder reflowed at 127 s of reflow time at 250 °C maximum temperature with the aid of small amount of flux using a desktop reflow oven with  $\text{N}_2$  gas flow. The solder reflow temperature profile used in preparing the solder joints is shown in Figure 1a.

**Table 1: Chemical composition of the Sn0.7Cu powder.**

	Sn	Cu	Ag	Fe	Bi	Al	Cd	Ni	Sb	Zn	Pb	As	Hg
Composition (wt%)	Balance	0.686	0.009	0.006	0.013	<0.001	<0.001	<0.002	0.020	<0.001	0.008	<0.005	<0.001

**Table 2: Chemical composition of the Sn0.7Cu0.05Ni powder.**

	Sn	Cu	Ni	Sb	Bi	Zn	Al	As	Sb	Cd	Pb
Composition (wt%)	Balance	0.620	0.056	0.08	0.013	<0.001	<0.001	<0.002	0.020	<0.001	0.686

## 2.2 Isothermal ageing and microstructure analysis

The growth of the interfacial intermetallic compound growth was studied by conducting isothermal annealing experiment at 150°C for 0, 500, 1000, 1500 and 2000 hours. In ensuring temperature uniformity throughout the samples during isothermal ageing, solder joints were isothermally annealed in an oven with a mechanical convection heating system supplied by Thermo Scientific.

Solder joints were then cross-sectioned for microstructure observations. The microstructures of the samples were analysed using a JEOL 6610 SEM/energy dispersive X-ray spectroscopy (EDS) in secondary and backscattered electron imaging mode at an accelerating voltage of 20 kV. For a top-down view of the intermetallic formation, solder joints were etched using solution of 2% 2-nitrophenol, 5% sodium hydroxide and 93% of distilled water. Before detailed SEM imaging and EDS were conducted, samples were thoroughly cleaned and rinsed using acetone in an ultrasonic bath. The interfacial IMC thickness of each sample was measured using ImageJ software. An average of the interfacial IMC thickness in each image was measured by dividing the total area by the total length.

## 2.3 High speed shear solder joint evaluation

In evaluating the solder joint strength of samples after isothermal ageing, solder joints were sheared using a Dage 4,000 high speed bond tester with a 60 µm shear height. A 50 N shear load cartridge was used at a 2,000 mm/s shear speed. The high speed shear test sample positioning is as in Figure 1b. Shear strength of the solder joints was determined by means of the maximum shear force of each solder ball shear test conducted while the total shear energy were determined by the total area of shear force and displacement. Shear

fracture initiation energy was determined base on the area of shear force and displacement graph from shear initiation until the maximum shear force while the shear fracture propagation energy was determined by the area from maximum shear force until the end of shear displacement. After high speed shear tests were conducted, samples were examined using scanning electron microscopy (SEM) to analyse the fracture surface and failure modes of each of the sheared solder joints. Failure mode distribution was analysed base on four different failure modes classified as ductile (100% area with bulk solder), quasi-ductile (>50% area with bulk solder), quasi-brittle (>50% area with exposed interfacial layer) and brittle (100% area with exposed interfacial layer) as shown in Figure 1a-f respectively.

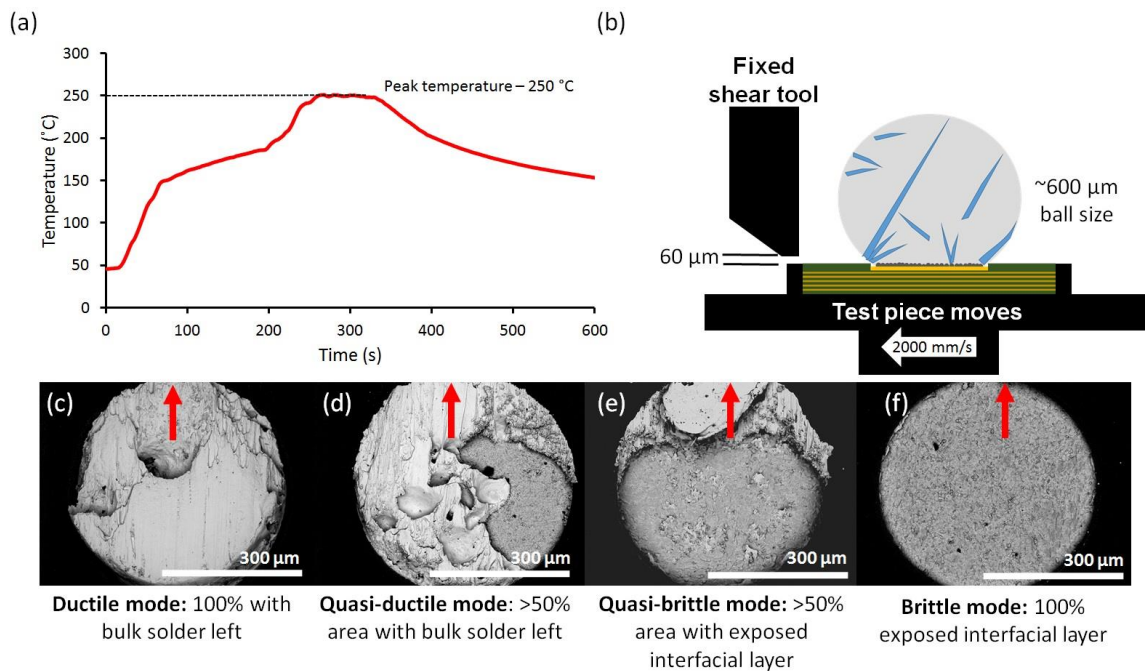


Figure 1: a) Solder reflow temperature profile for solder joint fabrication, b) high speed shear test setup and sample positioning and (c-f) backscattered electron SEM images of four different main solder joint fracture modes after high speed shear testing.

### 3.0 Results and Discussion

#### 3.1 Microstructure of annealed solder joints

Microstructure formations particularly on the growth of interfacial intermetallic layers in Sn0.7Cu, Sn0.7Cu+TiO<sub>2</sub>, Sn0.7Cu0.05Ni, Sn0.7Cu0.05Ni+TiO<sub>2</sub> solder joints after isothermal annealing were investigated. As in Figure 2a-d, it was observed that in Sn0.7Cu solder joints, a scallop-shape interfacial Cu<sub>6</sub>Sn<sub>5</sub> layer had formed with a planar layer of Cu<sub>3</sub>Sn. Both Cu<sub>6</sub>Sn<sub>5</sub> and Cu<sub>3</sub>Sn grew during isothermal annealing and became significantly thicker after 2000 hours of annealing. As in Figure 2d, after 2000 hours the scalloped morphology of the interfacial Cu<sub>6</sub>Sn<sub>5</sub> in Sn0.7Cu solder joints had become coarser and flatter

compared to the as-reflowed, 500, 1000 and 1500 hours of annealing conditions. In contrast, Figure 2e-f shows the formation and growth of interfacial  $\text{Cu}_6\text{Sn}_5$  and  $\text{Cu}_3\text{Sn}$  of Sn0.7Cu with  $\text{TiO}_2$  additions after isothermal annealing. It was observed that with additions of the reinforcement, a flatter  $\text{Cu}_6\text{Sn}_5$  layer formed with a less scallop-shaped morphology compared to the Sn0.7Cu solder joints. However, the interfacial  $\text{Cu}_3\text{Sn}$  layer of the reinforced Sn0.7Cu was slightly thicker compared to the non-reinforced Sn0.7Cu. As reported by Mohd Salleh et al. (2016b), the grooves between the  $\text{Cu}_6\text{Sn}_5$  scallops play a critical role in the growth of Cu-Sn interfacial layer and during annealing, the grooves serves as diffusion paths of Cu into the solder. It is also reported that during soldering, the  $\text{TiO}_2$  particles come into intimate contact with the  $\text{Cu}_6\text{Sn}_5$  interfacial layer modifying the Cu diffusion and dissolution path into the molten solder and preventing individual  $\text{Cu}_6\text{Sn}_5$  grains from growing further and reducing the  $\text{Cu}_6\text{Sn}_5$  channels. One result of less  $\text{Cu}_6\text{Sn}_5$  groove formation during soldering is that subsequent Cu diffusion from the substrate during thermal annealing will be unbalanced and the growth of the  $\text{Cu}_3\text{Sn}$  layer will be favoured. Besides that, as shown in Figure 2, in both the reinforced and non-reinforced Sn0.7Cu, Kirkendall voids on the  $\text{Cu}_3\text{Sn}$  layer were observed to increase after longer annealing times. Studies made by Yu et al. (2016) reported that Kirkendall voids were introduced by an unbalanced diffusion at the interface and are promoted by higher temperature and annealing times.

Comparing the 0.05wt% Ni additions to Sn0.7Cu, as in Figure 3a-d, the formations of interfacial  $(\text{Cu,Ni})_6\text{Sn}_5$  layer were rather finer scallop-shape and becomes courser after a longer annealing time. With additions of  $\text{TiO}_2$  reinforcement to the Sn0.7Cu0.05Ni as in Figure 3e-h, the morphology of the interfacial layer was similar to the non-reinforced solder joints. However, a thinner interfacial  $(\text{Cu,Ni})_6\text{Sn}_5$  layer was observed. From cross-sectioned microstructure observations on Sn0.7Cu0.05Ni samples regardless of reinforcement additions, fine primary  $(\text{Cu,Ni})_6\text{Sn}_5$  were observed near the interfacial layer. From Mohd Salleh et al. (2016a) study, this fine primary  $(\text{Cu,Ni})_6\text{Sn}_5$  forms in the bulk solder and sinks to the interfacial layer during solidification. In Sn0.7Cu, primary  $\text{Cu}_6\text{Sn}_5$  particles were larger and the majority were in the bulk solder. Figure 4a-c and 4d-f shows the interfacial intermetallic layer and primary intermetallic morphology after 2000 hours of annealing in the Sn0.7Cu+ $\text{TiO}_2$  and Sn0.7Cu0.05Ni+ $\text{TiO}_2$  samples respectively. A relatively flat and coarse interfacial  $\text{Cu}_6\text{Sn}_5$  layer and generally larger primary  $\text{Cu}_6\text{Sn}_5$  particles were observed in reinforced Sn0.7Cu solder joints.

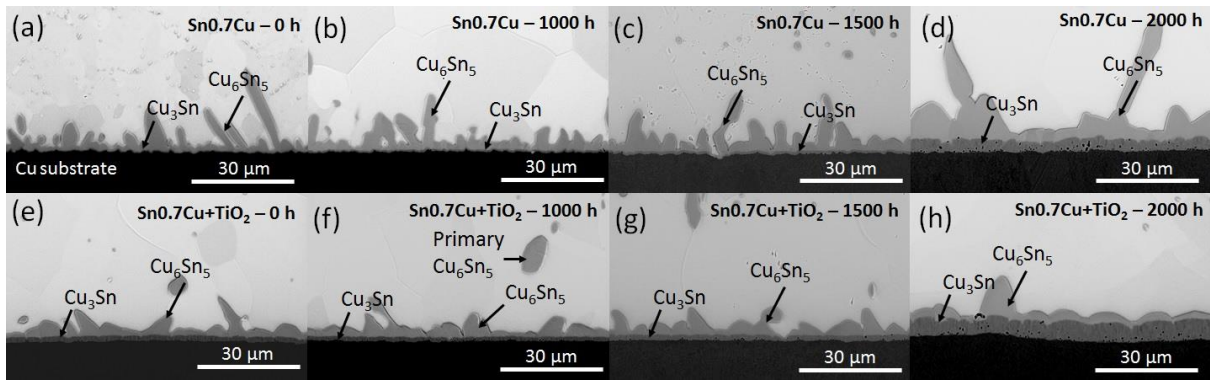


Figure 2: Backscattered electron SEM images of the interfacial  $\text{Cu}_6\text{Sn}_5$  and  $\text{Cu}_3\text{Sn}$  intermetallic compound layers in annealed  $\text{Sn}_{0.7}\text{Cu}$  after (a) 0 hours, (b) 1000 hours, (c) 1500 hours, (d) 2000 hours and  $\text{Sn}_{0.7}\text{Cu}+\text{TiO}_2$  after (e) 0 hours, (f) 1000 hours, (g) 1500 hours, (h) 2000 hours.

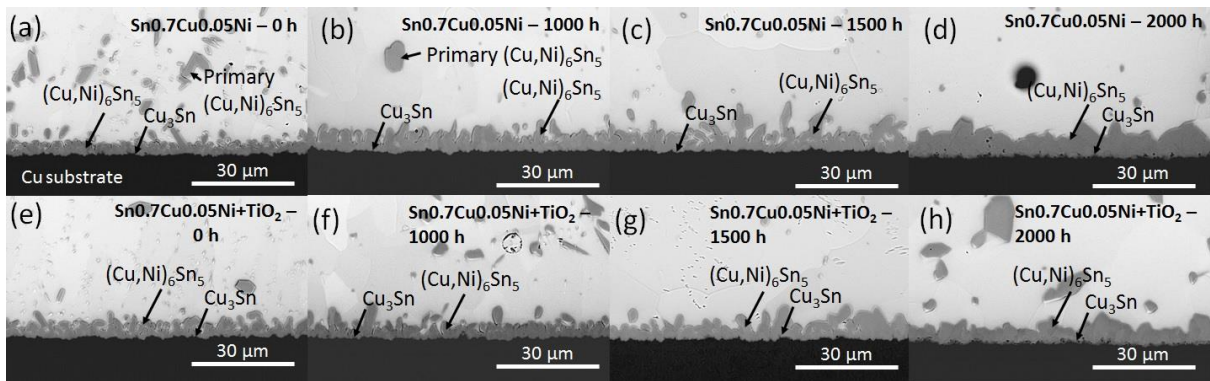


Figure 3: Backscattered electron SEM images of interfacial  $(\text{Cu,Ni})_6\text{Sn}_5$  and the  $\text{Cu}_3\text{Sn}$  intermetallic compound layers in annealed  $\text{Sn}_{0.7}\text{Cu}_{0.05}\text{Ni}$  after (a) 0 hours, (b) 1000 hours, (c) 1500 hours, (d) 2000 hours and  $\text{Sn}_{0.7}\text{Cu}_{0.05}\text{Ni}+\text{TiO}_2$  after (e) 0 hours, (f) 1000 hours, (g) 1500 hours, (h) 2000 hours.



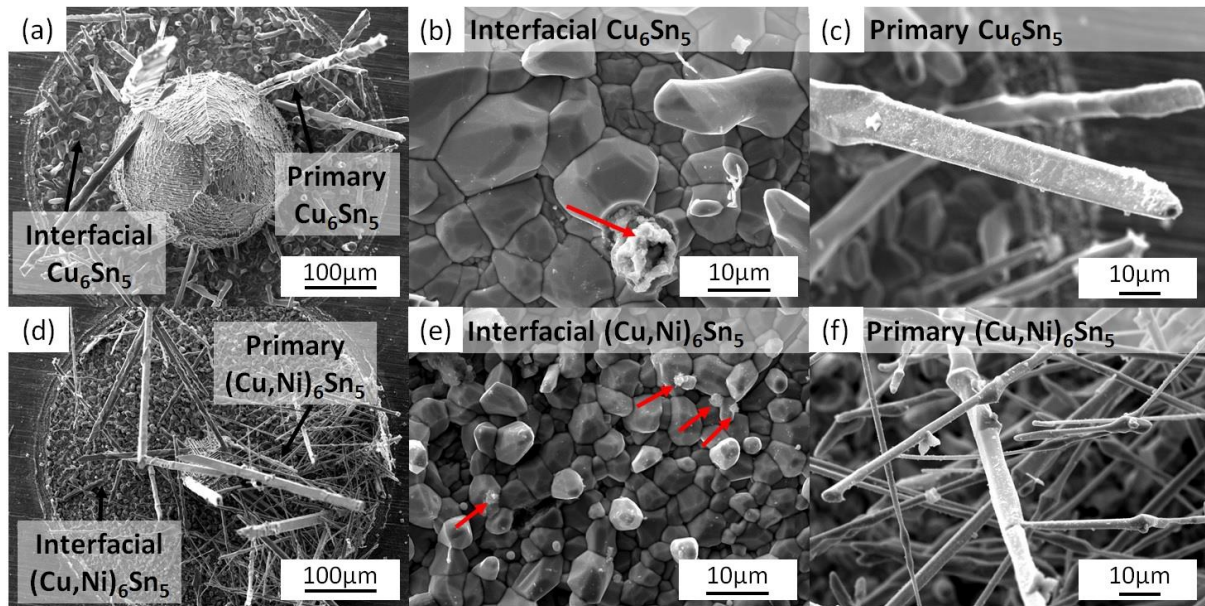


Figure 4: Secondary electron SEM images of deep etched solder joints after 2000 hours of isothermal annealing revealing the primary and interfacial intermetallic compounds of (a-c)  $\text{Sn}_{0.7}\text{Cu}+\text{TiO}_2$  and (d-f)  $\text{Sn}_{0.7}\text{Cu}_{0.05}\text{Ni}+\text{TiO}_2$ .

Investigations of the interfacial intermetallic compound layer growth after annealing were carried out by measuring the average thickness of the total interfacial layer ( $\text{Cu}_6\text{Sn}_5/(\text{Cu,Ni})_6\text{Sn}_5 + \text{Cu}_3\text{Sn}$ ) and  $\text{Cu}_3\text{Sn}$  layer after reflow and annealing. Figure 5a is the average thickness of total interfacial intermetallic compound layer of  $\text{Sn}_{0.7}\text{Cu}$ ,  $\text{Sn}_{0.7}\text{Cu}+\text{TiO}_2$ ,  $\text{Sn}_{0.7}\text{Cu}_{0.05}\text{Ni}$  and  $\text{Sn}_{0.7}\text{Cu}_{0.05}\text{Ni}+\text{TiO}_2$  solder joints after annealing. Generally, with the increase of annealing time, the total interfacial layer becomes thicker. From the graph, comparing  $\text{Sn}_{0.7}\text{Cu}$  and  $\text{Sn}_{0.7}\text{Cu}_{0.05}\text{Ni}$  solder joints, a slightly thinner total interfacial layer of Ni-containing solder joints was observed on as-reflowed samples however it grew thicker than  $\text{Sn}_{0.7}\text{Cu}$  after 500, 1000 and 1500 hours of annealing. After 2000 hours of annealing, the total thickness of the interfacial layer had increased significantly in  $\text{Sn}_{0.7}\text{Cu}$  which resulted in the thickest interfacial layer ( $\sim 12\text{--}13\text{ }\mu\text{m}$ ) compared to other solder joints. Across all samples, it was shown that additions of  $\text{TiO}_2$  in both  $\text{Sn}_{0.7}\text{Cu}$  and  $\text{Sn}_{0.7}\text{Cu}_{0.05}\text{Ni}$  had suppressed the interfacial layer by around 10-40% (compared to no  $\text{TiO}_2$ ) where the suppression percentage increases with the increase in annealing time.  $\text{Sn}_{0.7}\text{Cu}_{0.05}\text{Ni}+\text{TiO}_2$  resulted in the thinnest total interfacial layer after 2000 hours of annealing with approximately  $6.6\text{ }\mu\text{m}$  total interfacial layer thickness compared to approximately  $8.5\text{ }\mu\text{m}$  in  $\text{Sn}_{0.7}\text{Cu}_{0.05}\text{Ni}$ .

During early stages of  $\text{Sn}_{0.7}\text{Cu}$  solder wetting, Mohd Salleh et al. (2015b) found that interfacial  $\text{Cu}_6\text{Sn}_5$  will rapidly form followed by subsequent scallop shaped growth while the

Cu<sub>3</sub>Sn layer may form in between the Cu<sub>6</sub>Sn<sub>5</sub> layer and the Cu as result of continuous Cu diffusion from the substrate into the Cu<sub>6</sub>Sn<sub>5</sub> layer. It is reported by Wang et al. (2014) that Cu<sub>3</sub>Sn formation could be accelerated by annealing. From Figure 5b, it is observed that in Sn0.7Cu and Sn0.7Cu+TiO<sub>2</sub>, a significant layer of Cu<sub>3</sub>Sn forms changing from ~0.8 μm as-reflowed to ~5 μm after 2000 hours of annealing. However, with Ni additions, a relatively fine and thinner interfacial Cu<sub>3</sub>Sn layer were observed indicating the Ni additions were able to suppress the Cu diffusion from the substrate into the Cu<sub>6</sub>Sn<sub>5</sub> layer. Comparing samples with TiO<sub>2</sub> additions in both Sn0.7Cu and Sn0.7Cu0.05Ni, there is no significant growth or suppression of Cu<sub>3</sub>Sn and it appears that TiO<sub>2</sub> does not play a role in controlling the Cu diffusion from the substrate into the layer. It is believed that TiO<sub>2</sub> plays a significant role during the liquid solder wetting where TiO<sub>2</sub> nanoparticles between the liquid solder and substrate acts as a dissolution barrier which reduces the Cu dissolution from the substrate. Thus, excessive reinforcement may also result in a barrier for wetting. After the rapid formation of the Cu<sub>6</sub>Sn<sub>5</sub> layer during wetting, TiO<sub>2</sub> nanoparticles may be pushed above the Cu<sub>6</sub>Sn<sub>5</sub> layer and remain as a diffusion barrier from the matrix.

Although the TiO<sub>2</sub> nanoparticles density (4.2g/cm<sup>3</sup>) is much lower than the liquid Sn (6.98 g/cm<sup>3</sup>), a higher surface energy of TiO<sub>2</sub> nanoparticle (~1.9 J/m<sup>2</sup>) compared to Sn liquid (~0.5 J/m<sup>2</sup>) at 227 °C allows the liquid Sn to wet the nanoparticles. During soldering, with 1wt% of TiO<sub>2</sub> additions, some reinforcement will remain in the solder while some particles near the surface were observed to be pushed out during solidification. Stefanescu et al. (1988) reported that when a moving solidification front intercepts an insoluble particle, it can either be pushed or engulfed. Engulfment during solidification occurs when solid grows over the particle, followed by enclosure of the particle in the solid. Evidence of TiO<sub>2</sub> reinforcement remaining on the interfacial Cu<sub>6</sub>Sn<sub>5</sub> was observed in deep-etched reinforced solder balls with aggregation of TiO<sub>2</sub> particles as in Figure 4b, 4e (red arrow) and 6. Figure 6a and 6b indicate that TiO<sub>2</sub> may be pushed or engulfed by the interfacial compounds and Sn during solidification. As in Figure 6c, a cup shape of Cu<sub>6</sub>Sn<sub>5</sub> can be observed partially surrounding the TiO<sub>2</sub> aggregated particles while being pushed. Figure 6b and 6d confirms the presence of TiO<sub>2</sub> reinforcement by EDS point analysis. Thus, it is possible to use TiO<sub>2</sub> nanoparticles as reinforcement additions in soldering and suppress the total interfacial layer during soldering and annealing. Subsequently by controlling the microstructure in the solder joint, the solder joint strength could be improved.



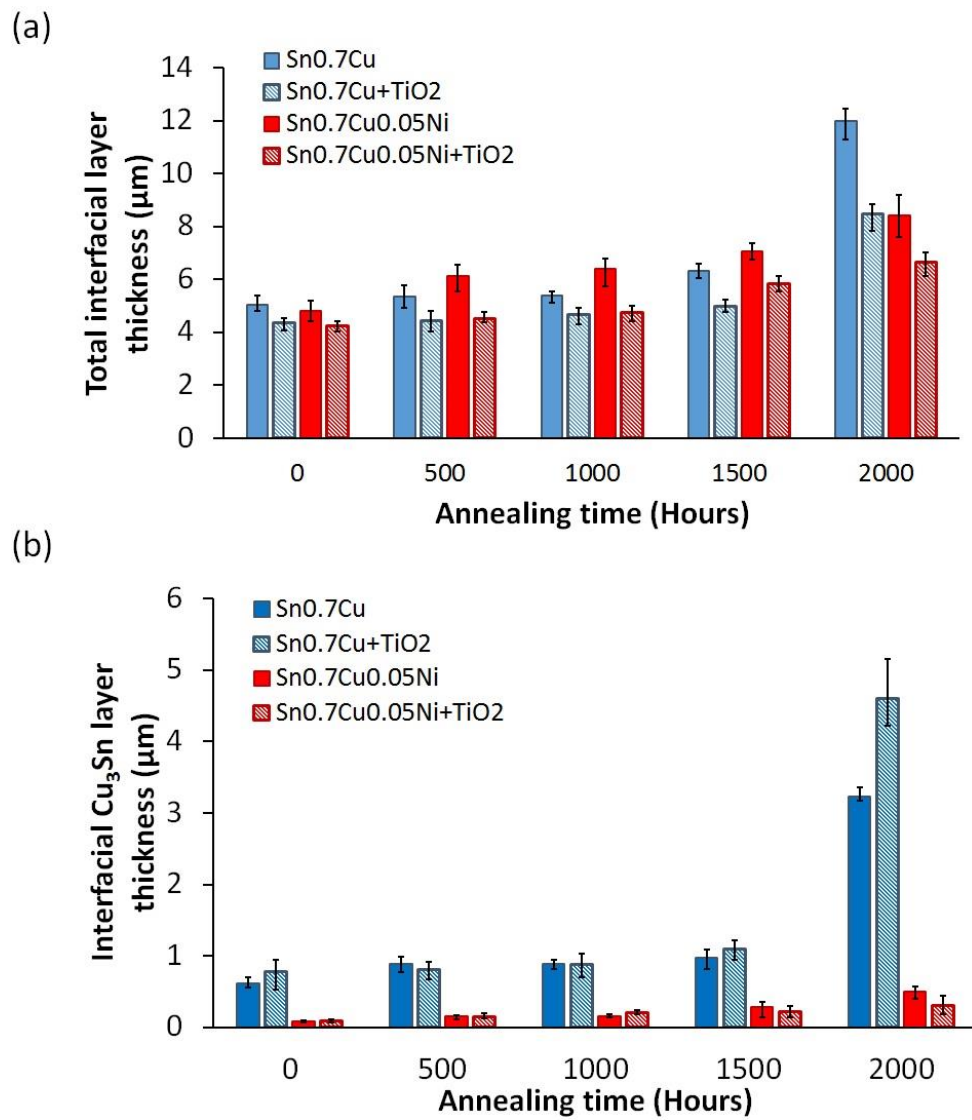


Figure 5: Average thickness of the (a) total interfacial intermetallic compound, (b) interfacial  $\text{Cu}_6\text{Sn}_5/(\text{Cu},\text{Ni})_6\text{Sn}_5$  intermetallic compound and (c) interfacial  $\text{Cu}_3\text{Sn}$  layer formation of isothermal annealed  $\text{Sn}_{0.7}\text{Cu}$ ,  $\text{Sn}_{0.7}\text{Cu}+\text{TiO}_2$ ,  $\text{Sn}_{0.7}\text{Cu}_{0.05}\text{Ni}$  and  $\text{Sn}_{0.7}\text{Cu}_{0.05}\text{Ni}+\text{TiO}_2$  after 0, 500, 1000, 1500 and 2000 hours.

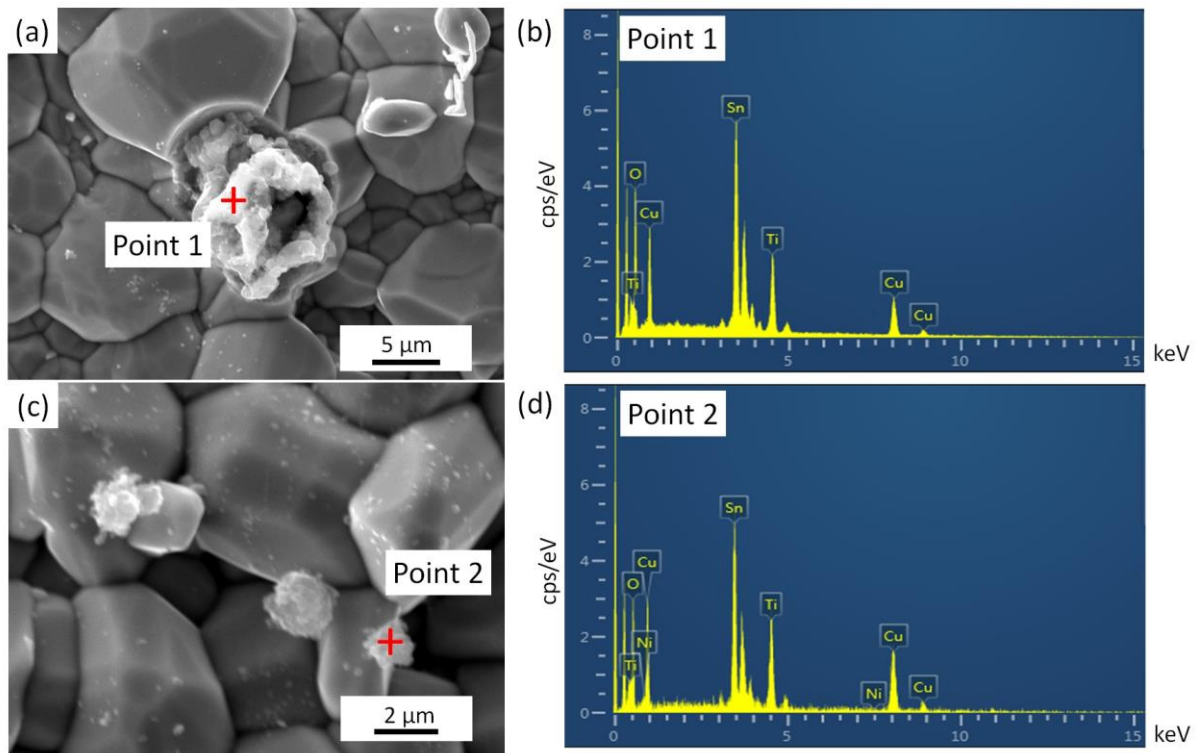


Figure 6: Secondary electron SEM images and EDS point analysis of agglomerated  $\text{TiO}_2$  found attached to the interfacial layers of (a-b)  $\text{Sn}_{0.7}\text{Cu}+\text{TiO}_2$  and (c-d)  $\text{Sn}_{0.7}\text{Cu}_{0.05}\text{Ni}+\text{TiO}_2$  after 2000 hour isothermal annealing.

### 3.2 Shear strength and fracture energy of solder joints

Mechanical performance of solder joints was conducted by evaluating the shear strength, total shear fracture energy, shear fracture initiation energy and shear fracture propagation energy. Figure 7a represents an example of a high speed solder ball shear strength result comparing as-reflowed  $\text{Sn}_{0.7}\text{Cu}$ ,  $\text{Sn}_{0.7}\text{Cu}+\text{TiO}_2$ ,  $\text{Sn}_{0.7}\text{Cu}_{0.05}\text{Ni}$  and  $\text{Sn}_{0.7}\text{Cu}_{0.05}\text{Ni}+\text{TiO}_2$ . As in Figure 7a, the shear force graph of as-reflowed  $\text{Sn}_{0.7}\text{Cu}$  and  $\text{Sn}_{0.7}\text{Cu}+\text{TiO}_2$  had a similar trend indicating a more brittle fracture characteristic with a steeper slope before and after the maximum shear force compared to as-reflowed  $\text{Sn}_{0.7}\text{Cu}_{0.05}\text{Ni}$  and  $\text{Sn}_{0.7}\text{Cu}_{0.05}\text{Ni}+\text{TiO}_2$  which indicates a more ductile fracture solder joint. Tsukamoto et al. (2010) reported that from a shear force graph, a steeper slope indicates a more brittle fracture characteristic. Results of the shear strength of each solder joint composition after annealing are plotted in Figure 7b. With 1wt% $\text{TiO}_2$  in the as-reflowed samples, the solder joint strength of  $\text{Sn}_{0.7}\text{Cu}$  had increased by about 20% of the average shear strength while the addition of 0.05wt%Ni had increased by about 28% (~16 N) of the average shear strength. The  $\text{Sn}_{0.7}\text{Cu}_{0.05}\text{Ni}+\text{TiO}_2$  samples had the highest average solder joint strength among all the solder joints of approximately 16.5 N while  $\text{Sn}_{0.7}\text{Cu}$  resulted in the lowest average solder joint strength of approximately 12.5 N. Annealed solder joints had a relatively

decreasing values of average shear strength after 500, 1000, 1500 and 2000 hours of annealing time. At the maximum annealing time (2000 hour), it was observed that solder joints with the additions of  $\text{TiO}_2$  had the highest average shear strength with a similar strength between  $\text{Sn0.7Cu}+\text{TiO}_2$  and  $\text{Sn0.7Cu0.05Ni}+\text{TiO}_2$ . This indicates that  $\text{TiO}_2$  additions had improved the solder joint strength in all annealed samples and a combination of 0.05wt%Ni and  $\text{TiO}_2$  to  $\text{Sn0.7Cu}$  resulted in the highest shear strength. Referring to the total interfacial intermetallic thickness and the  $\text{Cu}_3\text{Sn}$  interfacial thickness (Figure 4a and b) after annealing, the shear strength of the solder joint decreases as the thickness of these interfacial layer increases. It is believed that besides the suppression of the interfacial layer,  $\text{TiO}_2$  could also act to pin dislocations in the solder joint matrix which increases the solder joint. However, it is known that solder joint strength does not only rely on the interfacial layer thickness and could also be influenced by other factors such as flux void formation, Kirkendall void formation and large primary intermetallics in the solder joint matrix.

Figure 8 shows the total shear energy, fracture initiation energy and fracture propagation energy of the solder joint samples at 0, 500, 1000, 1500 and 2000 hours of annealing.  $\text{Sn0.7Cu0.05Ni}+\text{TiO}_2$  resulted in the highest shear energy value compared to other solder joint compositions. In contrast,  $\text{Sn0.7Cu}$  had the lowest shear energy value. It is observed that with an increasing annealing time, the total shear energy of  $\text{Sn0.7Cu0.05Ni}$  and  $\text{Sn0.7Cu0.05Ni}+\text{TiO}_2$  decreased while  $\text{Sn0.7Cu}$  and  $\text{Sn0.7Cu}+\text{TiO}_2$  did not display a decreasing shear energy value after annealing. This may be due to the low shear energy in as-reflowed samples of  $\text{Sn0.7Cu}$  and  $\text{Sn0.7Cu}+\text{TiO}_2$  which indicates a brittle fracture threshold value even before annealing. By distinguishing the fracture initiation and propagation energy, the relative energy required for a solder joint fracture to initiate and propagate could be determined. As shown in Figure 8b, fracture initiation energy of solder joints had a similar trend to the total fracture initiation energy. On as-reflowed solder joints, for  $\text{Sn0.7Cu0.05Ni}+\text{TiO}_2$ , approximately 1.8 mJ is required to initiate a solder joint fracture and this decreases after annealing time to 2000 hours to approximately 0.9 mJ. Similarly a decreasing trend of  $\text{Sn0.7Cu0.05Ni}$  fracture initiation energy is apparent, where the approximately 1.6 mJ is required to initiate a solder joint fracture decreases after annealing for 2000 hours to approximately 0.8 mJ. The fracture propagation energy of the sheared solder joints is shown in Figure 8c and it is seen in as-reflowed solder joints and after 2000 hours of annealing,  $\text{Sn0.7Cu0.05Ni}+\text{TiO}_2$  resulted in the highest value compared to other solder joints. However, no obvious trend in fracture propagation energy in all solder joints after annealing was apparent.

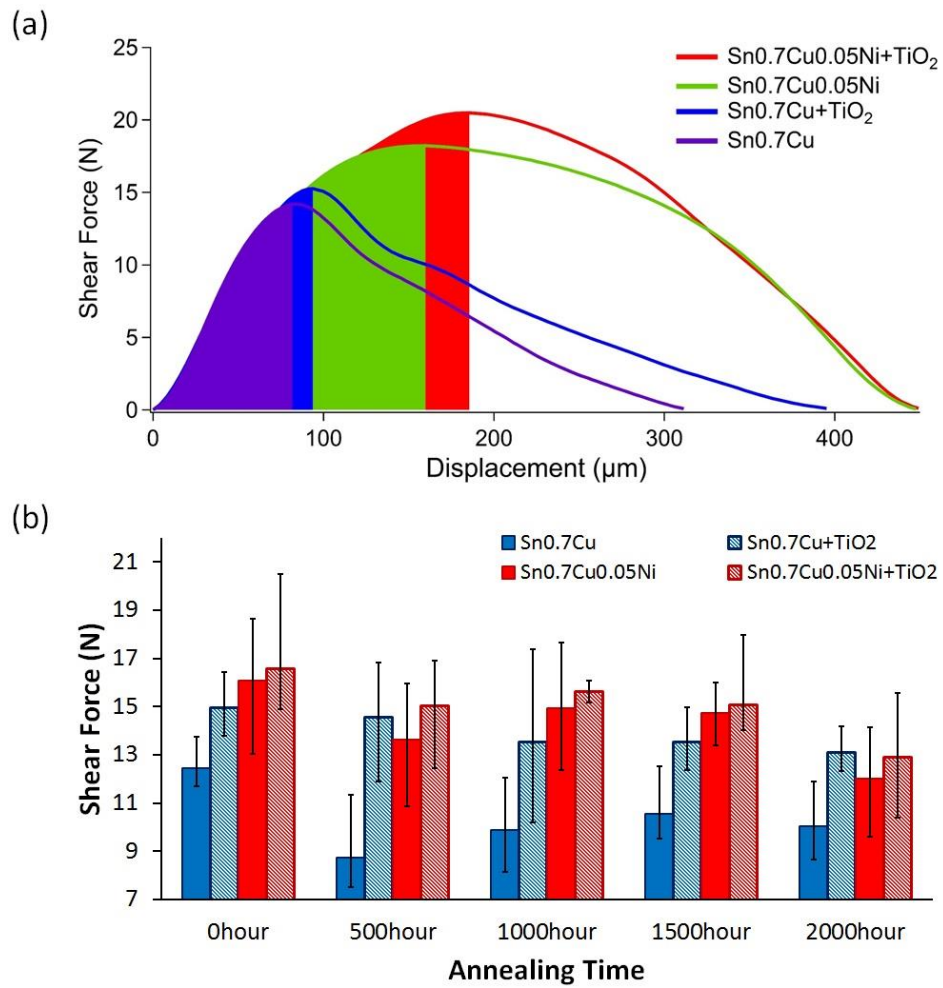


Figure 7: (a) Shear force versus displacement graph for high speed shear tests with the colored area showing the initial fracture energy of the as-soldered solder joint samples and (b) the shear force indicating the shear strength of solder joints after 0, 500, 1000, 1500 and 2000 hours of isothermal annealing.

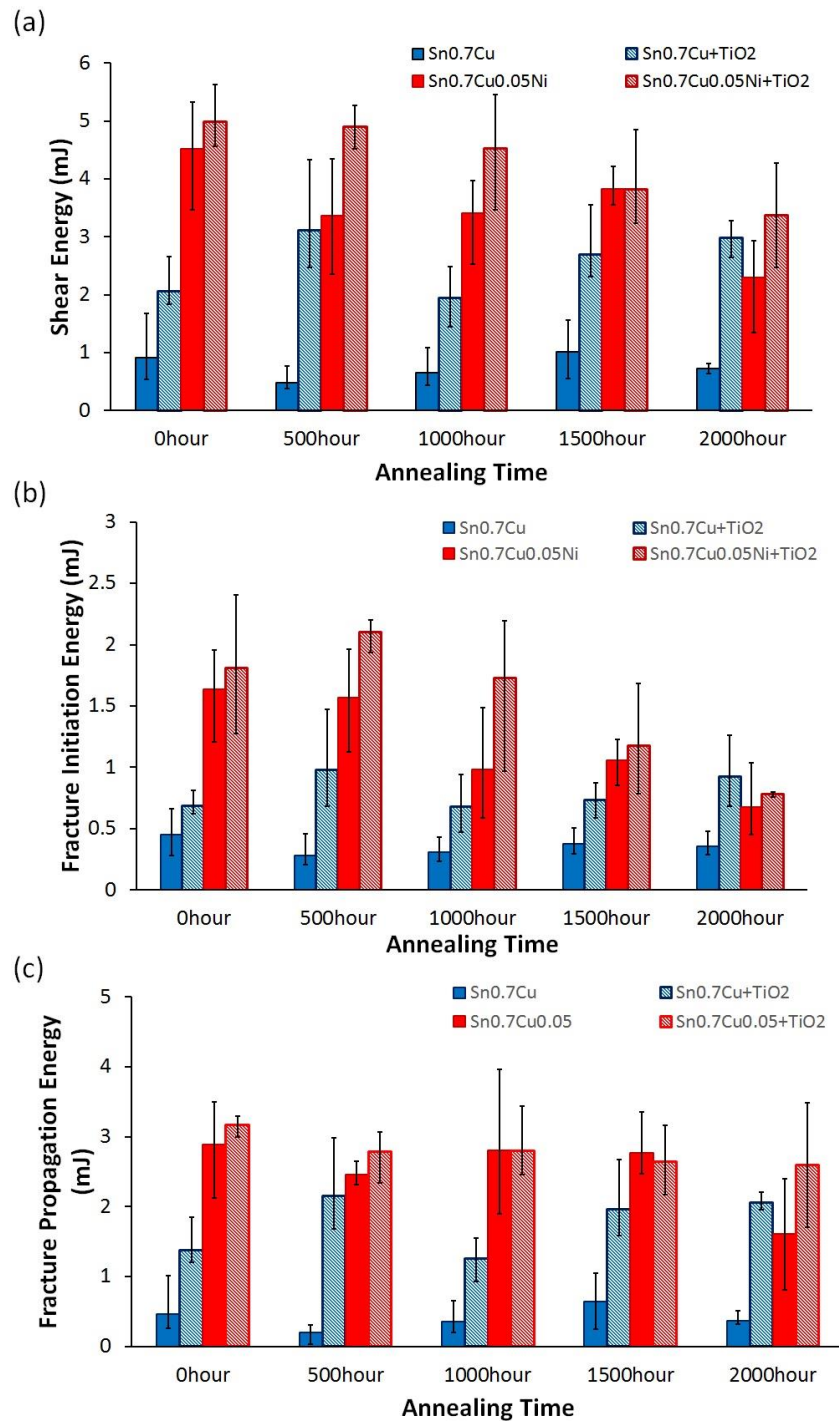


Figure 8: (a) Total shear energy, (b) fracture initiation energy and (c) fracture propagation energy of 0, 500, 1000, 1500 and 2000 hour isothermal annealed solder joints.

### 3.3 Fracture surface analysis

Figure 9 and Figure 10 show the fracture mode distributions of the high speed shear solder joint samples collected from SEM images based on the failure modes defined in Figure 1c-f. Figure 9a indicates the fracture mode distribution of Sn0.7Cu in as-reflowed solder joints and annealed solder joints. It is observed that the majority of the fracture modes for this solder joint composition were relatively brittle and a small percentage of quasi-brittle failure

was observed. When  $\text{TiO}_2$  additions were made to  $\text{Sn0.7Cu}$ , a less brittle fracture was observed and quasi-brittle failure dominated. It is likely the suppression of the total interfacial layer thickness as in Figure 4a has influenced the fracture mode and a reduced interfacial layer thickness resulted in more fracture in the bulk solder which resulted in quasi-brittle and quasi ductile failure modes at 2000 hours in annealed solder joints. In  $\text{Sn0.7Cu0.05Ni}$  and with the additions of  $\text{TiO}_2$ , less brittle failure was observed. After annealing to 2000 hours, 100% of samples experienced quasi-brittle failure in  $\text{Sn0.7Cu0.05Ni}$  solder joints while with  $\text{TiO}_2$  additions, a mixture of ductile, quasi-ductile and quasi-brittle failure modes were observed. It is apparent therefore that Ni and  $\text{TiO}_2$  additions can alter the failure mode from a more brittle failure mode to a more ductile failure mode. This may be attributed to a suppression of the  $\text{Cu}_3\text{Sn}$  layer and the total interfacial layer thickness. Koo et al. (2008) found that the  $\text{Cu}_3\text{Sn}$  layer may also be associated with Kirkendall voids which become more prevalent in annealed solder joints.

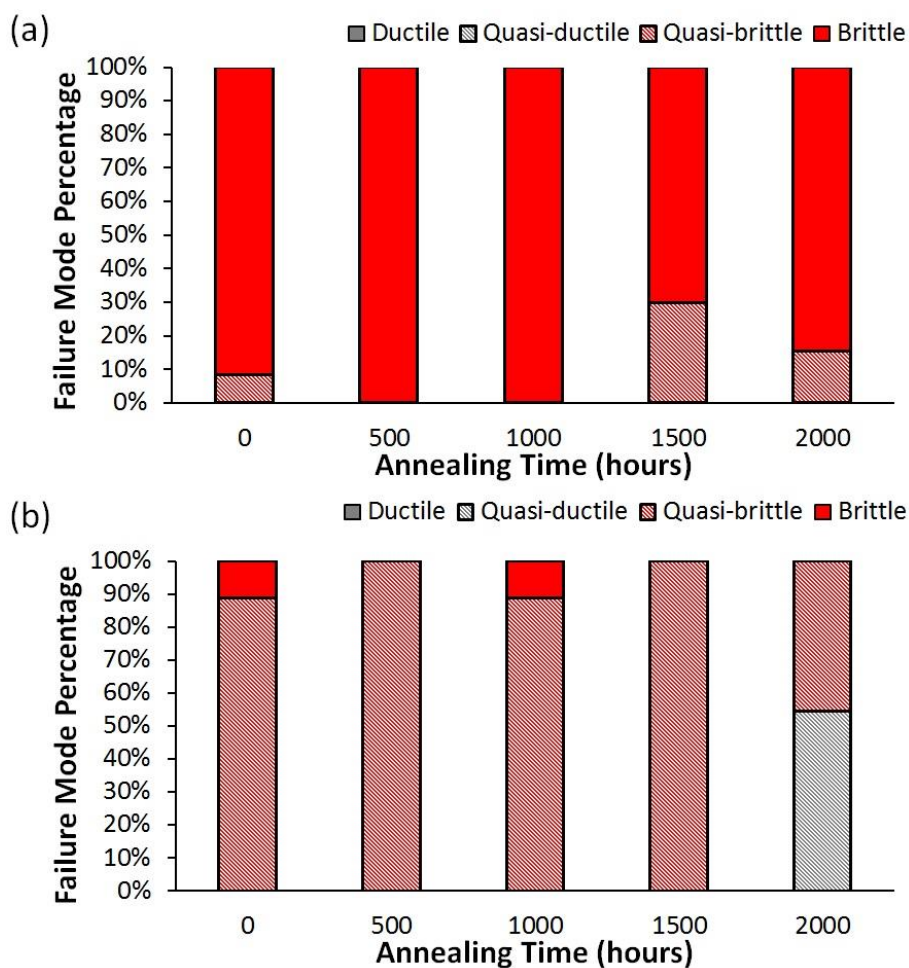


Figure 9: Fracture mode distribution of high speed shear results of annealed solder joints of (a)  $\text{Sn0.7Cu}$  and (b)  $\text{Sn0.7Cu+TiO}_2$  after 0, 500, 1000, 1500 and 2000 hours.



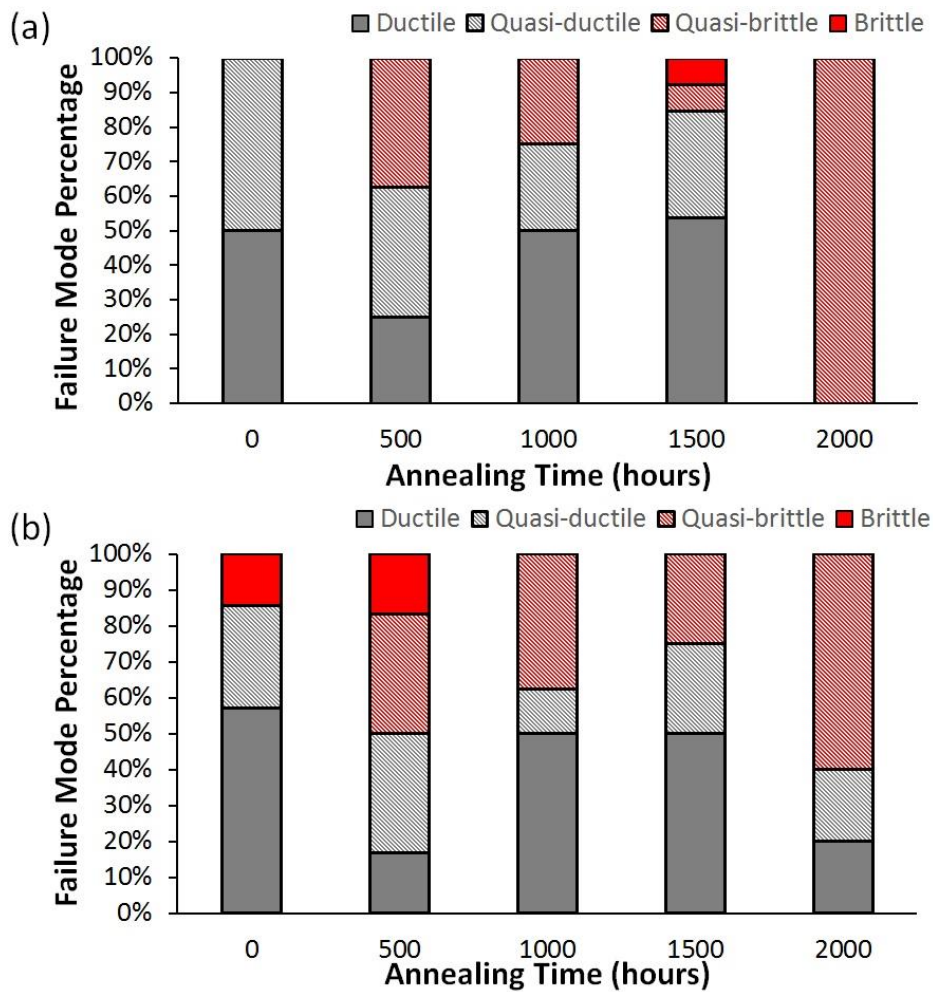


Figure 10: Fracture mode distribution of high speed shear results of annealed solder joints of (a) Sn0.7Cu0.05Ni and (b) Sn0.7Cu0.05Ni+TiO<sub>2</sub> after 0, 500, 1000, 1500 and 2000 hours.

For a clearer understanding on the factors that affect the failure modes, fracture surfaces were analysed. Figure 11 and 12 shows the SEM image of the fracture surfaces of all sheared solder joints after 2000 hours of annealing. As in Figure 11a and b in the Sn0.7Cu fracture surface, failure modes of brittle and quasi-brittle were majorly caused by the formation of Kirkendall voids with the sheared solder joint fracturing predominantly through the Cu<sub>3</sub>Sn and Cu<sub>6</sub>Sn<sub>5</sub> layer. From the fracture surface of the Cu<sub>3</sub>Sn layer as in Figure 11b, the Kirkendall voids played a major role. With additions of TiO<sub>2</sub>, although a thick layer of Cu<sub>3</sub>Sn was measured in the solder joints, the majority of the fracture surface was through the large Cu<sub>6</sub>Sn<sub>5</sub> interfacial layer and the bulk solder. In both samples, intergranular brittle cracks were observed (indicated by red arrows) on the Cu<sub>6</sub>Sn<sub>5</sub> interfacial scallop grooves where large Cu<sub>6</sub>Sn<sub>5</sub> scallop grooves were observed in cross section image of the interfacial layer as in Figure 2d and h.

Figure 12a and b are detailed fracture surfaces of Sn0.7Cu0.05Ni sheared solder joints after 2000 hours of annealing which show quasi-brittle failure modes of the solder joints were through the  $(\text{Cu,Ni})_6\text{Sn}_5$  layer and bulk solder. Evidence of the existence of solder voids were observed where cup-shaped fracture was observed in the bulk solder as indicated with the red arrow in Figure 12b. Fracture surfaces of Sn0.7Cu0.05Ni+TiO<sub>2</sub> as in Figure 12c and d show fracture of the solder joints occurred through the bulk solder, Cu<sub>3</sub>Sn and  $(\text{Cu,Ni})_6\text{Sn}_5$  layer. At the bulk solder near to the surface of the solder ball, primary  $(\text{Cu,Ni})_6\text{Sn}_5$  cracks were observed. These brittle primary intermetallics which exists at the edge of the solder ball may act as a weak point where fracture may initiate.

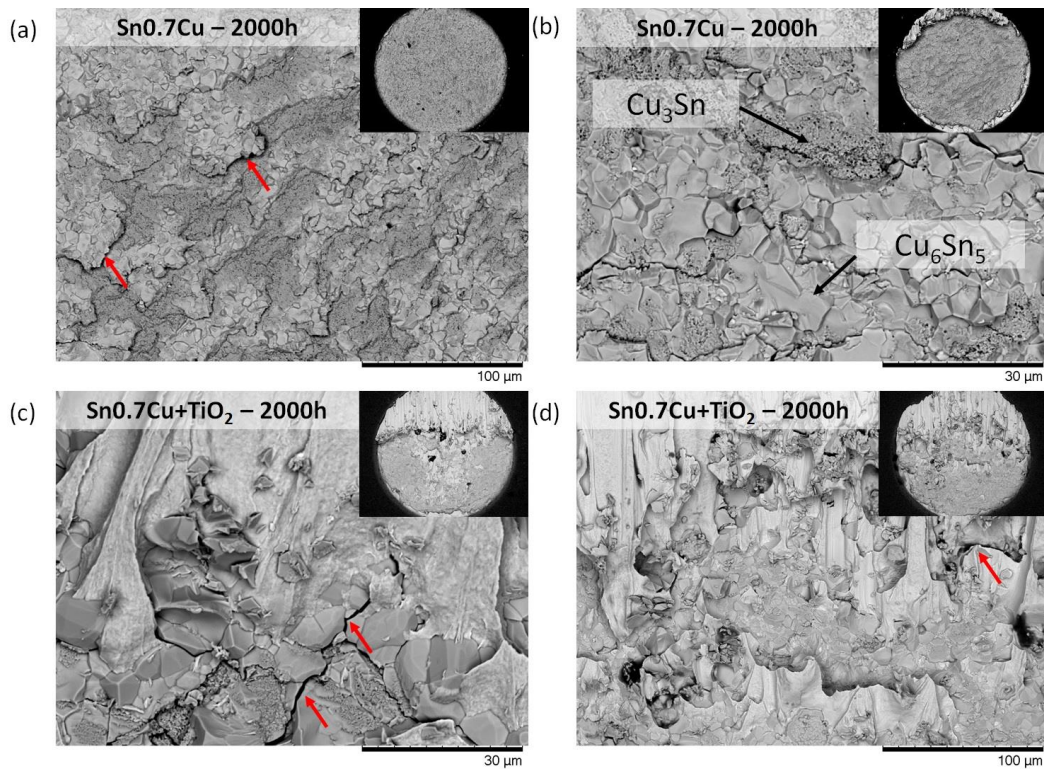


Figure 11: Detailed surface fracture backscattered electron SEM images of (a) brittle mode Sn0.7Cu annealed for 2000 hours, (b) quasi brittle mode Sn0.7Cu annealed for 2000 hours, (c) quasi brittle mode Sn0.7Cu+TiO<sub>2</sub> annealed for 2000 hour and (d) quasi ductile mode Sn0.7Cu annealed for 2000 hours. Red arrows indicate the intergranular brittle cracks at the Cu<sub>6</sub>Sn<sub>5</sub> grooves.



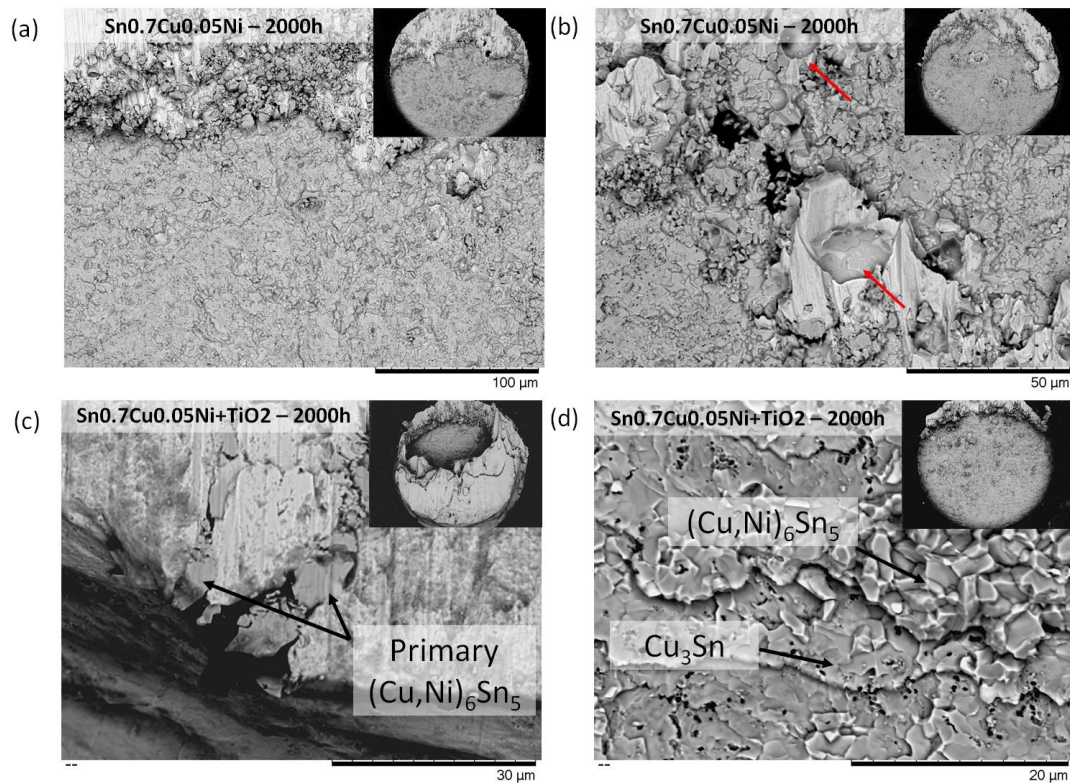


Figure 12: Detailed surface fracture backscattered electron SEM images of (a-b) quasi brittle mode Sn0.7Cu0.05Ni annealed for 2000 hours, (c) quasi ductile mode Sn0.7Cu0.05Ni+TiO<sub>2</sub> annealed for 2000 hours and (d) quasi brittle mode Sn0.7Cu0.05Ni+TiO<sub>2</sub> annealed for 2000 hours. Red arrows in (b) indicate the interfacial solder voids at the fracture surface.

#### 4.0 Conclusions

The effects of Ni, TiO<sub>2</sub> in isolation and when combined on the microstructure and properties of Sn0.7Cu solders on Cu substrates were examined for a range of annealing times.

The following conclusion can be made:

- a) A scallop-shaped interfacial Cu<sub>6</sub>Sn<sub>5</sub> layer with a planar layer of Cu<sub>3</sub>Sn formed when using Sn0.7Cu. With additions of TiO<sub>2</sub> reinforcement to Sn0.7Cu, a more planar scalloped Cu<sub>6</sub>Sn<sub>5</sub> morphology was present with reduced interfacial boundary grooves. A fine scallop-shaped interfacial (Cu,Ni)<sub>6</sub>Sn<sub>5</sub> layer was present when using Sn0.7Cu0.05Ni and Sn0.7Cu0.05Ni+TiO<sub>2</sub>.
- b) Additions of TiO<sub>2</sub> to both Sn0.7Cu and Sn0.7Cu0.05Ni suppressed the total interfacial layer by 10-40% with the suppression percentage increasing with an increase in annealing time.

- c) Kirkendall voids on the  $\text{Cu}_3\text{Sn}$  layer were observed to increase after longer annealing times where a fine and significantly thinner interfacial  $\text{Cu}_3\text{Sn}$  layer was observed in solder joints containing Ni. This shows that Ni was able to suppress the Cu diffusion from the substrate into the  $\text{Cu}_6\text{Sn}_5$  layer and suppress the  $\text{Cu}_3\text{Sn}$  layer.
- d) Evidence of  $\text{TiO}_2$  reinforcement remaining on the interfacial  $\text{Cu}_6\text{Sn}_5$  in deep etched reinforced solder balls indicates that  $\text{TiO}_2$  may be pushed or engulfed by the interfacial layer growth and Sn during solidification.  $\text{TiO}_2$  nanoparticles between the liquid solder and substrate may act as a dissolution barrier which reduces the Cu dissolution from the substrate during soldering and remain as a diffusion barrier from the matrix during annealing.
- e) The solder joint strength of solders containing  $\text{TiO}_2$  increased by about 20%-28% of the average shear strength compared to non-reinforced solder joints and  $\text{Sn}_{0.7}\text{Cu}_{0.05}\text{Ni}+\text{TiO}_2$  displayed the highest average solder joint shear strength and total fracture energy among all the solder joints after reflow and subsequent annealing.
- f) Ni and  $\text{TiO}_2$  additions altered the failure mode from brittle to a more ductile failure mode. This was attributed to the suppression of the  $\text{Cu}_3\text{Sn}$  layer and the total interfacial layer thickness.

## 5.0 Acknowledgement

This work was financially supported from the University of Queensland (UQ)-Nihon Superior (NS) collaboration research project, ARC Linkage project (LP140100485), Grant-in-Aid for Scientific Research (S) (24226018) from JSPS, Japan and scholarship from the Malaysian Higher Education Ministry and University Malaysia Perlis (UniMAP). Authors would like to thank Mr. Xuan Quy Tran for his kind help in preparing the metallography samples. High speed shear tests were conducted at Nihon Superior Japan.

## References

- Chellvarajoo, S., Abdullah, M.Z., 2016. Microstructure and mechanical properties of Pb-free Sn–3.0Ag–0.5Cu solder pastes added with NiO nanoparticles after reflow soldering process. *Materials & Design* 90, 499-507.
- Chuang, C.-M., Lin, K.-L., 2003. Effect of microelements addition on the interfacial reaction between Sn-Ag-Cu solders and the Cu substrate. *Journal of Electronic Materials* 32, 1426-1431.
- Chuang, T.H., Wu, M.W., Chang, S.Y., Ping, S.F., Tsao, L.C., 2010. Strengthening mechanism of nano-Al<sub>2</sub>O<sub>3</sub> particles reinforced Sn<sub>3.5</sub>Ag<sub>0.5</sub>Cu lead-free solder. *Journal of Materials Science: Materials in Electronics* 22, 1021-1027.
- El-Daly, A.A., Fawzy, A., Mansour, S.F., Younis, M.J., 2013. Novel SiC nanoparticles-containing Sn–1.0Ag–0.5Cu solder with good drop impact performance. *Materials Science and Engineering: A* 578, 62-71.
- Koo, J.-M., Kim, Y.-N., Yoon, J.-W., Kim, D.-G., Noh, B.-I., Kim, J.-W., Moon, J.-H., Jung, S.-B., 2008. Effect of displacement rate on bump shear properties of electroplated solder bumps in flip-chip packages. *Materials Science and Engineering: A* 483–484, 620-624.
- Liu, X.D., Han, Y.D., Jing, H.Y., Wei, J., Xu, L.Y., 2013. Effect of graphene nanosheets reinforcement on the performance of Sn-Ag-Cu lead-free solder. *Materials Science and Engineering: A* 562, 25-32.
- Mohd Salleh, M.A.A., Bakri, A.M.M.A., Kamarudin, H., Bnhussain, M., M.H, Z.H., Somidin, F., 2011. Solderability of Sn-0.7Cu/Si<sub>3</sub>N<sub>4</sub> lead-free composite solder on Cu-substrate. *Physics Procedia* 22, 299-304.
- Mohd Salleh, M.A.A., Bakri, A.M.M.A., Zan@Hazizi, M.H., Somidin, F., Mohd Alui, N.F., Ahmad, Z.A., 2012. Mechanical properties of Sn–0.7Cu/Si<sub>3</sub>N<sub>4</sub> lead-free composite solder. *Materials Science and Engineering: A* 556, 633-637.
- Mohd Salleh, M.A.A., McDonald, S.D., Gourlay, C.M., Belyakov, S.A., Yasuda, H., Nogita, K., 2016a. Effect of Ni on the Formation and Growth of Primary Cu<sub>6</sub>Sn<sub>5</sub> Intermetallics in Sn-0.7 wt.%Cu Solder Pastes on Cu Substrates During the Soldering Process. *Journal of Electronic Materials* 45, 154-163.
- Mohd Salleh, M.A.A., McDonald, S.D., Gourlay, C.M., Yasuda, H., Nogita, K., 2016b. Suppression of Cu<sub>6</sub>Sn<sub>5</sub> in TiO<sub>2</sub> reinforced solder joints after multiple reflow cycles. *Materials & Design* 108, 418-428.
- Mohd Salleh, M.A.A., McDonald, S.D., Terada, Y., Yasuda, H., Nogita, K., 2015a. Development of a microwave sintered TiO<sub>2</sub> reinforced Sn–0.7wt%Cu–0.05wt%Ni alloy. *Materials & Design* 82, 136-147.

Mohd Salleh, M.A.A., McDonald, S.D., Yasuda, H., Sugiyama, A., Nogita, K., 2015b. Rapid Cu<sub>6</sub>Sn<sub>5</sub> growth at liquid Sn/solid Cu interfaces. *Scripta Materialia* 100, 17-20.

Mohd Salleh, M.M.A., McDonald, S., Nogita, K., 2013. Non-metal reinforced lead-free composite solder fabrication methods and its reinforcing effects to the suppression of intermetallic formation: Short review, *Applied Mechanics and Materials*, pp. 260-266.

Said, R.M., Salleh, M.A.A.M., Derman, M.N., Ramli, M.I.I., Nasir, N.M., Saud, N., 2016. Isothermal aging affect to the growth of Sn-Cu-Ni-1 wt. % TiO<sub>2</sub> composite solder paste, *Key Engineering Materials*, pp. 123-131.

Shen, J., Chan, Y.C., 2009. Effects of ZrO<sub>2</sub> nanoparticles on the mechanical properties of Sn–Zn solder joints on Au/Ni/Cu pads. *Journal of Alloys and Compounds* 477, 552-559.

Shohji, I., Tsunoda, S., Watanabe, H., Asai, T., Nagano, M., 2005. Reliability of solder joint with Sn-Ag-Cu-Ni-Ge lead-free alloy under heat exposure conditions. *Materials Transactions* 46, 2737-2744.

Somidin, F., Salleh, M.A.A., Ahmad, K.R., 2013. Intermetallic compound formation on solder alloy/cu-substrate interface using lead-free Sn-0.7Cu/recycled-aluminum composite solder, *Advanced Materials Research*, pp. 105-111.

Stefanescu, D.M., Dhindaw, B.K., Kacar, S.A., Moitra, A., 1988. Behavior of ceramic particles at the solid- liquid metal interface in metal matrix composites. *Metallurgical Transactions A* 19, 2847-2855.

Tsao, L.C., Huang, C.H., Chung, C.H., Chen, R.S., 2012. Influence of TiO<sub>2</sub> nanoparticles addition on the microstructural and mechanical properties of Sn<sub>0.7</sub>Cu nano-composite solder. *Materials Science and Engineering: A* 545, 194-200.

Tsukamoto, H., Nishimura, T., Suenaga, S., Nogita, K., 2010. Shear and tensile impact strength of lead-free solder ball grid arrays placed on Ni (P)/Au surface-finished substrates. *Materials Science and Engineering: B* 171, 162-171.

Wang, K.-K., Gan, D., Hsieh, K.-C., 2014. The orientation relationships of the Cu<sub>3</sub>Sn/Cu interfaces and a discussion of the formation sequence of Cu<sub>3</sub>Sn and Cu<sub>6</sub>Sn<sub>5</sub>. *Thin Solid Films* 562, 398-404.

Yu, C., Chen, J., Cheng, Z., Huang, Y., Chen, J., Xu, J., Lu, H., 2016. Fine grained Cu film promoting Kirkendall voiding at Cu<sub>3</sub>Sn/Cu interface. *Journal of Alloys and Compounds* 660, 80-84.

Zeng, G., McDonald, S.D., Mu, D., Terada, Y., Yasuda, H., Gu, Q., Nogita, K., 2014. Ni segregation in the interfacial (Cu,Ni)<sub>6</sub>Sn<sub>5</sub> intermetallic layer of Sn-0.7Cu-0.05Ni/Cu ball grid array (BGA) joints. *Intermetallics* 54, 20-27.

## Chapter 7 Summary and future work

In this research, a number of peer reviewed journal articles have been published (or submitted for publication). The research has successfully contributed to an in-depth understanding of microstructure formation in reinforced Sn-Cu Pb-free solder joints. The study has focussed on both intrinsic and extrinsic reinforcing methods with  $\text{Cu}_6\text{Sn}_6$  intermetallic as an intrinsic and nano-size  $\text{TiO}_2$  particles as extrinsic reinforcing materials.

A microwave sintering PM method was successfully used to fabricate  $\text{TiO}_2$  reinforced solders. A homogenous distribution of  $\text{TiO}_2$  reinforcement was achieved using this technique which also resulted in samples with a higher density compared to conventional sintering techniques. With the unique heating characteristics obtained using microwave sintering, a fine distribution of  $\text{TiO}_2$  in the solder balls was achieved. Using this sintering technique, the hardness of the bulk solder increased and the CTE mismatch between copper at  $150^\circ\text{C}$  and the microwave sintered  $\text{TiO}_2$  containing samples was reduced relative to the non-reinforced samples. In addition to the fabrication of the  $\text{TiO}_2$  reinforced solder, a method of in situ soldering observation using an SXRI technique was developed which enabled a full soldering reaction process from the solder wetting until the solder joint solidification to be observed for the first time. This experiment technique was used as a main analytical tool in analysing the microstructure formation of the reinforced solder during soldering.

During early stages of soldering at the moment of solder wetting between Sn-0.7Cu/Cu, a significant thickness of  $\text{Cu}_6\text{Sn}_5$  of planar morphology formed almost instantly (within 0.05s) before further growth resulted in a subsequent scallop-shaped interface. The growth kinetics of the interfacial  $\text{Cu}_6\text{Sn}_5$  layer during soldering process were determined and 3 growth mechanism stages were observed mainly (i) a transient stage where the Cu concentration of the liquid at the interface was removed from the substrate, (ii) a growth stage dominated by grain boundary diffusion and (iii) a stage of slow intermetallic growth during cooling. In addition, primary  $\text{Cu}_6\text{Sn}_5$  nucleation and growth were observed in real time during the cooling stage of the soldering process. During subsequent heating in separate experiments, it was shown that a polymorphic transformation of monoclinic to hexagonal  $\text{Cu}_6\text{Sn}_5$  occurred and this was associated with strain development at the interface of Cu/ $\text{Cu}_3\text{Sn}$ / $\text{Cu}_6\text{Sn}_5$ /Sn-0.7Cu.

Microstructure formation in an intrinsic solder joint was studied using Sn-0.7Cu, Sn-3.0Ag-0.5Cu and Sn-0.7Cu-0.05Ni solder pastes on Cu substrates. Development of the microstructure during, melting, reactive wetting and solidification of Sn-0.7Cu and Sn-3.0Ag-0.5Cu solder pastes on Cu-plated FR-4 printed circuit boards (PCBs) was observed. The rapid interfacial  $\text{Cu}_6\text{Sn}_5$  layer formation is present within 0.05s of wetting, and the kinetics of flux void formation at the interface between the liquid and the  $\text{Cu}_6\text{Sn}_5$  layer were determined. Quantification of the nucleation locations and anisotropic growth kinetics of primary  $\text{Cu}_6\text{Sn}_5$  crystals revealed a competition between the nucleation of  $\text{Cu}_6\text{Sn}_5$  in the liquid versus growth of  $\text{Cu}_6\text{Sn}_5$  from the existing  $\text{Cu}_6\text{Sn}_5$  layer. Additions of 0.05 wt% of Ni to Sn-0.7Cu could significantly alter the formation and growth of the primary  $\text{Cu}_6\text{Sn}_5$  intermetallics making them small and flake-like. Ni additions appeared to promote the nucleation of a larger amount of small flake-like  $\text{Cu}_6\text{Sn}_5$ .

The influence of multiple reflows and isothermal annealing on microstructure formation in extrinsically reinforced solder joints was successfully studied. After the multiple reflow of  $\text{TiO}_2$  reinforced Sn-0.7Cu compared to  $\text{TiO}_2$ -free equivalents, a relative suppression of the primary  $\text{Cu}_6\text{Sn}_5$  and interfacial  $\text{Cu}_6\text{Sn}_5$  was observed where the suppression of  $\text{Cu}_6\text{Sn}_5$  resulted in a higher shear strength. Additions of 0.05 wt% Ni and  $\text{TiO}_2$  to Sn-0.7Cu resulted in the suppression of the  $\text{Cu}_6\text{Sn}_5$  and  $\text{Cu}_3\text{Sn}$  layers after isothermal annealing which resulted in a high solder joint strength and fracture energy.

The research relating to reinforced solder joint microstructure development performed in this study could be used as a basis for the design of an optimized and controlled microstructure in solder joints for future electronic interconnects technology and contribute towards producing high reliability solder joints. Areas of future research that would complement and build on the the research performed in this thesis are as follows:

- i. Explore how to control the microstructure in different solder alloys by manipulating the number and size of primary intermetallics and the thickness of interfacial intermetallic compounds.
- ii. Explore the unique characteristic of microwave sintering and develop a suitable microwave sintering powder metallurgy technique for high volume manufacturing of extrinsic reinforced solder suitable for industrial applications.

- iii. Further investigate the relationship of various reinforcement particles and their influence on microstructure, possibly coupled with a finite element analysis model to evaluate solder joint reliability in various processing and operating regimes.

# Bibliography

1. Waldrop, M.M., *The chips are down for Moore's law*. Nature, 2016. **530**(7589): p. 144-147.
2. Huang, M.L. and F. Yang, *Size effect model on kinetics of interfacial reaction between Sn-xAg-yCu solders and Cu substrate*. Scientific Reports, 2014. **4**: p. 7117.
3. McCormack, M., et al., *New Pb-free solder alloy with superior mechanical properties*. Applied Physics Letters, 1993. **63**(1): p. 15-17.
4. Hsiao, H.-Y., et al., *Unidirectional Growth of Microbumps on (111)-Oriented and Nanotwinned Copper*. Science, 2012. **336**(6084): p. 1007-1010.
5. Abtew, M. and G. Selvaduray, *Lead-free Solders in Microelectronics*. Materials Science and Engineering: R: Reports, 2000. **27**(5-6): p. 95-141.
6. Zheng, K. and K.N. Tu, *Six cases of reliability study of Pb-free solder joints in electronic packaging technology*. Materials Science and Engineering: R: Reports, 2002. **38**(2): p. 55-105.
7. Xin, T., *Diffusion of Lead-free Soldering in Electronics Industry in China*. China Population, Resources and Environment, 2007. **17**(6): p. 66-71.
8. Tsai, T.-N., *Improving the fine-pitch stencil printing capability using the taguchi method and taguchi fuzzy-based model*. Robotics and Computer-Integrated Manufacturing, 2011. **27**(4): p. 808-817.
9. Yang, F. and S.A. Meguid, *Efficient multi-level modeling technique for determining effective board drop reliability of PCB assembly*. Microelectronics Reliability, 2013. **53**(7): p. 975-984.
10. Nai, S.M.L., J. Wei, and M. Gupta, *Influence of ceramic reinforcements on the wettability and mechanical properties of novel lead-free solder composites*. Thin Solid Films, 2006. **504**(1-2): p. 401-404.
11. Guo, F., *Composite lead-free electronic solders*. Journal of Materials Science: Materials in Electronics, 2007. **18**(1-3): p. 129-145.
12. Shen, J. and Y.C. Chan, *Research advances in nano-composite solders*. Microelectronic Reliability, 2009. **49**: p. 223-234.
13. Tai, F., et al., *Creep and thermomechanical fatigue properties of in situ Cu<sub>6</sub>Sn<sub>5</sub> reinforced lead-free composite solder*. Materials Science and Engineering: A, 2010. **527**(15): p. 3335-3342.
14. Lee, J.G., K.C. Chen, and K.N. Subramanian, *Formation and growth of intermetallics around metallic particles in eutectic Sn-Ag solder*. Journal of Electronic Materials. **32**(11): p. 1240-1248.
15. Osorio, W.R., et al., *The effects of microstructure and Ag<sub>3</sub>Sn and Cu<sub>6</sub>Sn<sub>5</sub> intermetallics on the electrochemical behavior of Sn-Ag and Sn-Cu solder alloys*. International Journal of Electrochemical Science, 2012. **7**: p. 6436-6452.
16. Mohd Salleh, M.A.A., et al., *Research advances of composite solder materials fabricated via powder metallurgy route*. Advanced Materials Research, 2013. **626**: p. 791-796.
17. Gupta, M. and W.L.E. Wong, *Enhancing overall mechanical performance of metallic materials using two-directional microwave assisted rapid sintering*. Scripta Materialia, 2005. **52**(6): p. 479-483.
18. Oghbaei, M. and O. Mirzaee, *Microwave versus conventional sintering: A review of fundamentals, advantages and applications*. Journal of Alloys and Compounds, 2010. **494**(1-2): p. 175-189.
19. Luo, S.-d., et al., *Microwave sintering W-Cu composites: Analyses of densification and microstructural homogenization*. Journal of Alloys and Compounds, 2009. **473**(1-2): p. L5-L9.
20. Mondal, A., A. Upadhyaya, and D. Agrawal, *Microwave and conventional sintering of 90W-7Ni-3Cu alloys with premixed and prealloyed binder phase*. Materials Science and Engineering: A, 2010. **527**(26): p. 6870-6878.



21. Satyanarayan and K.N. Prabhu, *Effect of temperature and substrate surface texture on wettability and morphology of IMCs between Sn–0.7Cu solder alloy and copper substrate*. Journal of Materials Science: Materials in Electronics, 2012. **23**(9): p. 1664-1672.
22. Gary Delserro, P.E., *Lead-Free Reliability Issues and Test Methods*, in *Delserro Engineering Solutions*. 2006, EE Evaluation Engineering: Easton, PA
23. Babaghorbani, P., S.M.L. Nai, and M. Gupta, *Development of lead-free Sn3.5Ag/SnO<sub>2</sub> nanocomposite solders*. Journal of Materials Science-materials in Electronics, 2009. **20**(6): p. 571-576.
24. El-Daly, A.A., et al., *Novel SiC nanoparticles-containing Sn–1.0Ag–0.5Cu solder with good drop impact performance*. Materials Science and Engineering: A, 2013. **578**(0): p. 62-71.
25. Gain, A.K., Y.C. Chan, and W.K.C. Yung, *Microstructure, thermal analysis and hardness of a Sn–Ag–Cu–1wt% nano-TiO<sub>2</sub> composite solder on flexible ball grid array substrates*. Microelectronics Reliability, 2011. **51**(5): p. 975-984.
26. Geranmayeh, A.R., R. Mahmudi, and M. Kangooie, *High-temperature shear strength of lead-free Sn–Sb–Ag/Al<sub>2</sub>O<sub>3</sub> composite solder*. Materials Science and Engineering: A, 2011. **528**(12): p. 3967-3972.
27. Gupta, X.L.Z.a.M., *Development of lead-free Sn-0.7Cu/Al<sub>3</sub>O<sub>2</sub> nanocomposites solders with superior strength*. Journal of Physic D: Applied Physics, 2008. **41**: p. 7.
28. Jun SHEN, Y.L., Dongjiang WANG, *Nano ZrO<sub>2</sub> Particulate-reinforced Lead-Free Solder Composite*. J. Mater. Sci. Technol., 2006. **22**(04): p. 529-532.
29. Liu, P., P. Yao, and J. Liu, *Effect of SiC Nanoparticle Additions on Microstructure and Microhardness of Sn-Ag-Cu Solder Alloy*. Journal of Electronic Materials, 2008. **37**(6): p. 874-879.
30. M.A.A, M.S., et al., *Solderability of Sn-0.7Cu/Si<sub>3</sub>N<sub>4</sub> lead-free composite solder on Cu-substrate*. Physics Procedia, 2011. **22**(0): p. 299-304.
31. Mohd Salleh, M.A.A., et al., *Mechanical properties of Sn–0.7Cu/Si<sub>3</sub>N<sub>4</sub> lead-free composite solder*. Materials Science and Engineering: A, 2012. **556**(0): p. 633-637.
32. Shen, J. and Y.C. Chan, *Effects of ZrO<sub>2</sub> nanoparticles on the mechanical properties of Sn–Zn solder joints on Au/Ni/Cu pads*. Journal of Alloys and Compounds, 2009. **477**(1–2): p. 552-559.
33. Tang, Y., G.Y. Li, and Y.C. Pan, *Influence of TiO<sub>2</sub> nanoparticles on IMC growth in Sn–3.0Ag–0.5Cu–xTiO<sub>2</sub> solder joints in reflow process*. Journal of Alloys and Compounds, 2013. **554**(0): p. 195-203.
34. Tsao, L.C., et al., *Influence of TiO<sub>2</sub> nanoparticles addition on the microstructural and mechanical properties of Sn0.7Cu nano-composite solder*. Materials Science and Engineering: A, 2012. **545**(0): p. 194-200.
35. Tsao, L.C., et al., *Effects of nano-Al<sub>2</sub>O<sub>3</sub> particles on microstructure and mechanical properties of Sn3.5Ag0.5Cu composite solder ball grid array joints on Sn/Cu pads*. Materials & Design, 2013. **50**(0): p. 774-781.
36. Zhong, X. and M. Gupta, *High Strength Lead-Free Composite Solder Materials using Nano Al<sub>2</sub>O<sub>3</sub> as Reinforcement*. Advanced Engineering Materials, 2005. **7**(11): p. 1049-1054.
37. Ogunseitan, O.A., *Public Health and Environmental Benefits of Adopting Lead-Free Solders*. Journal of The Minerals, Metals & Materials Society, 2007. **59**(7): p. 12-17.
38. Suraski, K.S.a.D., *Lead Free Soldering Guide*. 2006, AIM Solder: Montreal.
39. Zhang, L. and K.N. Tu, *Structure and properties of lead-free solders bearing micro and nano particles*. Materials Science and Engineering: R: Reports, 2014. **82**: p. 1-32.
40. McDonald, S., et al., *Influence of Composition on the Morphology of Primary Cu<sub>6</sub>Sn<sub>5</sub> in Sn–4Cu Alloys*. Journal of Electronic Materials, 2013. **42**(2): p. 256-262.
41. Ma, H.T., et al., *In-situ study on growth behavior of Ag<sub>3</sub>Sn in Sn–3.5Ag/Cu soldering reaction by synchrotron radiation real-time imaging technology*. Journal of Alloys and Compounds, 2012. **537**(0): p. 286-290.
42. Yang, R.-W., et al., *Precipitation of large Ag<sub>3</sub>Sn intermetallic compounds in SnAg<sub>2.5</sub> microbumps after multiple reflows in 3D-IC packaging*. Materials Chemistry and Physics, 2012. **134**(1): p. 340-344.

43. Gain, A.K., Y.C. Chan, and W.K.C. Yung, *Effect of additions of ZrO<sub>2</sub> nano-particles on the microstructure and shear strength of Sn–Ag–Cu solder on Au/Ni metallized Cu pads*. Microelectronics Reliability, 2011. **51**(12): p. 2306-2313.
44. Tsao, L.C., et al., *Effects of nano-Al<sub>2</sub>O<sub>3</sub> additions on microstructure development and hardness of Sn<sub>3.5</sub>Ag<sub>0.5</sub>Cu solder*. Materials & Design, 2010. **31**(10): p. 4831-4835.
45. Chuang, T.H., et al., *Strengthening mechanism of nano-Al<sub>2</sub>O<sub>3</sub> particles reinforced Sn<sub>3.5</sub>Ag<sub>0.5</sub>Cu lead-free solder*. Journal of Materials Science: Materials in Electronics, 2010. **22**(8): p. 1021-1027.
46. El-Daly, A.A., et al., *Microstructural modifications and properties of SiC nanoparticles-reinforced Sn–3.0Ag–0.5Cu solder alloy*. Materials & Design, 2015. **65**(0): p. 1196-1204.
47. Nai, S.M.L., J. Wei, and M. Gupta, *Influence of ceramic reinforcements on the wettability and mechanical properties of novel lead-free solder composites*. Thin Solid Films, 2006. **504**(1–2): p. 401-404.
48. Guo, F., *Composite lead-free electronic solders*. Lead-Free Electronic Solders, 2006. **18**(1-3): p. 129-145.
49. Subramanian, K.N. and F. Guo, *High-Temperature Lead-Free Solders with Dispersoids*, in *Handbook of Lead-Free Solder Technology for Microelectronic Assemblies*. 2004, Marcel Dekker: New York. p. 301-330.
50. Shen, J. and Y.C. Chan, *Research advances in nano-composite solders*. Microelectronics Reliability, 2009. **49**(3): p. 223-234.
51. Hwang, S.-Y., J.-W. Lee, and Z.-H. Lee, *Microstructure of a lead-free composite solder produced by an in-situ process*. Journal of Electronic Materials, 2002. **31**(11): p. 1304-1308.
52. De Monlevade, E. and W. Peng, *Failure Mechanisms and Crack Propagation Paths in Thermally Aged Pb-Free Solder Interconnects*. Journal of Electronic Materials, 2007. **36**(7): p. 783-797.
53. Wang, M., et al., *In-situ observation of fracture behavior of Sn–3.0Ag–0.5Cu lead-free solder during three-point bending tests in ESEM*. Materials Science and Engineering: A, 2012. **558**: p. 649-655.
54. Xian, J.W., S.A. Belyakov, and C.M. Gourlay, *Controlling Bulk Cu<sub>6</sub>Sn<sub>5</sub> Nucleation in Sn<sub>0.7</sub>Cu/Cu Joints with Al Micro-alloying*. Journal of Electronic Materials, 2015. **45**(1): p. 69-78.
55. Hung, F.-Y., et al., *Resonant characteristics of the microelectronic Sn–Cu solder*. Journal of Alloys and Compounds, 2008. **457**(1–2): p. 171-176.
56. Lewis, D., et al., *Determination of the eutectic structure in the Ag–Cu–Sn system*. Journal of Electronic Materials. **31**(2): p. 161-167.
57. Park, J.Y., et al., *Phase equilibria studies of Sn–Ag–Cu eutectic solder using differential cooling of Sn–3.8Ag–0.7 Cu alloys*. Journal of Electronic Materials, 2003. **32**(11): p. 1297-1302.
58. Lee, H.-T. and Y.-F. Chen, *Evolution of Ag<sub>3</sub>Sn intermetallic compounds during solidification of eutectic Sn–3.5Ag solder*. Journal of Alloys and Compounds, 2011. **509**(5): p. 2510-2517.
59. Kim, K.S., S.H. Huh, and K. Suganuma, *Effects of intermetallic compounds on properties of Sn–Ag–Cu lead-free soldered joints*. Journal of Alloys and Compounds, 2003. **352**(1–2): p. 226-236.
60. Spinelli, J.E. and A. Garcia, *Microstructural development and mechanical properties of hypereutectic Sn–Cu solderalloys*. Materials Science and Engineering: A, 2013. **568**: p. 195-201.
61. Chinnam, R.K., et al., *Evolution of the microstructure of Sn–Ag–Cu solder joints exposed to ultrasonic waves during solidification*. Acta Materialia, 2011. **59**(4): p. 1474-1481.
62. Mardare, C.C. and A.W. Hassel, *Influence of cooling speed on the solidification of a hyper-eutectic Cu–Sn alloy*. physica status solidi (a), 2012. **209**(5): p. 825-831.
63. Tian, Y., et al., *Relationship between morphologies and orientations of Cu<sub>6</sub>Sn<sub>5</sub> grains in Sn<sub>3.0</sub>Ag<sub>0.5</sub>Cu solder joints on different Cu pads*. Materials Characterization, 2014. **88**: p. 58-68.
64. Tai, F., et al., *Processing and creep properties of Sn–Cu composite solders with small amounts of nanosized Ag reinforcement additions*. Journal of Electronic Materials, 2005. **34**(11): p. 1357-1362.

65. Shen, J., et al., *Strengthening effects of ZrO<sub>2</sub> nanoparticles on the microstructure and microhardness of Sn-3.5Ag lead-free solder*. Journal of Electronic Materials 2006. **35**: p. 1672-1679.
66. Kao, S.-T., Y.-C. Lin, and J.-G. Duh, *Controlling intermetallic compound growth in SnAgCu/Ni-P solder joints by nanosized Cu<sub>6</sub>Sn<sub>5</sub> addition*. Journal of Electronic Materials, 2006. **35**(3): p. 486-493.
67. Mavoori, H. and S. Jin, *New, creep-resistant, low melting point solders with ultrafine oxide dispersions*. Journal of Electronic Materials, 1998. **27**(11): p. 1216-1222.
68. Mavoori, H. and S. Jin, *Significantly enhanced creep resistance in low-melting-point solders through nanoscale oxide dispersions*. Applied Physics Letters, 1998. **73**(16): p. 2290-2292.
69. Lee, H.-Y. and J.-G. Duh, *Influence of Ni concentration and Ni<sub>3</sub>Sn<sub>4</sub> nanoparticles on morphology of Sn-Ag-Ni solders by mechanical alloying*. Journal of Electronic Materials, 2006. **35**(3): p. 494-503.
70. Lin, D., et al., *The influence of copper nanopowders on microstructure and hardness of lead-tin solder*. Materials Letters, 2002. **53**(4-5): p. 333-338.
71. Lin, D.C., et al., *An investigation of nanoparticles addition on solidification kinetics and microstructure development of tin-lead solder*. Materials Science and Engineering: A, 2003. **360**(1-2): p. 285-292.
72. Lin, D.C., et al., *Influence of titanium dioxide nanopowder addition on microstructural development and hardness of tin-lead solder*. Materials Letters, 2003. **57**(21): p. 3193-3198.
73. Liu, J.P., et al., *Development of creep-resistant, nanosized Ag particle-reinforced Sn-Pb composite solders*. Journal of Electronic Materials, 2004. **33**(9): p. 958-963.
74. Babaghorbani, P. and M. Gupta, *Enhancing the Mechanical Response of a Lead-Free Solder Using an Energy-Efficient Microwave Sintering Route*. Journal of Electronic Materials, 2008. **37**(6): p. 860-866.
75. Kumar, K.M., V. Kripesh, and A.A.O. Tay, *Single-wall carbon nanotube (SWCNT) functionalized Sn-Ag-Cu lead-free composite solders*. Journal of Alloys and Compounds, 2008. **450**(1-2): p. 229-237.
76. Nai, S.M.L., et al., *Using Microwave-Assisted Powder Metallurgy Route and Nano-size Reinforcements to Develop High-Strength Solder Composites*. Journal of Materials Engineering and Performance, 2010. **19**(3): p. 335-341.
77. Nai, S.M.L., J. Wei, and M. Gupta, *Interfacial intermetallic growth and shear strength of lead-free composite solder joints*. Journal of Alloys and Compounds, 2009. **473**(1-2): p. 100-106.
78. Niranjani, V.L., et al., *Influence of temperature and strain rate on tensile properties of single walled carbon nanotubes reinforced Sn-Ag-Cu lead free solder alloy composites*. Materials Science and Engineering: A, 2011. **529**(0): p. 257-264.
79. Zhong, X.L. and M. Gupta. *Effect of Type of Reinforcement at Nanolength Scale on the Tensile Properties of Sn-0.7Cu Solder Alloy*. in *Electronics Packaging Technology Conference, 2008. EPTC 2008. 10th*. 2008.
80. *Introducing PM: The Process*. Available from: <https://www.mpif.org/IntroPM/process.asp?linkid=2>.
81. Reardon, A.C., *Metallurgy for the Non-Metallurgist (2nd Edition)*. ASM International.
82. Buschow, K.H.J.r., et al., *Encyclopedia of Materials - Science and Technology, Volumes 1-11*. Elsevier.
83. DeGarmo, E.P., J.T. Black, and R.A. Kohser, *Materials & Processes in Manufacturing*. 10th Edition ed. 2003: Wiley.
84. Oghbaei, M. and O. Mirzaee, *Microwave versus conventional sintering: A review of fundamentals, advantages and applications*. Journal of Alloys and Compounds, 2010. **494**: p. 175-189.
85. Gupta, M. and E.W. Wai Leong, *Microwave Heating*, in *Microwaves and Metals*. 2007, John Wiley & Sons (Asia) Pte Ltd. p. 43-63.
86. German, R.M. *Powder metallurgy science*. 1994.
87. Senthilkumar, V., A. Balaji, and H. Ahamed, *Effect of secondary processing and nanoscale reinforcement on the mechanical properties of Al-TiC composites*. Journal of Minerals & Materials Characterization & Engineering, 2011. **10**(14): p. 1293-1306.

88. Dariavach, N., et al., *Intermetallic growth kinetics for Sn-Ag, Sn-Cu, and Sn-Ag-Cu lead-free solders on Cu, Ni, and Fe-42Ni substrates*. Journal of Electronic Materials, 2006. **35**(7): p. 1581-1592.
89. Mookam, N. and K. Kanlayasiri, *Evolution of Intermetallic Compounds between Sn-0.3Ag-0.7Cu Low-silver Lead-free Solder and Cu Substrate during Thermal Aging*. Journal of Materials Science & Technology, 2012. **28**(1): p. 53-59.
90. Mannan, S. and M.P. Clode, *Dissolution of solids in contact with liquid solder*. Soldering & Surface Mount Technology, 2004. **16**(3): p. 31-33.
91. Izuta, G., T. Tanabe, and K. Suganuma, *Dissolution of copper on Sn-Ag-Cu system lead free solder*. Soldering & Surface Mount Technology, 2007. **19**(2): p. 4-11.
92. Snugovsky, L., et al., *Experiments on interaction of liquid tin with solid copper*. Materials Science and Technology 2003. **19**: p. 866-874.
93. Shangguan, D., 2. *Microstructural Evolution and Interfacial Interactions in Lead-Free Solder Interconnects*, in *Lead-Free Solder - Interconnect Reliability*. ASM International.
94. Kim, J.-M., et al., *Impact reliability estimation of lead free solder joint with IMC layer*. Thin Solid Films, 2009. **517**(14): p. 4255-4259.
95. Qin, H.B., X.P. Li, and X.P. Zhang. *Influence of thickness of interfacial IMC layer and solder mask layer on mechanical reliability of micro-scale BGA structure interconnects*. in *Electronic Packaging Technology and High Density Packaging (ICEPT-HDP)*, 2012 13th International Conference on. 2012.
96. Yoon, J.-W., et al., *Reliability investigation and interfacial reaction of ball-grid-array packages using the lead-free Sn-Cu solder*. Journal of Electronic Materials, 2004. **33**(10): p. 1190-1199.
97. Tu, K.N., *Solder Joint Technology: Materials, Properties, and Reliability*. 2007: Springer.
98. Chao, B., et al., *Investigation of diffusion and electromigration parameters for Cu-Sn intermetallic compounds in Pb-free solders using simulated annealing*. Acta Materialia, 2007. **55**(8): p. 2805-2814.
99. He, M., Z. Chen, and G. Qi, *Solid state interfacial reaction of Sn-37Pb and Sn-3.5Ag solders with Ni-P under bump metallization*. Acta Materialia, 2004. **52**(7): p. 2047-2056.
100. Li, J.F., et al., *Interfacial reactions between molten Sn-Bi-X solders and Cu substrates for liquid solder interconnects*. Acta Materialia, 2006. **54**(11): p. 2907-2922.
101. Park, M.S. and R. Arróyave, *Early stages of intermetallic compound formation and growth during lead-free soldering*. Acta Materialia, 2010. **58**(14): p. 4900-4910.
102. Lee, B.-J., N.M. Hwang, and H.M. Lee, *Prediction of interface reaction products between Cu and various solder alloys by thermodynamic calculation*. Acta Materialia, 1997. **45**(5): p. 1867-1874.
103. Schaefer, M., R. Fournelle, and J. Liang, *Theory for intermetallic phase growth between cu and liquid Sn-Pb solder based on grain boundary diffusion control*. Journal of Electronic Materials, 1998. **27**(11): p. 1167-1176.
104. Tu, K.N., et al., *Wetting reaction versus solid state aging of eutectic SnPb on Cu*. Journal of Applied Physics, 2001. **89**(9): p. 4843-4849.
105. Liu, X.D., et al., *Effect of graphene nanosheets reinforcement on the performance of Sn-Ag-Cu lead-free solder*. Materials Science and Engineering: A, 2013. **562**(0): p. 25-32.
106. Tsao, L.C., *Suppressing effect of 0.5wt.% nano-TiO<sub>2</sub> addition into Sn-3.5Ag-0.5Cu solder alloy on the intermetallic growth with Cu substrate during isothermal aging*. Journal of Alloys and Compounds, 2011. **509**(33): p. 8441-8448.
107. Fouzder, T., et al., *Influence of SrTiO<sub>3</sub> nano-particles on the microstructure and shear strength of Sn-Ag-Cu solder on Au/Ni metallized Cu pads*. Journal of Alloys and Compounds, 2011. **509**(5): p. 1885-1892.
108. Gain, A.K. and Y.C. Chan, *Growth mechanism of intermetallic compounds and damping properties of Sn-Ag-Cu-1 wt% nano-ZrO<sub>2</sub> composite solders*. Microelectronics Reliability, 2014. **54**(5): p. 945-955.
109. Haseeb, A.S.M.A., M.M. Arafat, and M.R. Johan, *Stability of molybdenum nanoparticles in Sn-3.8Ag-0.7Cu solder during multiple reflow and their influence on interfacial intermetallic compounds*. Materials Characterization, 2012. **64**: p. 27-35.

110. Haseeb, A.S.M.A. and T.S. Leng, *Effects of Co nanoparticle addition to Sn–3.8Ag–0.7Cu solder on interfacial structure after reflow and ageing*. Intermetallics, 2011. **19**(5): p. 707-712.
111. Chan, Y.H., M.M. Arafat, and A.S.M.A. Haseeb, *Effects of reflow on the interfacial characteristics between Zn nanoparticles containing Sn-3.8Ag-0.7Cu solder and copper substrate*. Soldering & Surface Mount Technology, 2013. **25**(2): p. 91-98.
112. Wang, T., et al., *Growth behavior of Cu<sub>6</sub>Sn<sub>5</sub> in Sn–6.5 Cu solders under DC considering trace Al: In situ observation*. Intermetallics, 2015. **58**: p. 84-90.
113. El-Daly, A.A. and A.E. Hammad, *Enhancement of creep resistance and thermal behavior of eutectic Sn–Cu lead-free solder alloy by Ag and In-additions*. Materials & Design, 2012. **40**(0): p. 292-298.
114. Wang, X., et al., *Strengthening mechanism of SiC-particulate reinforced Sn–3.7Ag–0.9Zn lead-free solder*. Journal of Alloys and Compounds, 2009. **480**(2): p. 662-665.
115. El-Daly, A.A., et al., *Structural characterization and creep resistance of nano-silicon carbide reinforced Sn–1.0Ag–0.5Cu lead-free solder alloy*. Materials & Design, 2014. **55**(0): p. 837-845.
116. Gain, A.K., et al., *Microstructure, kinetic analysis and hardness of Sn–Ag–Cu–1 wt% nano-ZrO<sub>2</sub> composite solder on OSP-Cu pads*. Journal of Alloys and Compounds, 2011. **509**(7): p. 3319-3325.
117. Tsao, L.C., *An investigation of microstructure and mechanical properties of novel Sn<sub>3.5</sub>Ag<sub>0.5</sub>Cu–XTiO<sub>2</sub> composite solders as functions of alloy composition and cooling rate*. Materials Science and Engineering: A, 2011. **529**(0): p. 41-48.
118. Tang, Y., G.Y. Li, and Y.C. Pan, *Effects of TiO<sub>2</sub> nanoparticles addition on microstructure, microhardness and tensile properties of Sn–3.0Ag–0.5Cu–xTiO<sub>2</sub> composite solder*. Materials & Design, 2014. **55**(0): p. 574-582.
119. Tai, F., et al., *Effects of nano-structured particles on microstructure and microhardness of Sn–Ag solder alloy*. Journal of Materials Science: Materials in Electronics, 2010. **21**(7): p. 702-707.
120. El-Daly, A.A. and A.E. Hammad, *Development of high strength Sn–0.7Cu solders with the addition of small amount of Ag and In*. Journal of Alloys and Compounds, 2011. **509**(34): p. 8554-8560.
121. Zhao, Z., et al., *Effect of nano-Al<sub>2</sub>O<sub>3</sub> reinforcement on the microstructure and reliability of Sn–3.0Ag–0.5Cu solder joints*. Microelectronics Reliability, 2016. **60**: p. 126-134.
122. Zhao, X., et al., *Effect of  $\gamma$ -Fe<sub>2</sub>O<sub>3</sub> nanoparticles size on the properties of Sn-1.0Ag–0.5Cu nano-composite solders and joints*. Journal of Alloys and Compounds, 2016. **662**: p. 272-282.
123. Gu, Y., et al., *Effect of nano-Fe<sub>2</sub>O<sub>3</sub> additions on wettability and interfacial intermetallic growth of low-Ag content Sn–Ag–Cu solders on Cu substrates*. Journal of Alloys and Compounds, 2015. **627**: p. 39-47.
124. Xu, L., et al., *Design and performance of Ag nanoparticle-modified graphene/SnAgCu lead-free solders*. Materials Science and Engineering: A, 2016. **667**: p. 87-96.
125. Nai, S.M.L., J. Wei, and M. Gupta, *Lead-free solder reinforced with multiwalled carbon nanotubes*. Journal of Electronic Materials, 2006. **35**(7): p. 1518-1522.
126. Han, Y.D., et al., *Development of a Sn–Ag–Cu solder reinforced with Ni-coated carbon nanotubes*. Journal of Materials Science: Materials in Electronics, 2011. **22**(3): p. 315-322.
127. Wang, J., et al., *Microstructure and Mechanical Properties of Tin-Bismuth Solder Reinforced by Aluminum Borate Whiskers*. Journal of Electronic Materials, 2015. **44**(10): p. 3872-3879.
128. Mohd Salleh, M.A.A., et al., *Mechanical properties of Sn–0.7Cu/Si<sub>3</sub>N<sub>4</sub> lead-free composite solder*. Materials Science and Engineering: A, 2012. **556**: p. 633-637.
129. Tsao, L.C., et al., *Influence of TiO<sub>2</sub> nanoparticles addition on the microstructural and mechanical properties of Sn<sub>0.7</sub>Cu nano-composite solder*. Materials Science and Engineering: A, 2012. **545**: p. 194-200.
130. Chang, S.Y., et al., *Effect of addition of TiO<sub>2</sub> nanoparticles on the microstructure, microhardness and interfacial reactions of Sn<sub>3.5</sub>AgXCu solder*. Materials & Design, 2011. **32**(10): p. 4720-4727.

131. Tsao, L.C., *Suppressing effect of 0.5 wt.% nano-TiO<sub>2</sub> addition into Sn–3.5Ag–0.5Cu solder alloy on the intermetallic growth with Cu substrate during isothermal aging*. Journal of Alloys and Compounds, 2011. **509**(33): p. 8441-8448.
132. Tsao, L.C., *An investigation of microstructure and mechanical properties of novel Sn3.5Ag0.5Cu–XTiO<sub>2</sub> composite solders as functions of alloy composition and cooling rate*. Materials Science and Engineering: A, 2011. **529**: p. 41-48.
133. Tsao, L.C., et al., *Effect of nano-TiO<sub>2</sub> particles and cooling rate on the thermal, microstructure and mechanical properties of novel low-ag Sn1.5Sb1Ag solders*. Materials Science and Engineering: A, 2016. **658**: p. 159-166.
134. Boettinger, W.J., et al., *Solidification microstructures: recent developments, future directions*. Acta Materialia, 2000. **48**(1): p. 43-70.
135. Arfaei, B. and E. Cotts, *Correlations Between the Microstructure and Fatigue Life of Near-Eutectic Sn-Ag-Cu Pb-Free Solders*. Journal of Electronic Materials, 2009. **38**(12): p. 2617-2627.
136. Liu, W. and N.-C. Lee, *The effects of additives to SnAgCu alloys on microstructure and drop impact reliability of solder joints*. JOM, 2007. **59**(7): p. 26-31.
137. Lu, M., et al., *Effect of Sn grain orientation on electromigration degradation mechanism in high Sn-based Pb-free solders*. Applied Physics Letters, 2008. **92**(21): p. 211909.
138. Frear, D.R., *Issues related to the implementation of Pb-free electronic solders in consumer electronics*. Journal of Materials Science: Materials in Electronics, 2006. **18**(1): p. 319-330.